



December 1995 • NREL/TP-442-7817

Effects of Grit Roughness and Pitch Oscillations on the S809 Airfoil

Airfoil Performance Report, Revised (12/99)

R. Reuss Ramsay
M. J. Hoffmann
G.M. Gregorek
The Ohio State University
Columbus, Ohio

National Renewable Energy Laboratory
1617 Cole Boulevard
Golden, Colorado 80401-3393
A national laboratory of the U.S. Department of Energy
Managed by Midwest Research Institute
for the U.S. Department of Energy
under contract No. DE-AC36-83CH10093

Foreword

Airfoils for wind turbines have been selected by comparing data from different wind tunnels, tested under different conditions, making it difficult to make accurate comparisons. Most wind tunnel data sets do not contain airfoil performance in stall commonly experienced by turbines operating in the field. Wind turbines commonly experience extreme roughness for which there is very little data. Finally recent tests have shown that dynamic stall is a common occurrence for most wind turbines operating in yawed, stall or turbulent conditions. Very little dynamic stall data exists for the airfoils of interest to wind turbine designer. In summary, very little airfoil performance data exists which is appropriate for wind turbine design.

Recognizing the need for a wind turbine airfoil performance data base the National Renewable Energy Laboratory (NREL), funded by the US Department of Energy, awarded a contract to Ohio State University (OSU) to conduct a wind tunnel test program. Under this program OSU has tested a series of popular wind turbine airfoils. A standard test matrix has been developed to assure that each airfoil was tested under the same conditions. The test matrix was developed in partnership with industry and is intended to include all of the operating conditions experienced by wind turbines. These conditions include airfoil performance at high angles of attack, rough leading edge (bug simulation), steady and unsteady angles of attack.

Special care has been taken to report as much of the test conditions and raw as practical so that designers can make their own comparisons and focus on details of the data relevant to their design goals. Some of the airfoil coordinates are proprietary to NREL or an industry partner. To protect the information which defines the exact shape of the airfoil the coordinates have not been included in the report. Instructions on how to obtain these coordinates may be obtained by contacting C.P. (Sandy) Butterfield at NREL.

C. P. (Sandy) Butterfield
Wind Technology Division
National Renewable Energy Laboratory
1617 Cole Blvd.
Golden, Colorado, 80401 USA
Internet Address: Sandy_Butterfield@NREL.GOV
Phone 303-384-6902
FAX 303-384-6901

Preface

The Ohio State University Aeronautical and Astronautical Research Laboratory is conducting a series of steady state and unsteady wind tunnel tests on a set of airfoils that have been or will be used for horizontal-axis wind turbines. The purpose of these tests is to investigate the effect of pitch oscillations and leading edge grit roughness (LEGR) on airfoil performance. The study of pitch oscillation effects can help to understand the behavior of horizontal-axis wind turbines in yaw. The results of these tests will aid in the development of new airfoil performance codes that account for unsteady behavior and also aid in the design of new airfoils for wind turbines. The application of LEGR simulates surface irregularities that occur on wind turbine blades. These irregularities are caused by the accumulation of insect debris, ice, and/or the aging process and can significantly reduce the power output of horizontal-axis wind turbines. The experimental results from the application of LEGR will promote the development of airfoils which are less sensitive to this kind of roughness.

The present work was made possible by the efforts and financial support of the National Renewable Energy Laboratory which provided major funding and technical monitoring, the U.S. Department of Energy is credited for its funding of this document through the National Renewable Energy Laboratory under contract number DE-AC36-83CH10093 and U.S. Windpower Incorporated which provided technical assistance. The staff of The Ohio State University Aeronautical and Astronautical Research Laboratory appreciate the contributions made by personnel from both organizations. In addition, the authors would like to recognize the efforts of the following student research assistants: Fernando Falasca, Jolanta M. Janiszewska, and Monica Angelats i Coll.

Summary

The S809 airfoil was tested in The Ohio State University Aeronautical and Astronautical Research Laboratory 3x5 subsonic wind tunnel under steady state and unsteady conditions. The test defined baseline conditions for steady state angles of attack from -20° to $+40^\circ$ and examined unsteady behavior by oscillating the model about its pitch axis for three mean angles, three frequencies, and two amplitudes. For all oscillating cases, Reynolds numbers of 0.75, 1, 1.25, and 1.4 million were used. In addition, the above conditions were repeated after the application of leading edge grit roughness (LEGR) to determine contamination effects on airfoil performance.

Typical steady state results of the S809 testing at Reynolds number of 1 million, showed a baseline maximum lift coefficient of 1.03 at 15.2° angle of attack. The application of LEGR reduced the maximum lift coefficient by as much as 16% and increased the minimum drag coefficient by more than 41%. The zero lift pitching moment of -0.0356 showed a 27.5% reduction in magnitude to -0.0258 with LEGR applied.

Data were also obtained for two pitch oscillation amplitudes: $\pm 5.5^\circ$ and $\pm 10^\circ$. The larger amplitude consistently gave a higher maximum lift coefficient than the smaller amplitude and both unsteady maximum lift coefficients were greater than the steady state values. Stall is delayed on the airfoil while the angle of attack is increasing, thereby causing an increase in maximum lift coefficient. A hysteresis behavior was exhibited for all the unsteady test cases. The hysteresis loops were larger for the higher reduced frequencies and for the larger amplitude oscillations. As in the steady case, the effect of LEGR in the unsteady case was to reduce the lift coefficient at high angles of attack. In addition, with LEGR, the hysteresis behavior persisted into lower angles of attack than for the clean case.

In general, the unsteady maximum lift coefficient was from 4% to 86% higher than the steady state maximum lift coefficient, and variation in the quarter chord pitching moment coefficient magnitude was from -83% to 195% relative to steady state values at high angles of attack. These findings indicate the importance of considering the unsteady flow behavior occurring in wind turbine operation in order to obtain accurate load estimates.

Contents

	Page
--	-------------

Preface	iv
Summary	v
List of Symbols	ix
Introduction	1
Experimental Facility	2
Wind Tunnel	2
Oscillation System	2
Model Details	4
Test Equipment and Procedures	6
Data Acquisition	6
Data Reduction	7
Test Matrix	8
Results and Discussion	10
Comparison with Theory	10
Steady State Data	11
Unsteady Data	13
Summary of Results	20
References	23
Appendix A: Model and Surface Pressure Tap Coordinates	A-1
Appendix B: Steady State Data	B-1
Appendix C: Unsteady Integrated Coefficients	C-1

List of Figures

Page

1. 3x5 subsonic wind tunnel, top view.	2
2. 3x5 subsonic wind tunnel, side view.	2
3. 3x5 wind tunnel oscillation system.	3
4. S809 airfoil section with thickened trailing edge.	4
5. Measured-to-desired model coordinates difference curves.	4
6. Roughness pattern.	5
7. Data acquisition schematic.	6
8. Comparison with theory, C_l vs α	10
9. Comparison with theory, C_m vs α	10
10. Comparison with theory, C_p vs x/c , $\alpha=0.0^\circ$	10
11. Comparison with theory, C_p vs x/c , $\alpha=6.1^\circ$	10
12. C_l vs α , clean.	11
13. C_l vs α , LEGR, $k/c=0.0019$	11
14. C_m vs α , clean.	11
15. C_m vs α , LEGR, $k/c=0.0019$	11
16. Drag polar, clean.	12
17. Drag polar, LEGR, $k/c=0.0019$	12
18. Pressure distribution, $\alpha=2.0^\circ$	12
19. Pressure distribution, $\alpha=12.2^\circ$	12
20. Clean, C_l vs α , $\omega_{red}=0.026$, $\pm 5.5^\circ$	13
21. Clean, C_l vs α , $\omega_{red}=0.077$, $\pm 5.5^\circ$	13
22. Clean, C_m vs α , $\omega_{red}=0.026$, $\pm 5.5^\circ$	14
23. Clean, C_m vs α , $\omega_{red}=0.077$, $\pm 5.5^\circ$	14
24. LEGR, C_l vs α , $\omega_{red}=0.025$, $\pm 5.5^\circ$	14
25. LEGR, C_l vs α , $\omega_{red}=0.079$, $\pm 5.5^\circ$	14
26. LEGR, C_m vs α , $\omega_{red}=0.025$, $\pm 5.5^\circ$	15
27. LEGR, C_m vs α , $\omega_{red}=0.079$, $\pm 5.5^\circ$	15
28. Clean, C_l vs α , $\omega_{red}=0.026$, $\pm 10^\circ$	15
29. Clean, C_l vs α , $\omega_{red}=0.078$, $\pm 10^\circ$	15
30. Clean, C_m vs α , $\omega_{red}=0.026$, $\pm 10^\circ$	16
31. Clean, C_m vs α , $\omega_{red}=0.078$, $\pm 10^\circ$	16
32. LEGR, C_l vs α , $\omega_{red}=0.025$, $\pm 10^\circ$	16
33. LEGR, C_l vs α , $\omega_{red}=0.079$, $\pm 10^\circ$	16
34. LEGR, C_m vs α , $\omega_{red}=0.025$, $\pm 10^\circ$	17
35. LEGR, C_m vs α , $\omega_{red}=0.079$, $\pm 10^\circ$	17
36. Unsteady pressure distribution, clean, $\omega_{red}=0.053$, $14\pm 10^\circ$	17
37. Unsteady pressure distribution, LEGR, $\omega_{red}=0.053$, $14\pm 10^\circ$	18
38. Unsteady pressure distribution, clean, $\omega_{red}=0.050$, $14\pm 5.5^\circ$	18
39. Unsteady pressure distribution, clean, $\omega_{red}=0.055$, $20\pm 5.5^\circ$	19

List of Tables

	Page
1. S809 Aerodynamic Parameters Summary	20
2. S809, Unsteady, Clean, $\pm 5.5^\circ$	20
3. S809, Unsteady, LEGR, $\pm 5.5^\circ$	21
4. S809, Unsteady, Clean, $\pm 10^\circ$	21
5. S809, Unsteady, LEGR, $\pm 10^\circ$	22

List of Symbols

AOA	Angle of attack
A/C, a.c.	Alternating current
c	Model chord length
C_d	Drag coefficient
$C_{d\min}$	Minimum drag coefficient
C_{dp}	Pressure drag coefficient
C_{dw}	Wake drag coefficient
C_{du}	Uncorrected drag coefficient
C_l	Lift coefficient
$C_{l\max}$	Maximum lift coefficient
$C_{l\text{ dec}}$	Lift coefficient at angle of maximum lift, but with angle of attack decreasing
C_{lu}	Uncorrected lift coefficient
$C_m, C_{m\frac{1}{4}}$	Pitching moment coefficient about the quarter chord
$C_{m\text{ dec}}$	Pitching moment coefficient at angle of maximum lift, but with angle of attack decreasing
$C_{m\text{ inc}}$	Pitching moment coefficient at angle of maximum lift, but with angle of attack increasing
C_{mo}	Pitching moment coefficient about the quarter chord, at zero lift
$C_{m\frac{1}{4}u}$	Uncorrected pitching moment coefficient about the quarter chord
C_p	Pressure coefficient, $(p - p_\infty)/q_\infty$
$C_{p\min}$	Minimum pressure coefficient
f	Frequency
h	Wind tunnel test section height
hp, Hp, HP	Horsepower
Hz	Hertz
k	Grit particle size
k/c	Grit particle size divided by airfoil model chord length
p	Pressure
q	Dynamic pressure
q_u	Uncorrected dynamic pressure
q_w	Dynamic pressure through the model wake
q_∞	Free stream dynamic pressure
Re	Reynolds number
Re_u	Uncorrected Reynolds number
t	Time
U_∞	Corrected free stream velocity
V	Velocity
V_u	Uncorrected velocity
x	Axis parallel to model reference line
y	Axis perpendicular to model reference line

α	Angle of attack
α_{dec}	Decreasing angle of attack
α_{inc}	Increasing angle of attack
α_m	Median angle of attack
α_{mean}	Mean angle of attack
α_u	Uncorrected angle of attack
ϵ	Tunnel solid wall correction scalar
ϵ_{sb}	Solid blockage correction scalar
ϵ_{wb}	Wake blockage correction scalar
Λ	Body-shape factor
π	3.1416
σ	Tunnel solid wall correction parameter
$\omega_{\text{red}}, \omega_{\text{reduced}}$	Reduced frequency, $\pi f_c/U_\infty$

Introduction

Horizontal axis wind turbine rotors experience unsteady aerodynamics due to wind shear when the rotor is yawed, when the rotor blades pass through the support tower wake, and when the wind is gusting. An understanding of this unsteady behavior is necessary to assist in the design of new rotor airfoils. The rotors also experience performance degradation due to surface roughness. These surface irregularities are caused by the accumulation of insect debris, ice, and/or the aging process. Wind tunnel studies which examine both the steady and unsteady behavior of airfoils can help define the flow phenomena, and the resultant data can also be used to validate analytical computer codes.

An S809 airfoil model was tested in The Ohio State University Aeronautical and Astronautical Research Laboratory (OSU/AARL) 3x5 subsonic wind tunnel (3x5) under steady flow and stationary model conditions and also with the model undergoing pitch oscillations. To study the possible extent of performance loss due to surface roughness, a standard grit pattern (LEGR) was used to simulate leading edge contamination. After baseline cases were completed, the LEGR was applied for both steady state and model pitch oscillation cases. The Reynolds numbers used for steady state conditions were 0.75, 1, 1.25, and 1.5 million, while the angle of attack ranged from -20° to $+40^\circ$. With the model undergoing pitch oscillations, data were acquired at Reynolds numbers of 0.75, 1, 1.25, and 1.4 million, at frequencies of 0.6, 1.2, and 1.8 Hz. Two sine wave forcing functions were used, $\pm 5.5^\circ$ and $\pm 10^\circ$, at mean angles of attack of 8° , 14° , and 20° . For purposes herein, any reference to unsteady conditions means the model was in pitch oscillation about the quarter chord.

Experimental Facility

Wind Tunnel

The OSU/AARL 3×5 subsonic wind tunnel (3x5) was used to conduct tests on the S809 airfoil section. Schematics of the top and side views of the tunnel are shown in figures 1 and 2, respectively. This open circuit tunnel has a velocity range of 0 - 55 m/s (180 ft/sec) produced by a 2.4-meter (8-ft) diameter,

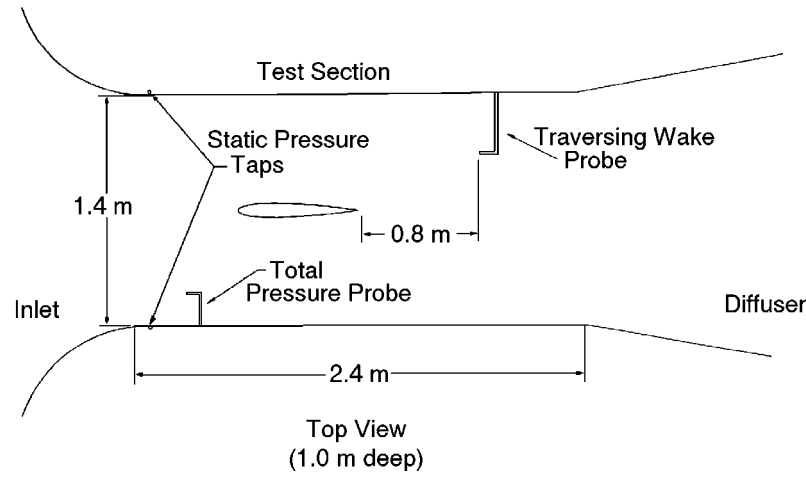


Figure 1. 3x5 subsonic wind tunnel, top view.

six-bladed fan. The fan is belt driven by a 93.2-kw (125-hp) three-phase a.c. motor connected to a variable frequency motor controller. Nominal test section dimensions are 1.0 m (39 inches) high by 1.4-m (55-inch) wide by 2.4-m (96-inch) long. The 457-mm (18-inch) chord airfoil model was mounted vertically in the test section. A steel tube through the quarter chord of the model was used to attach the model to the tunnel

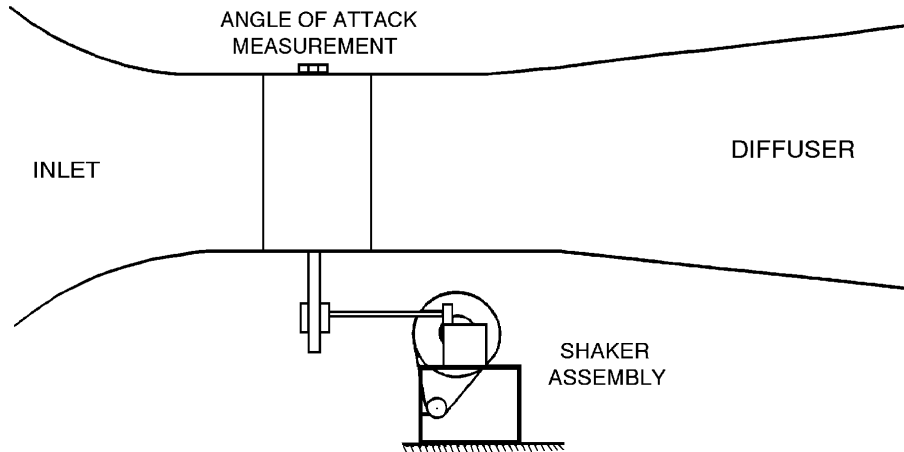


Figure 2. 3x5 subsonic wind tunnel, side view.

during testing. An angle of attack potentiometer was fastened to the model at the top of the tunnel, as shown in figure 2. The steady state angle of attack was adjusted with a worm gear drive attached to the model strut below the tunnel floor.

Oscillation System

Portions of the airfoil model testing required the use of a reliable pitch oscillation system. The OSU/AARL "shaker" system incorporated a face cam and follower arm attached to the model support tube below the wind tunnel floor, as shown in figure 3. The choice of cam governed the type and amplitude of the wave form produced. Sine wave forms having amplitudes of $\pm 5.5^\circ$ and $\pm 10^\circ$ were used for these tests. The wave form being defined by the equation

$$\alpha = \alpha_m + A \sin(2\pi ft)$$

where A is the respective amplitude. The shaker system was powered by a 5-hp a.c. motor with variable line frequency controller. The useable oscillating frequency range was 0.1 - 2.0 Hz, with three frequencies used for this test: 0.6, 1.2, and 1.8 Hz.

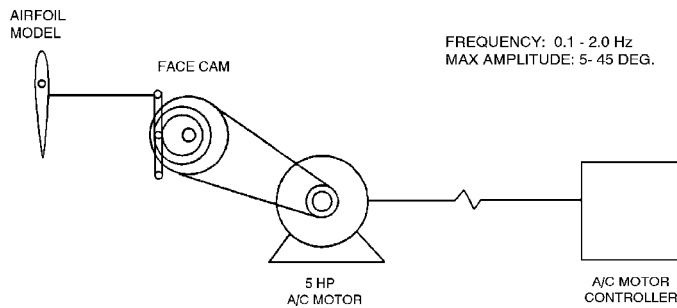


Figure 3. 3x5 wind tunnel oscillation system.

Model Details

A 457-mm (18-inch) constant chord S809 airfoil model was designed by OSU/AARL personnel and manufactured by others. Figure 4 shows the airfoil section while the model measured coordinates are given in Appendix A. The trailing edge was thickened to 1.25-mm (0.05-inch) for fabrication purposes. This

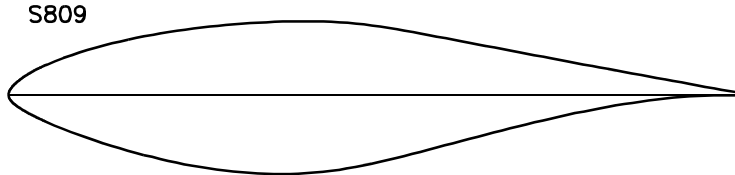


Figure 4. S809 airfoil section with thickened trailing edge.

thickness was added to the upper surface over the last 10% of the chord. The model was made of a sandwiched composite skin over ribs. The main load bearing member was a 38-mm (1.5-inch) diameter steel tube which passed through the model quarter chord station. Ribs and end plates were used to transfer loads from the composite skin to the steel tube. The final surface was hand worked using templates to attain given coordinates within a required tolerance of $\pm 0.25\text{-mm}$ ($\pm 0.01\text{-inch}$). The completed model was measured at three spanwise locations using a Sheffield-Cordax coordinate measurement machine. Measurements were made in English units and later converted to metric. Figure 5 shows the results of comparing measured-to-desired coordinates by calculating differences normal to the profiled surface at three stations on the model. The "spikes" apparent near the trailing edge are the result of the numerical methods used and are not real.

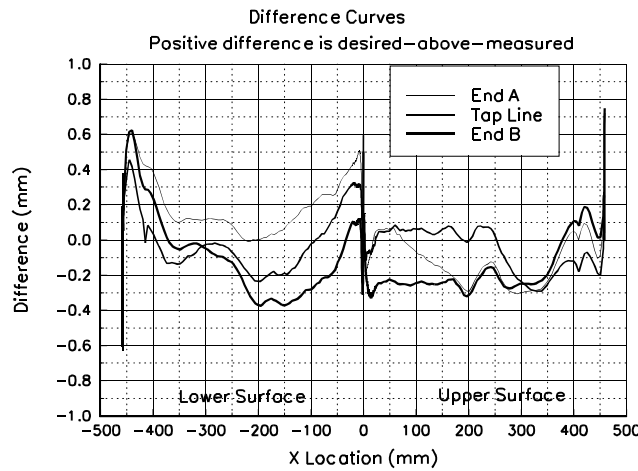


Figure 5. Measured-to-desired model coordinates difference curves.

To minimize pressure response times, which is important for the unsteady testing, the surface pressure tap lead-out lines had to be as short as possible. Consequently, a compartment was built into the model so pressure scanning modules could be installed inside the model. This compartment was accessed through a panel door fitted flush with the model contour on the lower (pressure) surface.

For test cases involving roughness, a standard, repeatable pattern with grit as roughness elements was desired. A roughness pattern, jointly developed by OSU/AARL and KENETECH, Windpower personnel using a molded insect pattern taken from a wind turbine in the field by personnel at the University of Texas

Permian Basin, was used. The particle density was 5 particles per cm^2 (32 particles per square inch) in the middle of the pattern, and thinned to 1.25 particles per cm^2 (8 particles per square inch) at the edge of the pattern. Figure 6 shows the roughness pattern. To make a usable template the pattern was repeatedly cut into a steel sheet 102 mm (4 inches) wide and 91 cm (3 ft) long with holes just large enough for one piece of grit. Based on average particle size from the field specimen, standard #40 lapidary grit was chosen for the roughness elements, giving $k/c=0.0019$ for a 457 mm (18 inch) chord model.

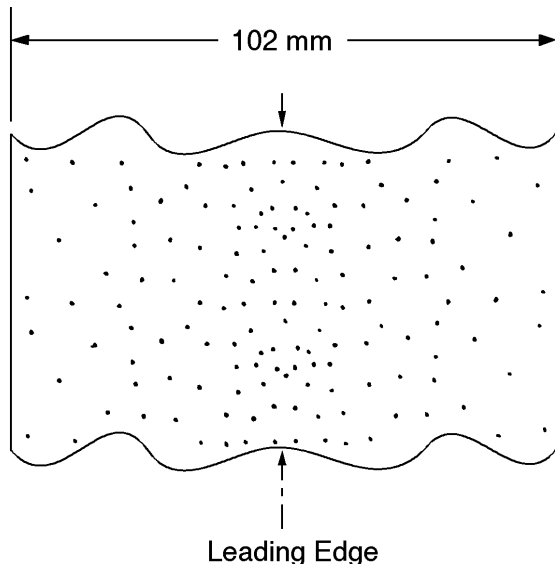


Figure 6. Roughness pattern.

To use the template, 102-mm (4-inch) wide double-tack tape was applied to one side of the template and grit was poured and brushed from the opposite side. The tape was then removed from the template and transferred to the model. This method allowed the same roughness pattern to be replicated for any test.

Test Equipment and Procedures

Data Acquisition

Data were acquired and processed from 60 surface pressure taps, four individual tunnel pressure transducers, an angle of attack potentiometer, a wake probe position potentiometer, and a tunnel thermocouple. The data acquisition system included an IBM PC-compatible, 80486-based computer connected to a Pressure Systems Incorporated (PSI) data scanning system. The PSI system included a 780B Data Acquisition and Control Unit (DACU), 780B Pressure Calibration Unit (PCU), 81-IFC scanning module interface, two 2.5-psid pressure scanning modules (ESPs), one 20-inch water column range pressure scanning module, and a 30-channel Remotely Addressed Millivolt Module (RAMM-30). Figure 7 shows the data acquisition system schematic.

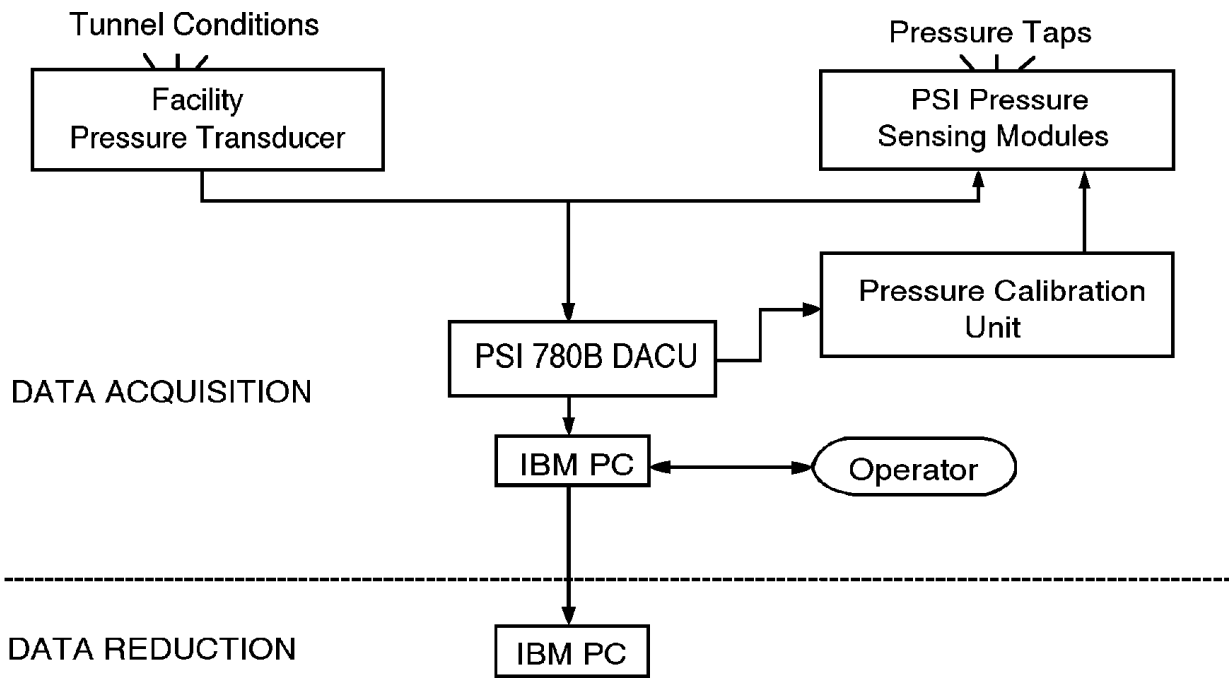


Figure 7. Data acquisition schematic.

Four individual pressure transducers read tunnel total pressure, tunnel north static pressure, tunnel south static pressure, and wake dynamic pressure. Before the test began, these transducers were bench calibrated using a water manometer to determine their sensitivities and offsets. Related values were entered into the data acquisition and reduction program so the transducers could be shunt resistor calibrated before each series of wind tunnel runs.

The rotary angle of attack potentiometer of 0.5% linearity was regularly calibrated during the tunnel pressure transducers shunt calibration. The angle of attack calibration was accomplished by taking voltage readings at known values of set angle of attack. This calibration method gave angle of attack readings within $\pm 0.25^\circ$ over the entire angle range. The wake probe position potentiometer was also a linear potentiometer and it was also regularly calibrated during the shunt calibration of the tunnel pressure transducers.

Calibration of the three ESPs was done simultaneously using the DACU and PCU. At operator request, the DACU commanded the PCU to apply known regulated pressures to the ESPs and read the output voltages from each integrated pressure sensor. From these values, the DACU calculated the calibration coefficients and stored them internally until the coefficients were requested by the controlling computer. This calibration was done several times during a run set because the ESPs were installed inside the model and their outputs

tended to drift with temperature changes during a test sequence. Frequent on-line calibrations minimized the effect.

For steady state cases, the model was set to angle of attack and the tunnel conditions were adjusted. At operator request, pressure measurements from the airfoil surface taps and all other channels of information were acquired and stored by the DACU and subsequently passed to the controlling computer for final processing. The angles of attack were always set in the same progression, from negative to positive values.

For model oscillating cases, the tunnel conditions were set while the model was stationary at the desired mean angle of attack. The "shaker" was started, after approximately 10 seconds the model surface pressure and tunnel condition data were acquired. Generally, 120 data scans were acquired over three model oscillation cycles. Since surface pressures were scanned sequentially, the data rate was set so the model rotated through less than 0.50° during any data burst. Finally, due to the unsteady and complex nature of the pitch oscillation cases, model wake surveys (for drag) were not conducted.

Data Reduction

The data reduction routine was included as a section of the data acquisition program. This combination of data acquisition and reduction routines allowed data to be reduced on-line during a test. By quickly reducing selected runs, integrity checks could be made to ensure the equipment was working properly and to allow timely decisions about the test matrix.

The ambient pressure was manually input into the computer and was updated regularly. This value, as well as the measurements from the tunnel pressure transducers and the tunnel thermocouple, were used to calculate tunnel airspeed. As a continuous check of readings, the tunnel total and static pressures were read by both the tunnel individual pressure transducers and the 20-inch water column ESP.

A typical steady state datum point was derived by acquiring 10 data scans of all channels over a 10-second window at each angle of attack and tunnel condition. The reduction portion of the program processed each data scan to coefficient forms (C_p , C_l , $C_{m\frac{1}{4}}$, and C_{dp}) using the measured surface pressure voltages, calibration coefficients, tap locations and wind tunnel conditions. Then, all scan sets for a given condition were ensemble averaged to provide one data set and that data set was then corrected for the effects of solid tunnel walls. All data was saved in electronic form and selected final data were printed to paper.

Corrections due to solid tunnel sidewalls were applied to the wind tunnel data. As described by Pope and Harper (1966), tunnel conditions are represented by the following equations:

$$q = q_u(1 + 2\epsilon)$$

$$V = V_u(1 + \epsilon)$$

$$R_e = R_{e_u}(1 + \epsilon)$$

Airfoil aerodynamic characteristics are corrected by:

$$\alpha = \alpha_u + \frac{57.3\sigma}{2\pi} (C_{l_u} + 4C_{m\frac{1}{4}})$$

$$C_l = C_{l_u}(1 - \sigma - 2\epsilon)$$

$$C_{m_{\frac{1}{4}}} = C_{m_{\frac{1}{4}_u}} (1 - 2\epsilon) + \frac{\sigma}{4} C_l$$

$$C_d = C_{d_u} (1 - 3\epsilon_{sb} - 2\epsilon_{wb})$$

where

$$\sigma = \frac{\pi^2}{48} \left(\frac{c}{h} \right)^2$$

$$\epsilon = \epsilon_{sb} + \epsilon_{wb}$$

$$\epsilon_{sb} = \Lambda \sigma$$

$$\epsilon_{wb} = \frac{c}{h4} C_{d_u}$$

Model wake data were taken for steady state cases when the wake could be completely traversed. Pressures were acquired from a pitot-static probe which was connected to measure incompressible dynamic pressure through the wake. These pressure measurements were used to calculate drag coefficient using a form of the Jones equation derived from Schlichting (1979).

$$C_{dw} = \frac{2}{c} \int \sqrt{\frac{q_w}{q_\infty}} \left(1 - \sqrt{\frac{q_w}{q_\infty}} \right) dy$$

This equation assumes that static pressure at the measurement site is the free-stream value. The integration was done automatically except the computer operator chose the end points of the integration from a plot of the wake survey displayed on the computer screen.

For pitch oscillation cases, model surface pressures were reduced to pressure coefficient form with subsequent integrations and angle of attack considerations giving lift, moment and pressure drag coefficients. The wind tunnel was not calibrated for unsteady model pitch conditions; therefore, the unsteady pressure data were not corrected for any possible effects due to time dependent pitching or solid tunnel walls. Also, for these cases, the wind tunnel contraction pressures (used for steady state cases) could not be used to calculate instantaneous freestream conditions due to slow response. The tunnel conditions were obtained from a total pressure probe and the average of opposing static pressure taps in the test section entrance; thereby giving near instantaneous flow pressure conditions for the pitching frequencies used.

Test Matrix

The test was designed to study steady state and unsteady pitch oscillation data. Steady state data were acquired at Reynolds numbers of 0.75, 1, 1.25, and 1.5 million with and without LEGR. Refer to the tabular data in Appendix B for the actual Reynolds number for each angle of attack for the steady state data. The angle of attack increment was two degrees when $-20^\circ < \alpha < +10^\circ$ or $+20^\circ < \alpha < +40^\circ$ and one degree when $+10^\circ < \alpha < +20^\circ$. Wake surveys were conducted to find total airfoil drag over an approximate angle of attack range of -10° to $+10^\circ$. Unsteady data were taken for Reynolds numbers of 0.75, 1, 1.25, and 1.4 million. Sine wave cams with amplitudes $\pm 5.5^\circ$ and $\pm 10^\circ$ were used for pitch oscillations, and the mean angles for

both these amplitudes were 8° , 14° , and 20° . For all these conditions, the frequencies were varied to 0.6 Hz, 1.2 Hz, and 1.8 Hz. All data points for the unsteady cases were acquired for both clean and LEGR cases.

Results and Discussion

The S809 airfoil model was tested under steady state and pitch oscillation conditions. A brief discussion of the results follows, beginning with a comparison of experimental data and computational predictions.

Comparison with Theory

Comparisons were made between present wind tunnel steady state data and computed predictions made using the North Carolina State Airfoil Analysis Code. This analysis code has proven to be accurate for moderate angles of attack. The analysis was made with specifications set to allow for free transition from laminar to turbulent flow, and the pressure distribution comparisons were matched to the same angle of attack as the wind tunnel cases.

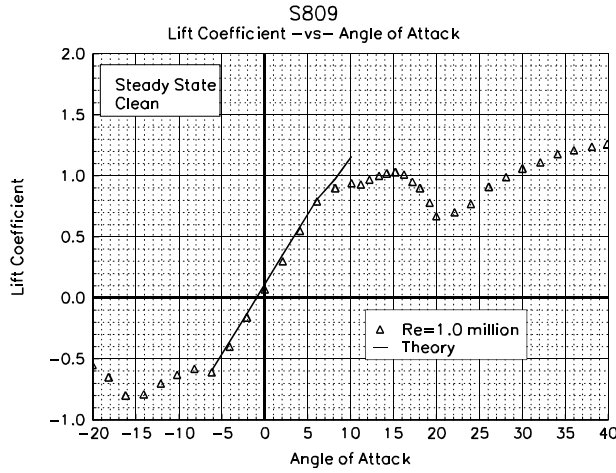


Figure 8. Comparison with theory, C_l vs α .

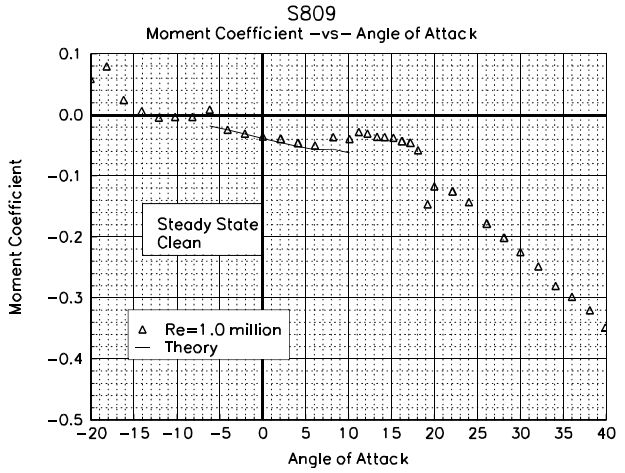


Figure 9. Comparison with theory, C_m vs α .

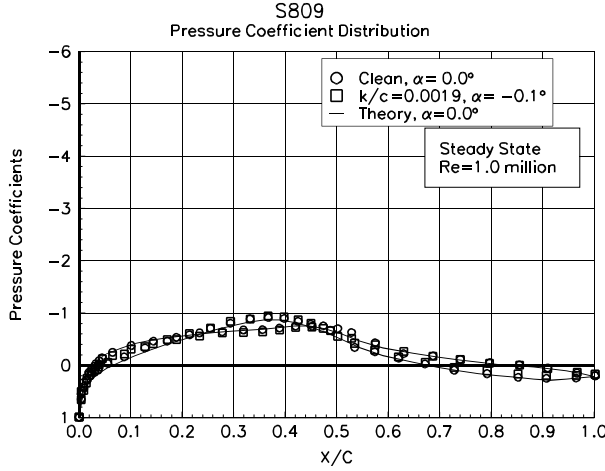


Figure 10. Comparison with theory, C_p vs x/c , $\alpha=0.0^\circ$.

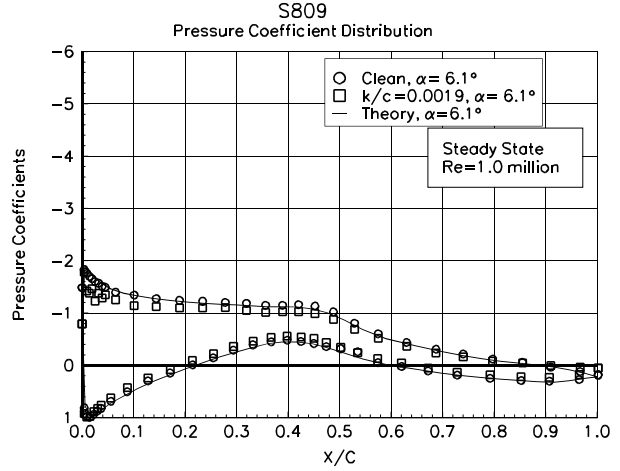


Figure 11. Comparison with theory, C_p vs x/c , $\alpha=6.1^\circ$.

Figure 8 shows the lift coefficient versus angle of attack for the 1 million Reynolds number case. For moderate angles of attack, where the analysis code is valid, the comparison shows good agreement. The pitching moment about the quarter chord, figure 9, also shows good agreement for angles of attack from -4° to 6° . The pressure distributions, shown in figures 10 and 11, show angles of attack of 0.0° and 6.1° , respectively, and include clean and LEGR wind tunnel data as compared to computed free transition pressure

distributions. For both angles of attack, there is excellent correlation between the experimental and predicted values.

Steady State Data

The S809 airfoil model was tested at four Reynolds numbers at nominal angles of attack from -20° to $+40^\circ$. Figures 12 and 13 show lift coefficients for all the test Reynolds numbers for model clean and with LEGR

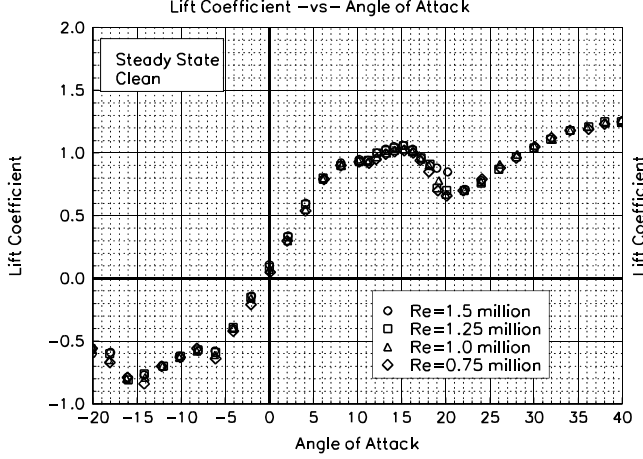


Figure 12. C_l vs α , clean.

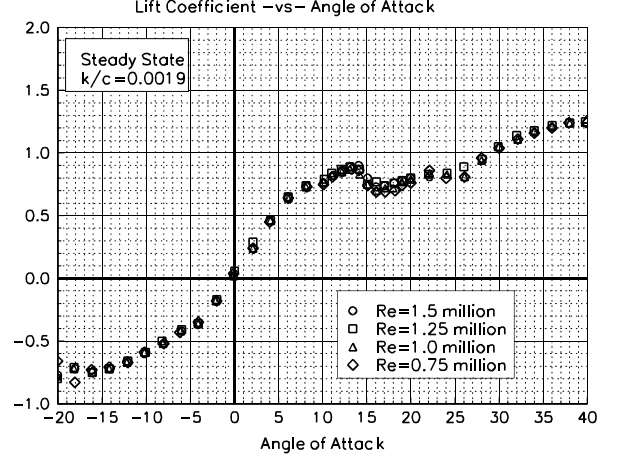


Figure 13. C_l vs α , LEGR, $k/c=0.0019$.

applied, respectively. The maximum positive lift coefficient for the clean cases is about 1.06 and about 0.87 for the LEGR cases, a 16% reduction. Not only is the lift coefficient lower for the LEGR case, but the stall starts at a slightly lower angle of attack than for the clean case. Finally, the average lift curve slope for clean data is about 0.12 and is slightly lower for the LEGR case at 0.10. The associated average lift coefficients at zero angle of attack are 0.08 for the clean case and 0.04 for the LEGR case.

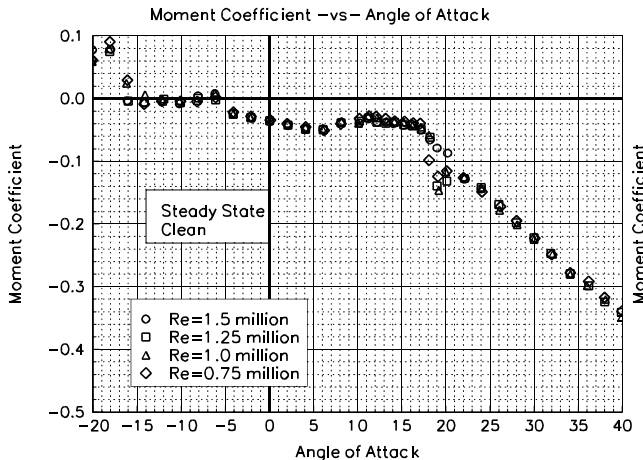


Figure 14. C_m vs α , clean.

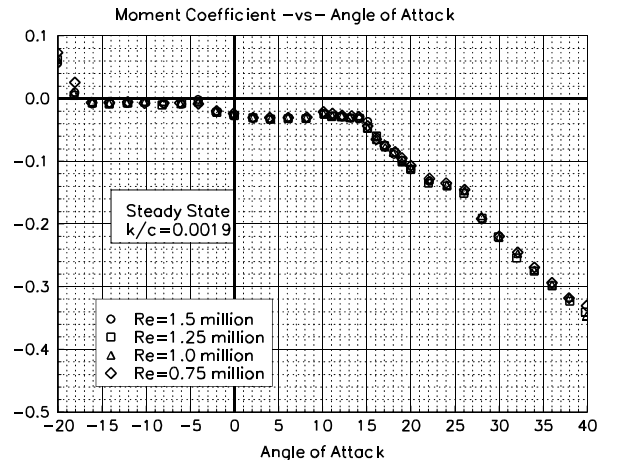


Figure 15. C_m vs α , LEGR, $k/c=0.0019$.

Figure 14 shows the pitching moment about the quarter chord for the clean cases, and figure 15 shows the same for the LEGR cases. The LEGR data have slightly more positive pitching moment and a flatter curve for angles of attack near zero lift. The pitching moment coefficient about the quarter chord for the 1 million Reynolds number, is -0.0356 for the clean case and -0.0258 for the LEGR case.

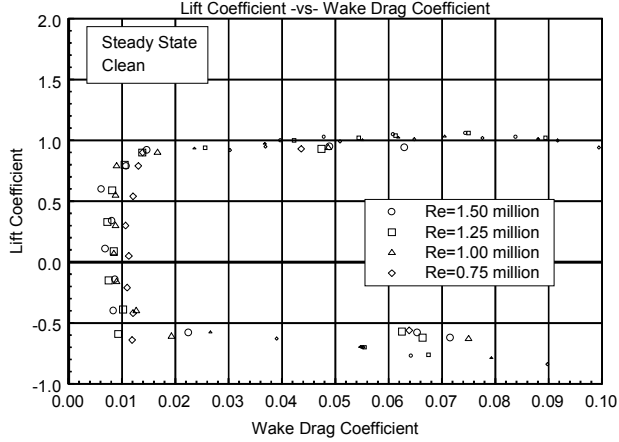


Figure 16. Drag polar, clean.

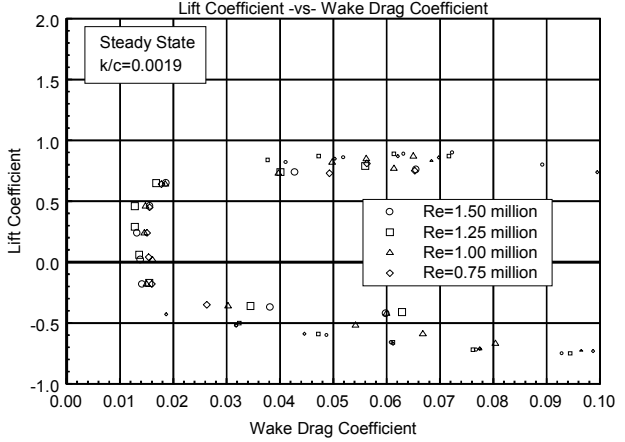


Figure 17. Drag polar, LEGR, $k/c=0.0019$.

Total wake drag data were obtained for both the clean and LEGR cases over a nominal angle of attack range of -10° to 10° . A pitot-static probe was used to describe the wake profile. This method is reliable when there is relatively low turbulence in the wake flow; therefore, only moderate angles of attack have reliable total drag coefficient data. At angles of attack other than -10° to 10° , surface pressure data were integrated to give C_{dp} and are shown in the drag polars as small symbols. The model clean drag data are shown in figure 16 and the LEGR case is shown in figure 17. At 1 million Reynolds number, minimum drag coefficient for the clean cases was measured as 0.0085 and 0.0146 for LEGR, a 72% increase. The general effect of LEGR is to increase drag consistently through most angles of attack.

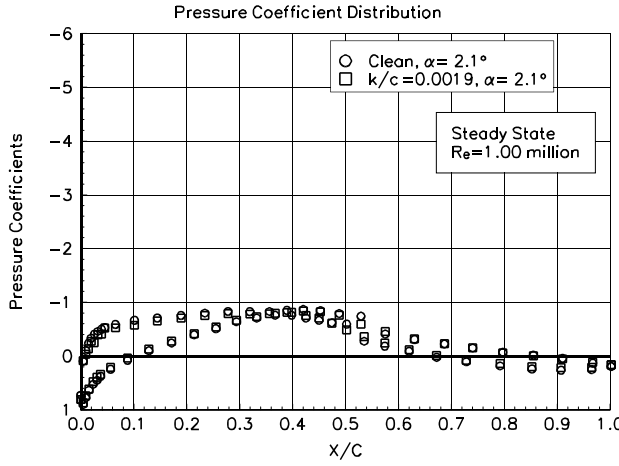


Figure 18. Pressure distribution, $\alpha=2.0^\circ$.

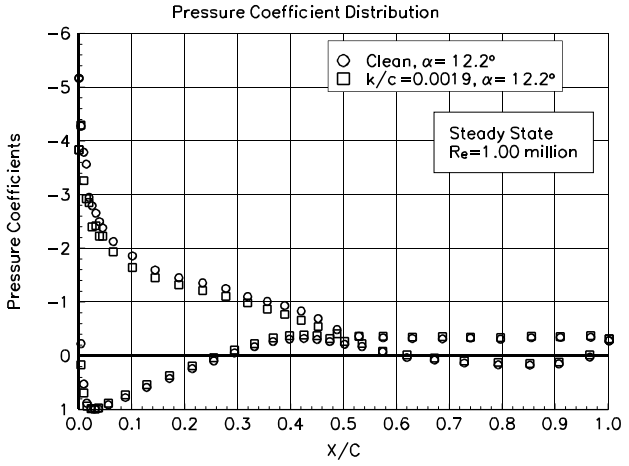


Figure 19. Pressure distribution, $\alpha=12.2^\circ$.

Two examples of the surface pressure distributions are shown in figures 18 and 19 for 2.1° and 12.2° , respectively, at 1 million Reynolds number. At angles of attack close to zero degrees, the LEGR does not appear to significantly affect the pressure distribution compared to the clean case distribution. Although, there is an effect apparent in the lift coefficient with values of 0.24 for the LEGR case and 0.30 for the clean case. Another difference between the two cases, which cannot be observed from the pressure distribution, is that the drag increases from 0.0108 for the clean case to 0.0176 for the LEGR case. For the higher angle of attack, figure 19, the effect of LEGR is to reduce the magnitude of the pressure peak from -5.2 to -4.2, which contributes to a reduction in lift coefficient from 0.97 to 0.85, a 12% decrease. The pitching moment is affected at this angle of attack also, the clean case is -0.0307 whereas the LEGR case is -0.0276.

Unsteady Data

Unsteady experimental data were obtained for the S809 airfoil model undergoing sinusoidal pitch oscillations. As mentioned earlier, no attempt was made to calibrate the wind tunnel for the unsteady oscillating model conditions; the steady state tunnel calibration was used to set flow conditions while the model was stationary at its mean angle of attack. The use of the unsteady data should be limited to comparisons with other models tested in this same facility and can be used to detect possible trends. A comprehensive set of test conditions was used to describe unsteady behavior of an airfoil, including two angle of attack amplitudes, $\pm 5.5^\circ$ and $\pm 10^\circ$; four Reynolds numbers, 0.75, 1, 1.25, and 1.4 million; three pitch oscillation frequencies, 0.6, 1.2, and 1.8; and three mean angles of attack, 8° , 14° , and 20° .

Figure 20 shows the lift coefficient versus angle of attack for the $\pm 5.5^\circ$ amplitude, model clean case, at reduced frequency of 0.026 and 1 million Reynolds number. Note that all three mean angles of attack are plotted on the same figure. The maximum pre-stall lift coefficient for this case is near 1.09 and occurs when the airfoil is traveling with the angle of attack increasing. In contrast, when the model is traveling through decreasing angles of attack the stall recovery is delayed and a hysteresis behavior is exhibited in the lift coefficient that can be seen throughout all of the unsteady data. To obtain some measure of this hysteresis behavior, the lift coefficient on the "return" portion of the curve, at the angle of attack where maximum lift coefficient occurs, can be used. For the case discussed here, the hysteresis or decreasing angle of attack lift coefficient is 0.96, a 12% decrease from the 1.09 unsteady maximum value. In comparison, the steady state maximum lift coefficient is 1.03. At higher reduced frequency of 0.077, the hysteresis behavior is more pronounced, as seen in figure 21. In addition to greater hysteresis, the maximum lift coefficient is increased to about 1.21 which is a 17% increase over the steady state value. The corresponding hysteresis lift coefficient is 0.72. This difference between steady state behavior and unsteady hysteresis behavior is a main reason that unsteady testing should be required for airfoils used in wind turbine applications.

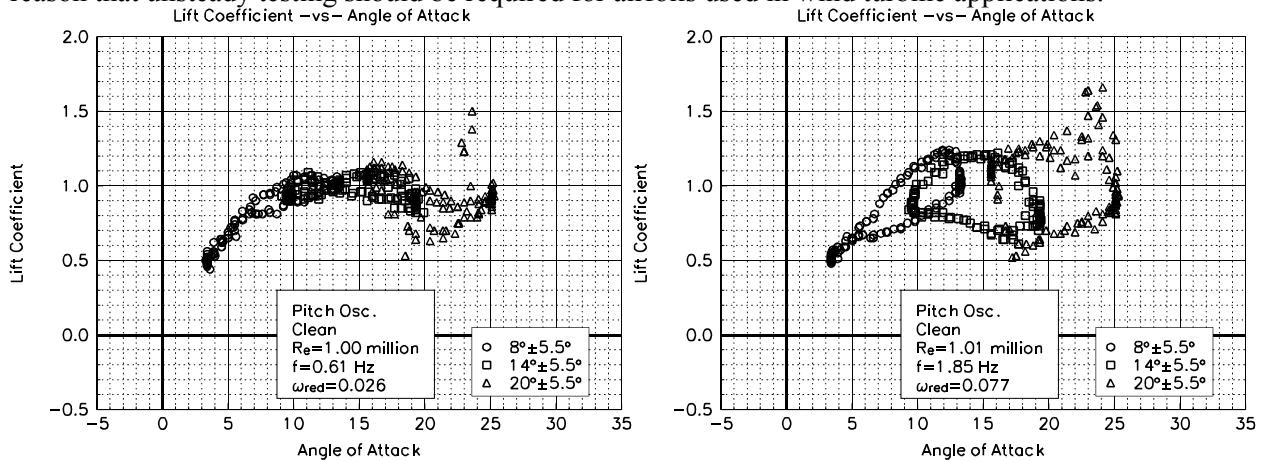


Figure 20. Clean, C_l vs α , $w_{red}=0.026$, $\pm 5.5^\circ$.

Figure 21. Clean, C_l vs α , $w_{red}=0.077$, $\pm 5.5^\circ$.

The pitching moment shown in figures 22 and 23 corresponds to the same conditions as the two lift coefficient plots previously discussed. There is indication that the hysteresis behavior is present but it is not as apparent as in the lift coefficient plots. However, the higher reduced frequency case does show hysteresis more than the lower reduced frequency case. For reference, the steady state maximum lift occurs near 15° angle of attack, and the steady state pitching moment at this maximum lift point is -0.0362. In comparison, when the airfoil is undergoing pitch oscillation for the lower frequency, pitching moment varies from -0.0449 to -0.0401 (at the angle of attack where maximum lift occurs), a 24% to 11% increase in magnitude from the steady state value. Note the angle of attack where the maximum lift coefficient occurs does not necessarily show the greatest hysteresis behavior but does give a relative indication of the effect.

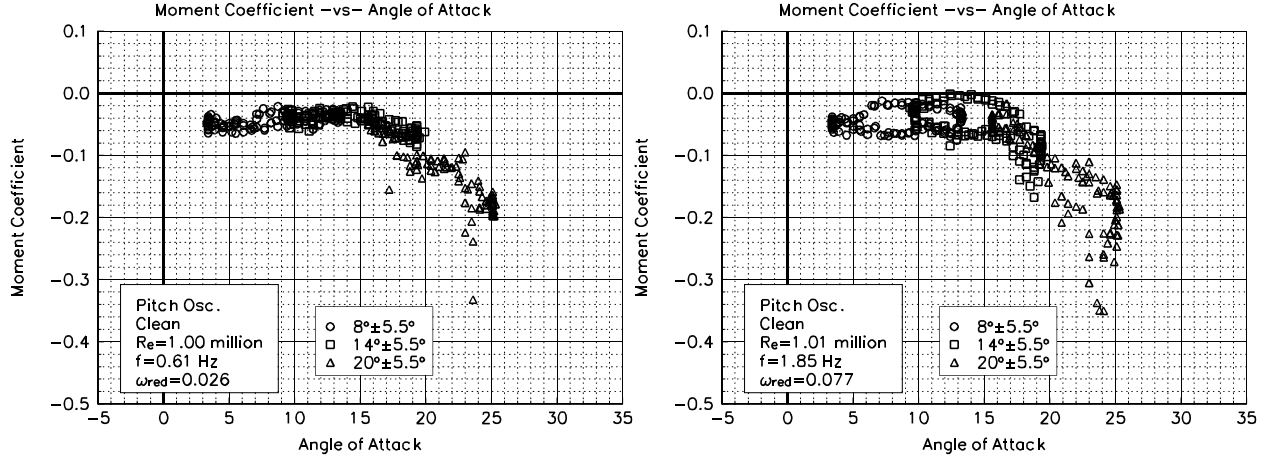


Figure 22. Clean, C_m vs α , $\omega_{red}=0.026, \pm 5.5^\circ$.

Figure 23. Clean, C_m vs α , $\omega_{red}=0.077, \pm 5.5^\circ$.

Compared to the clean data, the application of LEGR reduces the maximum lift coefficient in the pitch oscillation cases. Lift coefficient versus angle of attack with LEGR applied is shown in figure 24 for the 0.025 reduced frequency case. The 0.079 reduced frequency case is shown in figure 25. Both plots correspond to the same run conditions described earlier for the clean cases. For the lower reduced frequency, the maximum unsteady lift coefficient is reduced to 0.93 from the corresponding clean case of 1.09, a 15% decrease. Hysteresis behavior is apparent at this frequency, but the loops are not as large as in the clean case; the corresponding hysteresis lift coefficient is 0.69 when LEGR is applied. The higher frequency, LEGR case has a maximum lift coefficient of 1.12 while the model is increasing, in angle of attack and the corresponding decreasing angle of attack lift coefficient is 0.57. The application of LEGR in this case, also, reduces the hysteresis loop behavior when compared to the clean case at the same run conditions.

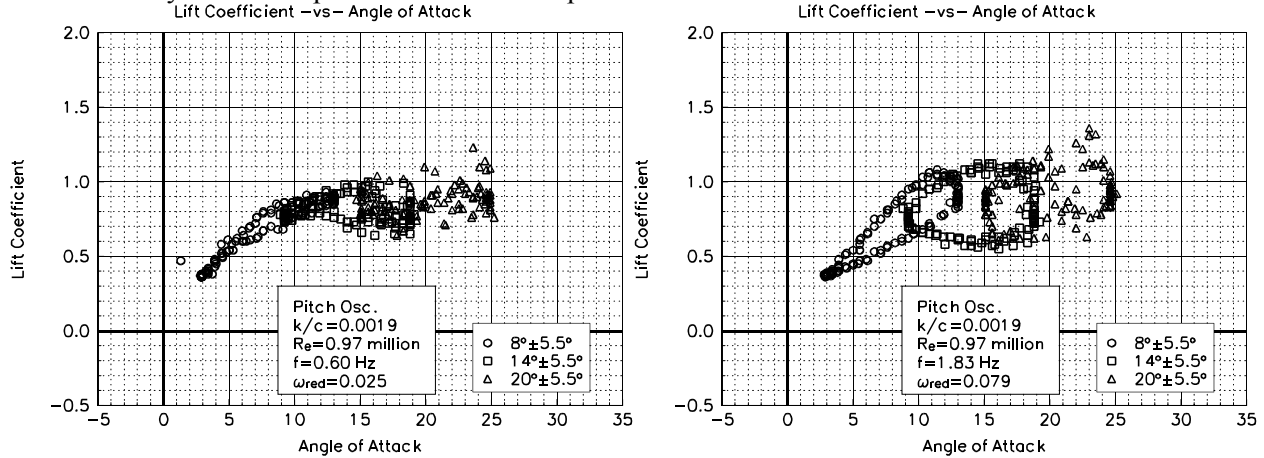


Figure 24. LEGR, C_l vs α , $\omega_{red}=0.025, \pm 5.5^\circ$.

Figure 25. LEGR, C_l vs α , $\omega_{red}=0.079, \pm 5.5^\circ$.

The pitching moment coefficient shown in figure 26 is for 0.025 reduced frequency with LEGR applied. At the angle of unsteady maximum lift, the pitching moment ranges from -0.0326 to -0.0241, while the steady state LEGR pitching moment is -0.0295 at the steady state stall angle of attack (13.1°). The higher reduced frequency of 0.079 with LEGR applied is shown in figure 27. As was seen with the lift coefficient, pitching moment hysteresis is more apparent at the higher reduced frequency than at the lower reduced frequency. Unsteady maximum lift angle of attack for this reduced frequency occurs at 15.4° and the pitching moment ranges from -0.0740 to -0.0421 at that angle. Throughout the higher angle of attack range, the magnitude of the unsteady pitching moment can be much different than that resulting from steady state, clean conditions

(steady state pitching moment at maximum lift is -0.0575). It seems these differences can have significant impact on the fatigue life predictions of a wind turbine system.

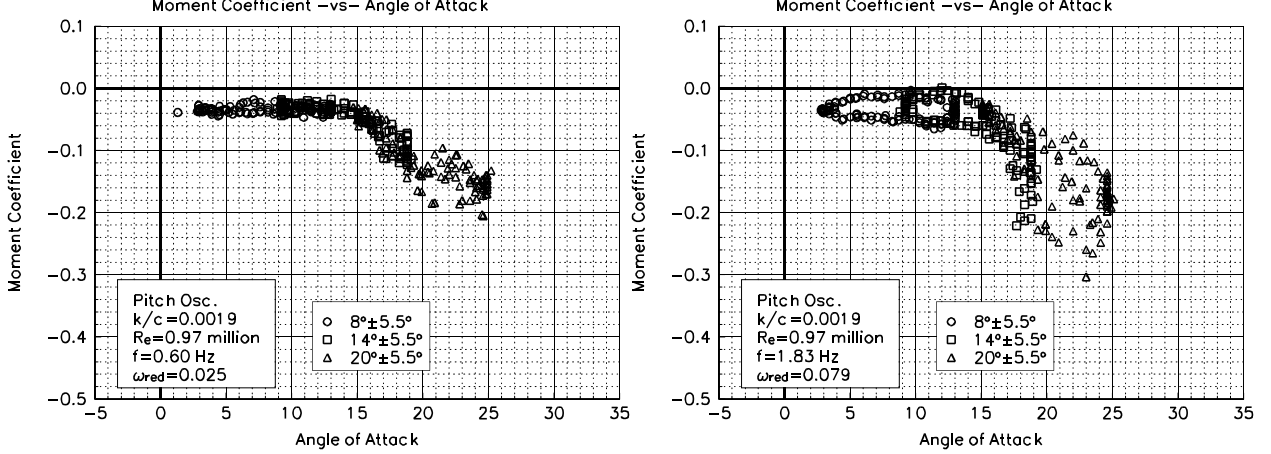


Figure 26. LEGR, C_m vs α , $\omega_{red}=0.025, \pm 5.5^\circ$.

Figure 27. LEGR, C_m vs α , $\omega_{red}=0.079, \pm 5.5^\circ$.

In addition to the $\pm 5^\circ$ unsteady experimental data, $\pm 10^\circ$ unsteady data were obtained with and without LEGR. The data were taken at 1 million Reynolds number using the same mean angle and frequencies as the 5.5° amplitude cases. Figures 28 and 29 show the $\pm 10^\circ$, unsteady, clean, lift coefficient for the reduced frequencies of 0.026 and 0.078, respectively. The maximum lift coefficient for the lower frequency is 1.21 and occurs, as expected, when the airfoil is traveling through increasing angle of attack. The hysteresis lift coefficient (at 12.9°) is 0.93. At the higher reduced frequency, the maximum lift coefficient occurs at a higher angle of attack, 16.1° , and is 1.65. The corresponding hysteresis lift coefficient is 0.40. The difference between the maximum lift coefficient and the hysteresis lift coefficient indicates a much larger hysteresis response than experienced for the lower reduced frequency. The steady state, clean, maximum lift coefficient is 1.03; therefore, the unsteady behavior created lift coefficients up to 60% higher than the steady state conditions.

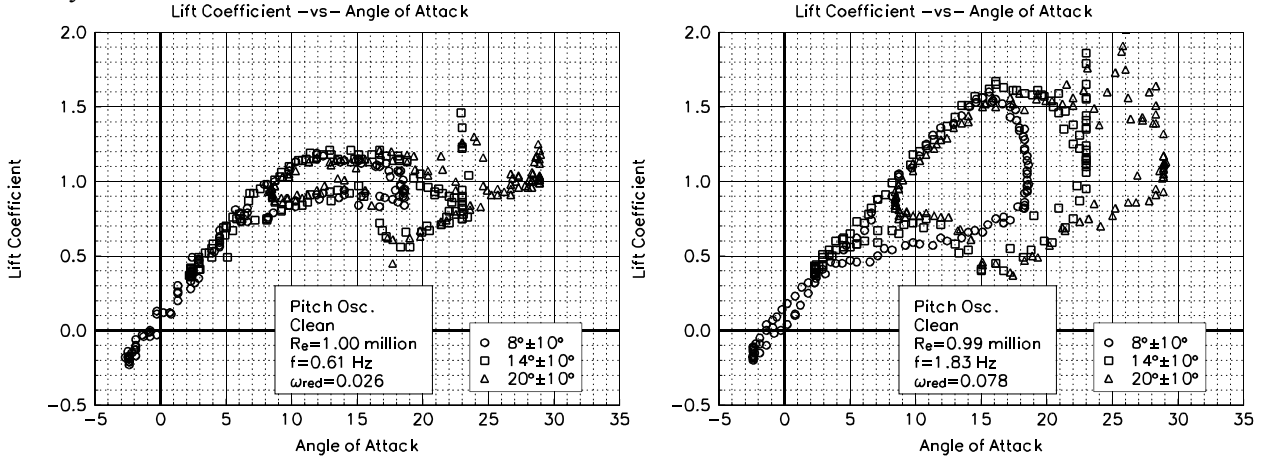


Figure 28. Clean, C_l vs α , $\omega_{red}=0.026, \pm 10^\circ$.

Figure 29. Clean, C_l vs α , $\omega_{red}=0.078, \pm 10^\circ$.

The quarter chord pitching moments with the same reduced frequencies as the lift coefficient cases are shown in figures 30 and 31. The hysteresis behavior observed in the lift coefficient plots is also reflected in this pitching moment data. Near the maximum lift angle of attack, 12.9° , for the lower frequency, the pitching moment coefficient ranges from -0.0736 to -0.0255; the 0.078 reduced frequency case has maximum lift near 16.1° and pitching moment ranges from -0.1163 to -0.0429. The higher reduced frequency again shows large

hysteresis loops for all three mean angles of attack. In comparison, the steady state pitching moment is -0.0375 near the steady state maximum lift coefficient angle of attack of 15.2°.

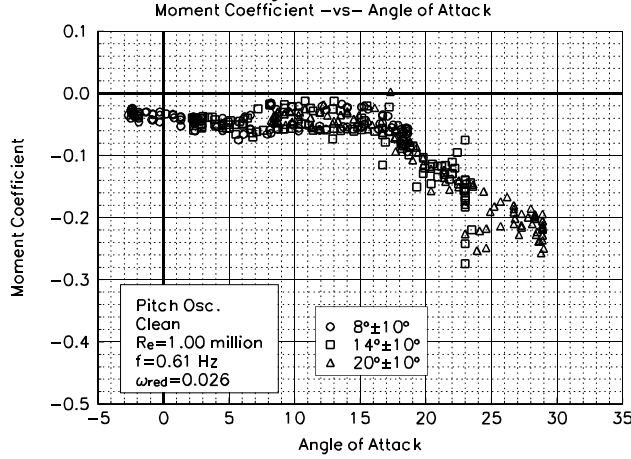


Figure 30. Clean, C_m vs α , $\omega_{red}=0.026, \pm 10^\circ$.

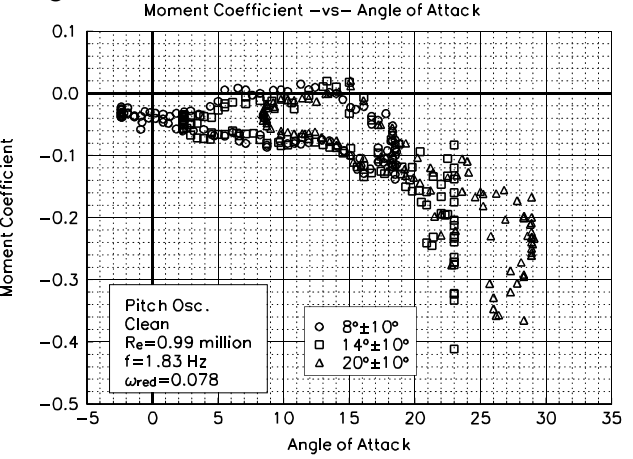


Figure 31. Clean, C_m vs α , $\omega_{red}=0.078, \pm 10^\circ$.

The application of LEGR degrades the lift performance of the airfoil, as would be expected from the results discussed previously. The LEGR lift coefficient data for reduced frequencies of 0.025 and 0.079 are shown in figures 32 and 33, respectively. The maximum lift coefficient is reduced to 1.09 from 1.21 for the low frequency case. Although there is a reduction, this value is still significantly higher than the LEGR steady state case, which has a maximum lift coefficient of 0.87 at 13.1° angle of attack. The higher reduced frequency has a maximum lift coefficient of 1.47, which occurs near 17.8° angle of attack. The corresponding lift coefficient at 17.8° for the airfoil oscillating with decreasing angle of attack is 0.64 which is less than half of the maximum.

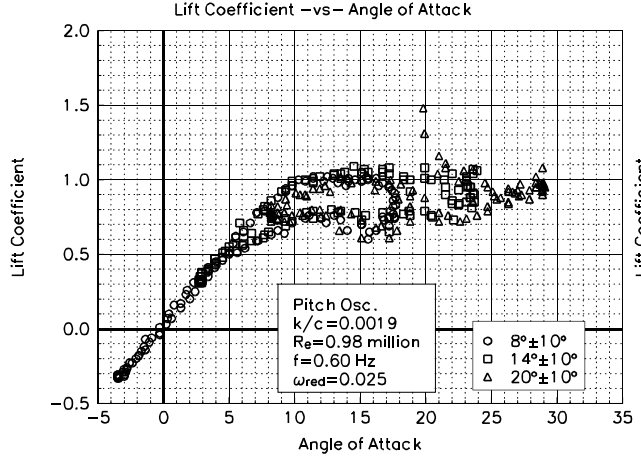


Figure 32. LEGR, C_l vs α , $\omega_{red}=0.025, \pm 10^\circ$.

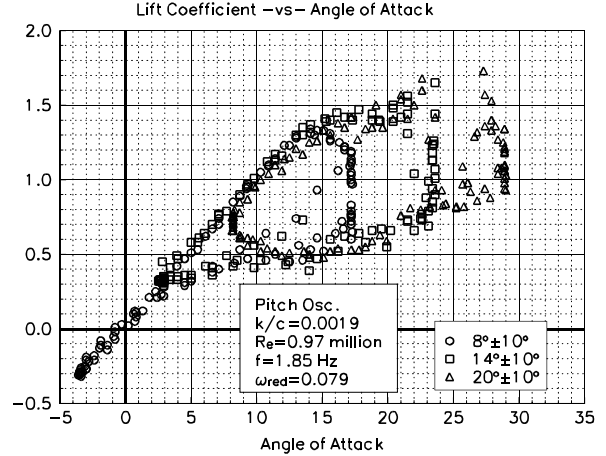


Figure 33. LEGR, C_l vs α , $\omega_{red}=0.079, \pm 10^\circ$.

Figures 34 and 35 show the corresponding pitching moment coefficients for the reduced frequencies of 0.025 and 0.079. For the 0.025 reduced frequency case, the pitching moment varies from -0.0650 to -0.0312 at 14.5° (where the maximum lift occurs). The hysteresis behavior is more pronounced for the higher reduced frequency case, where the range of pitching moments at the maximum lift angle of 17.8° is from -0.1237 to -0.0582. These values are much higher in magnitude than the steady state, LEGR value of -0.0295.

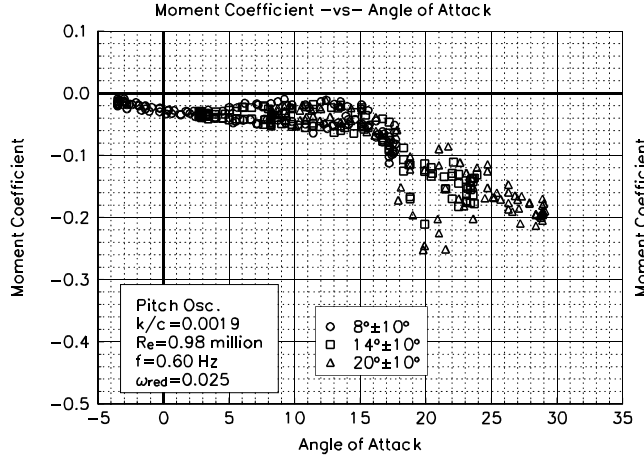


Figure 34. LEGR, C_m vs α , $\omega_{red}=0.025$, $\pm 10^\circ$.

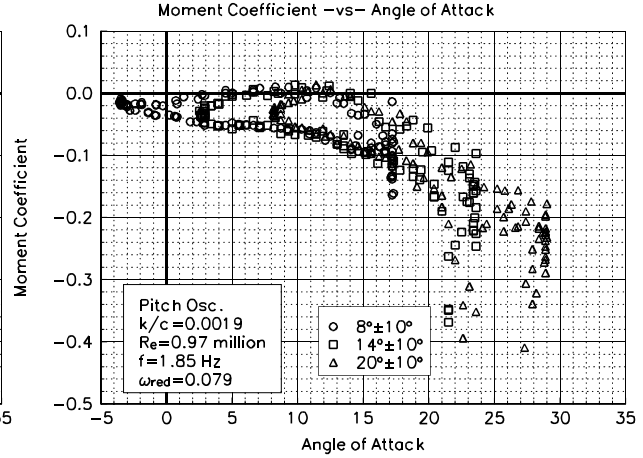


Figure 35. LEGR, C_m vs α , $\omega_{red}=0.079$, $\pm 10^\circ$.

Although all the unsteady data have not been discussed here, the previous discussion included typical examples of the wind tunnel data. The remaining cases of the $\pm 5^\circ$ and $\pm 10^\circ$ oscillation data for all the Reynolds numbers are included in Appendix C.

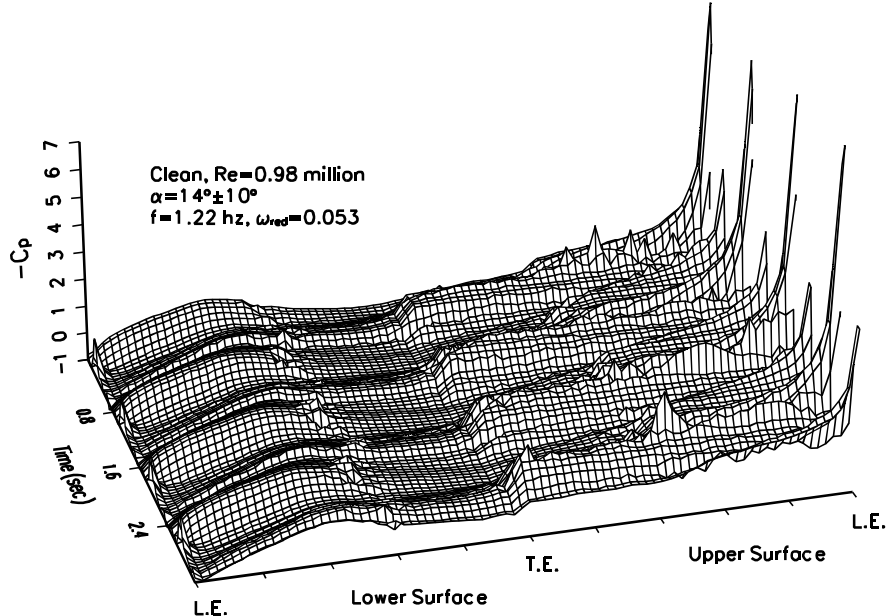


Figure 36. Unsteady pressure distribution, clean, $\omega_{red}=0.053$, $14\pm 10^\circ$

The following four unsteady pressure distributions show examples of the data used to calculate the lift, pressure drag, and pitching moment coefficients. Figure 36 shows the distribution for a clean model with a reduced frequency of 0.053, 14° mean angle of attack, and $\pm 10^\circ$ pitch oscillation. For plotting clarity, the model pressures were "unwrapped" about the trailing edge. The upper surface pressures are depicted on the right side of the surface plot; lower surface values are on the left. The trailing edge is at the midpoint of the x-axis, with the leading edge at each extreme. The time scale corresponds to angle of attack. The upper surface pressure peaks correspond to the maximum lift locations in the sweeps. For this case, during high angle of attack oscillations, much of the airfoil upper surface separated. Separation areas are defined by the irregular, "rough" areas in the plot surface. The lower surface stays attached through most of the airfoil travel. On the lower surface before the reflex area near the trailing edge, there were pressure fluxuations

which could be localized flow separation and reattachment through this region. Figure 37 shows the LEGR case for the same test conditions as the previous figure. In this case, the pressure peaks were not as high as for the clean case and the stall behavior is more pronounced. The pressure fluctuation on the lower surface, although still there, is not as apparent as in the clean case.

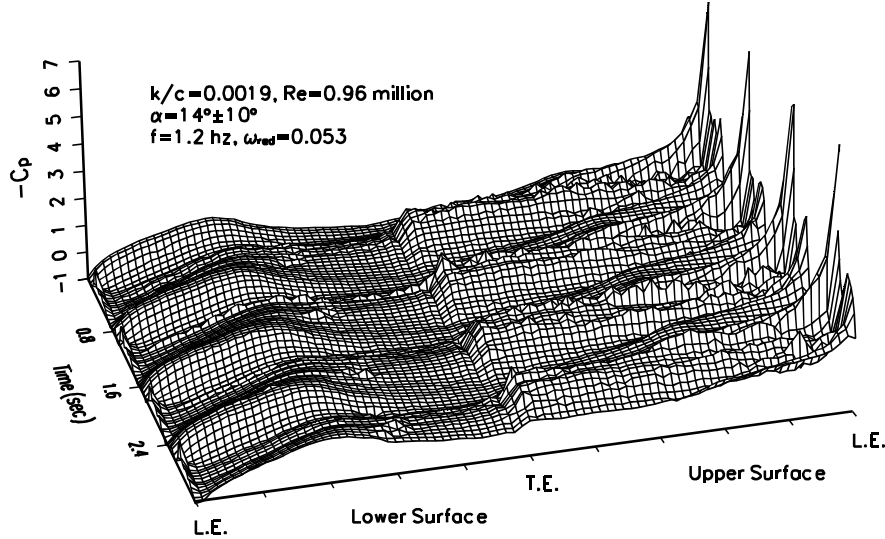


Figure 37. Unsteady pressure distribution, LEGR, $\omega_{\text{red}}=0.053$, $14\pm 10^\circ$

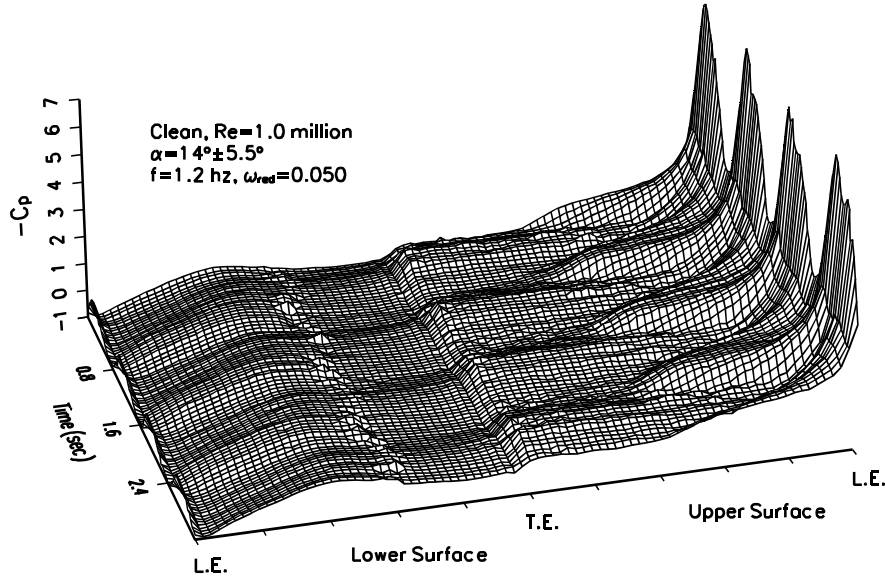


Figure 38. Unsteady pressure distribution, clean, $\omega_{\text{red}}=0.050$, $14\pm 5.5^\circ$

Figure 38 shows the same clean run conditions as above except at a smaller mean angle of attack. The structure is different than the previous because less of the upper surface flow is separated, the consequence of lower maximum angles of attack.

Figure 39 shows clean run conditions for a $\pm 5.5^\circ$ oscillation at a higher Reynolds number, reduced frequency, and mean angle of attack. Because of the high angle of attack, much of the upper surface has stalled and stays stalled even when going through the lower angles of attack. Only pressure peaks can be seen emerging from the unstable upper surface flow.

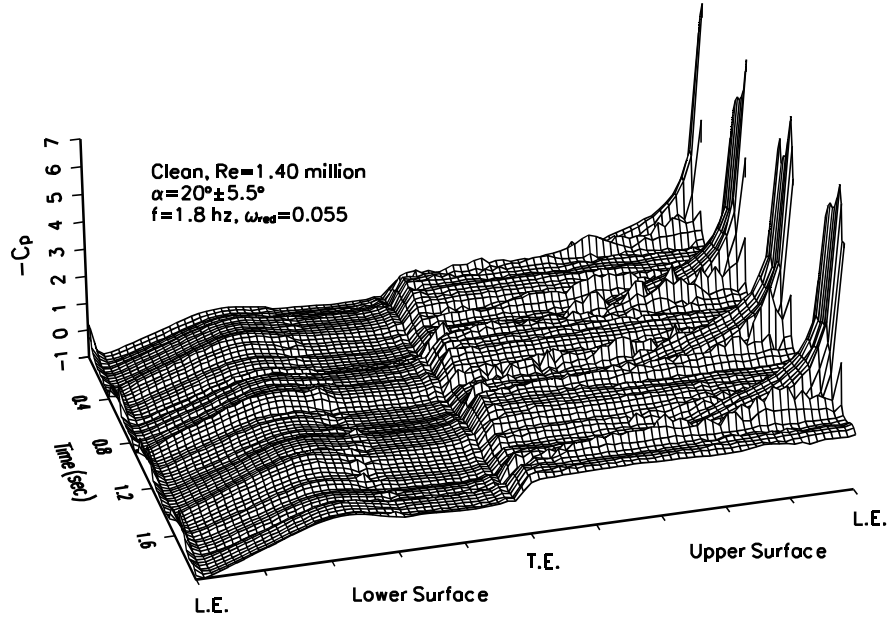


Figure 39. Unsteady pressure distribution, clean, $\omega_{red}=0.055$, $20\pm 5.5^\circ$

Summary of Results

The S809 airfoil was tested under steady state and pitch oscillation conditions. Baseline tests were made while the model was clean, and then corresponding tests were conducted with LEGR applied.

A summary of the steady state aerodynamic parameters is shown in table 1. As observed, the application of LEGR reduced the maximum lift of the airfoil up to 16% and the minimum drag coefficient increased from 41% to 116%. The zero lift pitching moment coefficient is also affected from the application of LEGR by reducing the magnitude an average of 27%.

Table 1. S809 Aerodynamic Parameters Summary

Grit Pattern	Reynolds no.	$C_{l\max}$	$C_{d\min}$	C_{m0}
Clean	0.75×10^6	1.02 @ 15.3	0.0107	-0.0346
k/c=0.0019	0.75×10^6	0.87 @ 13.3	0.0151	-0.0237
Clean	1.00×10^6	1.03 @ 15.2	0.0085	-0.0356
k/c=0.0019	1.00×10^6	0.87 @ 13.1	0.0146	-0.0258
Clean	1.25×10^6	1.06 @ 15.2	0.0073	-0.0354
k/c=0.0019	1.25×10^6	0.89 @ 13.1	0.0128	-0.0272
Clean	1.50×10^6	1.06 @ 15.2	0.0061	-0.0366
k/c=0.0019	1.50×10^6	0.90 @ 14.1	0.0132	-0.0275

Table 2. S809, Unsteady, Clean, $\pm 5.5^\circ$

ω_{red}	$Rex \times 10^{-6}$	f	$C_{l\max}$	$\alpha_{Cl\max}$	$C_{l\text{dec}}$	$C_{m\text{inc}}$	$C_{m\text{dec}}$
0.033	0.75	0.60	1.09	11.7	0.92	-0.0511	-0.0262
0.066	0.76	1.19	1.21	14.0	0.78	-0.0676	-0.0059
0.103	0.75	1.85	1.30	15.3	0.57	-0.0814	-0.0723
0.026	1.00	0.61	1.09	15.1	0.96	-0.0449	-0.0401
0.050	1.01	1.19	1.15	15.1	0.82	-0.0460	-0.0167
0.077	1.01	1.85	1.21	14.5	0.72	-0.0695	-0.0094
0.020	1.26	0.60	1.13	15.3	1.03	-0.0486	-0.0451
0.040	1.26	1.19	1.16	16.1	0.87	-0.0553	-0.0222
0.061	1.26	1.83	1.26	14.6	0.85	-0.0721	-0.0213
0.018	1.41	0.60	1.13	15.6	0.97	-0.0488	-0.0371
0.035	1.41	1.19	1.15	15.6	0.89	-0.0511	-0.0262
0.054	1.41	1.85	1.21	14.7	0.85	-0.0718	-0.0210

The pitch oscillation data can be divided into two groups, the $\pm 5.5^\circ$ amplitude and $\pm 10^\circ$ amplitude oscillations, which show similar trends. For both $\pm 5.5^\circ$ and $\pm 10^\circ$, the unsteady test conditions and some parameters are listed in tables 2, 3, 4, and 5. As the reduced frequency, which takes oscillation and tunnel speed into account, is increased, the maximum lift coefficient, also increases. In addition, the hysteresis behavior becomes increasingly apparent with increased reduced frequency.

Table 3. S809, Unsteady, LEGR, $\pm 5.5^\circ$

ω_{red}	Rex 10^{-6}	f	$C_{l\max}$	$\alpha_{Cl\max}$	$C_{l\text{dec}}$	$C_{m\text{ inc}}$	$C_{m\text{ dec}}$
0.034	0.74	0.60	0.98	15.6	0.60	-0.0558	-0.0519
0.067	0.74	1.19	1.13	15.6	0.68	-0.0744	-0.0233
0.104	0.73	1.83	1.20	15.6	0.66	-0.0862	-0.0591
0.025	0.97	0.60	0.93	14.0	0.69	-0.0326	-0.0241
0.051	0.97	1.19	1.06	15.5	0.65	-0.0562	-0.0423
0.079	0.97	1.83	1.12	15.4	0.57	-0.0740	-0.0421
0.020	1.25	0.60	1.00	15.6	0.79	-0.0620	-0.0337
0.040	1.24	1.19	1.02	14.5	0.75	-0.0555	-0.0173
0.060	1.24	1.79	1.06	15.1	0.60	-0.0563	-0.0347
0.017	1.42	0.60	0.94	13.5	0.88	-0.0438	-0.0337
0.035	1.42	1.19	0.98	14.1	0.75	-0.0403	-0.0189
0.053	1.42	1.83	1.02	15.1	0.65	-0.0624	-0.0360

Table 4. S809, Unsteady, Clean, $\pm 10^\circ$

ω_{red}	Rex 10^{-6}	f	$C_{l\max}$	$\alpha_{Cl\max}$	$C_{l\text{dec}}$	$C_{m\text{ inc}}$	$C_{m\text{ dec}}$
0.034	0.76	0.60	1.29	14.8	0.86	-0.0796	-0.0368
0.068	0.75	1.19	1.60	15.7	0.37	-0.1100	-0.0343
0.105	0.74	1.83	1.89	18.7	0.74	-0.1940	-0.0792
0.026	1.00	0.61	1.21	12.9	0.93	-0.0736	-0.0255
0.052	0.99	1.22	1.41	15.1	0.72	-0.0899	-0.0343
0.078	0.99	1.83	1.65	16.1	0.40	-0.1163	-0.0429
0.020	1.25	0.60	1.18	12.4	0.91	-0.0720	-0.0223
0.041	1.24	1.19	1.34	15.1	0.87	-0.0773	-0.0383
0.062	1.24	1.83	1.55	16.1	0.55	-0.1201	-0.0281
0.018	1.41	0.60	1.21	15.4	0.98	-0.0596	-0.0290
0.035	1.40	1.18	1.32	15.0	1.01	-0.0774	-0.0321
0.054	1.40	1.81	1.49	15.1	0.86	-0.1048	-0.0321

As expected, the application of LEGR reduces the aerodynamic performance of the airfoil. The maximum lift coefficient is reduced by 5% - 15% for both amplitude cases. As well as following the same trends as the clean, unsteady data discussed previously, the LEGR causes the hysteresis behavior to persist into lower angles of attack than do the clean cases. Overall, the unsteady wind tunnel data show hysteresis behavior that becomes more apparent with increased, reduced frequency. The maximum unsteady lift coefficient can be up to 38% higher for the $\pm 5.5^\circ$ amplitude and up to 86% higher for the $\pm 10^\circ$ amplitude than the steady state maximum lift coefficient. Variation in the quarter chord pitching moment coefficient can be up to three times greater than that indicated by steady state results. These findings indicate that it is very important to consider the unsteady loading that will occur in wind turbine operation because steady state results can greatly underestimate the forces.

Table 5. S809, Unsteady, LEGR, $\pm 10^\circ$

ω_{red}	$Rex \cdot 10^{-6}$	f	$C_{l\max}$	$\alpha_{Cl\max}$	$C_{l\text{ dec}}$	$C_{m\text{ inc}}$	$C_{m\text{ dec}}$
0.033	0.74	0.59	1.11	15.7	0.72	-0.0670	-0.0467
0.067	0.74	1.19	1.46	17.2	0.61	-0.1276	-0.0452
0.103	0.73	1.83	1.62	18.3	0.76	-0.1546	-0.0700
0.025	0.98	0.60	1.09	14.5	0.78	-0.0650	-0.0312
0.052	0.96	1.21	1.31	17.2	0.70	-0.1232	-0.0680
0.079	0.97	1.85	1.47	17.8	0.64	-0.1237	-0.0582
0.020	1.21	0.61	1.02	16.2	0.61	-0.0612	-0.0560
0.040	1.21	1.18	1.18	15.1	0.63	-0.0761	-0.0403
0.062	1.22	1.83	1.33	16.9	0.51	-0.0932	-0.0538
0.018	1.38	0.60	1.03	15.0	0.71	-0.0571	-0.0287
0.036	1.37	1.19	1.15	16.7	0.69	-0.0826	-0.0654
0.053	1.40	1.83	1.27	14.0	0.61	-0.0899	-0.0168

References

Pope, A.; Harper, J.J. 1966. *Low Speed Wind Tunnel Testing*. New York, NY: John Wiley & Sons, Inc.

Schlichting, H. 1979. *Boundary Layer Theory*. New York, NY: McGraw-Hill Inc.

Smetana, F., Summey, D., et-al. 1975. *Light Aircraft Lift, Drag, and Moment Prediction - a Review and Analysis*. North Carolina State University. NASA CR-2523.

Appendix A: Model and Surface Pressure Tap Coordinates

List of Tables

	Page
Table A1. S809 Measured Model Coordinates	A-3
Table A2. S809 Surface Pressure Taps, Non-Dimensional Coordinates	A-10

Table A1. S809 Measured Model Coordinates, 18-inch Desired Cord.

Chord Station (in)	Upper Ordinate (in)	Chord Station (in)	Lower Ordinate (in)
0.0040	0.0080	0.0040	0.0080
0.0045	0.0211	0.0100	-0.0401
0.0105	0.0553	0.0143	-0.0545
0.0147	0.0696	0.0185	-0.0662
0.0190	0.0811	0.0228	-0.0766
0.0234	0.0915	0.0271	-0.0856
0.0277	0.1013	0.0314	-0.0940
0.0320	0.1098	0.0354	-0.1012
0.0366	0.1186	0.0400	-0.1088
0.0411	0.1267	0.0445	-0.1162
0.0453	0.1336	0.0486	-0.1223
0.0498	0.1412	0.0532	-0.1291
0.0542	0.1481	0.0574	-0.1349
0.0590	0.1555	0.0618	-0.1406
0.0634	0.1621	0.0664	-0.1462
0.0678	0.1680	0.0711	-0.1520
0.0726	0.1748	0.0751	-0.1564
0.0769	0.1806	0.0800	-0.1616
0.0818	0.1867	0.0849	-0.1673
0.0865	0.1928	0.0891	-0.1718
0.0910	0.1983	0.0934	-0.1757
0.0959	0.2043	0.0989	-0.1814
0.1006	0.2099	0.1035	-0.1861
0.1056	0.2159	0.1080	-0.1904
0.1102	0.2212	0.1132	-0.1952
0.1149	0.2264	0.1183	-0.2005
0.1197	0.2318	0.1222	-0.2042
0.1246	0.2375	0.1263	-0.2075
0.1290	0.2421	0.1321	-0.2125
0.1342	0.2475	0.1372	-0.2171
0.1391	0.2530	0.1419	-0.2215
0.1435	0.2574	0.1457	-0.2246
0.1487	0.2629	0.1507	-0.2286
0.1534	0.2673	0.1558	-0.2328
0.1585	0.2726	0.1603	-0.2364

Table A1. S809 Measured Model Coordinates, 18-inch Desired Cord.

Chord Station (in)	Upper Ordinate (in)	Chord Station (in)	Lower Ordinate (in)
0.1628	0.2767	0.1645	-0.2396
0.1679	0.2814	0.1749	-0.2480
0.1733	0.2871	0.1839	-0.2542
0.1820	0.2953	0.1942	-0.2622
0.1920	0.3041	0.2036	-0.2693
0.2018	0.3129	0.2128	-0.2759
0.2110	0.3206	0.2221	-0.2821
0.2211	0.3291	0.2322	-0.2891
0.2307	0.3372	0.2416	-0.2961
0.2404	0.3453	0.2504	-0.3014
0.2500	0.3532	0.2608	-0.3090
0.2595	0.3610	0.2692	-0.3141
0.2692	0.3686	0.2795	-0.3208
0.2788	0.3764	0.2890	-0.3272
0.2881	0.3834	0.2982	-0.3328
0.2979	0.3909	0.3083	-0.3393
0.3076	0.3985	0.3178	-0.3457
0.3171	0.4059	0.3268	-0.3510
0.3260	0.4122	0.3370	-0.3572
0.3364	0.4199	0.3469	-0.3635
0.3457	0.4267	0.3561	-0.3694
0.3554	0.4336	0.3654	-0.3744
0.3648	0.4405	0.3758	-0.3815
0.3738	0.4462	0.3841	-0.3857
0.3843	0.4533	0.3950	-0.3923
0.3937	0.4600	0.4042	-0.3981
0.4027	0.4654	0.4130	-0.4025
0.4130	0.4722	0.4238	-0.4089
0.4224	0.4785	0.4332	-0.4149
0.4322	0.4849	0.4420	-0.4192
0.4415	0.4911	0.4528	-0.4262
0.4507	0.4963	0.4609	-0.4302
0.4615	0.5035	0.4715	-0.4364
0.4707	0.5095	0.4807	-0.4410
0.4799	0.5148	0.4910	-0.4472
0.4901	0.5211	0.4994	-0.4508

Table A1. S809 Measured Model Coordinates, 18-inch Desired Cord.

Chord Station (in)	Upper Ordinate (in)	Chord Station (in)	Lower Ordinate (in)
0.4998	0.5269	0.5109	-0.4574
0.5094	0.5326	0.5201	-0.4629
0.5196	0.5387	0.5289	-0.4668
0.5291	0.5447	0.5397	-0.4730
0.5379	0.5492	0.5488	-0.4777
0.5488	0.5562	0.5587	-0.4831
0.5572	0.5605	0.5683	-0.4881
0.5680	0.5667	0.5779	-0.4930
0.5772	0.5719	0.5877	-0.4980
0.5869	0.5771	0.5975	-0.5031
0.5966	0.5826	0.6068	-0.5077
0.6060	0.5877	0.6169	-0.5128
0.6160	0.5930	0.6261	-0.5174
0.6257	0.5988	0.6357	-0.5220
0.6344	0.6026	0.6457	-0.5270
0.6454	0.6090	0.6556	-0.5320
0.6541	0.6135	0.6650	-0.5370
0.6640	0.6181	0.6738	-0.5407
0.6742	0.6236	0.6850	-0.5460
0.6838	0.6288	0.6952	-0.5518
0.6932	0.6336	0.7036	-0.5555
0.7034	0.6386	0.7138	-0.5603
0.7134	0.6440	0.7235	-0.5648
0.7229	0.6486	0.7340	-0.5698
0.7325	0.6534	0.7436	-0.5747
0.7426	0.6585	0.7521	-0.5782
0.7526	0.6636	0.7627	-0.5835
0.7608	0.6671	0.7720	-0.5880
0.7718	0.6724	0.7822	-0.5925
0.7815	0.6775	0.7918	-0.5971
0.7912	0.6824	0.8016	-0.6018
0.8012	0.6872	0.8114	-0.6062
0.8107	0.6919	0.8209	-0.6106
0.8204	0.6967	0.8307	-0.6150
0.8298	0.7010	0.8409	-0.6196
0.8395	0.7054	0.8504	-0.6242

Table A1. S809 Measured Model Coordinates, 18-inch Desired Cord.

Chord Station (in)	Upper Ordinate (in)	Chord Station (in)	Lower Ordinate (in)
0.8494	0.7098	0.8599	-0.6286
0.8589	0.7140	0.8699	-0.6329
0.8690	0.7185	0.8792	-0.6371
0.8782	0.7226	0.8894	-0.6418
0.8883	0.7269	0.8993	-0.6463
0.8986	0.7314	0.9087	-0.6507
0.9078	0.7359	0.9187	-0.6552
0.9177	0.7402	0.9282	-0.6594
0.9279	0.7446	0.9371	-0.6633
0.9375	0.7492	1.1374	-0.7504
0.9463	0.7530	1.3368	-0.8329
1.1471	0.8375	1.5360	-0.9117
1.3469	0.9151	1.7355	-0.9862
1.5469	0.9867	1.9349	-1.0585
1.7469	1.0528	2.1344	-1.1275
1.9468	1.1146	2.3340	-1.1948
2.1470	1.1717	2.5333	-1.2578
2.3470	1.2252	2.7329	-1.3184
2.5469	1.2765	2.9325	-1.3757
2.7471	1.3249	3.1320	-1.4315
2.9471	1.3696	3.3315	-1.4839
3.1468	1.4121	3.5312	-1.5341
3.3471	1.4518	3.7308	-1.5818
3.5468	1.4890	3.9303	-1.6275
3.7467	1.5237	4.1299	-1.6699
3.9468	1.5566	4.3296	-1.7105
4.1466	1.5873	4.5291	-1.7481
4.3467	1.6160	4.7287	-1.7826
4.5467	1.6430	4.9282	-1.8142
4.7465	1.6680	5.1278	-1.8430
4.9465	1.6912	5.3276	-1.8691
5.1464	1.7124	5.5271	-1.8915
5.3461	1.7314	5.7268	-1.9108
5.5462	1.7485	5.9267	-1.9273
5.7459	1.7636	6.1262	-1.9396
5.9459	1.7767	6.3259	-1.9484

Table A1. S809 Measured Model Coordinates, 18-inch Desired Cord.

Chord Station (in)	Upper Ordinate (in)	Chord Station (in)	Lower Ordinate (in)
6.1458	1.7882	6.5257	-1.9537
6.3456	1.7977	6.7252	-1.9553
6.5455	1.8059	6.9254	-1.9521
6.7454	1.8125	7.1248	-1.9448
6.9453	1.8177	7.3246	-1.9335
7.1449	1.8207	7.5247	-1.9178
7.3447	1.8214	7.7244	-1.8981
7.5444	1.8198	7.9244	-1.8746
7.7444	1.8159	8.1241	-1.8469
7.9439	1.8086	8.3241	-1.8155
8.1435	1.7978	8.5242	-1.7803
8.3433	1.7832	8.7244	-1.7415
8.5426	1.7655	8.9245	-1.6995
8.7423	1.7443	9.1249	-1.6547
8.9422	1.7199	9.3252	-1.6078
9.1415	1.6920	9.5256	-1.5589
9.3413	1.6608	9.7260	-1.5089
9.5413	1.6275	9.9266	-1.4576
9.7409	1.5924	10.1268	-1.4058
9.9413	1.5565	10.3278	-1.3528
10.1410	1.5197	10.5283	-1.2997
10.3410	1.4819	10.7285	-1.2464
10.5410	1.4433	10.9294	-1.1930
10.7409	1.4053	11.1296	-1.1398
10.9408	1.3667	11.3301	-1.0863
11.1409	1.3283	11.5308	-1.0332
11.3410	1.2898	11.7311	-0.9805
11.5408	1.2511	11.9316	-0.9283
11.7410	1.2123	12.1325	-0.8765
11.9410	1.1737	12.3329	-0.8252
12.1413	1.1352	12.5336	-0.7743
12.3416	1.0969	12.7342	-0.7246
12.5418	1.0588	12.9347	-0.6761
12.7420	1.0207	13.1351	-0.6288
12.9423	0.9826	13.3358	-0.5818
13.1423	0.9448	13.5361	-0.5361

Table A1. S809 Measured Model Coordinates, 18-inch Desired Cord.

Chord Station (in)	Upper Ordinate (in)	Chord Station (in)	Lower Ordinate (in)
13.3427	0.9071	13.7366	-0.4916
13.5429	0.8691	13.9370	-0.4488
13.7427	0.8311	14.1373	-0.4075
13.9427	0.7932	14.3380	-0.3677
14.1427	0.7555	14.5383	-0.3290
14.3427	0.7181	14.7387	-0.2919
14.5426	0.6809	14.9394	-0.2574
14.7425	0.6435	15.1396	-0.2250
14.9424	0.6065	15.3402	-0.1941
15.1424	0.5697	15.5407	-0.1650
15.3422	0.5332	15.7409	-0.1377
15.5422	0.4967	15.9415	-0.1123
15.7423	0.4597	16.1418	-0.0888
15.9423	0.4228	16.3418	-0.0628
16.1423	0.3861	16.5433	-0.0482
16.3423	0.3493	16.7431	-0.0331
16.5424	0.3119	16.9441	-0.0218
16.7423	0.2745	17.1445	-0.0141
16.9430	0.2371	17.3448	-0.0092
17.1429	0.1995	17.5453	-0.0071
17.3430	0.1622	17.7458	-0.0078
17.5433	0.1261	17.9456	-0.0072
17.7435	0.0917	17.9498	-0.0071
17.9430	0.0567	17.9545	-0.0069
17.9474	0.0558	17.9589	-0.0067
17.9525	0.0548	17.9638	-0.0066
17.9574	0.0538	17.9684	-0.0064
17.9622	0.0528	17.9729	-0.0062
17.9668	0.0519	17.9772	-0.0059
17.9717	0.0508	17.9818	-0.0056
17.9768	0.0498	17.9867	-0.0054
17.9814	0.0488	17.9915	-0.0050
17.9860	0.0477	17.9960	-0.0047
17.9909	0.0467	18.0005	-0.0043
17.9956	0.0456	18.0052	-0.0039
18.0003	0.0444	18.0100	-0.0035

Table A1. S809 Measured Model Coordinates, 18-inch Desired Cord.

Chord Station (in)	Upper Ordinate (in)	Chord Station (in)	Lower Ordinate (in)
18.0051	0.0432	18.0145	-0.0029
18.0099	0.0420	18.0178	-0.0022
18.0146	0.0408	18.0196	-0.0011
18.0190	0.0394	18.0205	-0.0015
18.0225	0.0379	18.0212	0.0028
18.0242	0.0362	18.0247	0.0080
18.0241	0.0340		
18.0274	0.0287		

End of Table A1

**Table A2. S809 Surface Pressure Taps,
Non-Dimensional Coordinates**

Tap Number	Chord Station	Ordinate
1	1.0023	0.0019
2	0.9652	-0.0009
3	0.9069	-0.0042
4	0.8522	-0.0111
5	0.7919	-0.0216
6	0.7280	-0.0356
7	0.6716	-0.0495
8	0.6196	-0.0631
9	0.5738	-0.0752
10	0.5346	-0.0853
11	0.5018	-0.0931
12	0.4743	-0.0988
13	0.4497	-0.1028
14	0.4251	-0.1059
15	0.3983	-0.1079
16	0.3672	-0.1086
17	0.3322	-0.1073
18	0.2945	-0.1036
19	0.2547	-0.0976
20	0.2136	-0.0893
21	0.1713	-0.0787
22	0.1284	-0.0658
23	0.0882	-0.0516
24	0.0556	-0.0383
25	0.0375	-0.0299
26	0.0302	-0.0262
27	0.0233	-0.0224
28	0.0154	-0.0176
29	0.0087	-0.0129
30	0.0040	-0.0085
31	0.0000	0.0010
32	0.0045	0.0109
33	0.0088	0.0156
34	0.0138	0.0200
35	0.0195	0.0243
36	0.0252	0.0281

**Table A2. S809 Surface Pressure Taps,
Non-Dimensional Coordinates**

Tap Number	Chord Station	Ordinate
137	0.0318	0.0320
38	0.0389	0.0357
39	0.0455	0.0389
40	0.0646	0.0472
41	0.1011	0.0601
42	0.1437	0.0717
43	0.1889	0.0814
44	0.2342	0.0889
45	0.2784	0.0945
46	0.3189	0.0980
47	0.3557	0.1001
48	0.3886	0.1011
49	0.4198	0.1011
50	0.4516	0.0999
51	0.4880	0.0966
52	0.5294	0.0904
53	0.5753	0.0820
54	0.6301	0.0715
55	0.6870	0.0605
56	0.7398	0.0504
57	0.7975	0.0395
58	0.8548	0.0288
59	0.9096	0.0187
60	0.9675	0.0065
End of Table A2		

Appendix B: Steady State Data Integrated Coefficients and Pressure Distributions

List of Figures

Page

Pressure Distributions, Steady State, Re = 0.75 million	B-20
B1. $\alpha = -20.1^\circ$	B-21
B2. $\alpha = -18.1^\circ$	B-21
B3. $\alpha = -16.1^\circ$	B-21
B4. $\alpha = -14.2^\circ$	B-21
B5. $\alpha = -12.2^\circ$	B-22
B6. $\alpha = -10.1^\circ$	B-22
B7. $\alpha = -8.2^\circ$	B-22
B8. $\alpha = -6.1^\circ$	B-22
B9. $\alpha = -4.1^\circ$	B-23
B10. $\alpha = -2.1^\circ$	B-23
B11. $\alpha = 0.1^\circ$	B-23
B12. $\alpha = 2.0^\circ$	B-23
B13. $\alpha = 4.1^\circ$	B-24
B14. $\alpha = 6.2^\circ$	B-24
B15. $\alpha = 8.1^\circ$	B-24
B16. $\alpha = 10.2^\circ$	B-24
B17. $\alpha = 11.3^\circ$	B-25
B18. $\alpha = 12.1^\circ$	B-25
B19. $\alpha = 13.2^\circ$	B-25
B20. $\alpha = 14.2^\circ$	B-25
B21. $\alpha = 15.3^\circ$	B-26
B22. $\alpha = 16.3^\circ$	B-26
B23. $\alpha = 17.1^\circ$	B-26
B24. $\alpha = 18.1^\circ$	B-26
B25. $\alpha = 19.1^\circ$	B-27
B26. $\alpha = 20.1^\circ$	B-27
B27. $\alpha = 22.0^\circ$	B-27
B28. $\alpha = 24.1^\circ$	B-27
B29. $\alpha = 26.2^\circ$	B-28
B30. $\alpha = 28.0^\circ$	B-28
B31. $\alpha = 30.1^\circ$	B-28
B32. $\alpha = 32.0^\circ$	B-28
B33. $\alpha = 34.1^\circ$	B-29
B34. $\alpha = 36.2^\circ$	B-29
B35. $\alpha = 38.0^\circ$	B-29
B36. $\alpha = 40.0^\circ$	B-29
 Pressure Distributions, Steady State, Re = 1 million	 B-30
B37. $\alpha = -20.1^\circ$	B-31
B38. $\alpha = -18.2^\circ$	B-31
B39. $\alpha = -16.2^\circ$	B-31
B40. $\alpha = -14.1^\circ$	B-31
B41. $\alpha = -12.1^\circ$	B-32
B42. $\alpha = -10.2^\circ$	B-32
B43. $\alpha = -8.2^\circ$	B-32
B44. $\alpha = -6.2^\circ$	B-32
B45. $\alpha = -4.1^\circ$	B-33

B46. $\alpha = -2.1^\circ$	B-33
B47. $\alpha = 0.0^\circ$	B-33
B48. $\alpha = 2.1^\circ$	B-33
B49. $\alpha = 4.1^\circ$	B-34
B50. $\alpha = 6.1^\circ$	B-34
B51. $\alpha = 8.2^\circ$	B-34
B52. $\alpha = 10.1^\circ$	B-34
B53. $\alpha = 11.2^\circ$	B-35
B54. $\alpha = 12.2^\circ$	B-35
B55. $\alpha = 13.3^\circ$	B-35
B56. $\alpha = 14.2^\circ$	B-35
B57. $\alpha = 15.2^\circ$	B-36
B58. $\alpha = 16.2^\circ$	B-36
B59. $\alpha = 17.2^\circ$	B-36
B60. $\alpha = 18.1^\circ$	B-36
B61. $\alpha = 19.2^\circ$	B-37
B62. $\alpha = 20.0^\circ$	B-37
B63. $\alpha = 22.1^\circ$	B-37
B64. $\alpha = 24.0^\circ$	B-37
B65. $\alpha = 26.1^\circ$	B-38
B66. $\alpha = 28.1^\circ$	B-38
B67. $\alpha = 30.0^\circ$	B-38
B68. $\alpha = 32.1^\circ$	B-38
B69. $\alpha = 34.1^\circ$	B-39
B70. $\alpha = 36.0^\circ$	B-39
B71. $\alpha = 38.1^\circ$	B-39
B72. $\alpha = 39.9^\circ$	B-39
Pressure Distributions, Steady State, $Re = 1.25$ million	B-40
B73. $\alpha = -20.2^\circ$	B-41
B74. $\alpha = -18.1^\circ$	B-41
B75. $\alpha = -16.0^\circ$	B-41
B76. $\alpha = -14.2^\circ$	B-41
B77. $\alpha = -12.0^\circ$	B-42
B78. $\alpha = -10.1^\circ$	B-42
B79. $\alpha = -8.1^\circ$	B-42
B80. $\alpha = -6.1^\circ$	B-42
B81. $\alpha = -4.1^\circ$	B-43
B82. $\alpha = -2.1^\circ$	B-43
B83. $\alpha = 0.0^\circ$	B-43
B84. $\alpha = 2.1^\circ$	B-43
B85. $\alpha = 4.1^\circ$	B-44
B86. $\alpha = 6.1^\circ$	B-44
B87. $\alpha = 8.1^\circ$	B-44
B88. $\alpha = 10.2^\circ$	B-44
B89. $\alpha = 11.2^\circ$	B-45
B90. $\alpha = 12.2^\circ$	B-45
B91. $\alpha = 13.2^\circ$	B-45
B92. $\alpha = 14.2^\circ$	B-45
B93. $\alpha = 15.2^\circ$	B-46

B94. $\alpha = 16.2^\circ$	B-46
B95. $\alpha = 17.2^\circ$	B-46
B96. $\alpha = 18.2^\circ$	B-46
B97. $\alpha = 19.0^\circ$	B-47
B98. $\alpha = 20.1^\circ$	B-47
B99. $\alpha = 22.1^\circ$	B-47
B100. $\alpha = 24.0^\circ$	B-47
B101. $\alpha = 26.0^\circ$	B-48
B102. $\alpha = 28.0^\circ$	B-48
B103. $\alpha = 30.0^\circ$	B-48
B104. $\alpha = 31.9^\circ$	B-48
B105. $\alpha = 34.1^\circ$	B-49
B106. $\alpha = 36.2^\circ$	B-49
B107. $\alpha = 38.0^\circ$	B-49
B108. $\alpha = 39.9^\circ$	B-49
Pressure Distributions, Steady State, Re = 1.5 million	B-50
B109. $\alpha = -20.1^\circ$	B-51
B110. $\alpha = -18.0^\circ$	B-51
B111. $\alpha = -16.1^\circ$	B-51
B112. $\alpha = -14.2^\circ$	B-51
B113. $\alpha = -12.2^\circ$	B-52
B114. $\alpha = -10.2^\circ$	B-52
B115. $\alpha = -8.1^\circ$	B-52
B116. $\alpha = -6.2^\circ$	B-52
B117. $\alpha = -4.1^\circ$	B-53
B118. $\alpha = -2.0^\circ$	B-53
B119. $\alpha = 0.0^\circ$	B-53
B120. $\alpha = 2.1^\circ$	B-53
B121. $\alpha = 4.1^\circ$	B-54
B122. $\alpha = 6.1^\circ$	B-54
B123. $\alpha = 8.1^\circ$	B-54
B124. $\alpha = 10.2^\circ$	B-54
B125. $\alpha = 11.2^\circ$	B-55
B126. $\alpha = 12.2^\circ$	B-55
B127. $\alpha = 13.2^\circ$	B-55
B128. $\alpha = 14.1^\circ$	B-55
B129. $\alpha = 15.2^\circ$	B-56
B130. $\alpha = 16.2^\circ$	B-56
B131. $\alpha = 17.2^\circ$	B-56
B132. $\alpha = 18.2^\circ$	B-56
B133. $\alpha = 19.0^\circ$	B-57
B134. $\alpha = 20.2^\circ$	B-57
B135. $\alpha = 22.2^\circ$	B-57

List of Tables Page

B1. S809, Clean, Re=0.75 x 10 ⁶	B-6
B2. S809, Clean, Re = 1 x 10 ⁶	B-8
B3. S809, Clean, Re = 1.25 x 10 ⁶	B-10
B4. S809, Clean, Re = 1.5 x 10 ⁶	B-12
B5. S809, LEGR, Re = 0.75 x 10 ⁶	B-13
B6. S809, LEGR, Re = 1 x 10 ⁶	B-15
B7. S809, LEGR, Re = 1.25 x 10 ⁶	B-17
B8. S809, LEGR, Re = 1.5 x 10 ⁶	B-19

Table B1. S809, Clean, Re=0.75 x 10⁶

Run	AOA	C _l	C _{dp}	C _{m^{1/4}}	Re x 10 ⁻⁶	C _{dw}
91	-20.1	-0.56	0.3027	0.0612	0.76	--
90	-18.1	-0.67	0.3069	0.0904	0.75	--
89	-16.1	-0.79	0.1928	0.0293	0.75	--
88	-14.2	-0.84	0.0898	-0.0090	0.75	--
87	-12.2	-0.70	0.0553	-0.0045	0.75	--
86	-10.1	-0.63	0.0390	-0.0044	0.73	--
85	-8.2	-0.56	0.0233	-0.0051	0.74	0.0639
84	-6.1	-0.64	0.0112	0.0018	0.74	0.0119
83	-4.1	-0.42	-0.0004	-0.0216	0.76	0.0121
82	-2.1	-0.21	-0.0003	-0.0282	0.75	0.0110
92	0.1	0.05	0.0029	-0.0346	0.75	0.0113
93	2.0	0.30	0.0056	-0.0405	0.74	0.0107
94	4.1	0.54	0.0067	-0.0455	0.75	0.0121
95	6.2	0.79	0.0085	-0.0507	0.74	0.0131
96	8.1	0.90	0.0127	-0.0404	0.75	0.0139
97	10.2	0.93	0.0274	-0.0321	0.75	0.0436
98	11.3	0.92	0.0303	-0.0281	0.74	--
99	12.1	0.95	0.0369	-0.0284	0.74	--
100	13.2	0.99	0.0509	-0.0322	0.74	--
101	14.2	1.01	0.0648	-0.0361	0.74	--
102	15.3	1.02	0.0776	-0.0363	0.74	--
103	16.3	1.00	0.0917	-0.0393	0.74	--
104	17.1	0.94	0.0994	-0.0398	0.73	--
105	18.1	0.85	0.2306	-0.0983	0.77	--
106	19.1	0.70	0.3142	-0.1242	0.76	--
107	20.1	0.66	0.3186	-0.1155	0.76	--
108	22.0	0.70	0.3694	-0.1265	0.76	--
109	24.1	0.79	0.4457	-0.1488	0.77	--
110	26.2	0.88	0.5260	-0.1723	0.76	--

Table B1. S809, Clean, Re=0.75 x 10⁶

Run	AOA	C _l	C _{dp}	C _{m¼}	Re x 10 ⁻⁶	C _{dw}
111	28.0	0.96	0.6042	-0.1949	0.76	--
112	30.1	1.05	0.7005	-0.2229	0.74	--
113	32.0	1.12	0.7908	-0.2490	0.75	--
114	34.1	1.18	0.8940	-0.2779	0.75	--
115	36.2	1.19	0.9647	-0.2916	0.74	--
116	38.0	1.23	1.0523	-0.3171	0.74	--
117	40.0	1.25	1.1403	-0.3391	0.73	--

End of Table B1

Table B2. S809, Clean, Re = 1 x 10⁶

Run	AOA	C _l	C _{dp}	C _{m½}	Re x 10 ⁻⁶	C _{dw}
129	-20.1	-0.55	0.2983	0.0590	1.01	--
128	-18.2	-0.65	0.2955	0.0797	1.02	--
127	-16.2	-0.80	0.1826	0.0244	1.01	--
126	-14.1	-0.79	0.0793	0.0060	0.99	--
125	-12.1	-0.70	0.0547	-0.0043	1.01	--
124	-10.2	-0.63	0.0401	-0.0035	1.00	0.0750
123	-8.2	-0.58	0.0266	-0.0032	1.00	--
122	-6.2	-0.61	0.0183	0.0088	1.00	0.0193
121	-4.1	-0.40	0.0004	-0.0245	0.99	0.0127
120	-2.1	-0.16	0.0009	-0.0308	1.00	0.0090
130	0.0	0.07	0.0022	-0.0356	1.01	0.0085
131	2.1	0.30	0.0037	-0.0394	1.00	0.0088
132	4.1	0.55	0.0050	-0.0461	1.00	0.0088
133	6.1	0.79	0.0063	-0.0499	1.00	0.0090
134	8.2	0.90	0.0096	-0.0364	1.00	0.0167
135	10.1	0.94	0.0231	-0.0396	1.00	0.0487
136	11.2	0.93	0.0236	-0.0280	1.00	--
137	12.2	0.97	0.0368	-0.0307	1.00	--
138	13.3	1.00	0.0551	-0.0362	0.99	--
139	14.2	1.02	0.0618	-0.0365	0.99	--
140	15.2	1.03	0.0705	-0.0375	0.99	--
141	16.2	1.01	0.0880	-0.0430	1.00	--
142	17.2	0.95	0.1043	-0.0456	0.99	--
143	18.1	0.90	0.1325	-0.0581	1.00	--
144	19.2	0.78	0.3474	-0.1464	1.02	--
145	20.0	0.67	0.3211	-0.1171	1.02	--
146	22.1	0.70	0.3699	-0.1253	1.02	--
147	24.0	0.77	0.4348	-0.1430	1.03	--
148	26.1	0.91	0.5356	-0.1783	1.04	--

Table B2. S809, Clean, Re = 1 x 10⁶

Run	AOA	C _l	C _{dp}	C _{m¼}	Re x 10 ⁻⁶	C _{dw}
149	28.1	0.99	0.6192	-0.2013	1.04	--
150	30.0	1.06	0.7025	-0.2247	1.06	--
151	32.1	1.11	0.7916	-0.2483	1.06	--
152	34.1	1.18	0.8963	-0.2804	1.07	--
153	36.0	1.21	0.9737	-0.2984	1.08	--
154	38.1	1.24	1.0627	-0.3204	1.10	--
155	39.9	1.26	1.1509	-0.3492	1.10	--

End of Table B2

Table B3. S809, Clean, Re = 1.25 x 10⁶

Run	AOA	C _l	C _{dp}	C _{m½}	Re x 10 ⁻⁶	C _{dw}
23	-20.2	-0.56	0.3016	0.0599	1.26	--
22	-18.1	-0.60	0.2783	0.0747	1.29	--
21	-16.0	-0.81	0.1250	-0.0042	1.24	--
20	-14.2	-0.76	0.0675	-0.0058	1.25	--
19	-12.0	-0.70	0.0555	-0.0009	1.25	--
18	-10.1	-0.62	0.0371	-0.0066	1.26	0.0664
17	-8.1	-0.57	0.0293	0.0008	1.25	0.0625
16	-6.1	-0.59	0.0142	-0.0021	1.24	0.0093
15	-4.1	-0.39	0.0011	-0.0251	1.25	0.0102
14	-2.1	-0.15	0.0011	-0.0301	1.26	0.0075
24	0.0	0.09	0.0012	-0.0354	1.24	0.0085
25	2.1	0.33	0.0030	-0.0423	1.24	0.0073
26	4.1	0.59	0.0037	-0.0490	1.25	0.0082
27	6.1	0.80	0.0033	-0.0495	1.24	0.0105
28	8.1	0.90	0.0112	-0.0387	1.25	0.0138
29	10.2	0.93	0.0203	-0.0362	1.25	0.0474
30	11.2	0.94	0.0256	-0.0310	1.24	--
31	12.2	1.00	0.0423	-0.0380	1.25	--
32	13.2	1.02	0.0544	-0.0392	1.25	--
33	14.2	1.04	0.0613	-0.0379	1.25	--
34	15.2	1.06	0.0750	-0.0419	1.25	--
35	16.2	1.02	0.0894	-0.0435	1.25	--
36	17.2	0.96	0.1060	-0.0491	1.25	--
37	18.2	0.91	0.1373	-0.0619	1.26	--
38	19.0	0.72	0.3302	-0.1395	1.28	--
39	20.1	0.70	0.3394	-0.1317	1.27	--
40	22.1	0.70	0.3725	-0.1274	1.28	--
41	24.0	0.76	0.4299	-0.1416	1.29	--
42	26.0	0.87	0.5161	-0.1688	1.29	--

Table B3. S809, Clean, Re = 1.25×10^6

Run	AOA	C _l	C _{dp}	C _{m^{1/4}}	Re x 10 ⁻⁶	C _{dw}
43	28.0	0.97	0.6104	-0.1980	1.31	--
44	30.0	1.04	0.6970	-0.2220	1.31	--
45	31.9	1.11	0.7858	-0.2470	1.33	--
46	34.1	1.18	0.8939	-0.2794	1.34	--
47	36.2	1.21	0.9802	-0.2987	1.36	--
48	38.0	1.25	1.0677	-0.3246	1.36	--
49	39.9	1.25	1.1411	-0.3409	1.36	--

End of Table B3

Table B4. S809, Clean, Re = 1.5×10^6

Run	AOA	C _l	C _{dp}	C _{m^{1/4}}	Re x 10 ⁻⁶	C _{dw}
61	-20.1	-0.60	0.3210	0.0777	1.53	--
60	-18.0	-0.59	0.2866	0.0785	1.53	--
59	-16.1	-0.79	0.1241	-0.0040	1.51	--
58	-14.2	-0.77	0.0642	-0.0074	1.50	--
57	-12.2	-0.70	0.0550	-0.0034	1.49	--
56	-10.2	-0.62	0.0361	-0.0081	1.50	0.0716
55	-8.1	-0.58	0.0314	0.0042	1.50	0.0654
54	-6.2	-0.58	0.0208	0.0073	1.50	0.0225
53	-4.1	-0.40	0.0018	-0.0232	1.50	0.0084
52	-2.0	-0.14	0.0008	-0.0311	1.50	0.0087
62	0.0	0.11	0.0004	-0.0366	1.50	0.0069
63	2.1	0.34	0.0027	-0.0430	1.50	0.0081
64	4.1	0.60	0.0026	-0.0490	1.50	0.0061
65	6.1	0.79	0.0035	-0.0484	1.50	0.0108
66	8.1	0.92	0.0079	-0.0381	1.50	0.0147
67	10.2	0.95	0.0209	-0.0392	1.50	0.0490
68	11.2	0.94	0.0252	-0.0321	1.51	0.0630
69	12.2	1.00	0.0397	-0.0376	1.50	--
70	13.2	1.03	0.0479	-0.0380	1.49	--
71	14.1	1.05	0.0608	-0.0398	1.50	--
72	15.2	1.06	0.0744	-0.0426	1.50	--
73	16.2	1.03	0.0838	-0.0415	1.50	--
74	17.2	0.96	0.1073	-0.0504	1.51	--
75	18.2	0.90	0.1429	-0.0658	1.50	--
76	19.0	0.88	0.1733	-0.0790	1.50	--
77	20.2	0.85	0.2020	-0.0870	1.50	--
78	22.2	0.71	0.3767	-0.1285	1.54	--
79	24.0	0.78	0.4369	-0.1439	1.54	--

End of Table B4

Table B5. S809, LEGR, Re = 0.75 x 10⁶

Run	AOA	C _l	C _{dp}	C _{m½}	Re x 10 ⁻⁶	C _{dw}
167	-20.1	-0.66	0.2943	0.0732	0.75	--
166	-18.1	-0.83	0.1648	0.0259	0.75	--
165	-16.2	-0.73	0.0987	-0.0067	0.75	--
164	-14.2	-0.71	0.0775	-0.0066	0.75	--
163	-12.1	-0.67	0.0612	-0.0056	0.75	--
162	-10.2	-0.59	0.0446	-0.0077	0.75	--
161	-8.0	-0.52	0.0318	-0.0068	0.75	--
160	-6.2	-0.43	0.0187	-0.0069	0.75	--
159	-4.1	-0.35	0.0105	-0.0084	0.76	0.0263
158	-2.0	-0.18	0.0040	-0.0195	0.75	0.0160
168	-0.1	0.04	0.0038	-0.0237	0.75	0.0154
169	2.1	0.24	0.0052	-0.0304	0.75	0.0151
170	4.0	0.45	0.0075	-0.0306	0.75	0.0156
171	6.1	0.64	0.0099	-0.0305	0.75	0.0178
172	8.2	0.73	0.0195	-0.0298	0.75	0.0493
173	10.1	0.75	0.0285	-0.0215	0.75	0.0653
174	11.1	0.81	0.0411	-0.0241	0.74	0.0563
175	12.2	0.85	0.0503	-0.0266	0.75	--
176	13.3	0.87	0.0621	-0.0278	0.75	--
177	14.1	0.86	0.0698	-0.0289	0.75	--
178	15.1	0.74	0.0995	-0.0437	0.75	--
179	16.1	0.69	0.1461	-0.0652	0.75	--
180	17.1	0.69	0.1791	-0.0758	0.76	--
181	18.2	0.70	0.2118	-0.0851	0.75	--
182	19.0	0.74	0.2395	-0.0950	0.75	--
183	20.0	0.76	0.2761	-0.1072	0.75	--
184	22.1	0.86	0.3589	-0.1277	0.76	--
185	24.0	0.80	0.4141	-0.1348	0.76	--
186	26.1	0.81	0.4718	-0.1452	0.77	--

Table B5. S809, LEGR, Re = 0.75 x 10⁶

Run	AOA	C _l	C _{dp}	C _{m<4}	Re x 10 ⁻⁶	C _{dw}
187	28.0	0.96	0.6002	-0.1917	0.76	--
188	30.0	1.04	0.6938	-0.2198	0.75	--
189	32.1	1.11	0.7862	-0.2454	0.75	--
190	34.0	1.16	0.8765	-0.2693	0.74	--
191	36.0	1.20	0.9690	-0.2939	0.73	--
192	37.9	1.24	1.0549	-0.3184	0.74	--
193	39.9	1.24	1.1238	-0.3306	0.74	--

End of Table B5

Table B6. S809, LEGR, Re = 1 x 10⁶

Run	AOA	C _l	C _{dp}	C _{m^{1/4}}	Re x 10 ⁻⁶	C _{dw}
205	-20.1	-0.78	0.2837	0.0643	1.00	--
204	-18.2	-0.72	0.1470	0.0101	1.00	--
203	-16.1	-0.73	0.0965	-0.0054	1.00	--
202	-14.2	-0.72	0.0776	-0.0070	0.99	--
201	-12.2	-0.67	0.0633	-0.0067	0.99	0.0804
200	-10.2	-0.59	0.0475	-0.0057	1.00	0.0668
199	-8.1	-0.52	0.0326	-0.0051	1.00	0.0542
198	-6.1	-0.42	0.0202	-0.0085	1.00	0.0600
197	-4.1	-0.36	0.0121	-0.0056	1.00	0.0303
196	-2.1	-0.18	0.0063	-0.0199	1.00	0.0150
206	-0.1	0.02	0.0051	-0.0258	0.99	0.0161
207	2.1	0.24	0.0069	-0.0304	1.00	0.0146
208	4.1	0.46	0.0078	-0.0324	1.00	0.0148
209	6.1	0.64	0.0101	-0.0297	1.00	0.0185
210	8.1	0.73	0.0205	-0.0310	1.00	0.0397
211	10.1	0.77	0.0275	-0.0242	1.00	0.0614
212	11.1	0.82	0.0409	-0.0275	1.00	0.0498
213	12.2	0.85	0.0497	-0.0276	0.99	0.0562
214	13.1	0.87	0.0593	-0.0295	0.99	0.0650
215	14.2	0.83	0.0684	-0.0280	1.00	--
216	15.1	0.75	0.1020	-0.0467	0.99	--
217	16.1	0.70	0.1449	-0.0655	1.00	--
218	17.1	0.72	0.1771	-0.0773	1.00	--
219	18.0	0.72	0.2070	-0.0861	1.00	--
220	19.0	0.77	0.2432	-0.1011	1.00	--
221	20.0	0.79	0.2776	-0.1103	1.00	--
222	22.1	0.84	0.3598	-0.1298	1.01	--
223	24.1	0.83	0.4166	-0.1380	1.01	--
224	26.1	0.81	0.4705	-0.1471	1.01	--

Table B6. S809, LEGR, Re = 1 x 10⁶

Run	AOA	C _l	C _{dp}	C _{m<4}	Re x 10 ⁻⁶	C _{dw}
225	28.0	0.94	0.5845	-0.1872	1.02	--
226	30.0	1.05	0.6954	-0.2215	1.02	--
227	32.1	1.11	0.7869	-0.2471	1.03	--
228	34.0	1.17	0.8805	-0.2730	1.03	--
229	36.0	1.21	0.9673	-0.2963	1.02	--
230	38.0	1.24	1.0568	-0.3170	1.02	--
231	39.9	1.27	1.1540	-0.3466	1.02	--

End of Table B6

Table B7. S809, LEGR, Re = 1.25 x 10⁶

Run	AOA	C _l	C _{dp}	C _{m^{1/4}}	Re x 10 ⁻⁶	C _{dw}
243	-20.1	-0.80	0.2750	0.0622	1.25	--
242	-18.2	-0.71	0.1344	0.0050	1.24	--
241	-16.1	-0.75	0.0944	-0.0070	1.24	--
240	-14.2	-0.72	0.0762	-0.0088	1.25	--
239	-12.1	-0.66	0.0612	-0.0073	1.25	--
238	-10.1	-0.59	0.0472	-0.0051	1.26	--
237	-8.2	-0.50	0.0324	-0.0103	1.24	--
236	-6.0	-0.41	0.0209	-0.0080	1.26	0.0629
235	-4.1	-0.36	0.0130	-0.0045	1.25	0.0345
234	-2.0	-0.17	0.0062	-0.0219	1.25	0.0155
244	0.0	0.06	0.0045	-0.0272	1.26	0.0136
245	2.1	0.29	0.0051	-0.0306	1.26	0.0128
246	4.1	0.46	0.0079	-0.0327	1.25	0.0128
247	6.1	0.65	0.0105	-0.0318	1.24	0.0168
248	8.1	0.74	0.0211	-0.0319	1.26	0.0401
249	10.2	0.79	0.0298	-0.0254	1.25	0.0560
250	11.0	0.84	0.0377	-0.0286	1.25	--
251	12.1	0.87	0.0473	-0.0291	1.25	--
252	13.1	0.89	0.0614	-0.0308	1.25	--
253	14.2	0.87	0.0717	-0.0315	1.24	--
254	15.1	0.75	0.1023	-0.0475	1.23	--
255	16.1	0.77	0.1333	-0.0596	1.24	--
256	17.0	0.74	0.1719	-0.0753	1.24	--
257	18.1	0.76	0.2054	-0.0861	1.27	--
258	19.0	0.78	0.2393	-0.0992	1.25	--
259	20.0	0.80	0.2822	-0.1129	1.26	--
260	22.0	0.83	0.3627	-0.1350	1.28	--
261	24.1	0.84	0.4112	-0.1395	1.25	--
262	26.0	0.89	0.4757	-0.1512	1.25	--

Table B7. S809, LEGR, Re = 1.25 x 10⁶

Run	AOA	C _l	C _{dp}	C _{m¼}	Re x 10 ⁻⁶	C _{dw}
263	28.1	0.95	0.5908	-0.1911	1.24	--
264	29.9	1.05	0.6884	-0.2207	1.24	--
265	32.0	1.14	0.7978	-0.2542	1.23	--
266	34.0	1.18	0.8853	-0.2751	1.23	--
267	36.0	1.22	0.9739	-0.2988	1.22	--
268	38.0	1.24	1.0647	-0.3233	1.21	--
269	39.8	1.25	1.1371	-0.3404	1.20	--

End of Table B7

Table B8. S809, LEGR, Re = 1.5 x 10⁶

Run	AOA	C _l	C _{dp}	C _{m½}	Re x 10 ⁻⁶	C _{dw}
281	-20.1	-0.77	0.2771	0.0562	1.50	--
280	-18.1	-0.72	0.1419	0.0096	1.50	--
279	-16.1	-0.75	0.0929	-0.0082	1.49	--
278	-14.1	-0.72	0.0768	-0.0076	1.49	--
277	-12.2	-0.66	0.0608	-0.0079	1.49	--
276	-10.2	-0.60	0.0488	-0.0059	1.50	--
275	-8.0	-0.52	0.0318	-0.0086	1.50	--
274	-6.0	-0.42	0.0205	-0.0087	1.51	0.0599
273	-4.1	-0.37	0.0143	-0.0017	1.50	0.0382
272	-2.1	-0.18	0.0059	-0.0216	1.50	0.0142
282	-0.1	0.02	0.0055	-0.0275	1.50	0.0139
283	2.1	0.24	0.0082	-0.0320	1.50	0.0132
284	4.0	0.46	0.0088	-0.0334	1.50	0.0156
285	6.1	0.65	0.0114	-0.0307	1.50	0.0187
286	8.1	0.74	0.0204	-0.0311	1.50	0.0428
287	10.1	0.76	0.0291	-0.0237	1.51	0.0655
288	11.2	0.82	0.0411	-0.0274	1.50	--
289	12.2	0.86	0.0519	-0.0294	1.49	--
290	13.2	0.89	0.0632	-0.0315	1.50	--
291	14.1	0.90	0.0723	-0.0322	1.50	--
292	15.1	0.80	0.0892	-0.0368	1.50	--
293	16.1	0.73	0.1374	-0.0613	1.52	--
294	17.0	0.74	0.1692	-0.0742	1.50	--
295	18.1	0.76	0.2075	-0.0888	1.50	--
296	19.0	0.78	0.2403	-0.0991	1.50	--
297	20.0	0.80	0.2815	-0.1135	1.52	--
298	22.1	0.81	0.3545	-0.1316	1.49	--

End of Table B8

S809

Pressure Distributions, Steady State, Re = 0.75 million

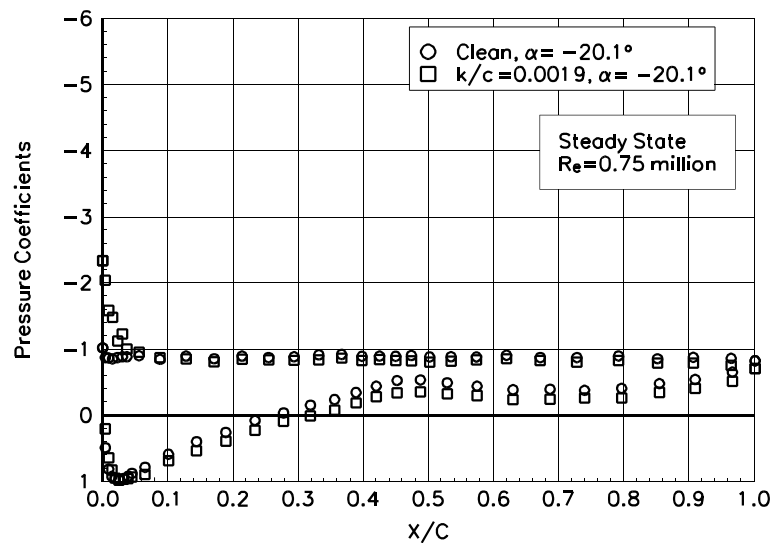


Figure B1. $\alpha = -20.1^\circ$

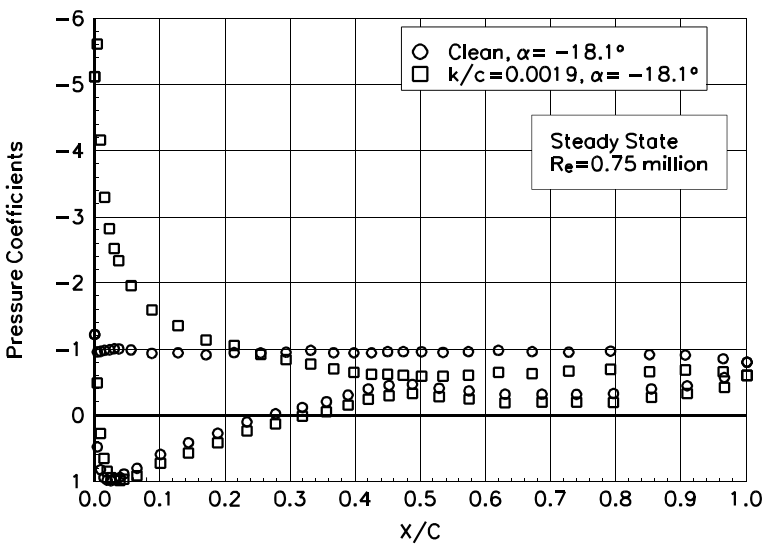


Figure B2. $\alpha = -18.1^\circ$

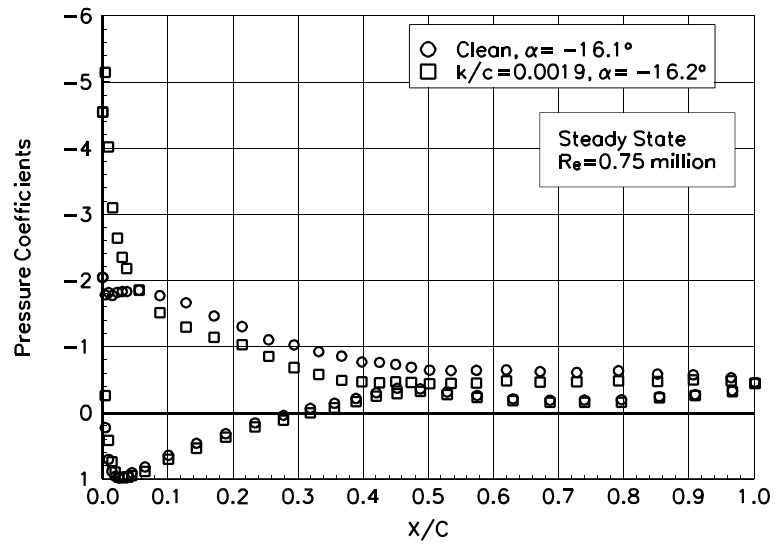


Figure B3. $\alpha = -16.1^\circ$

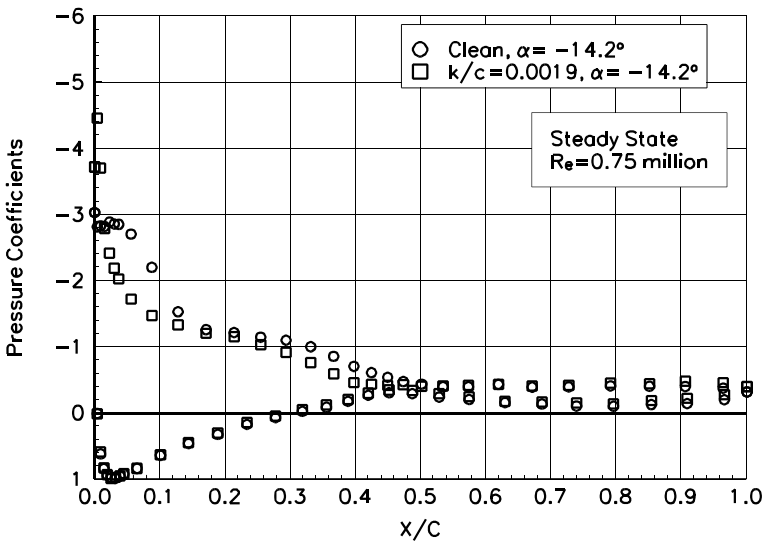


Figure B4. $\alpha = -14.2^\circ$

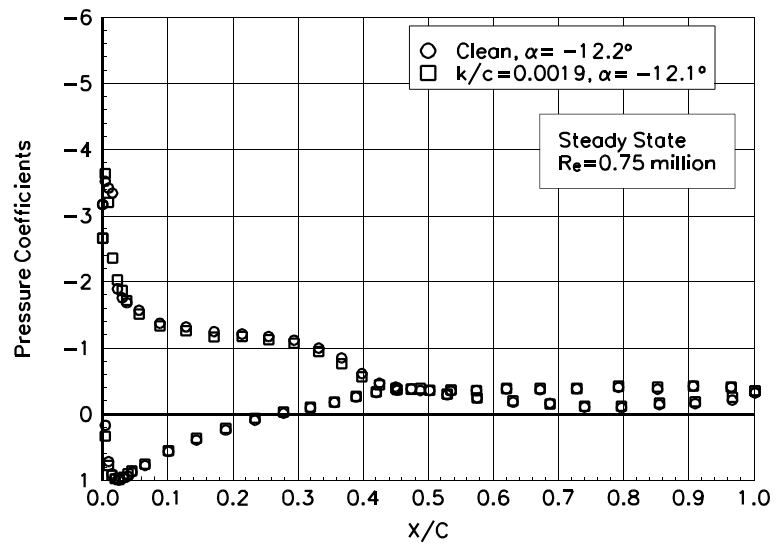


Figure B5. $\alpha = -12.2^\circ$

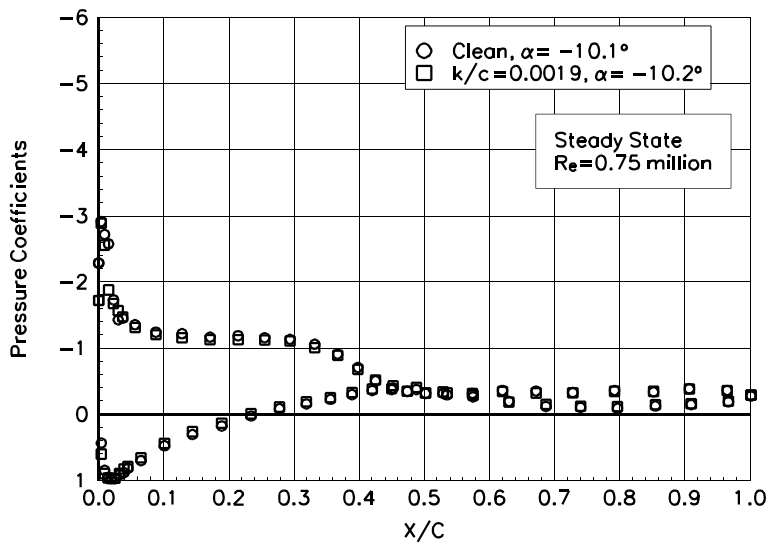


Figure B6. $\alpha = -10.1^\circ$

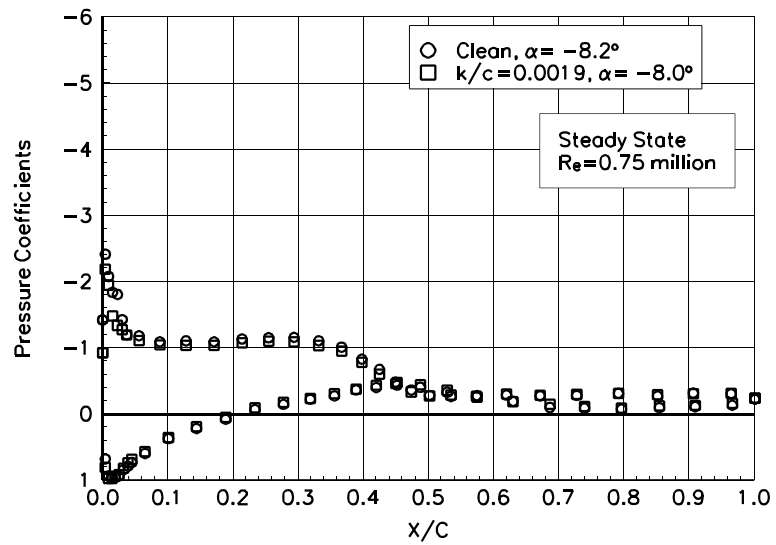


Figure B7. $\alpha = -8.2^\circ$

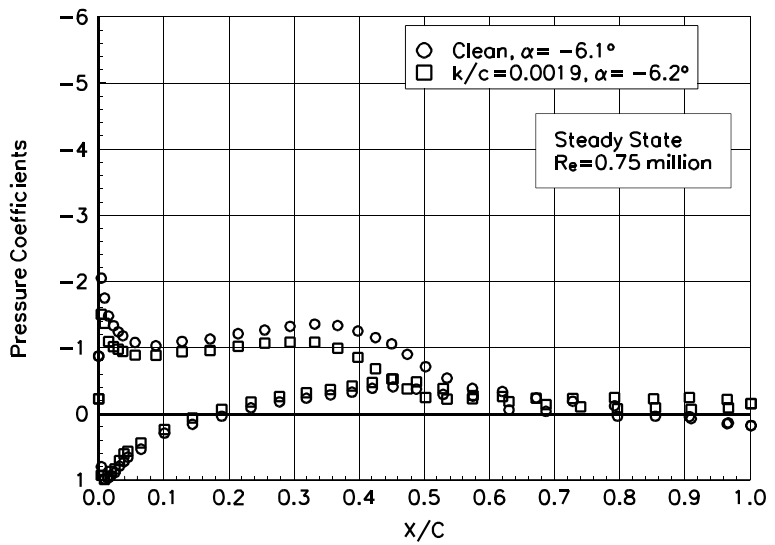


Figure B8. $\alpha = -6.1^\circ$

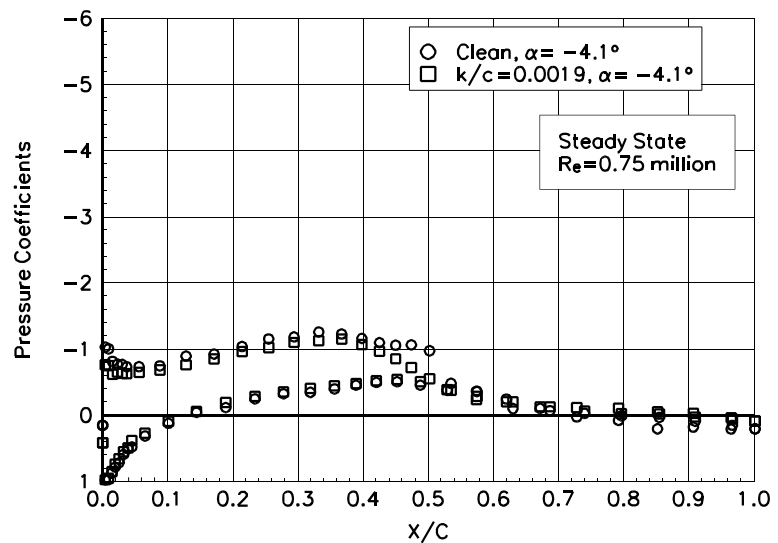


Figure B9. $\alpha = -4.1^\circ$

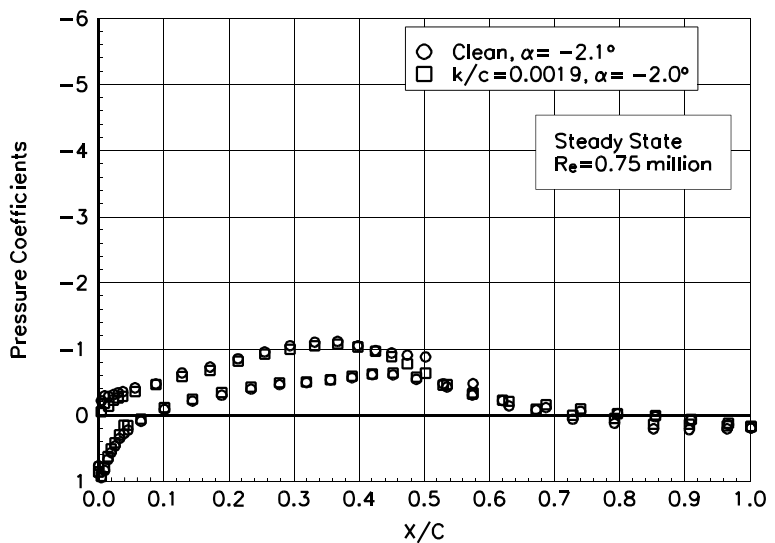


Figure B10. $\alpha = -2.1^\circ$

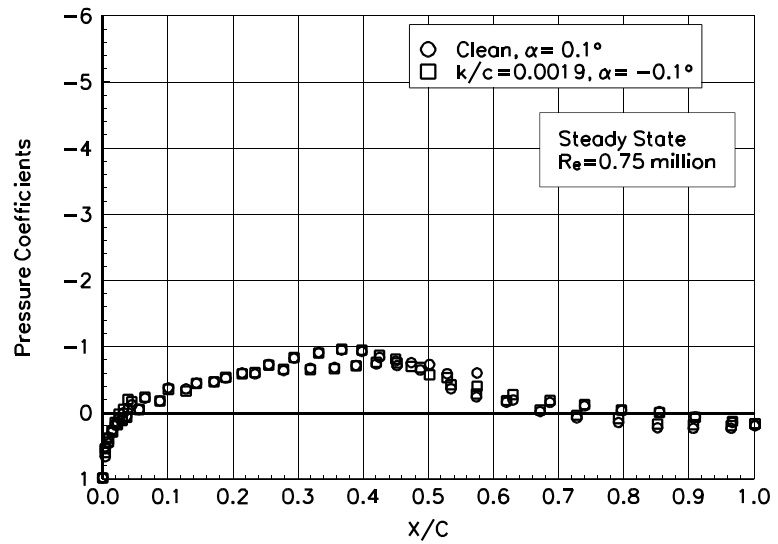


Figure B11. $\alpha = 0.1^\circ$

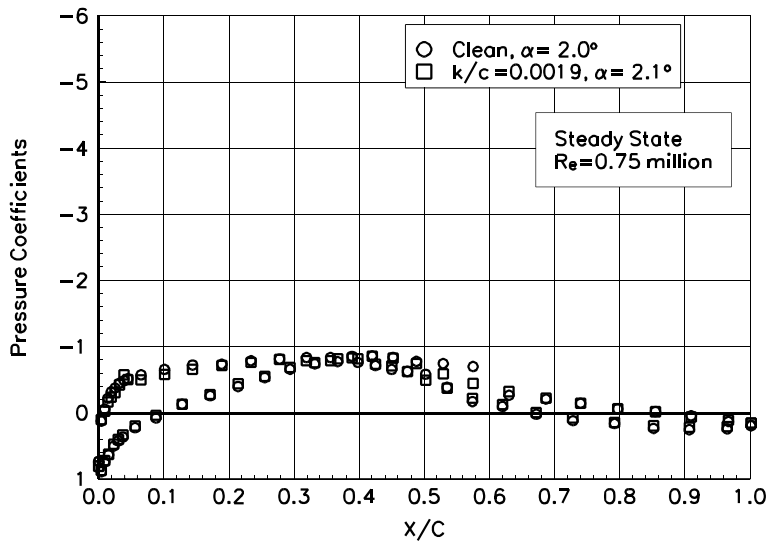


Figure B12. $\alpha = 2.0^\circ$

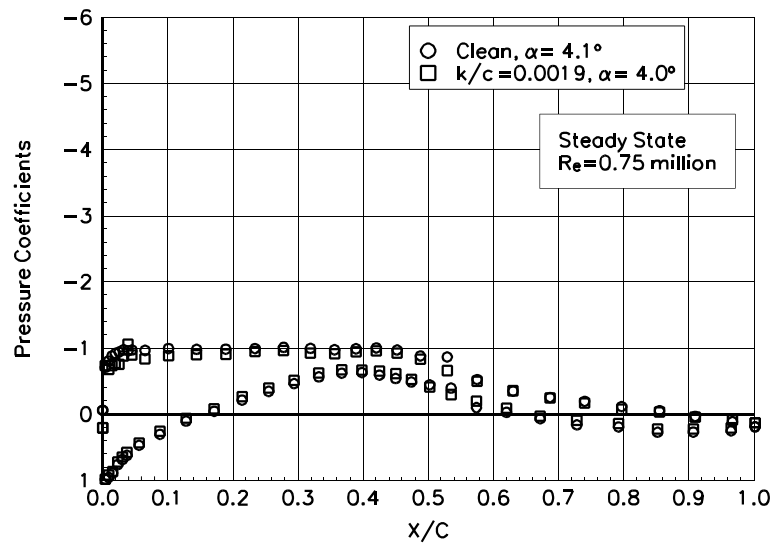


Figure B13. $\alpha = 4.1^\circ$

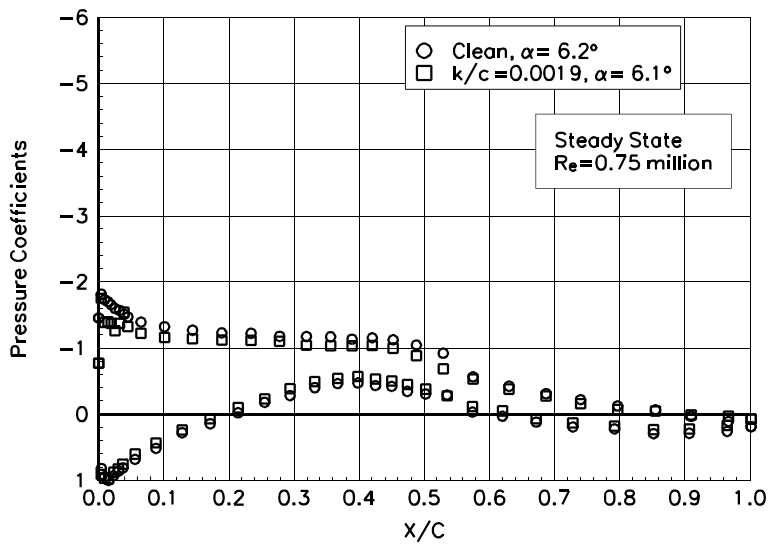


Figure B14. $\alpha = 6.2^\circ$

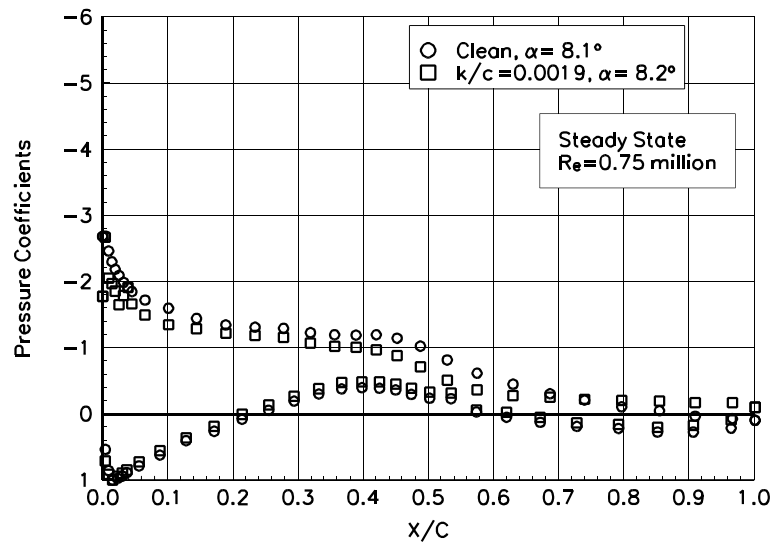


Figure B15. $\alpha = 8.1^\circ$

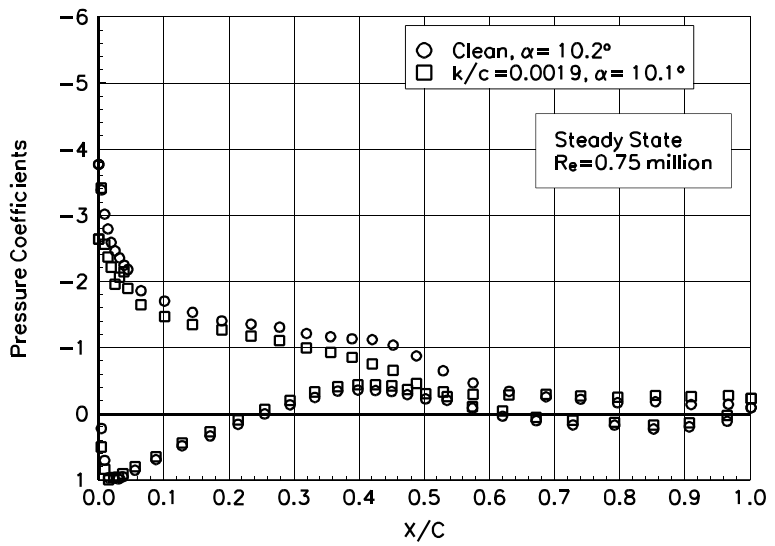


Figure B16. $\alpha = 10.2^\circ$

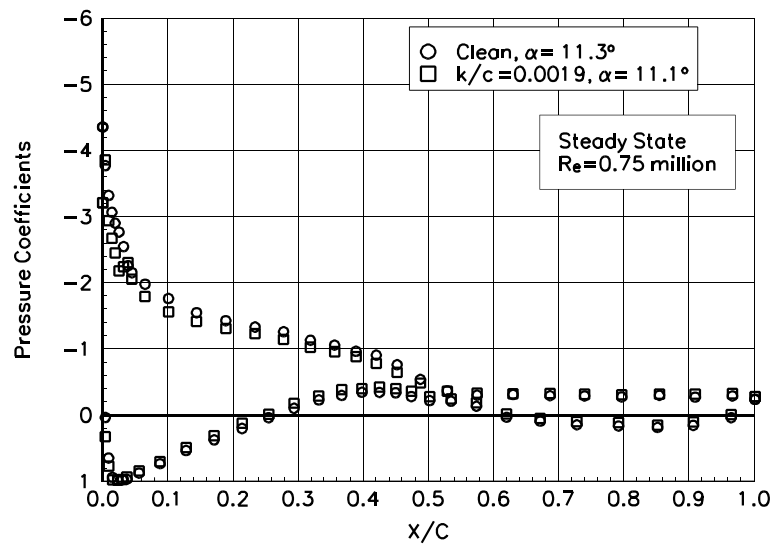


Figure B17. $\alpha = 11.3^\circ$

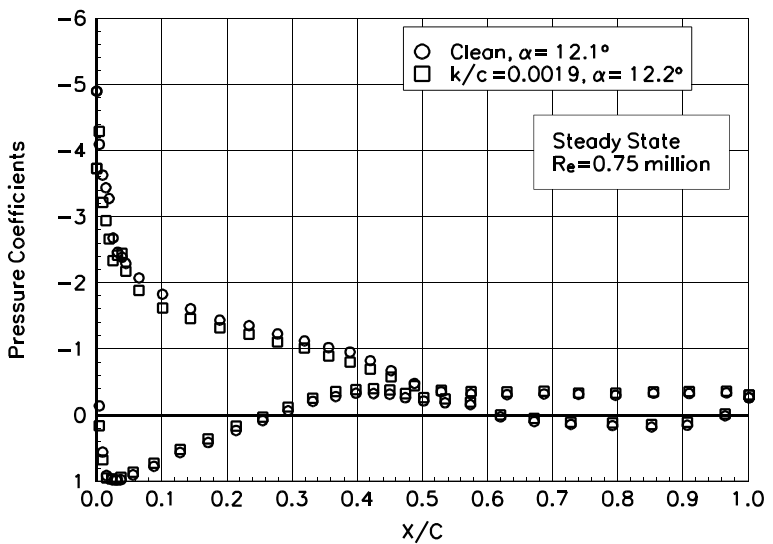


Figure B18. $\alpha = 12.1^\circ$

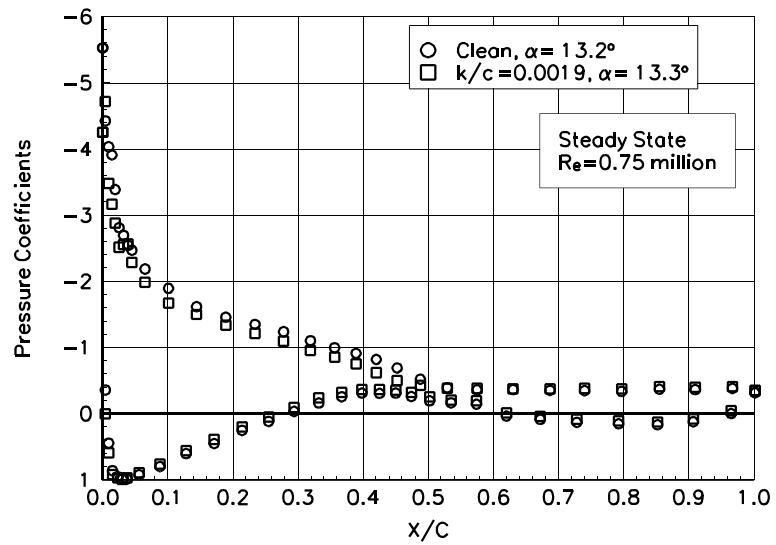


Figure B19. $\alpha = 13.2^\circ$

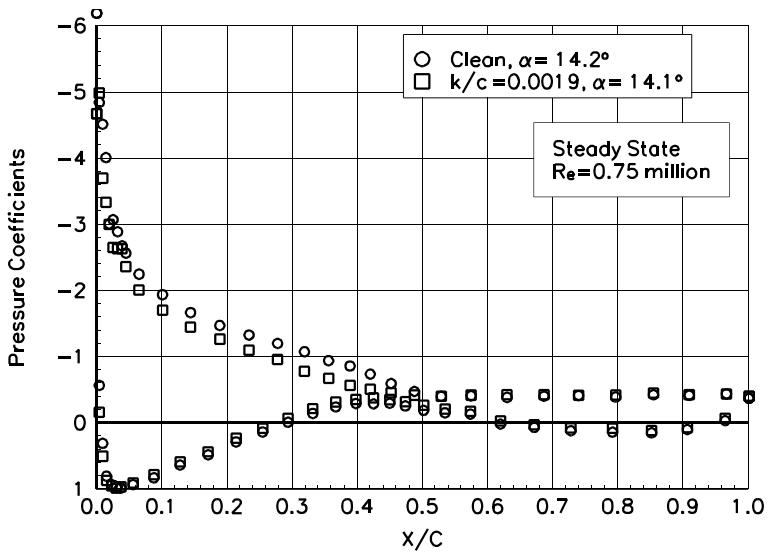


Figure B20. $\alpha = 14.2^\circ$

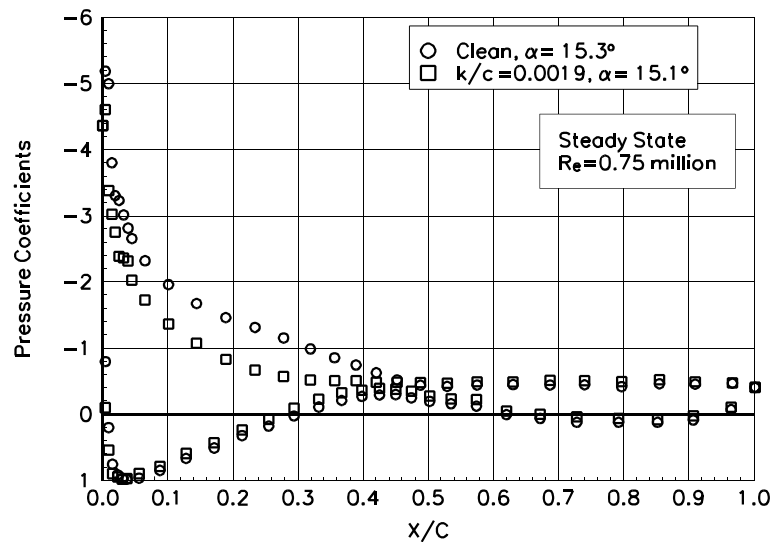


Figure B21. $\alpha = 15.3^\circ$

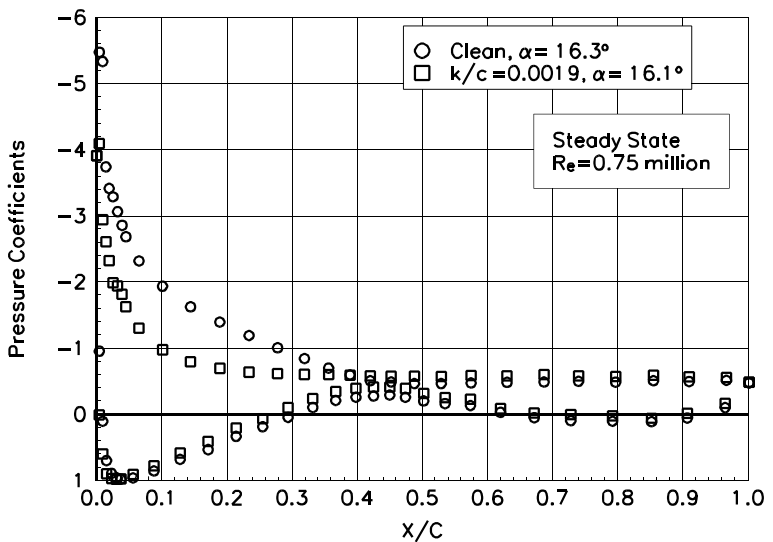


Figure B22. $\alpha = 16.3^\circ$

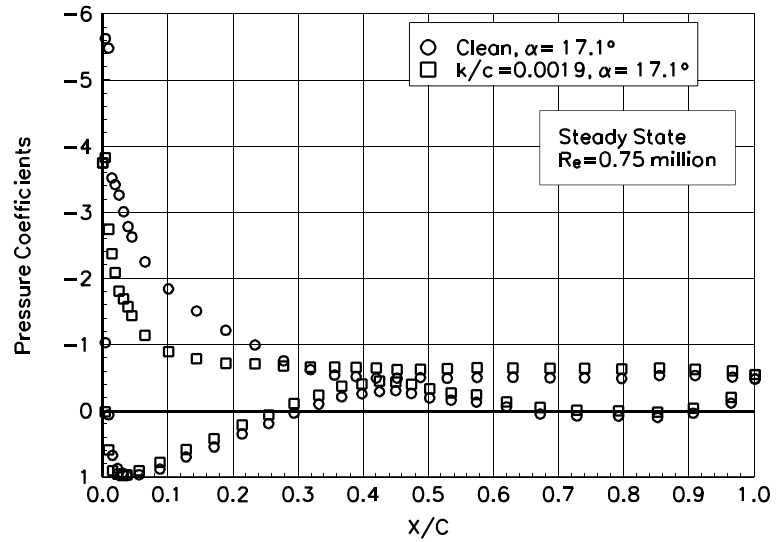


Figure B23. $\alpha = 17.1^\circ$

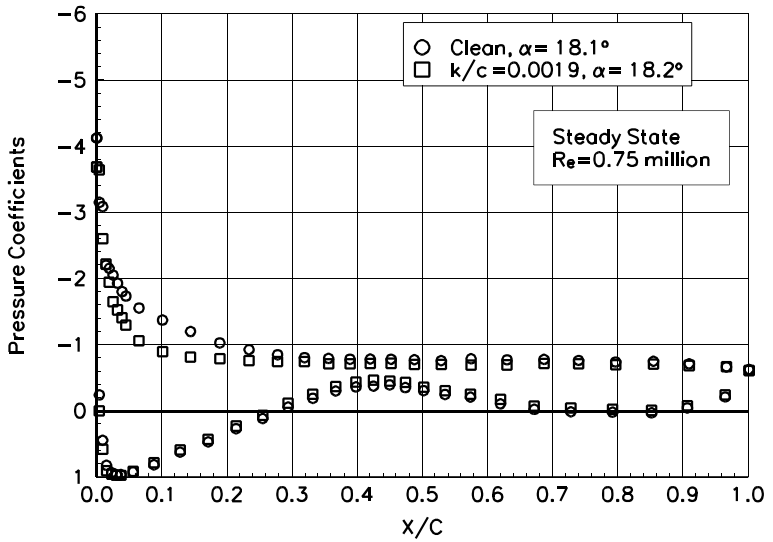


Figure B24. $\alpha = 18.1^\circ$

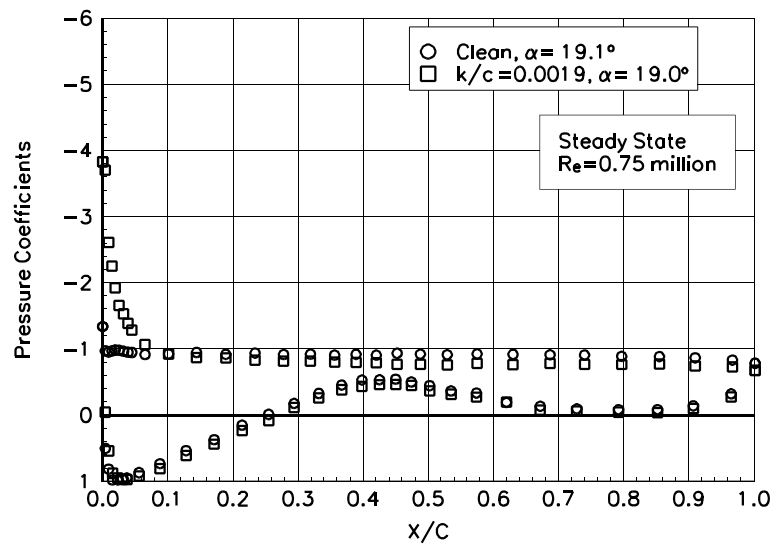


Figure B25. $\alpha = 19.1^\circ$

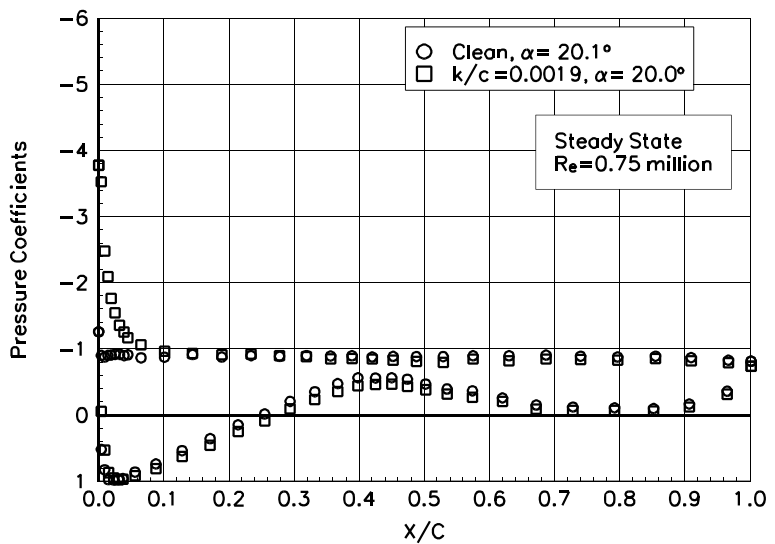


Figure B26. $\alpha = 20.1^\circ$

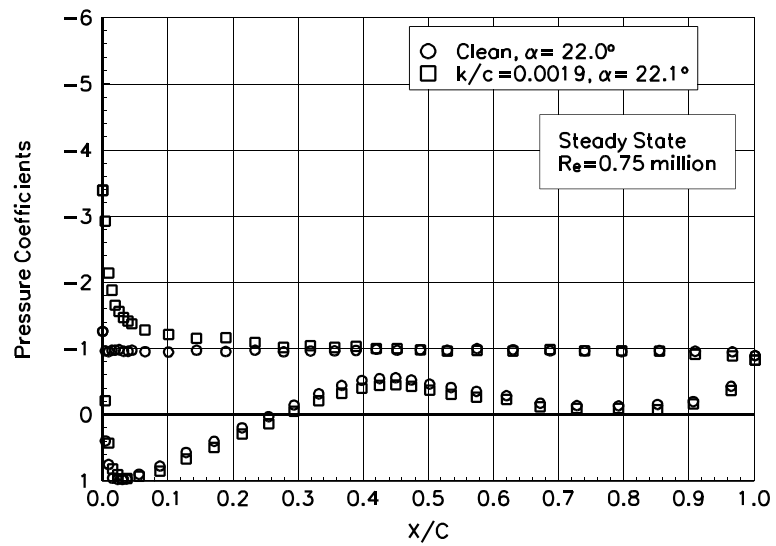


Figure B27. $\alpha = 22.0^\circ$

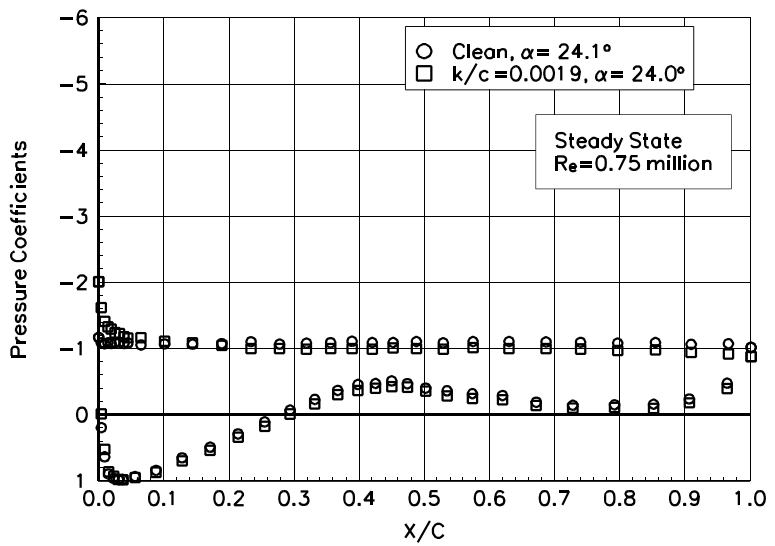


Figure B28. $\alpha = 24.1^\circ$

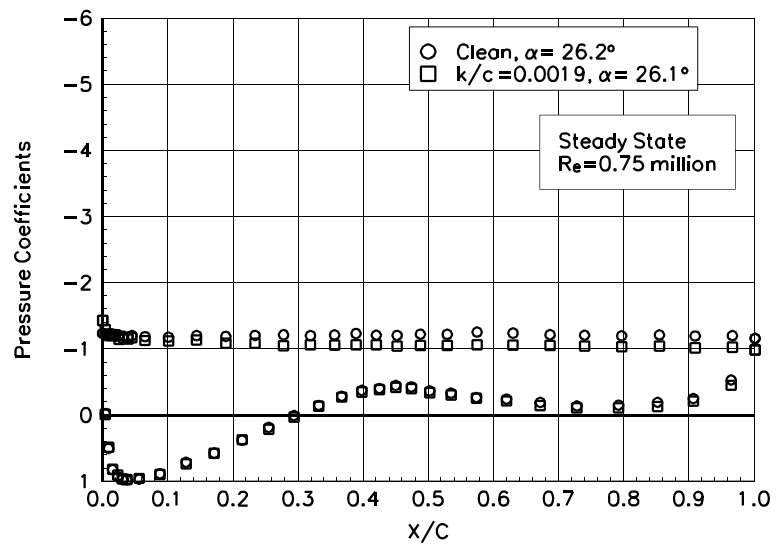


Figure B29. $\alpha = 26.2^\circ$

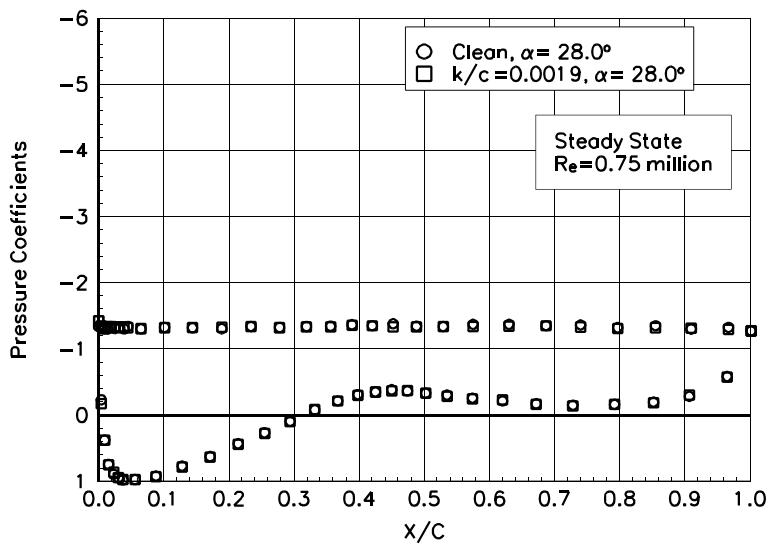


Figure B30. $\alpha = 28.0^\circ$

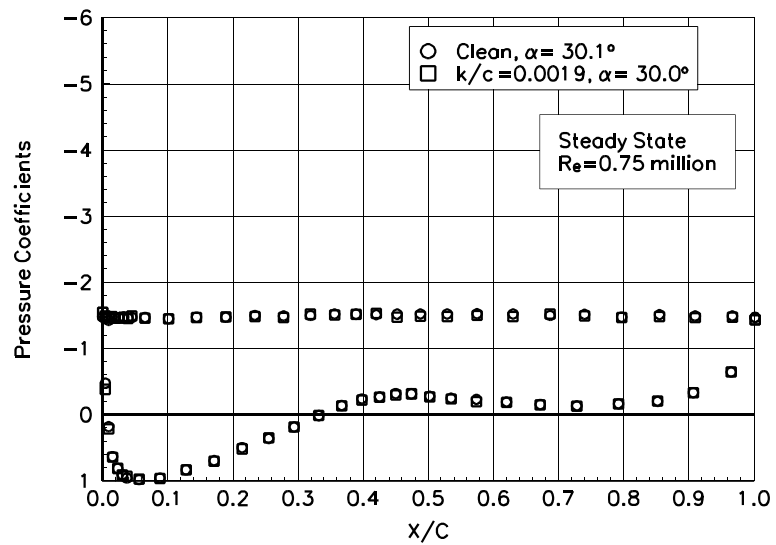


Figure B31. $\alpha = 30.1^\circ$

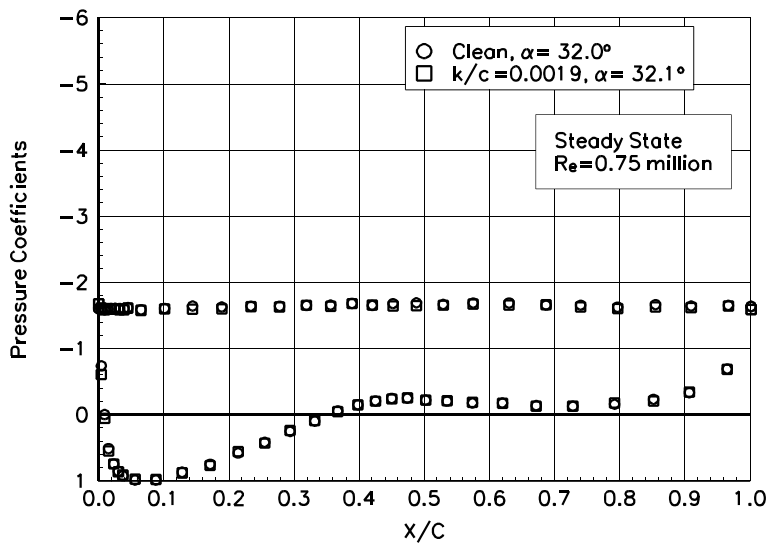


Figure B32. $\alpha = 32.0^\circ$

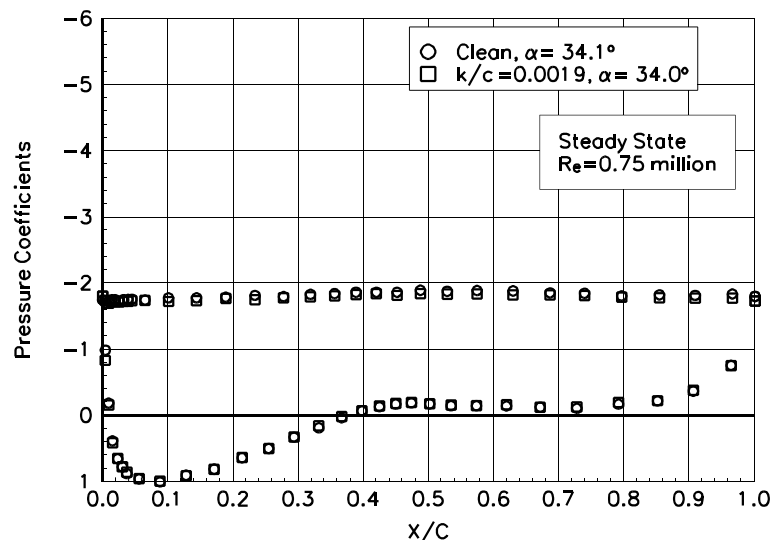


Figure B33. $\alpha = 34.1^\circ$

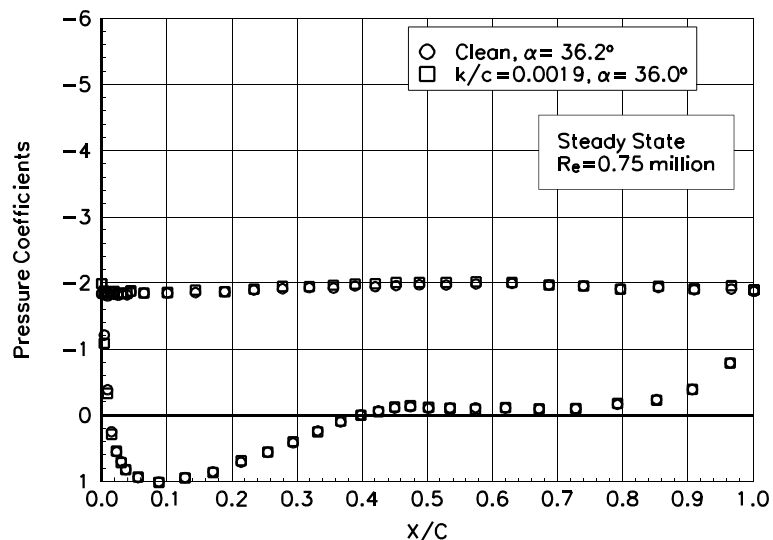


Figure B34. $\alpha = 36.2^\circ$

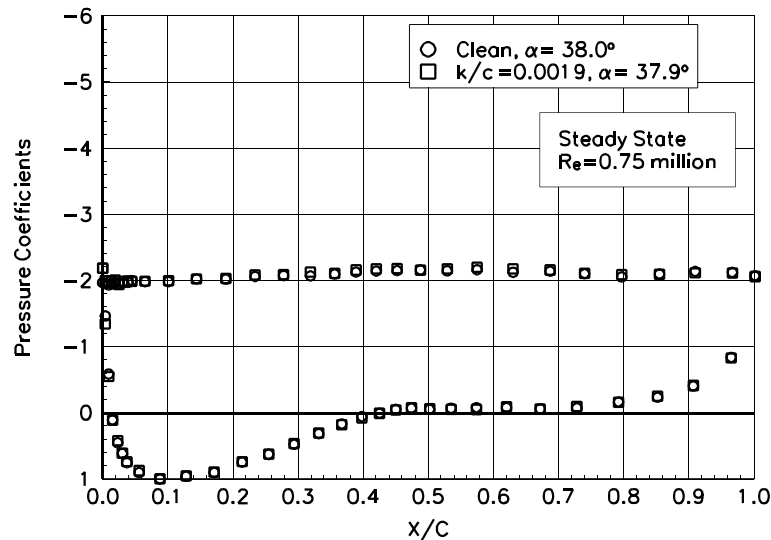


Figure B35. $\alpha = 38.0^\circ$

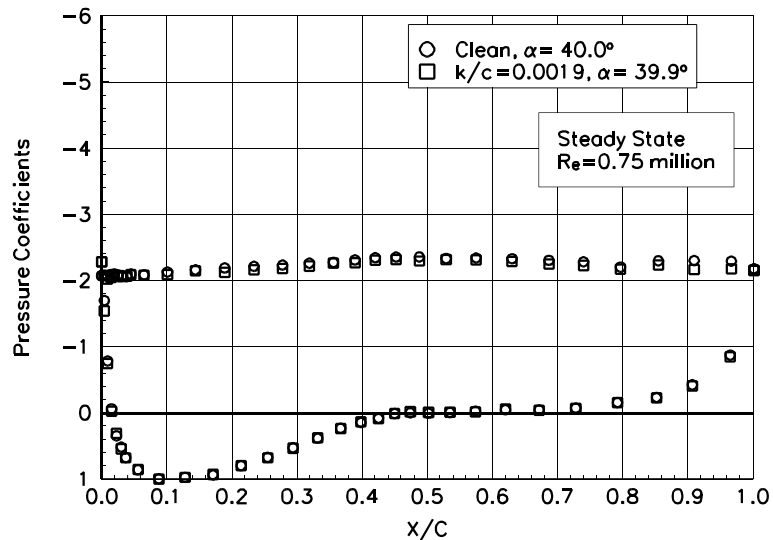


Figure B36. $\alpha = 40.0^\circ$

S809

Pressure Distributions, Steady State, Re = 1 million

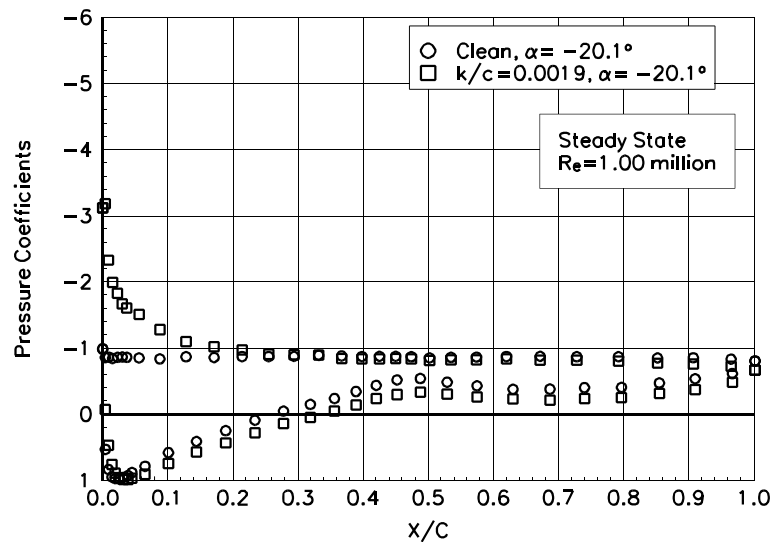


Figure B37. $\alpha = -20.1^\circ$

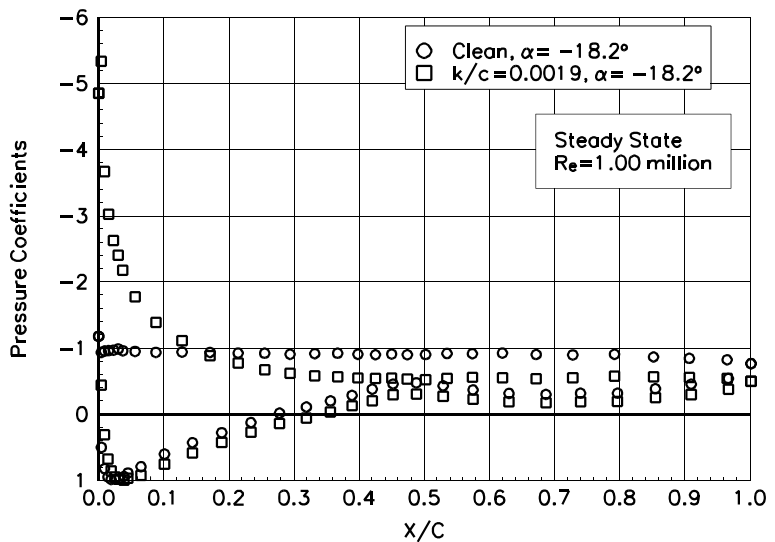


Figure B38. $\alpha = -18.2^\circ$

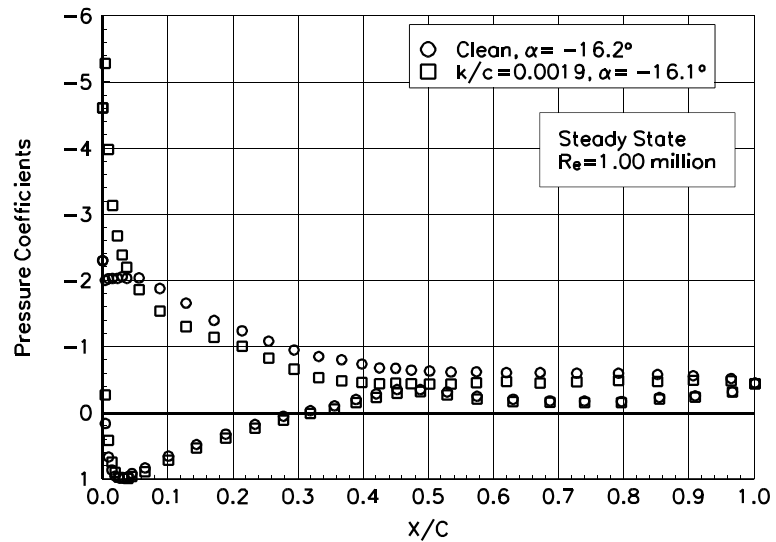


Figure B39. $\alpha = -16.2^\circ$

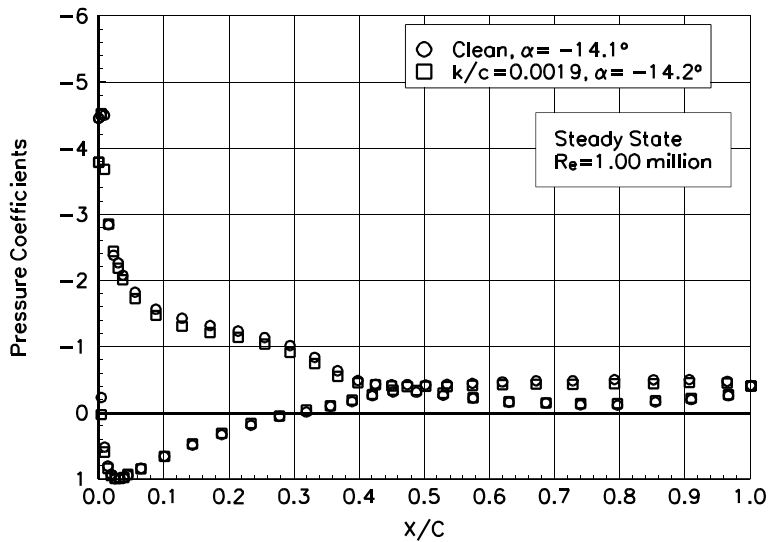


Figure B40. $\alpha = -14.1^\circ$

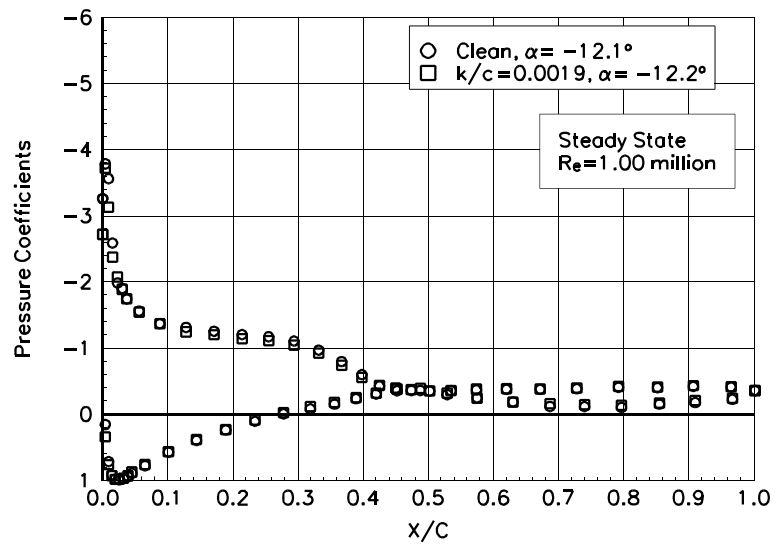


Figure B41. $\alpha = -12.1^\circ$

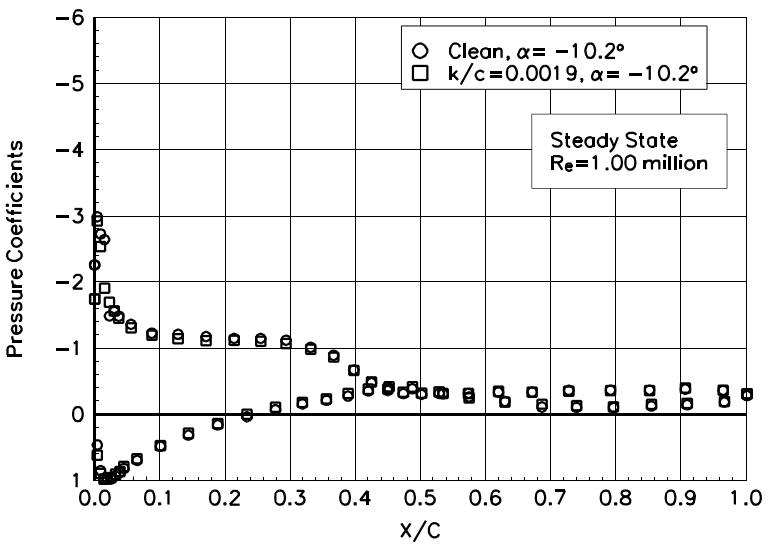


Figure B42. $\alpha = -10.2^\circ$

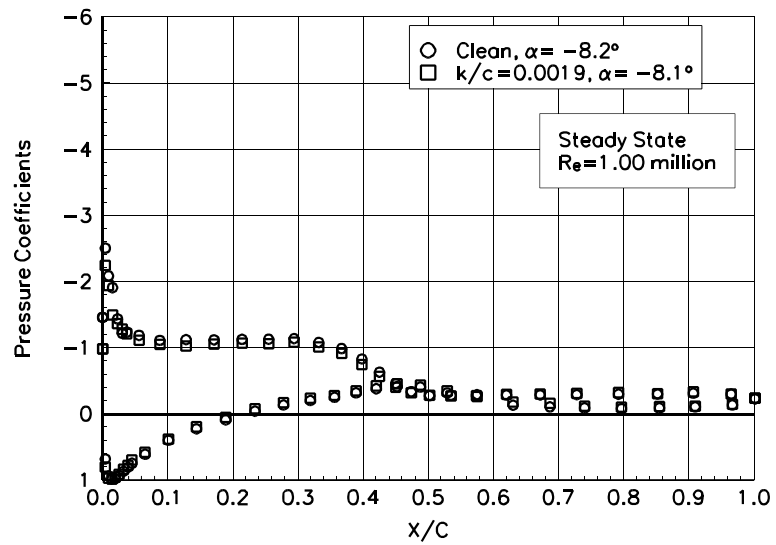


Figure B43. $\alpha = -8.2^\circ$

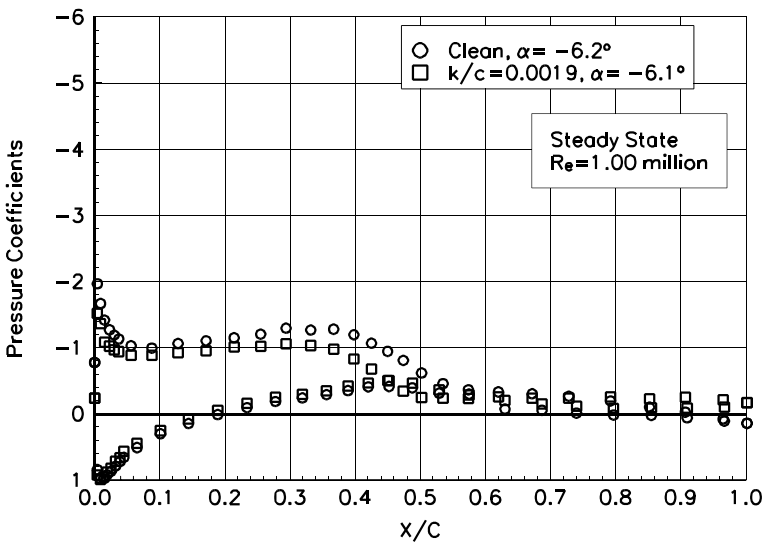


Figure B44. $\alpha = -6.2^\circ$

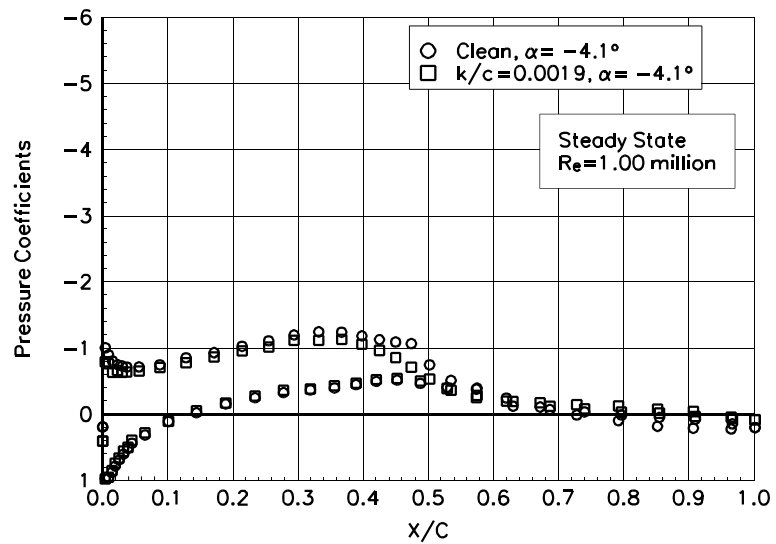


Figure B45. $\alpha = -4.1^\circ$

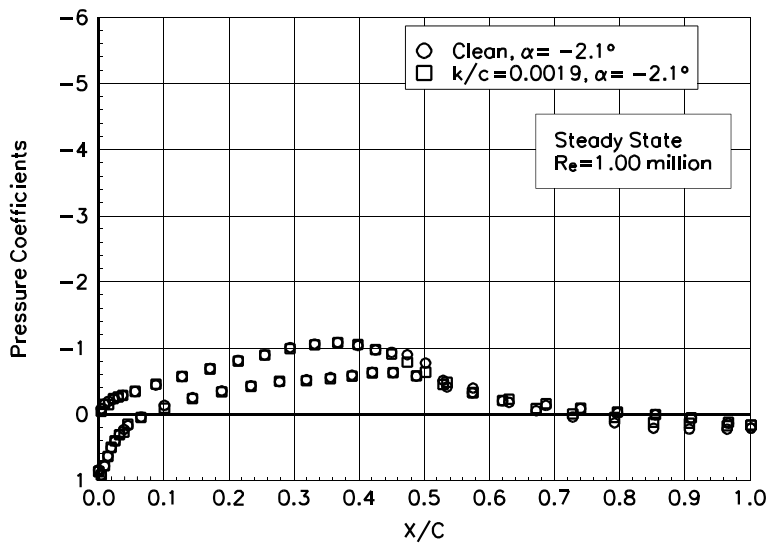


Figure B46. $\alpha = -2.1^\circ$

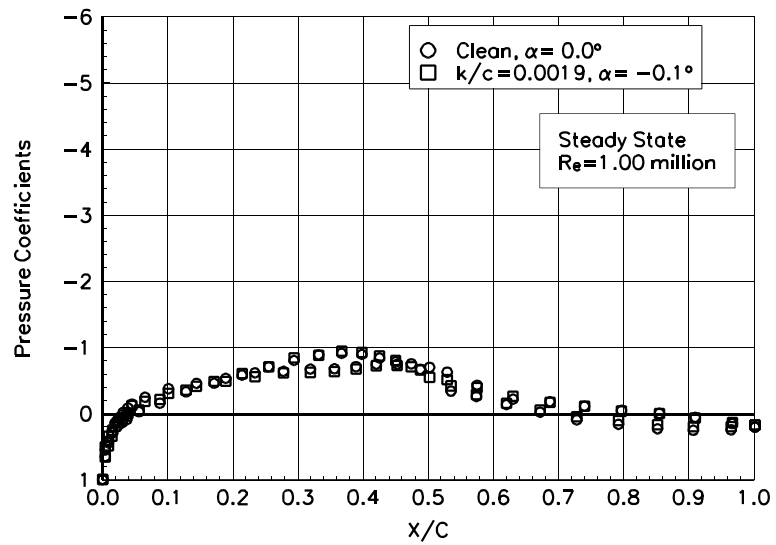


Figure B47. $\alpha = 0.0^\circ$

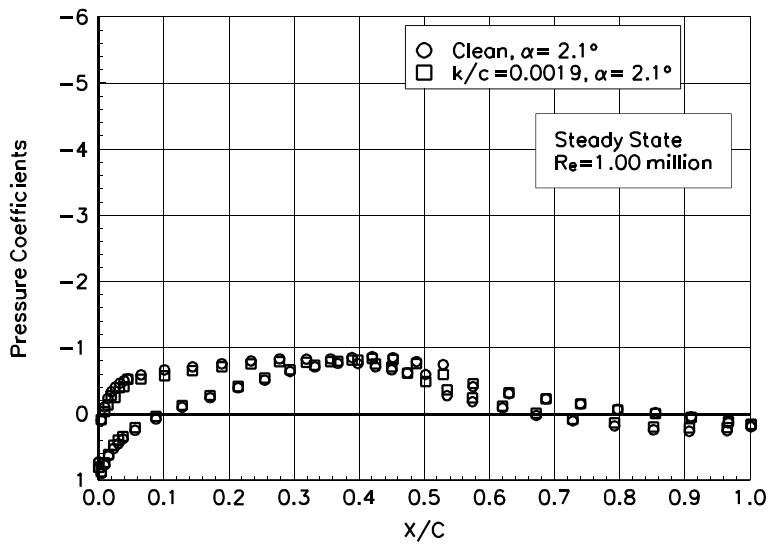


Figure B48. $\alpha = 2.1^\circ$

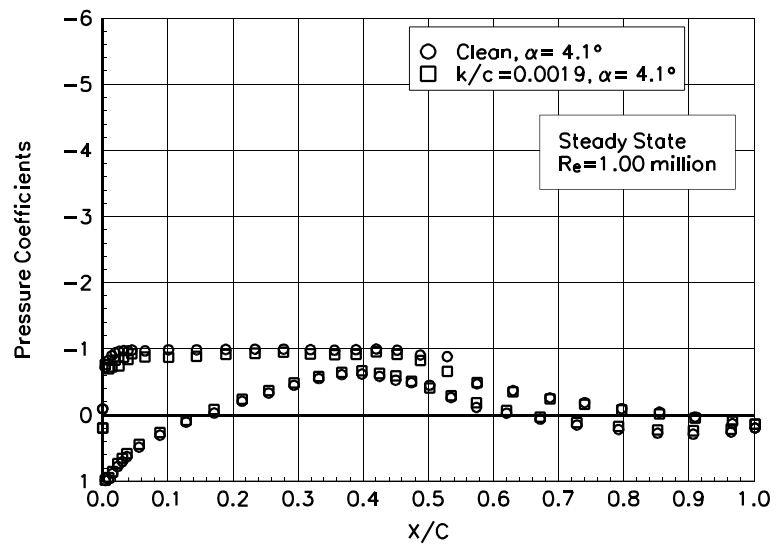


Figure B49. $\alpha = 4.1^\circ$

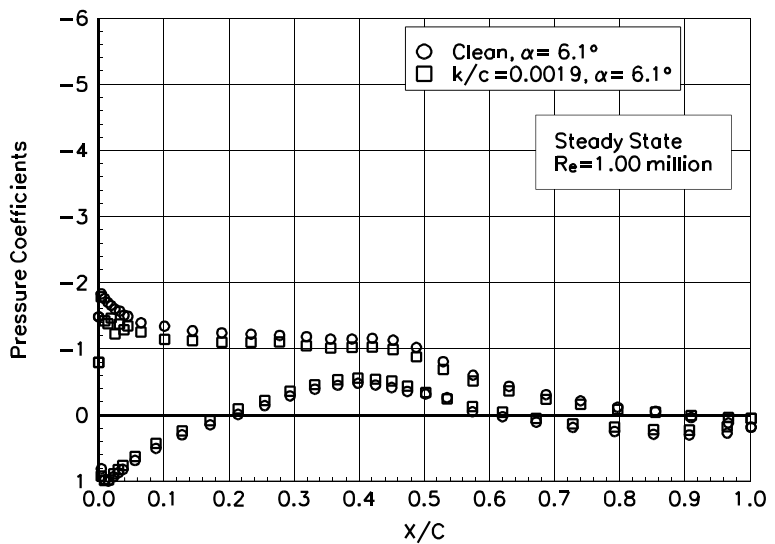


Figure B50. $\alpha = 6.1^\circ$

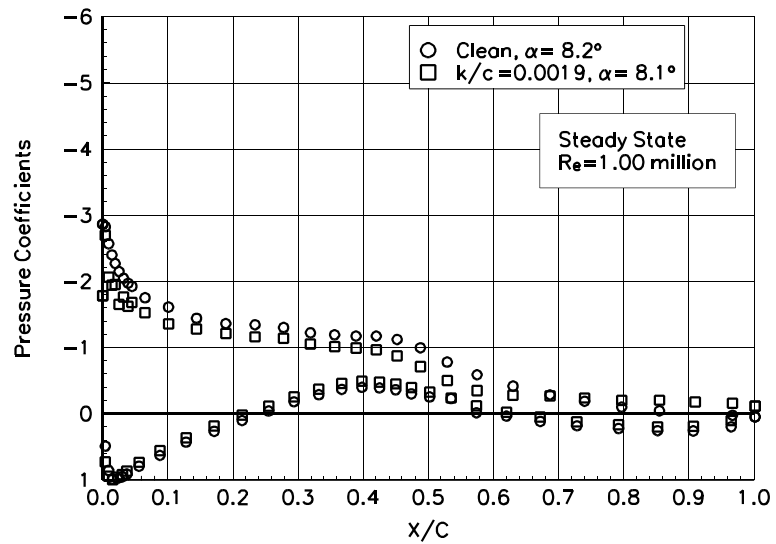


Figure B51. $\alpha = 8.2^\circ$

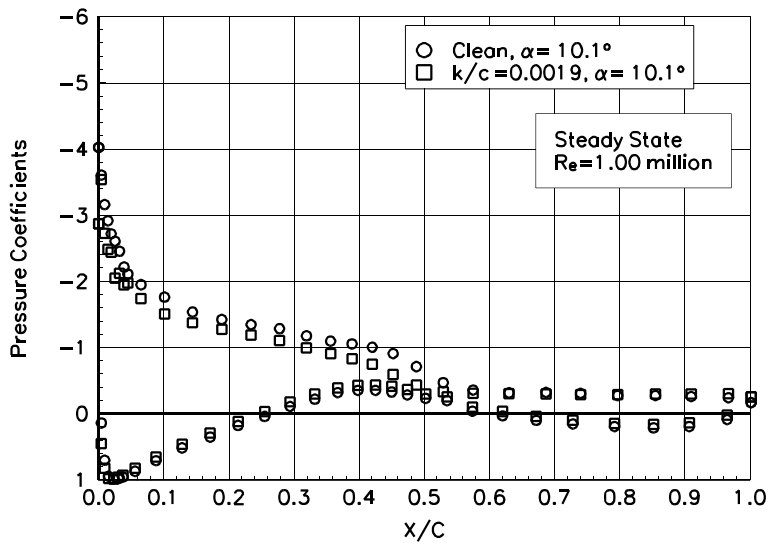


Figure B52. $\alpha = 10.1^\circ$

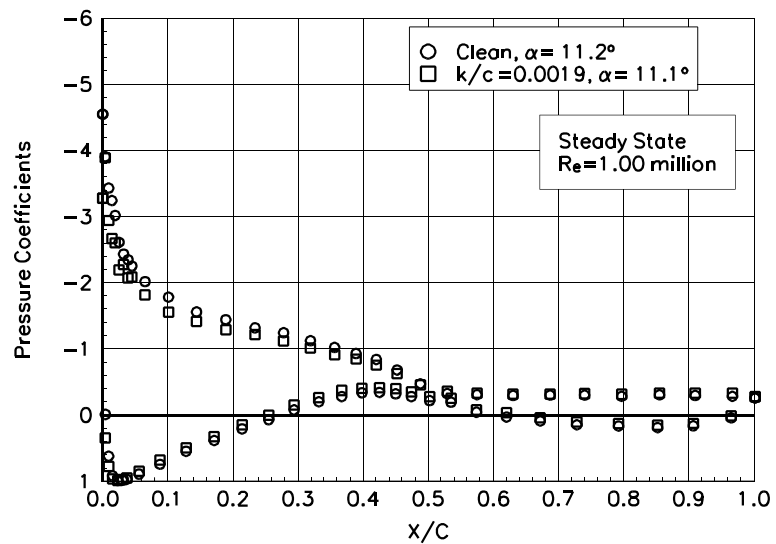


Figure B53. $\alpha = 11.2^\circ$

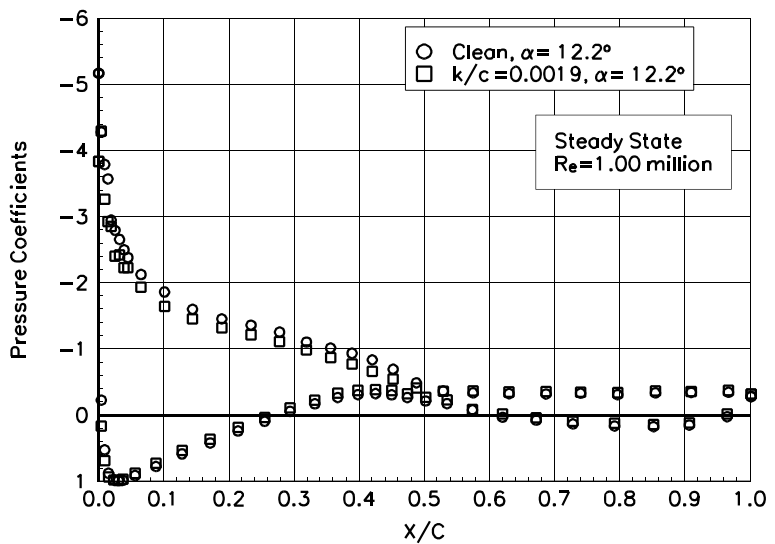


Figure B54. $\alpha = 12.2^\circ$

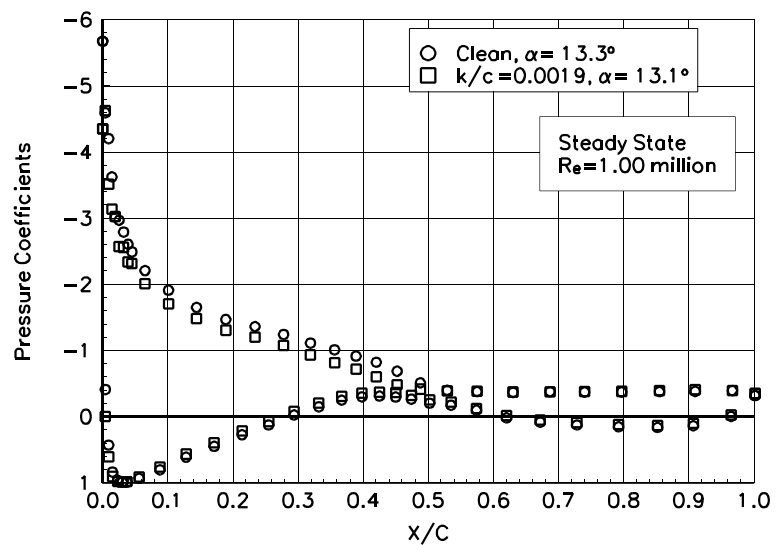


Figure B55. $\alpha = 13.3^\circ$

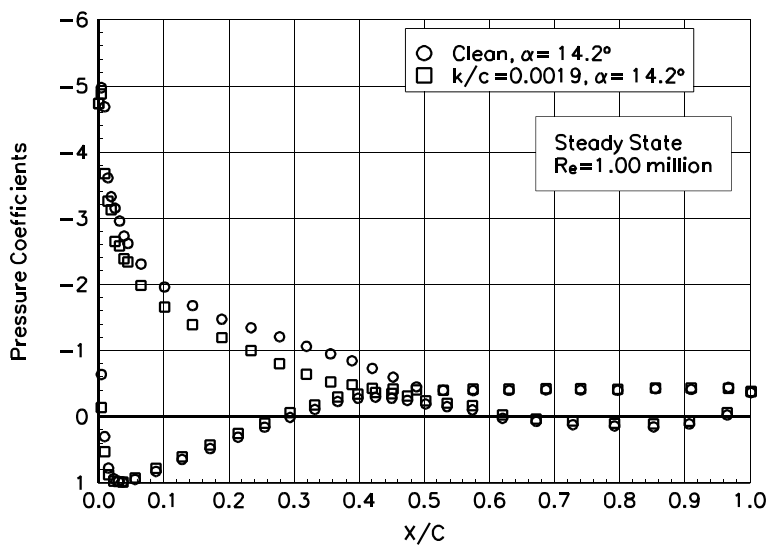


Figure B56. $\alpha = 14.2^\circ$

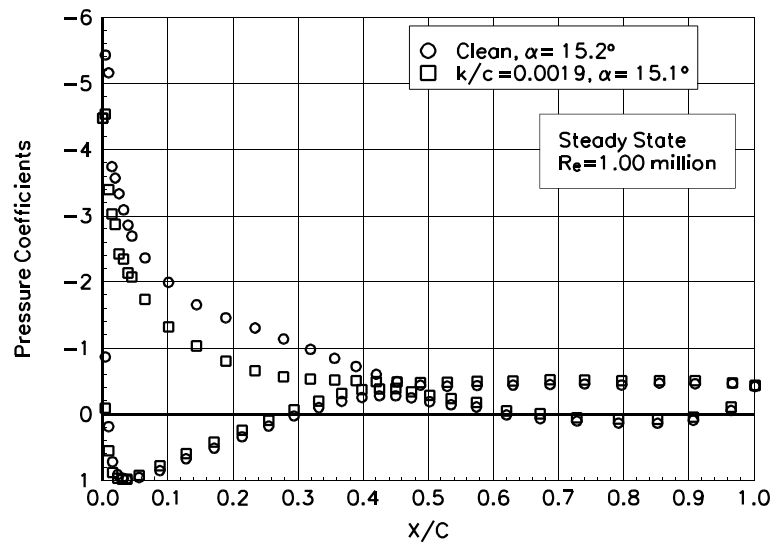


Figure B57. $\alpha = 15.2^\circ$

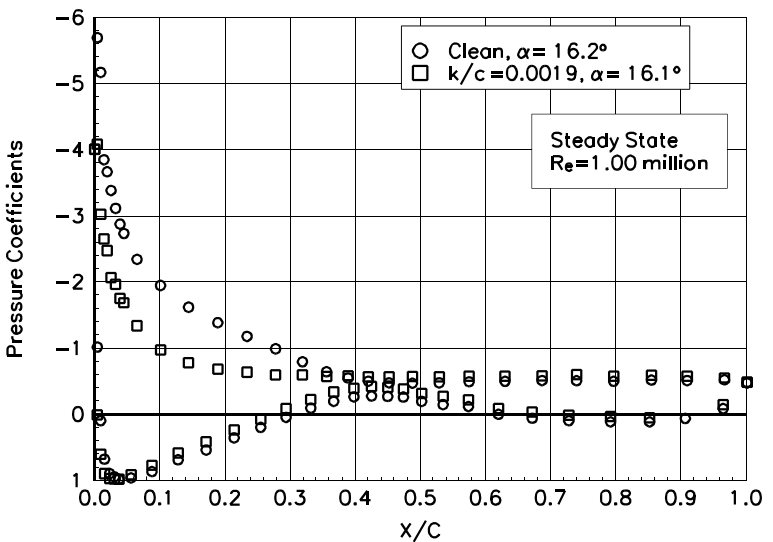


Figure B58. $\alpha = 16.2^\circ$

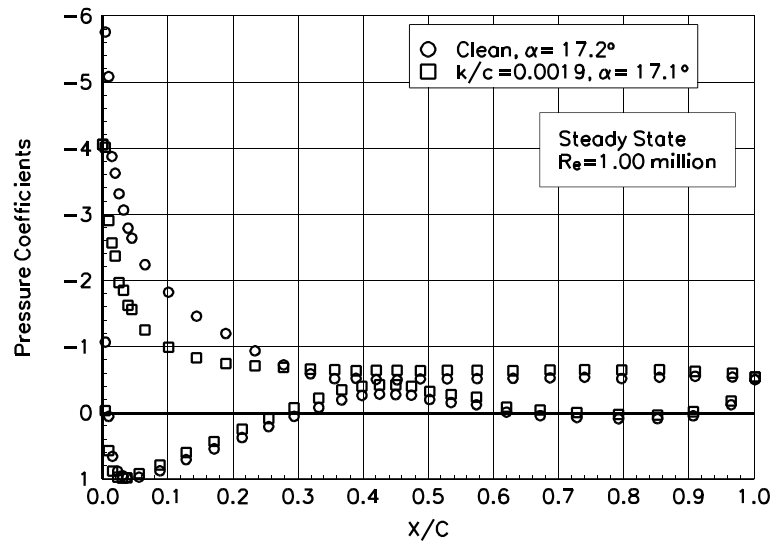


Figure B59. $\alpha = 17.2^\circ$

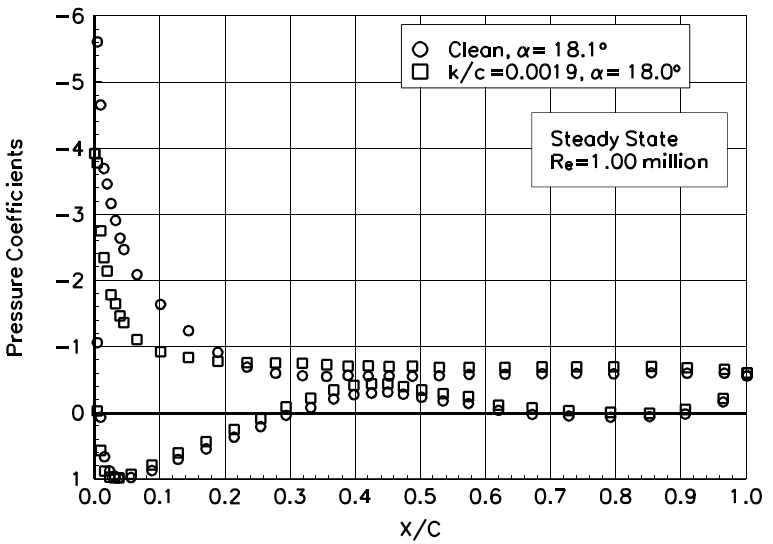


Figure B60. $\alpha = 18.1^\circ$

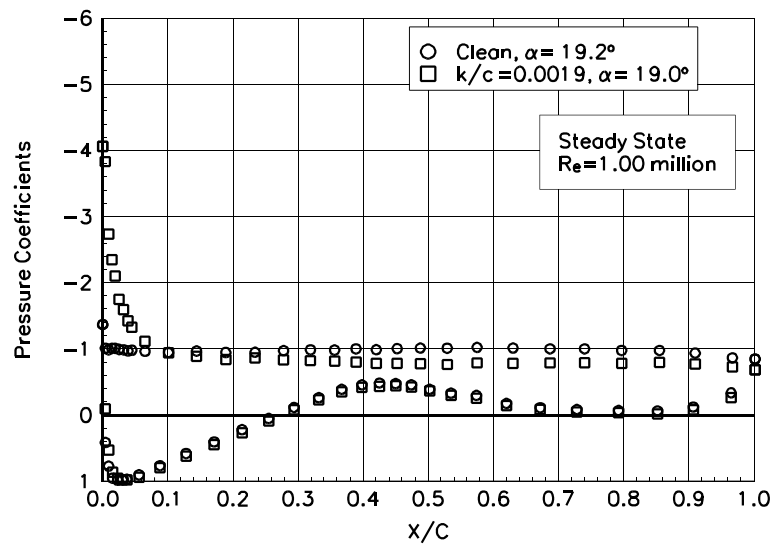


Figure B61. $\alpha = 19.2^\circ$

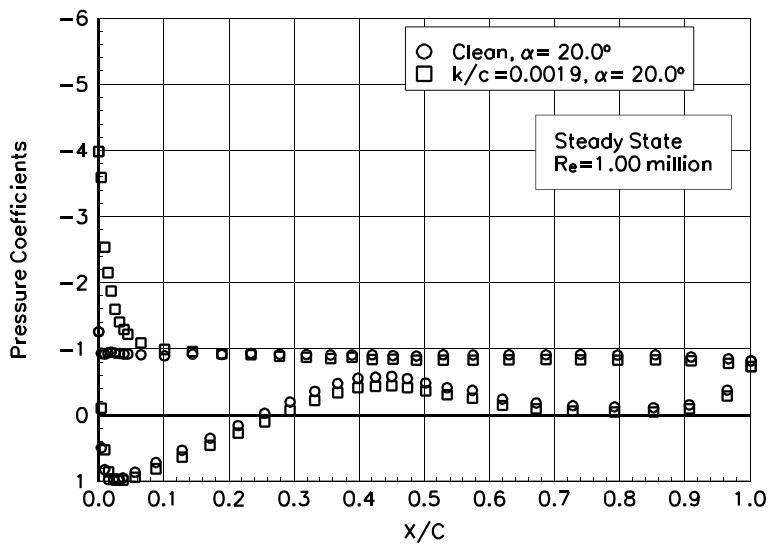


Figure B62. $\alpha = 20.0^\circ$

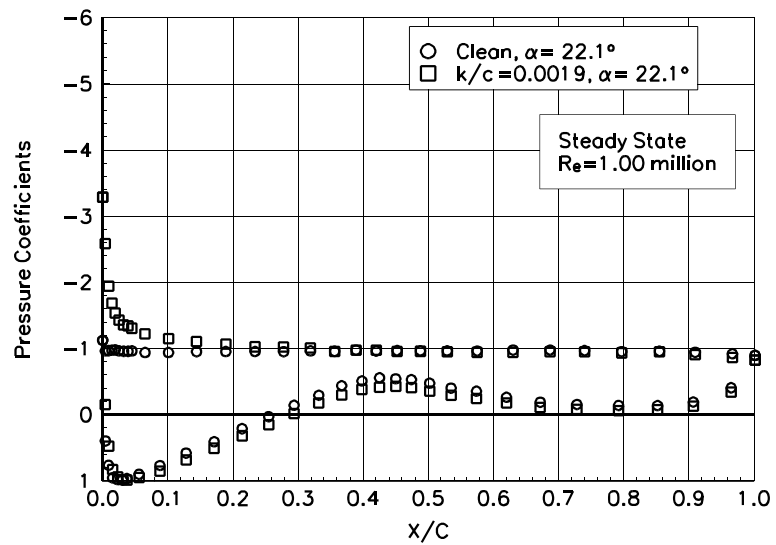


Figure B63. $\alpha = 22.1^\circ$

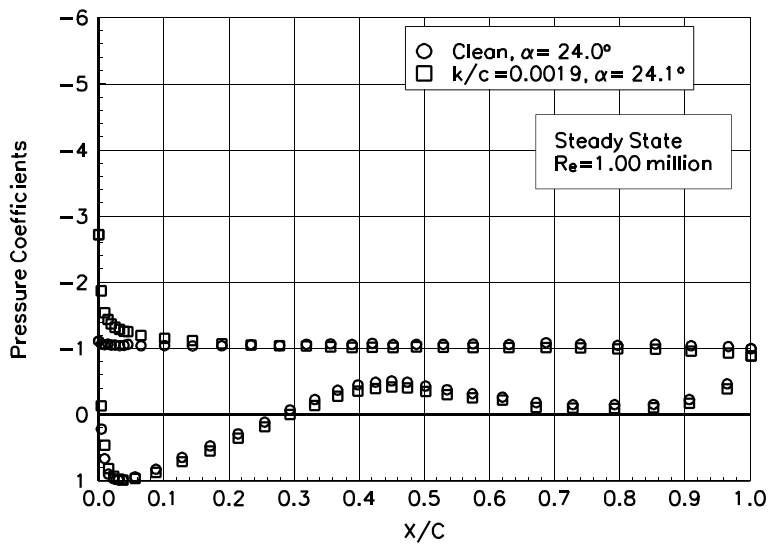


Figure B64. $\alpha = 24.0^\circ$

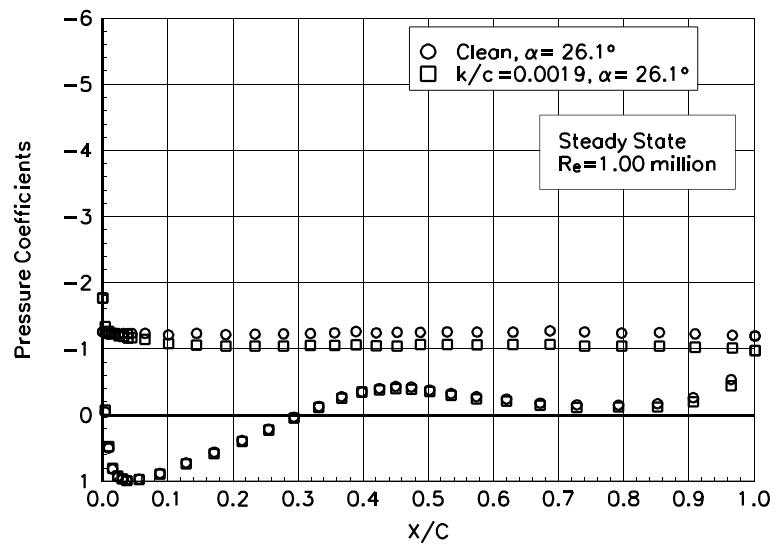


Figure B65. $\alpha = 26.1^\circ$

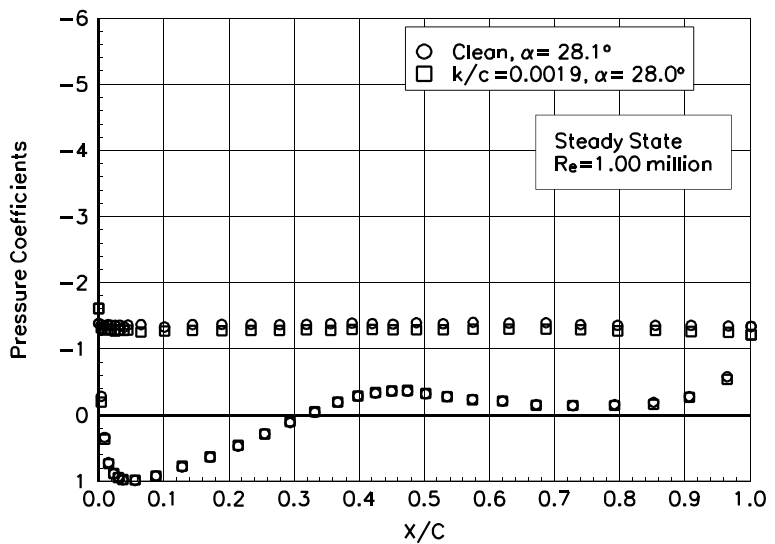


Figure B66. $\alpha = 28.1^\circ$

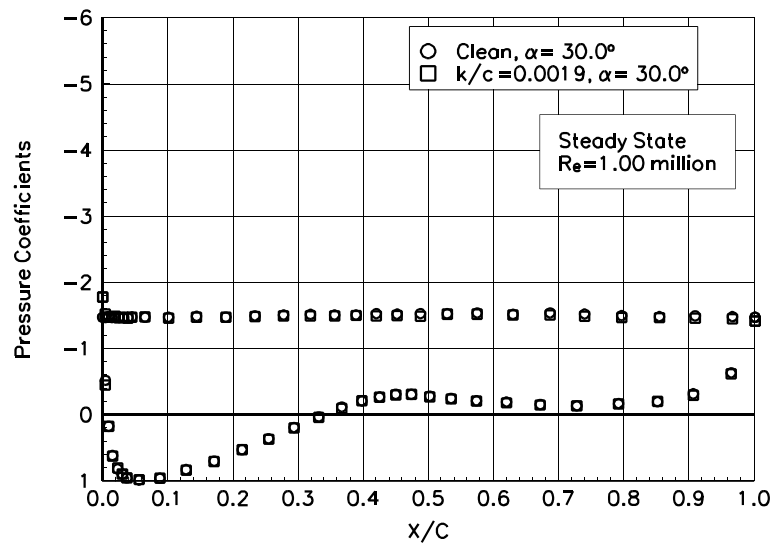


Figure B67. $\alpha = 30.0^\circ$

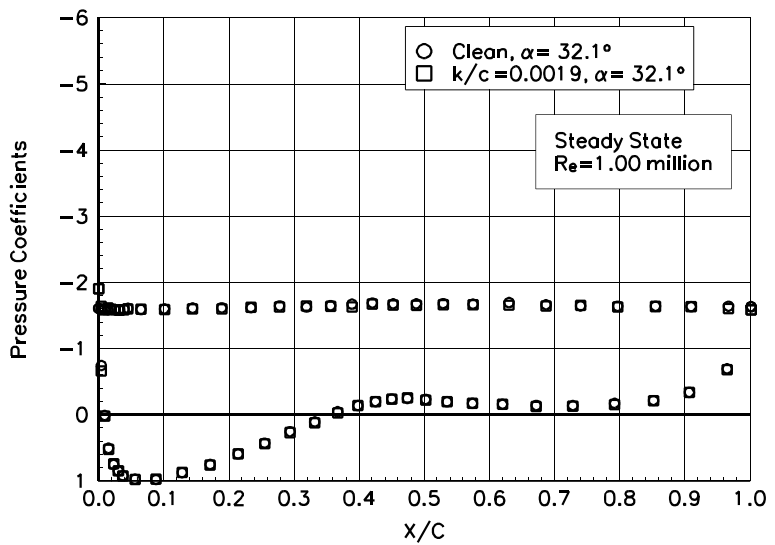


Figure B68. $\alpha = 32.1^\circ$

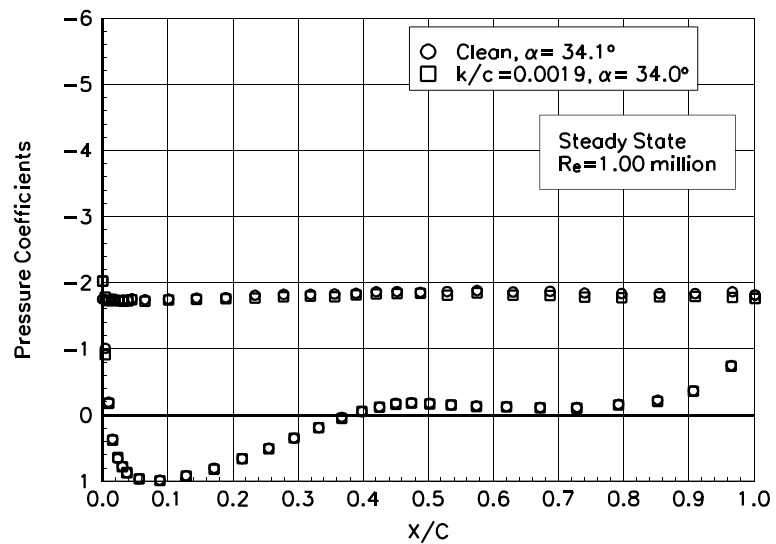


Figure B69. $\alpha = 34.1^\circ$

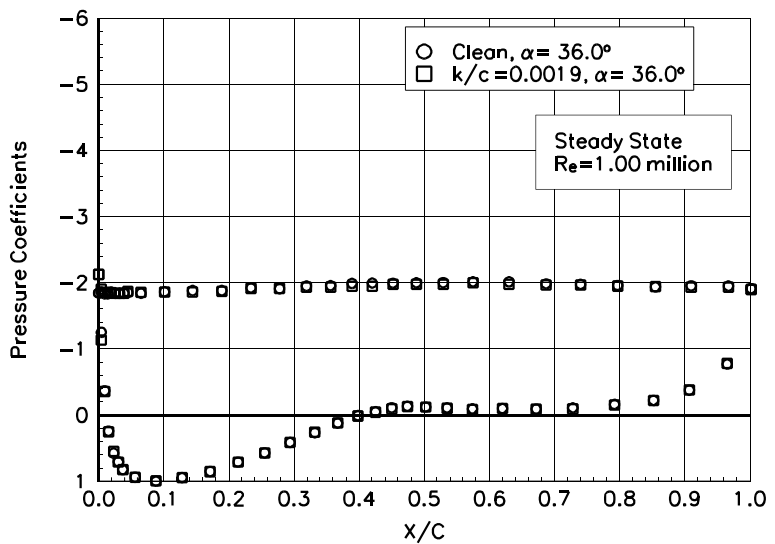


Figure B70. $\alpha = 36.0^\circ$

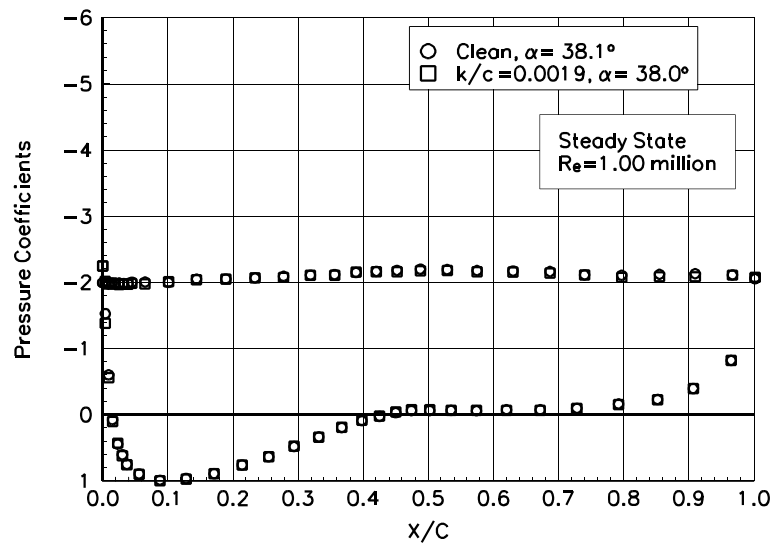


Figure B71. $\alpha = 38.1^\circ$

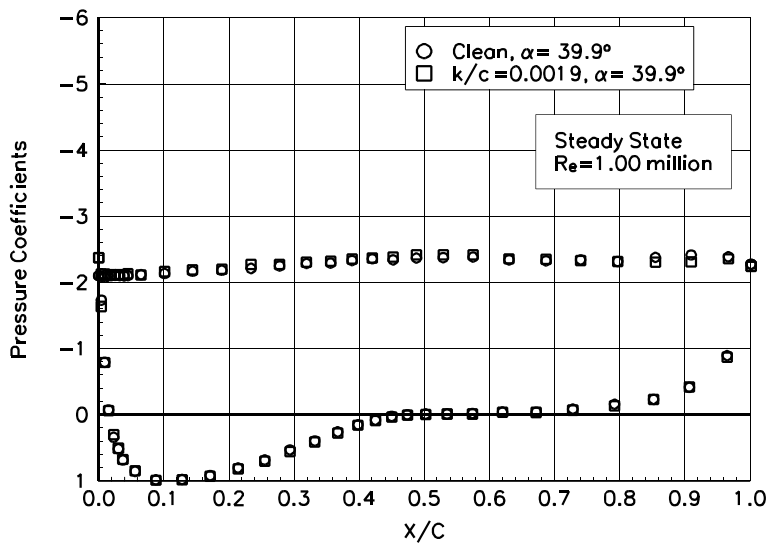


Figure B72. $\alpha = 39.9^\circ$

S809

Pressure Distributions, Steady State, Re = 1.25 million

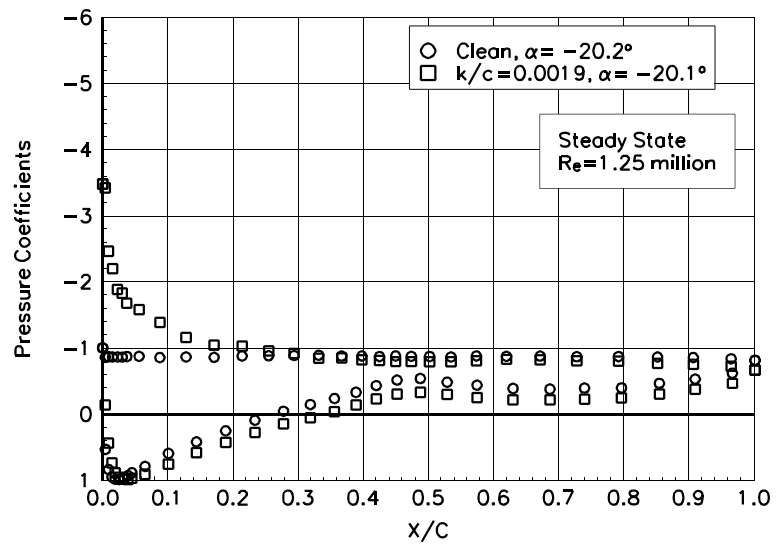


Figure B73. $\alpha = -20.2^\circ$

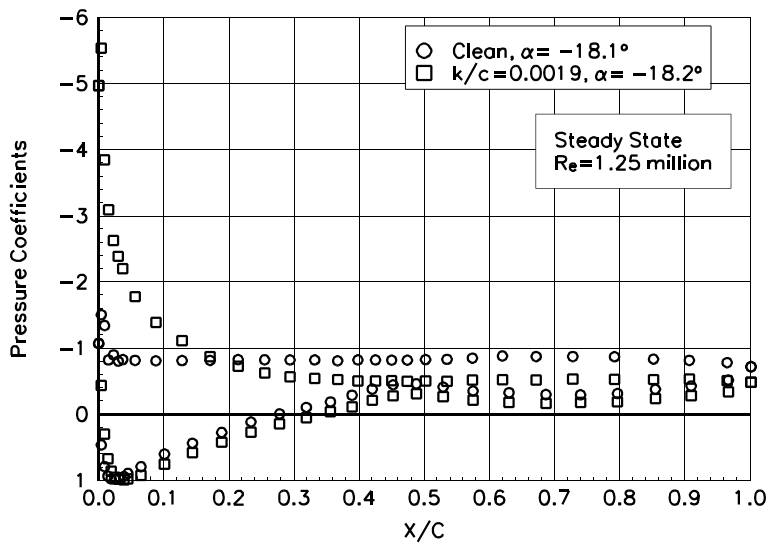


Figure B74. $\alpha = -18.1^\circ$

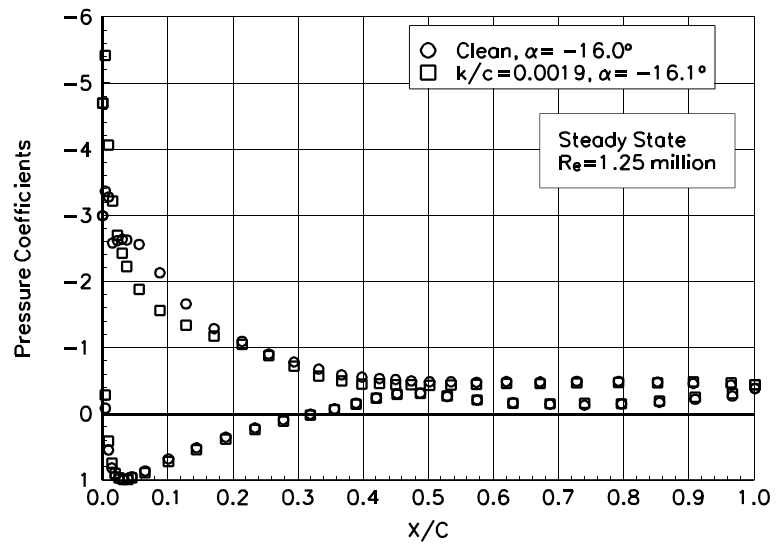


Figure B75. $\alpha = -16.0^\circ$

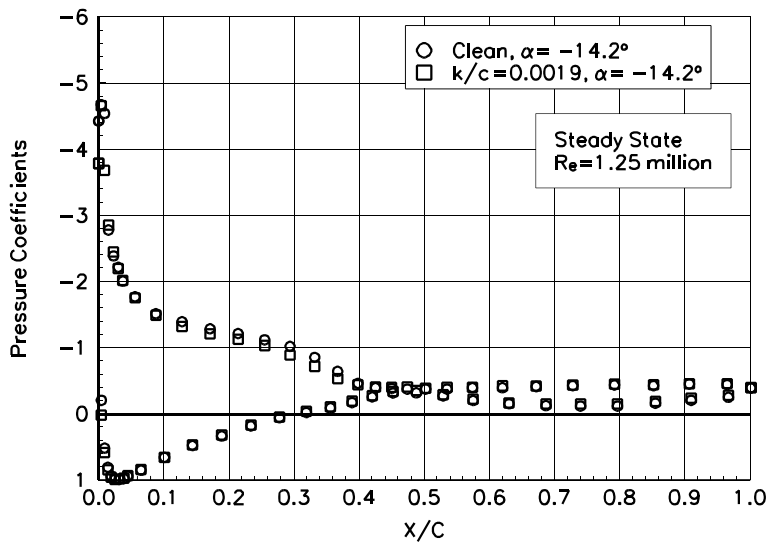


Figure B76. $\alpha = -14.2^\circ$

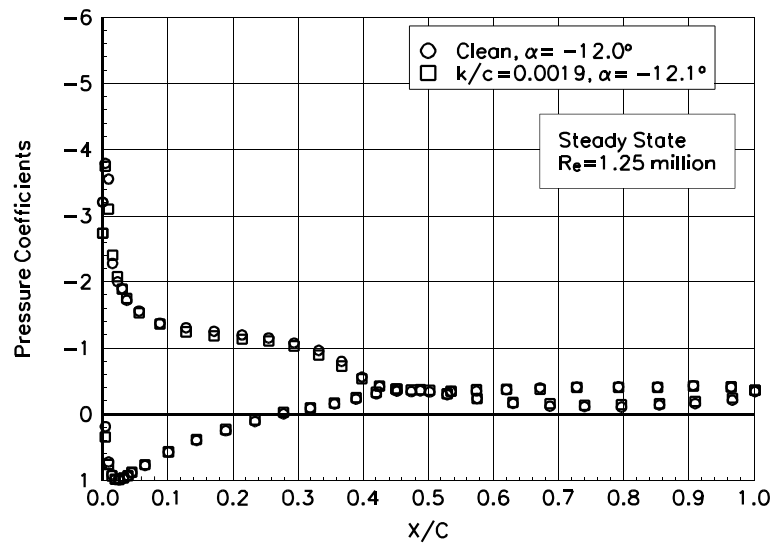


Figure B77. $\alpha = -12.0^\circ$

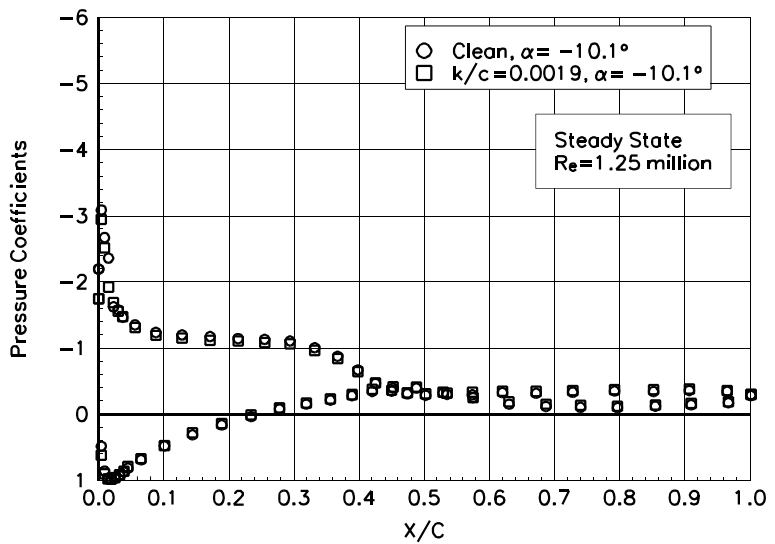


Figure B78. $\alpha = -10.1^\circ$

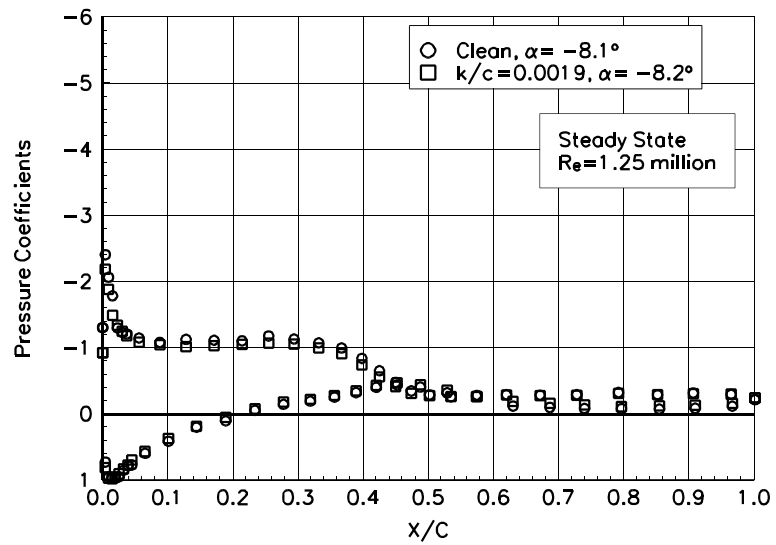


Figure B79. $\alpha = -8.1^\circ$

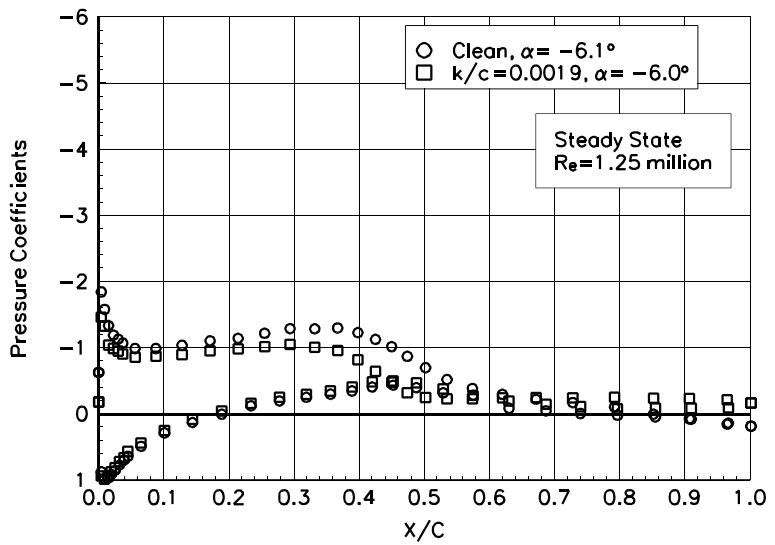


Figure B80. $\alpha = -6.1^\circ$

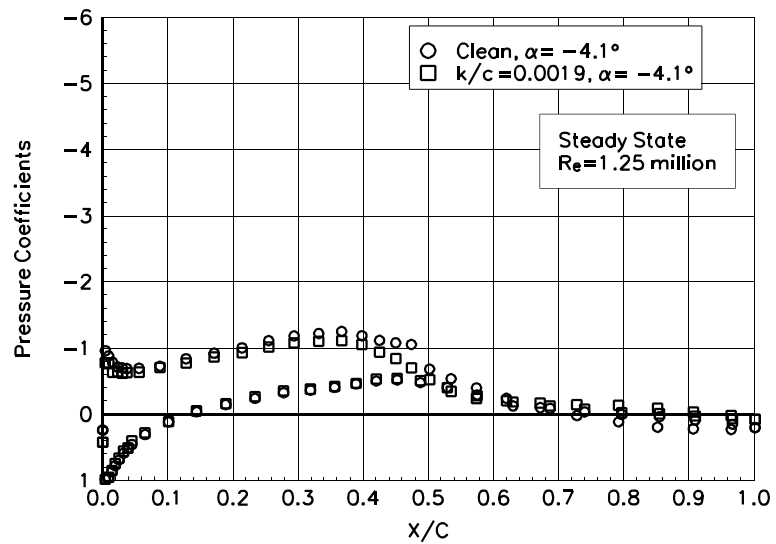


Figure B81. $\alpha = -4.1^\circ$

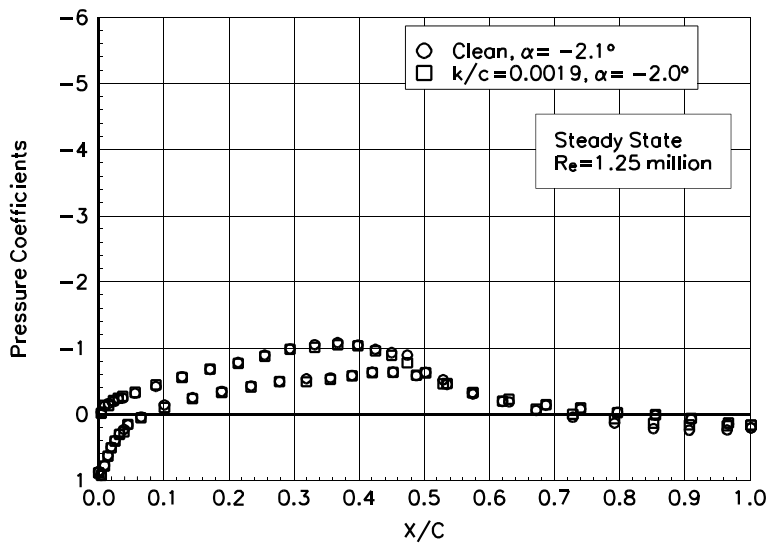


Figure B82. $\alpha = -2.1^\circ$

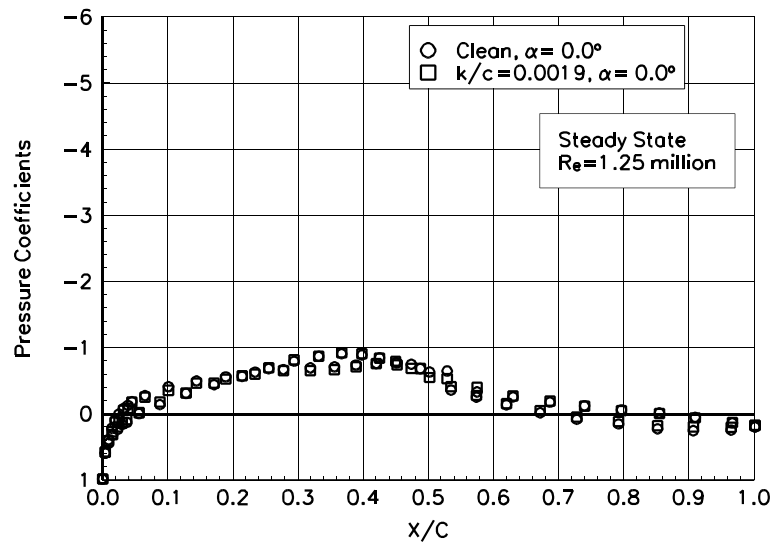


Figure B83. $\alpha = 0.0^\circ$

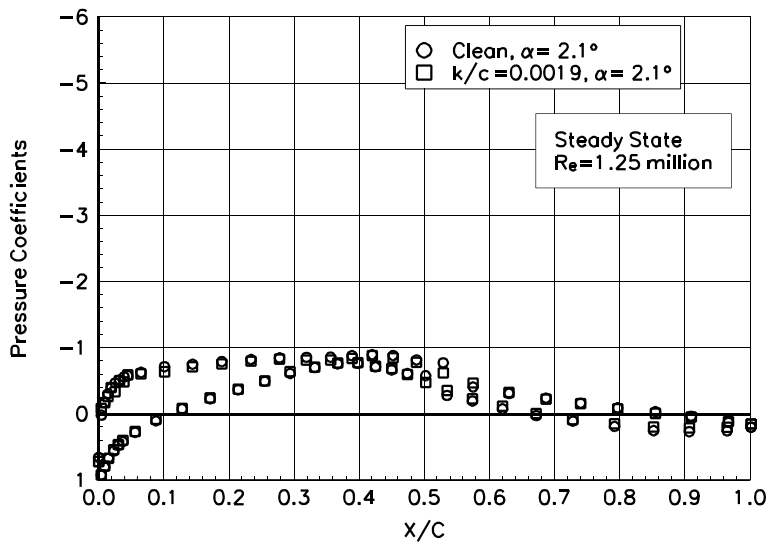


Figure B84. $\alpha = 2.1^\circ$

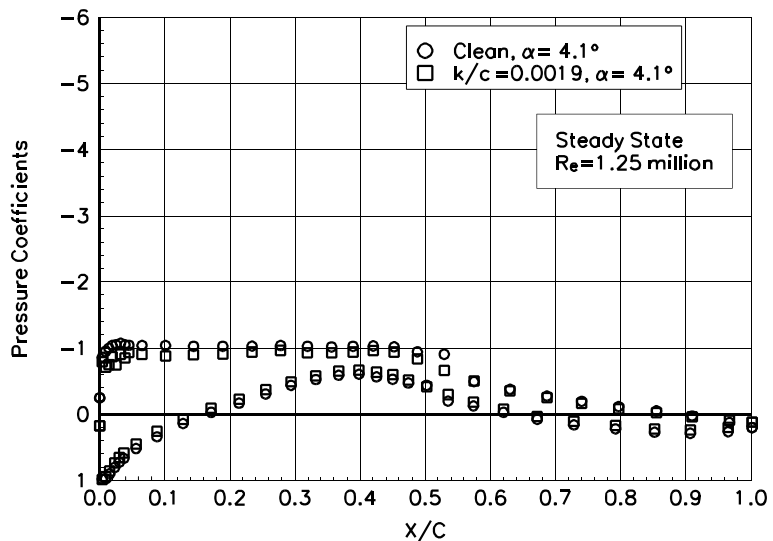


Figure B85. $\alpha = 4.1^\circ$

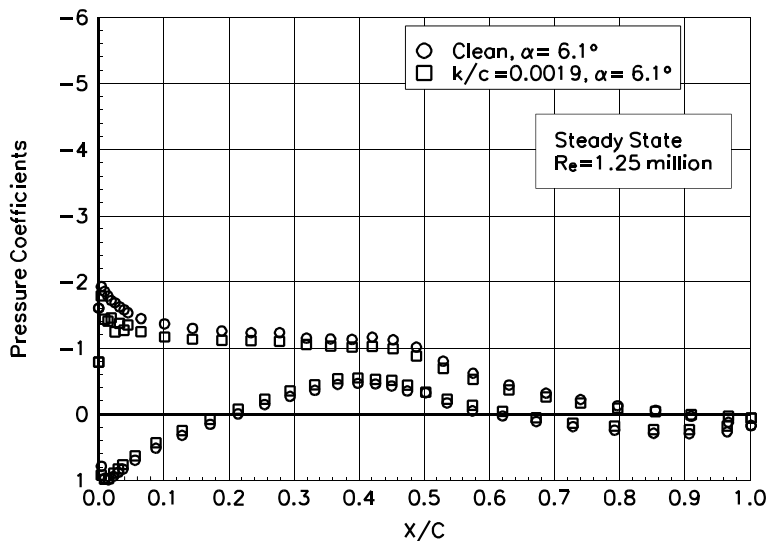


Figure B86. $\alpha = 6.1^\circ$

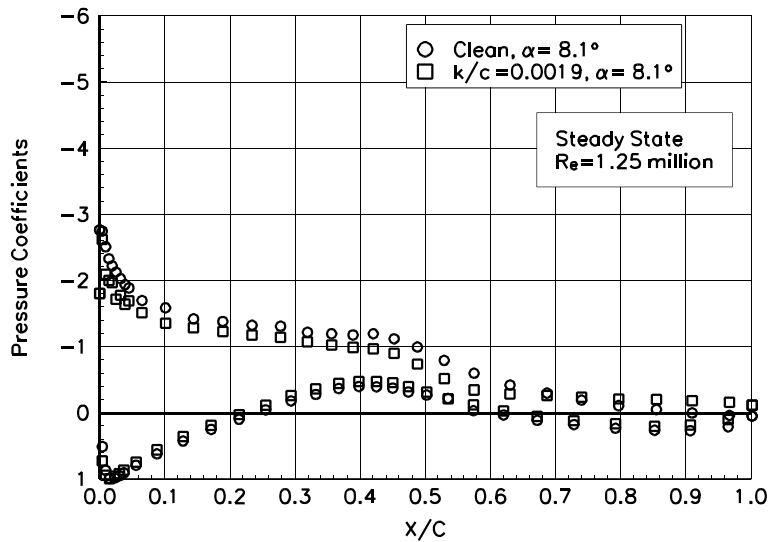


Figure B87. $\alpha = 8.1^\circ$

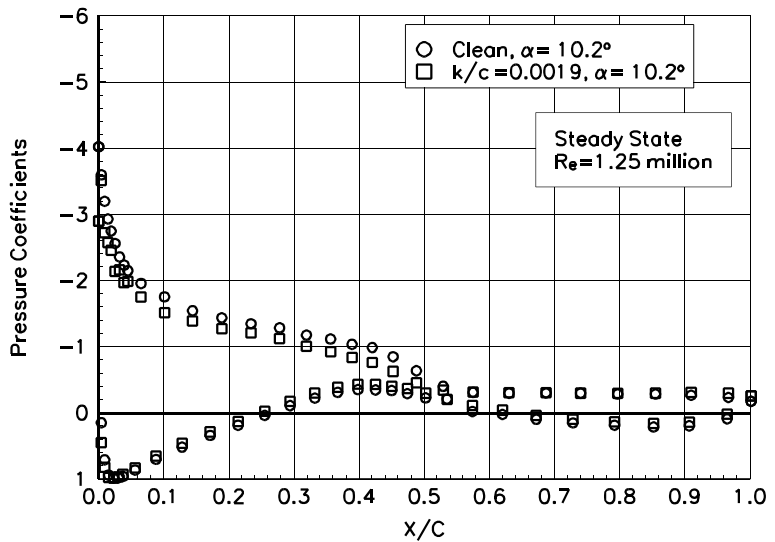


Figure B88. $\alpha = 10.2^\circ$

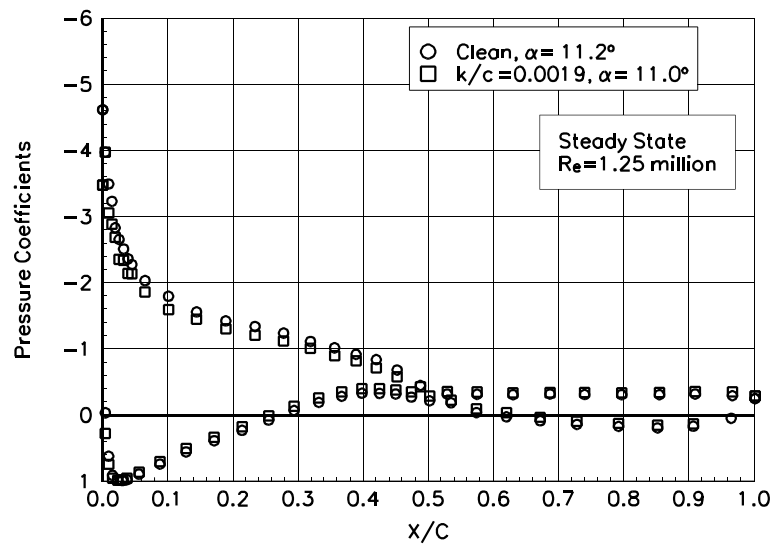


Figure B89. $\alpha = 11.2^\circ$

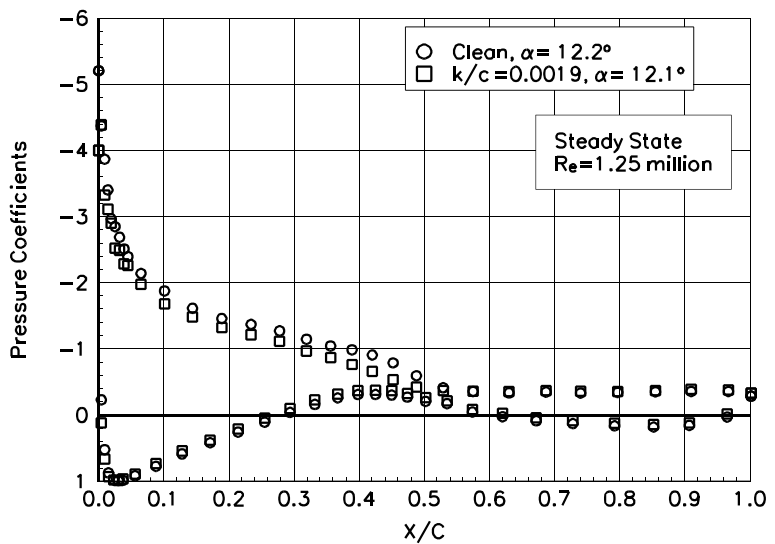


Figure B90. $\alpha = 12.2^\circ$

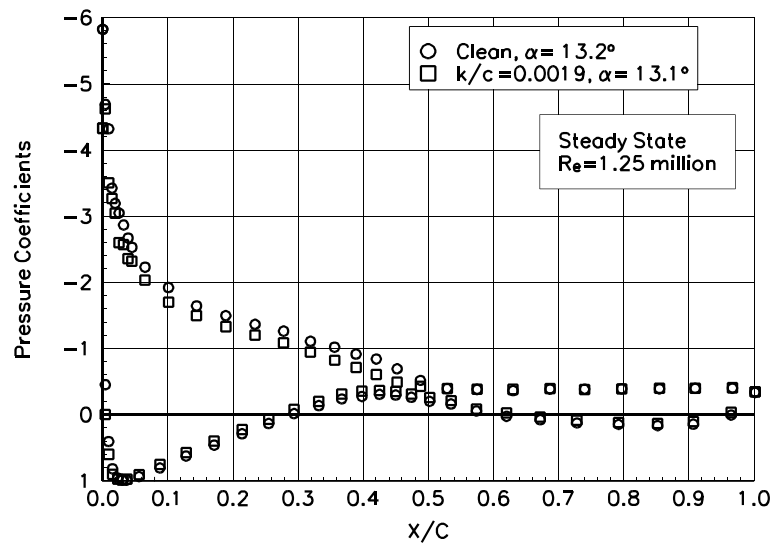


Figure B91. $\alpha = 13.2^\circ$

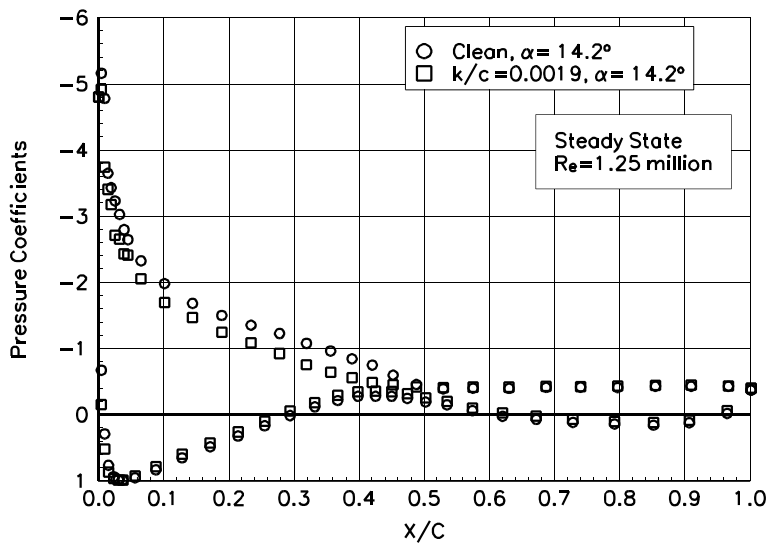


Figure B92. $\alpha = 14.2^\circ$

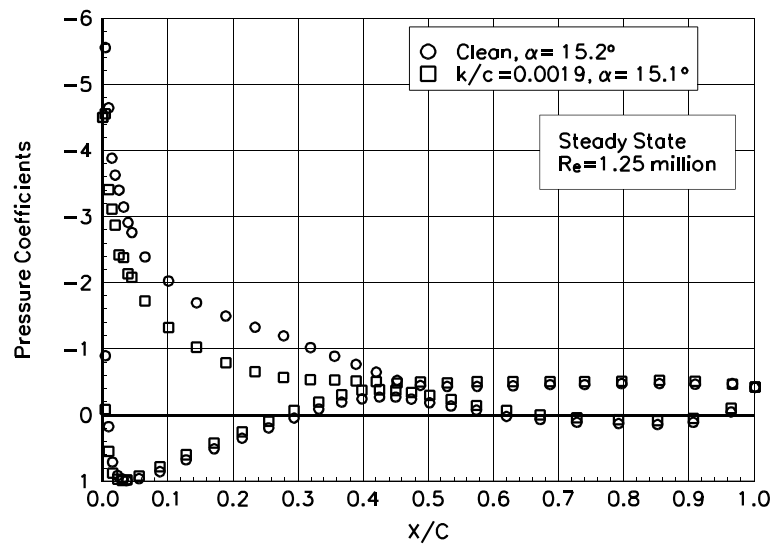


Figure B93. $\alpha = 15.2^\circ$

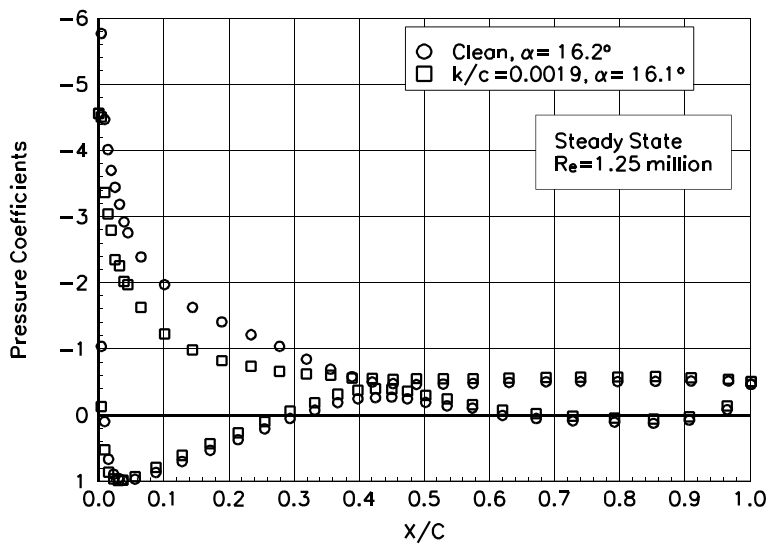


Figure B94. $\alpha = 16.2^\circ$

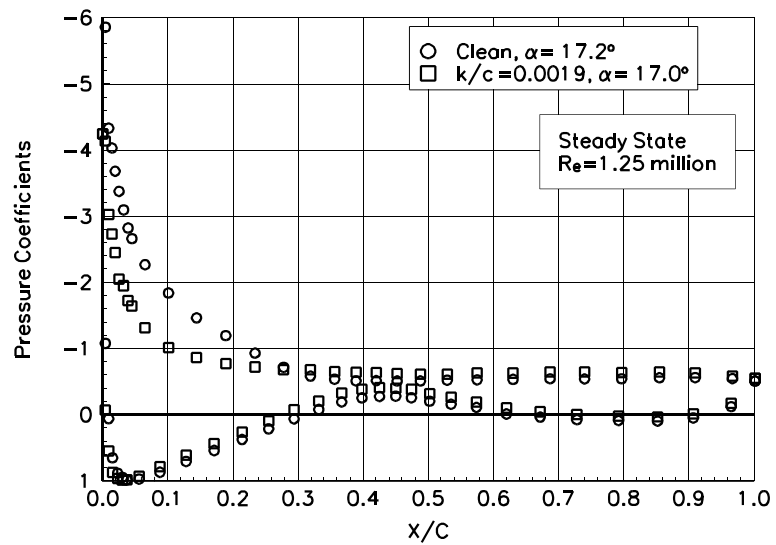


Figure B95. $\alpha = 17.2^\circ$

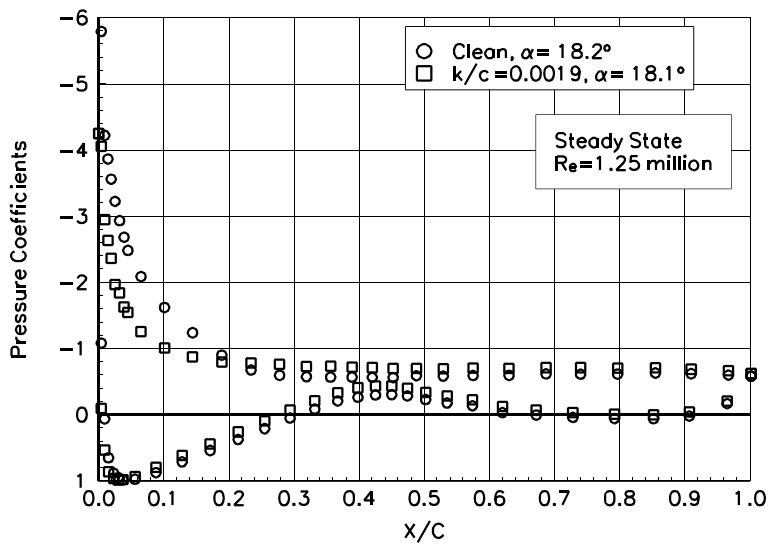


Figure B96. $\alpha = 18.2^\circ$

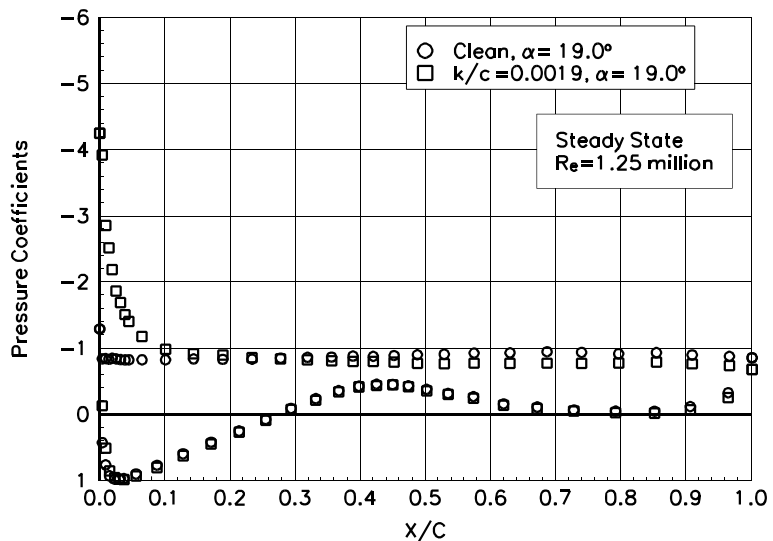


Figure B97. $\alpha = 19.0^\circ$

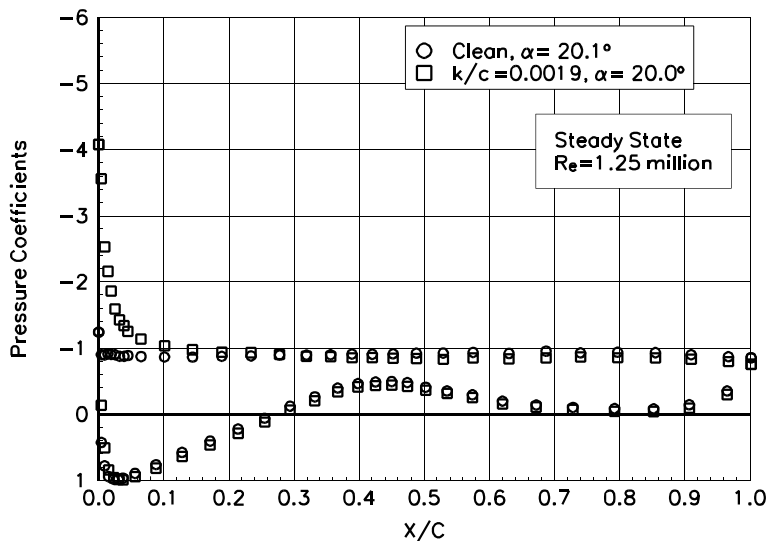


Figure B98. $\alpha = 20.1^\circ$

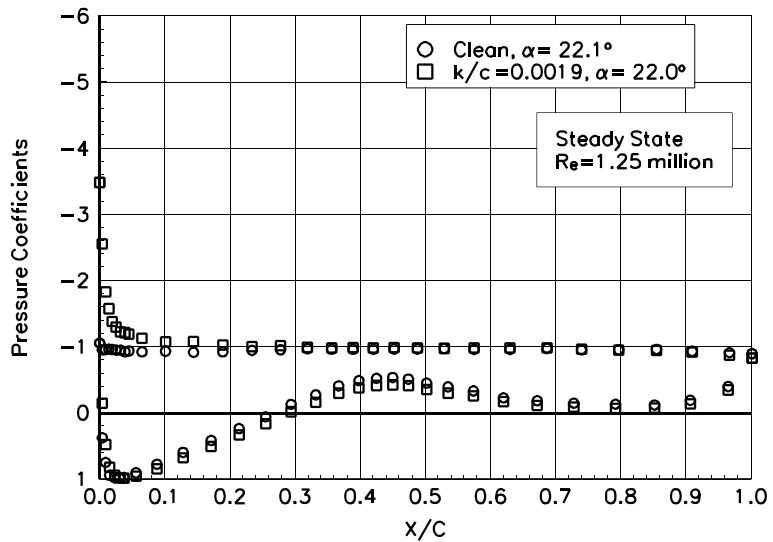


Figure B99. $\alpha = 22.1^\circ$

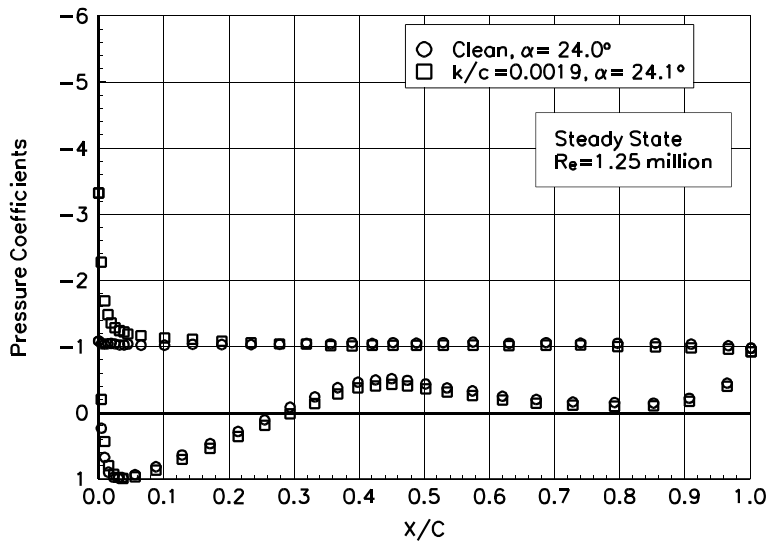


Figure B100. $\alpha = 24.0^\circ$

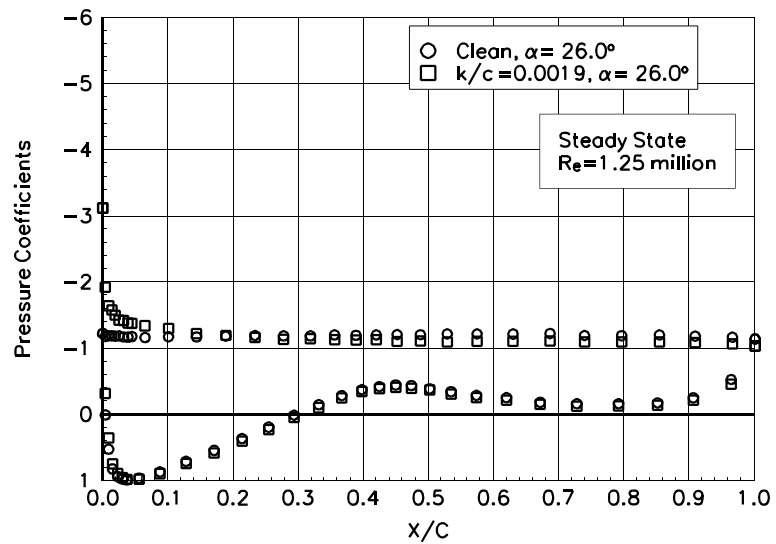


Figure B101. $\alpha = 26.0^\circ$

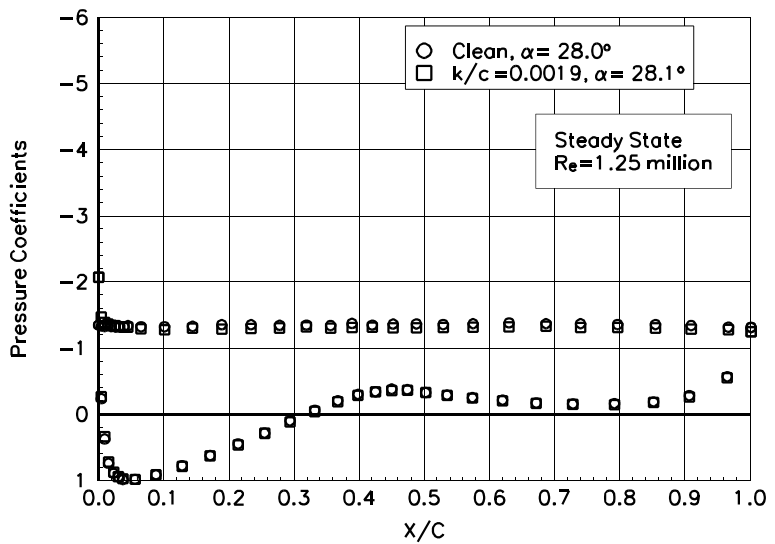


Figure B102. $\alpha = 28.0^\circ$

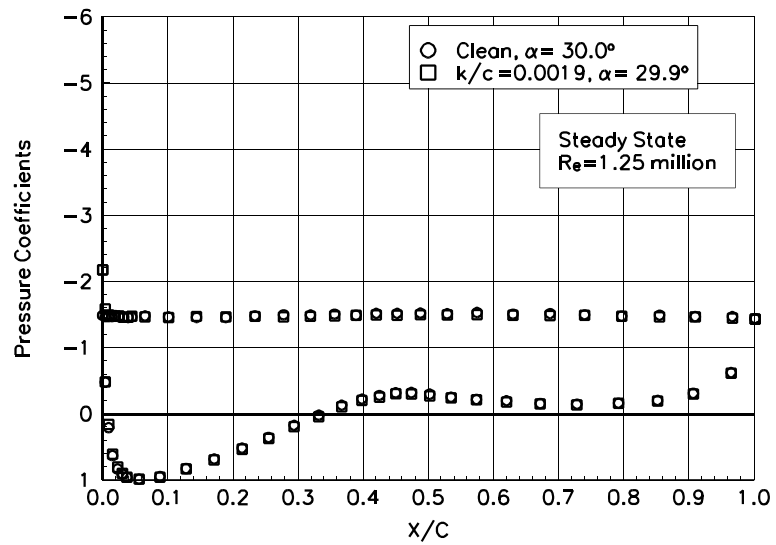


Figure B103. $\alpha = 30.0^\circ$

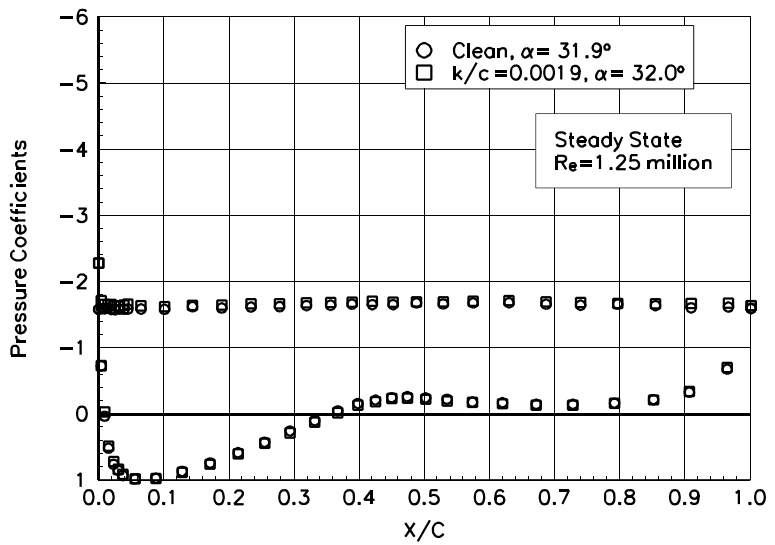


Figure B104. $\alpha = 31.9^\circ$

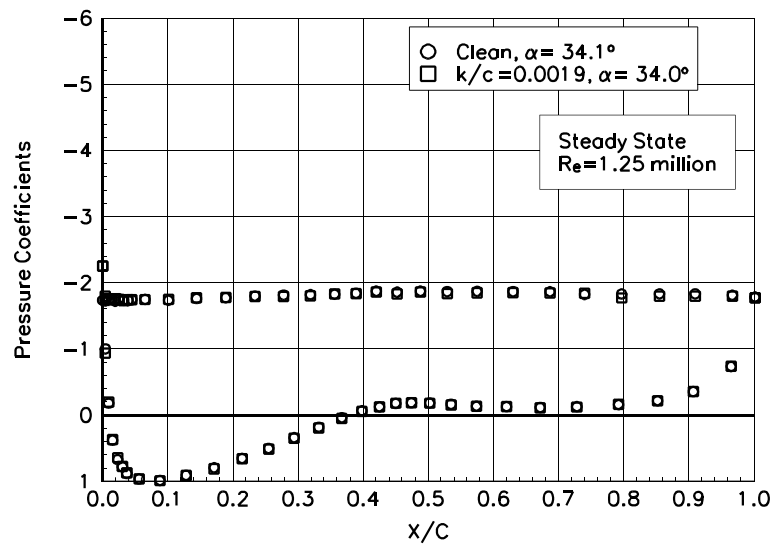


Figure B105. $\alpha = 34.1^\circ$

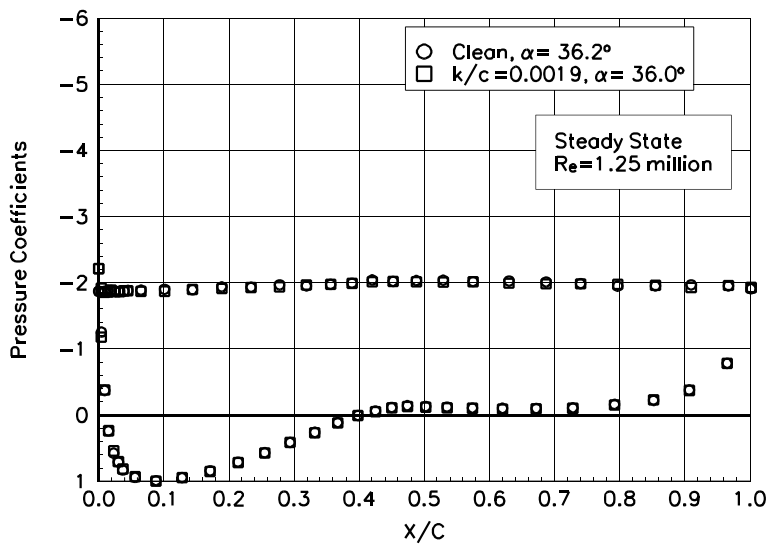


Figure B106. $\alpha = 36.2^\circ$

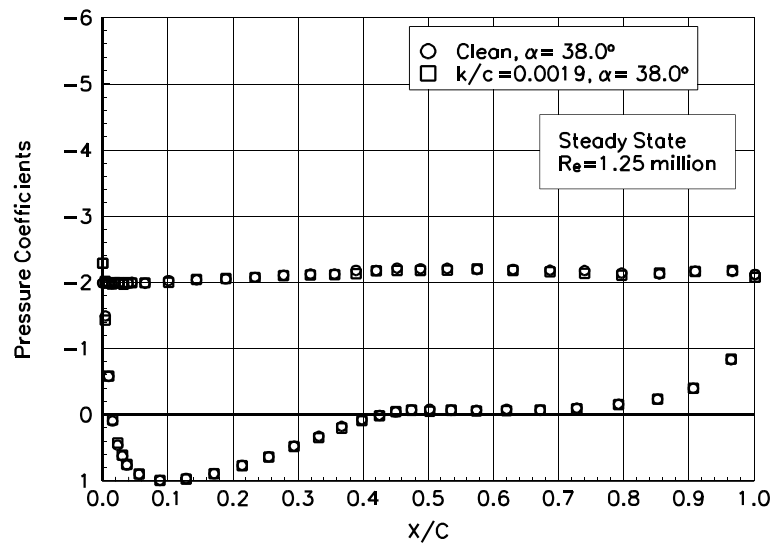


Figure B107. $\alpha = 38.0^\circ$

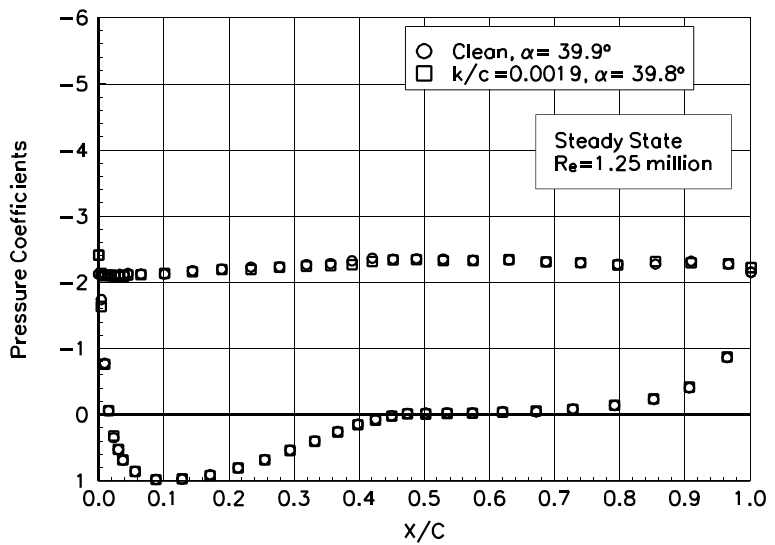


Figure B108. $\alpha = 39.9^\circ$

S809

Pressure Distributions, Steady State, Re = 1.5 million

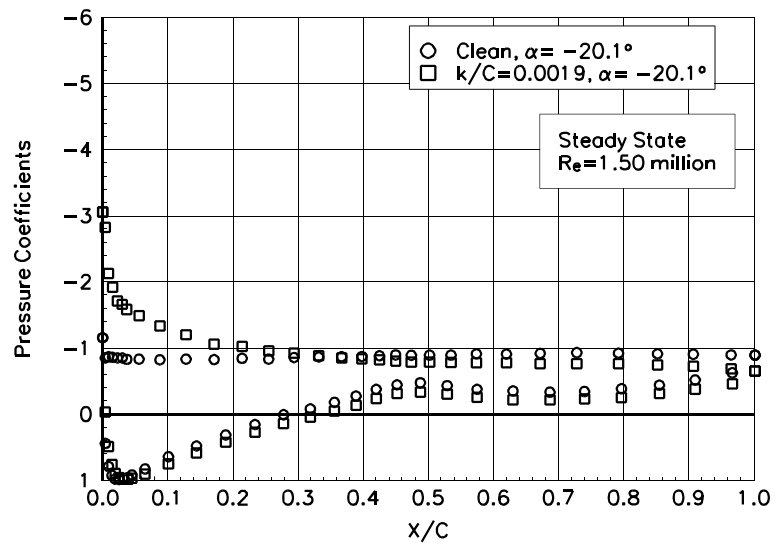


Figure B109. $\alpha = -20.1^\circ$

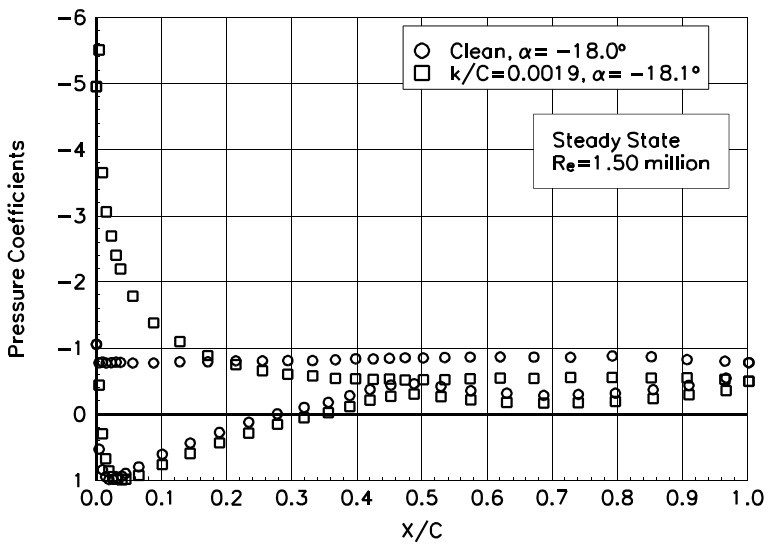


Figure B110. $\alpha = -18.0^\circ$

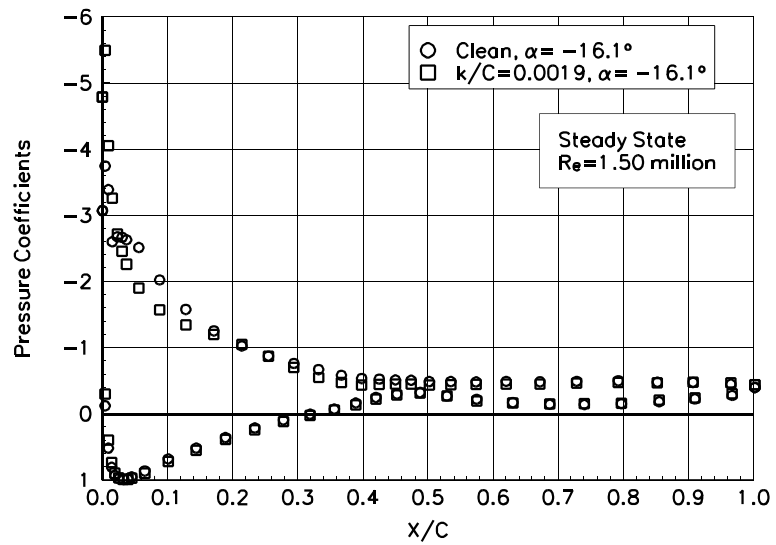


Figure B111. $\alpha = -16.1^\circ$

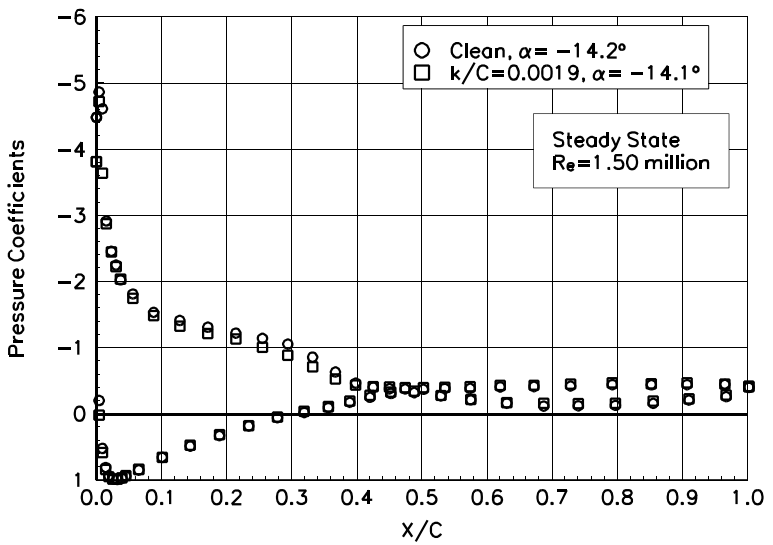


Figure B112. $\alpha = -14.2^\circ$

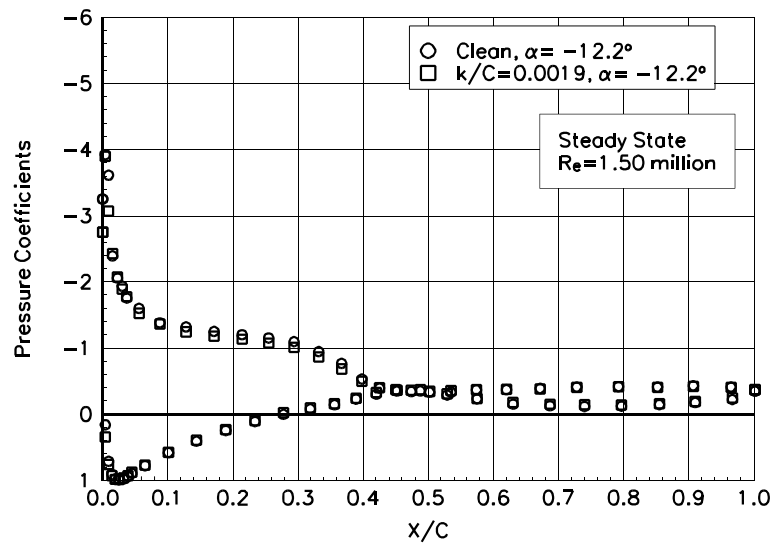


Figure B113. $\alpha = -12.2^\circ$

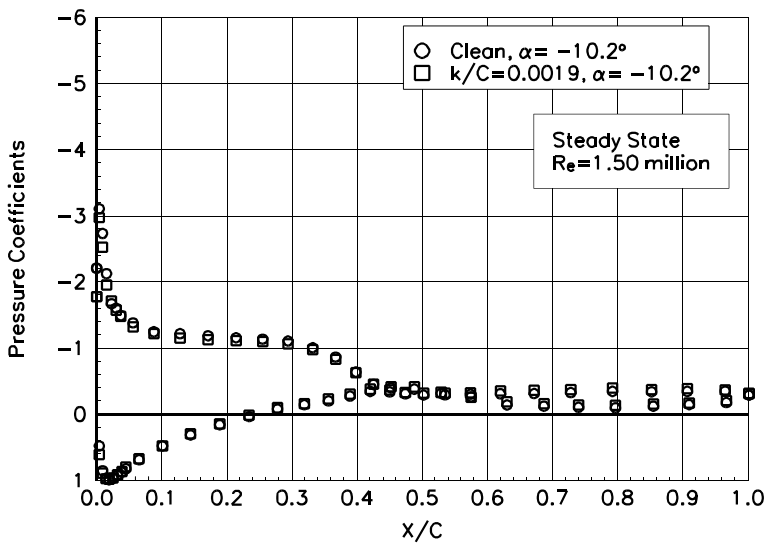


Figure B114. $\alpha = -10.2^\circ$

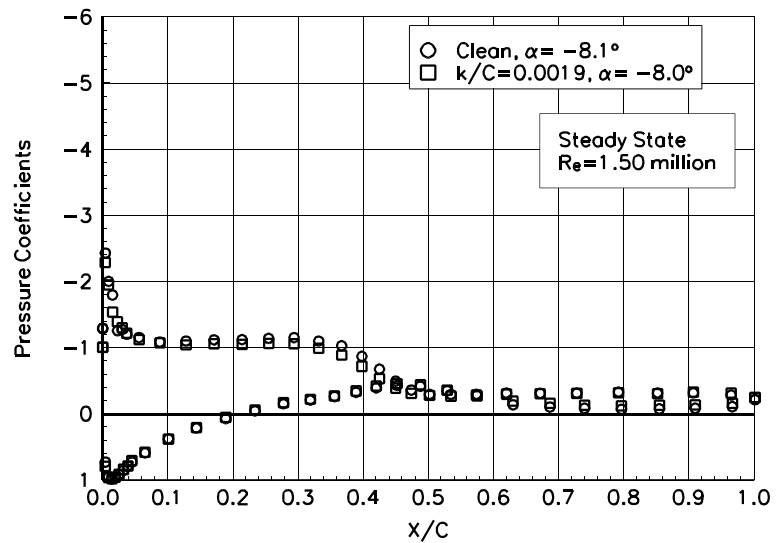


Figure B115. $\alpha = -8.1^\circ$

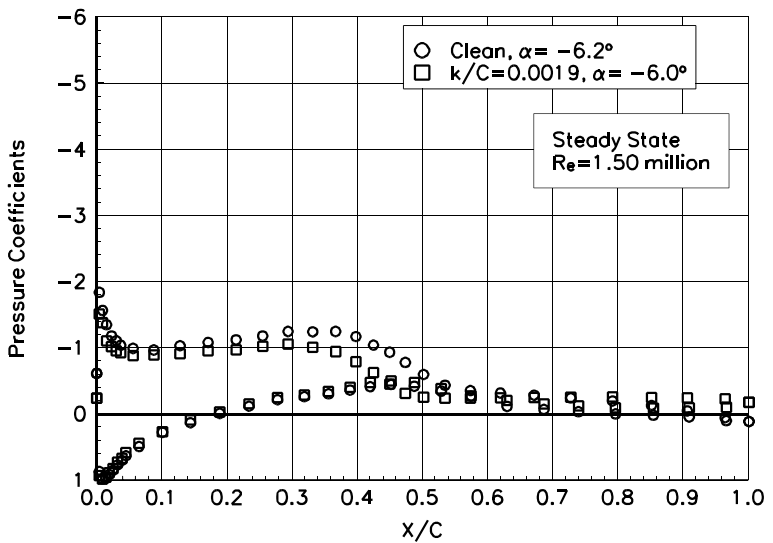


Figure B116. $\alpha = -6.2^\circ$

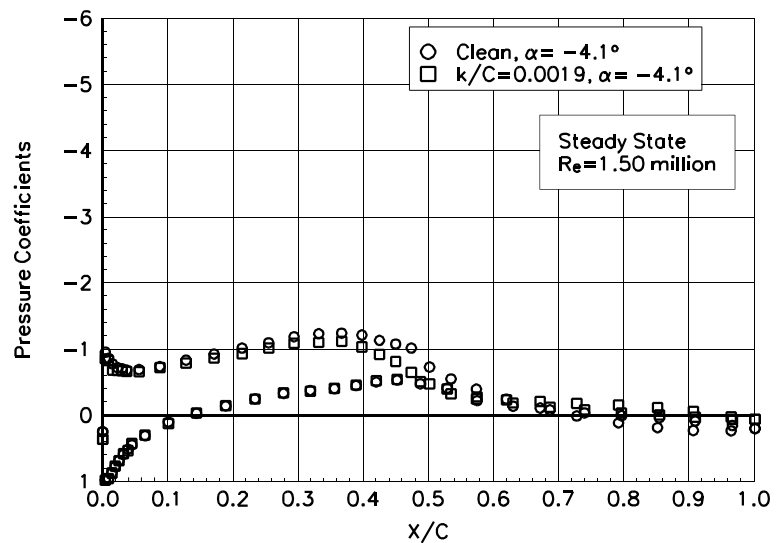


Figure B117. $\alpha = -4.1^\circ$

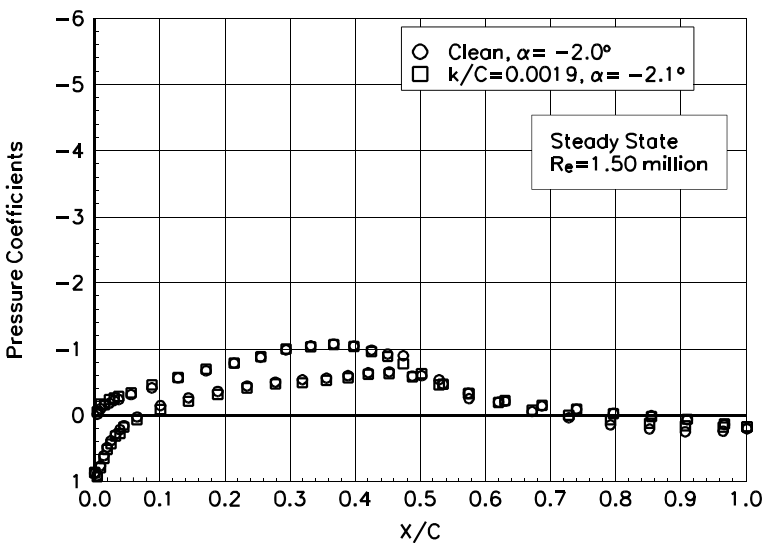


Figure B118. $\alpha = -2.0^\circ$

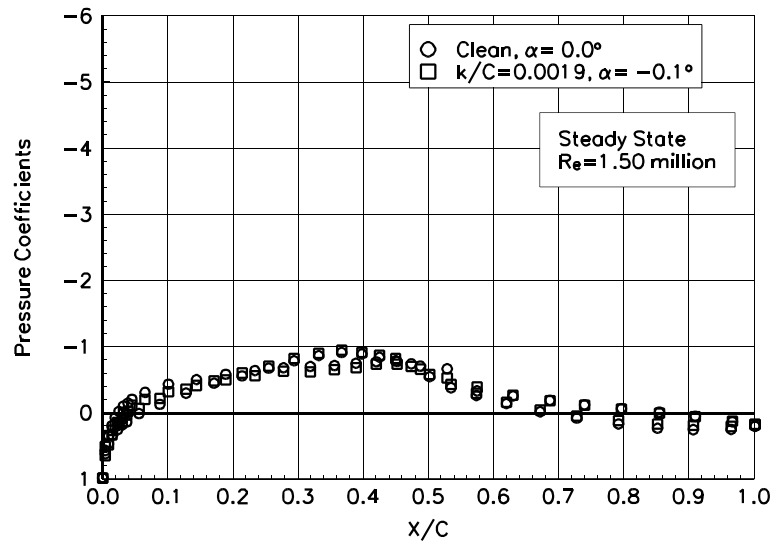


Figure B119. $\alpha = 0.0^\circ$

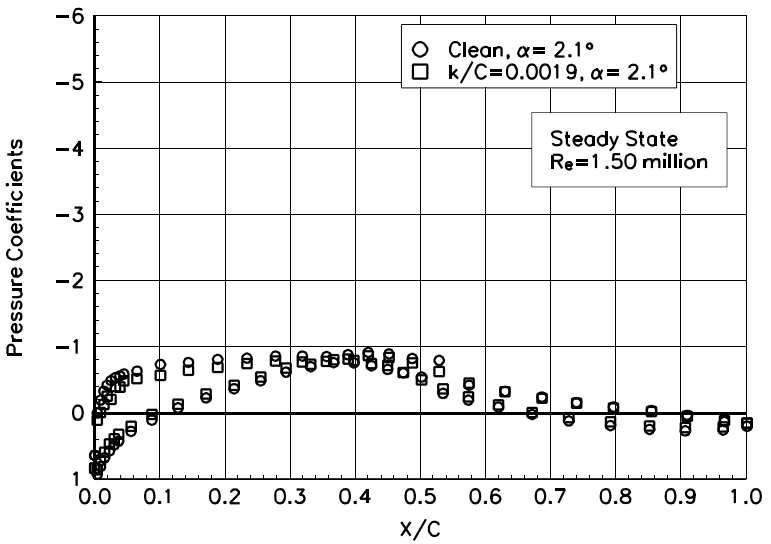


Figure B120. $\alpha = 2.1^\circ$

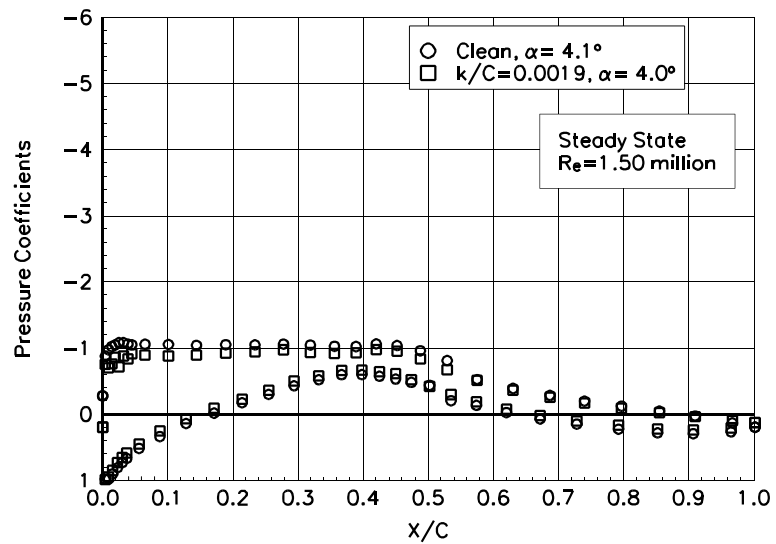


Figure B121. $\alpha = 4.1^\circ$

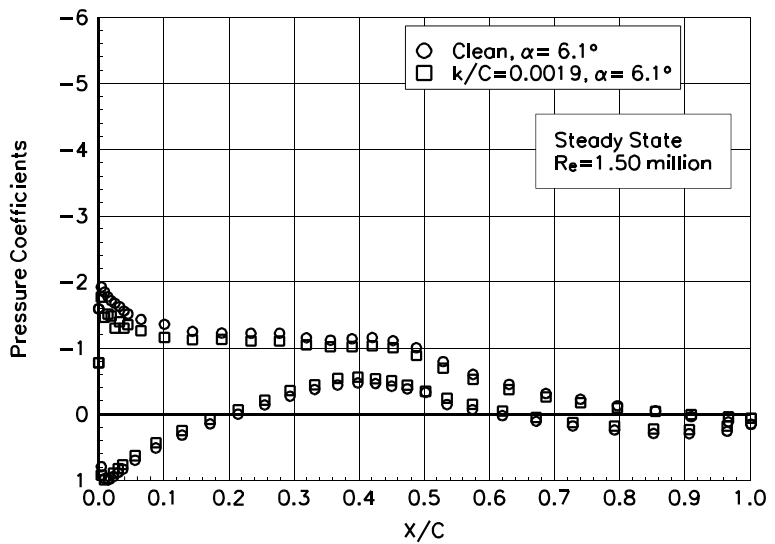


Figure B122. $\alpha = 6.1^\circ$

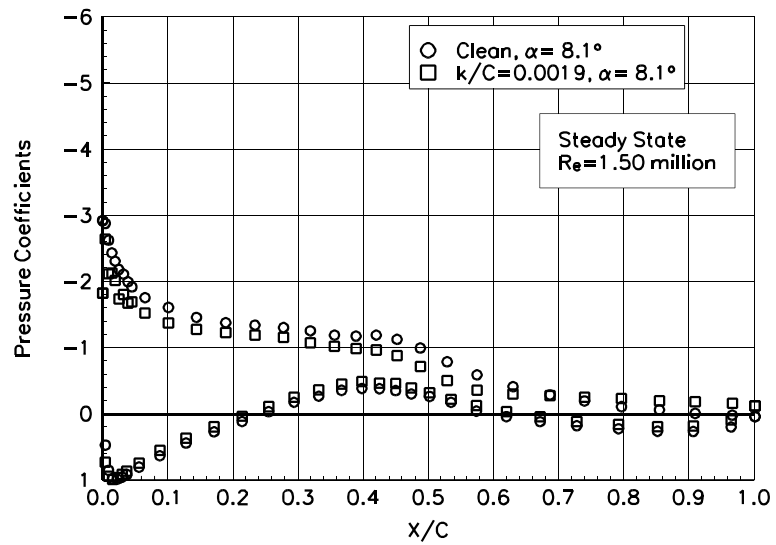


Figure B123. $\alpha = 8.1^\circ$

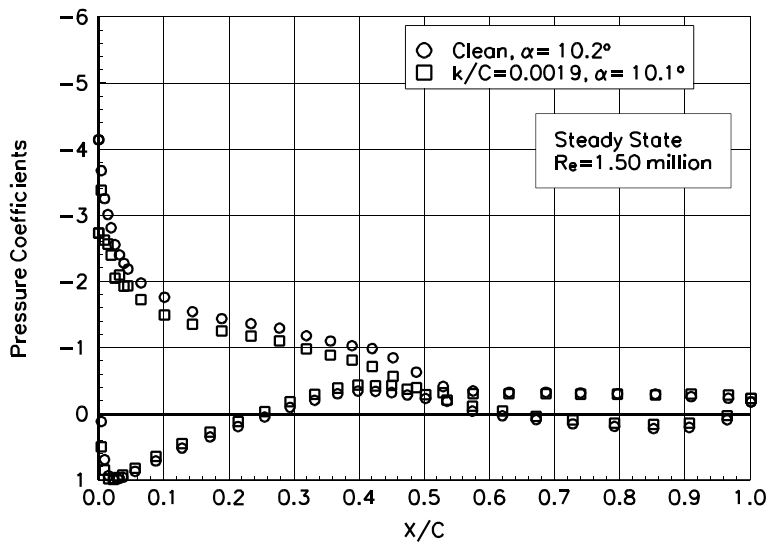


Figure B124. $\alpha = 10.2^\circ$

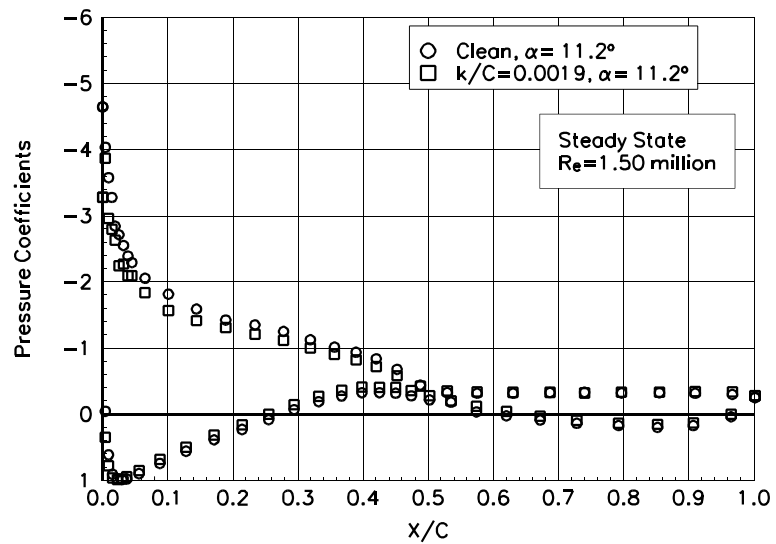


Figure B125. $\alpha = 11.2^\circ$

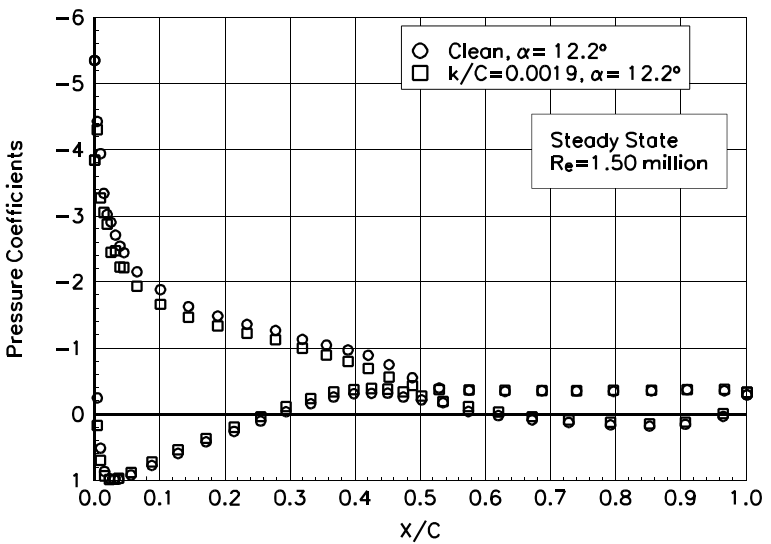


Figure B126. $\alpha = 12.2^\circ$

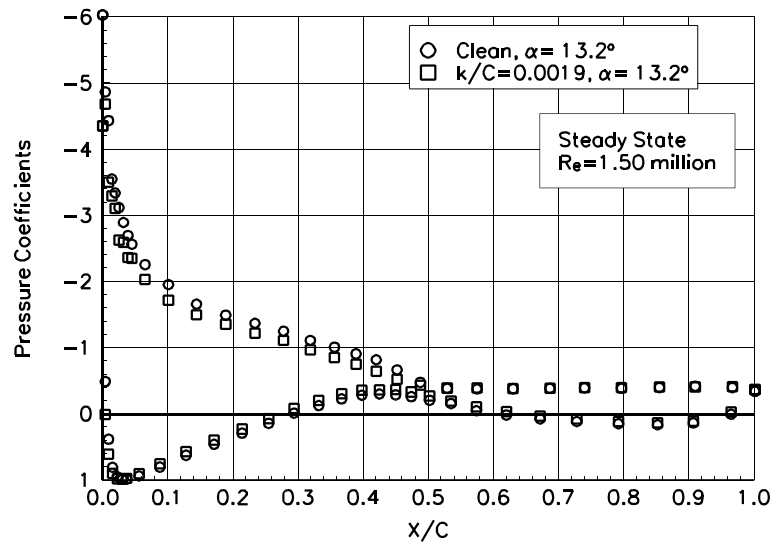


Figure B127. $\alpha = 13.2^\circ$

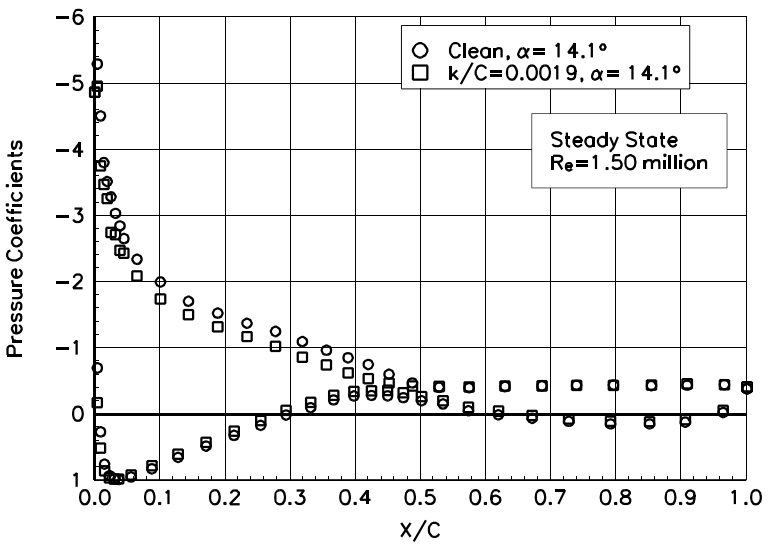


Figure B128. $\alpha = 14.1^\circ$

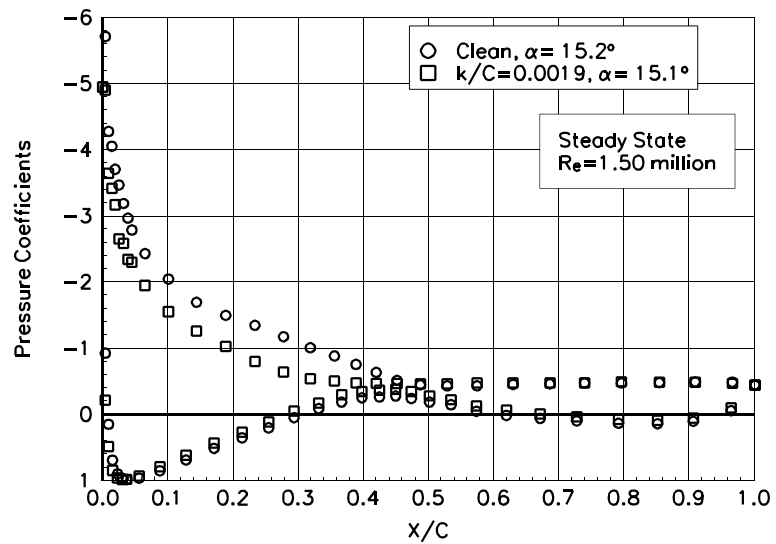


Figure B129. $\alpha = 15.2^\circ$

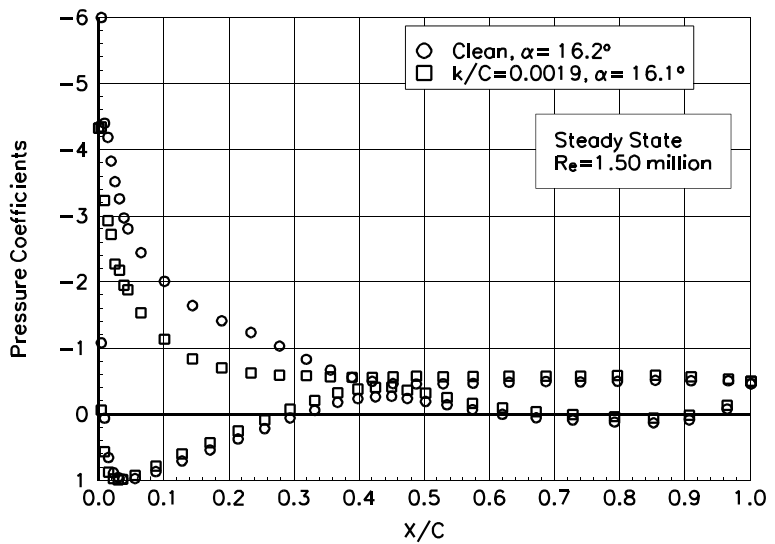


Figure B130. $\alpha = 16.2^\circ$

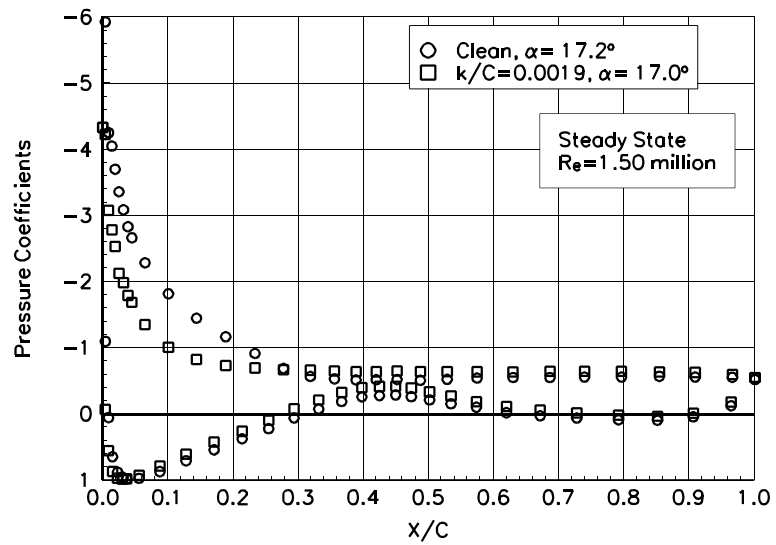


Figure B131. $\alpha = 17.2^\circ$

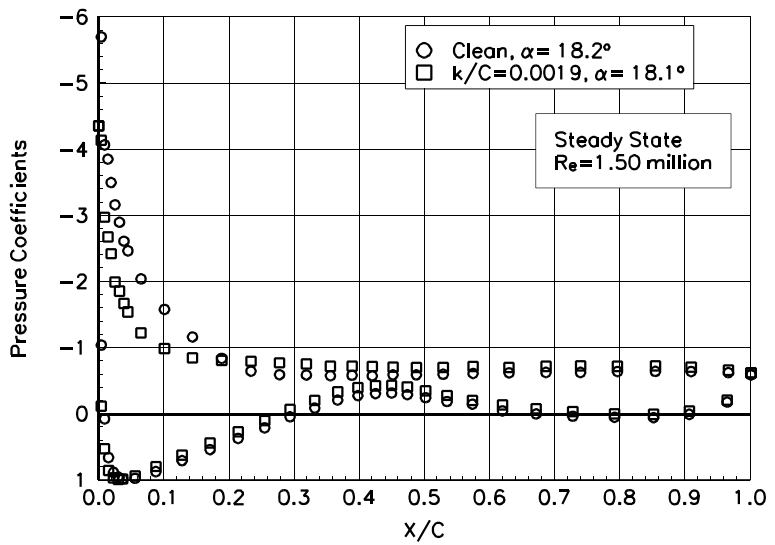


Figure B132. $\alpha = 18.2^\circ$

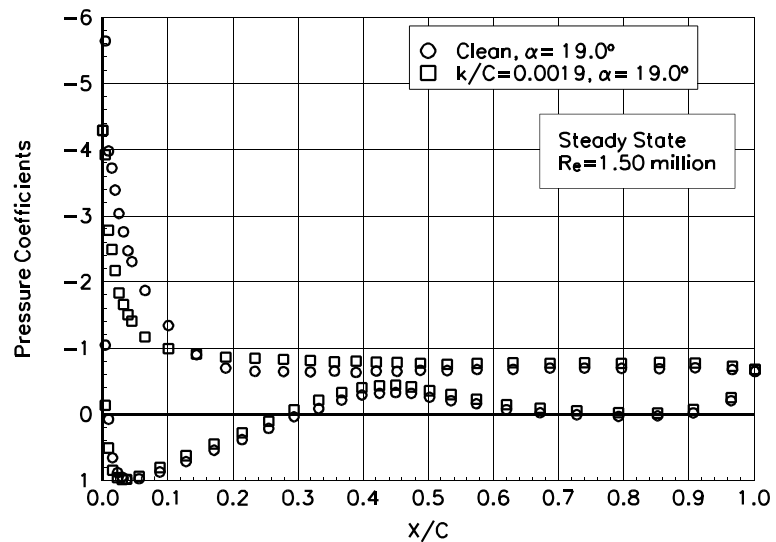


Figure B133. $\alpha = 19.0^\circ$

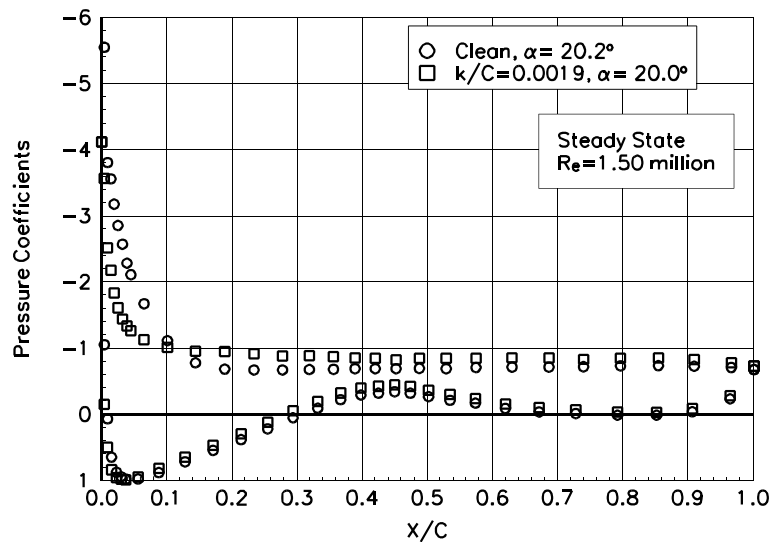


Figure B134. $\alpha = 20.2^\circ$

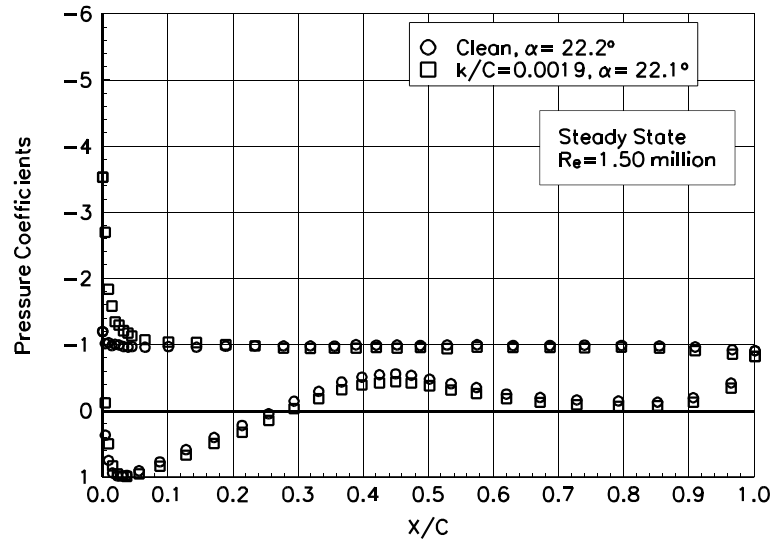


Figure B135. $\alpha = 22.2^\circ$

Appendix C: Unsteady Integrated Coefficients

List of Figures

Page

±5.5° Sine, Re = 0.75 million	C-3
±5.5° Sine, Re = 1 million	C-10
±5.5° Sine, Re= 1.25 million	C-17
±5.5° Sine, Re = 1.4 million	C-24
±10° Sine, Re = 0.75 million	C-31
±10° Sine, Re = 1 million	C-38
±10° Sine, Re = 1.25 million	C-45
±10° Sine, Re = 1.4 million	C-52

Unsteady Airfoil Characteristics

$\pm 5.5^\circ$ Sine, $Re = 0.75$ million

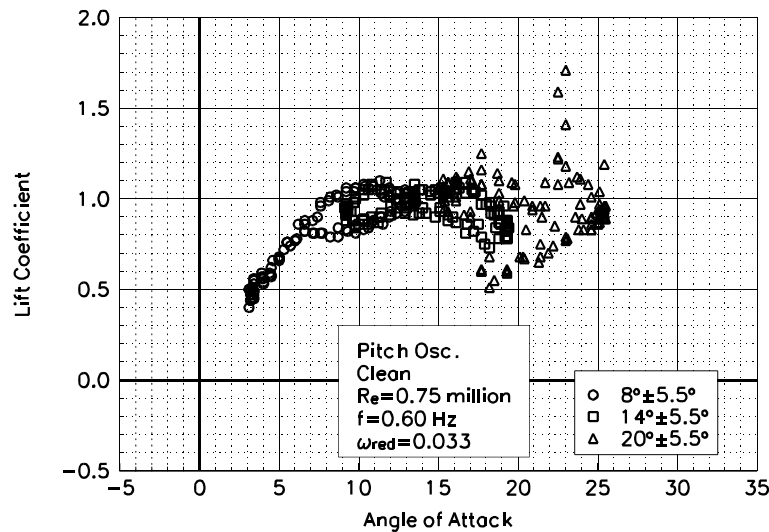


Figure C1. Lift coefficient vs α .

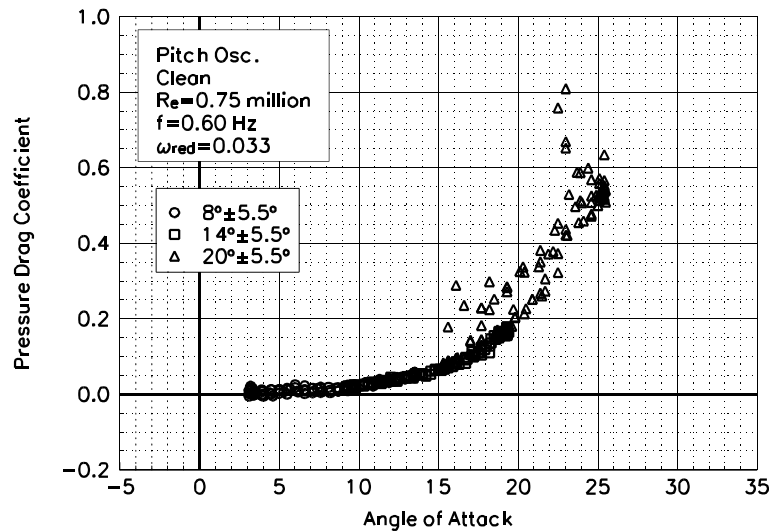


Figure C2. Pressure drag coefficient vs α .

S809
Clean
 $Re=0.75$ million
 $\omega_{reduced}=0.033$

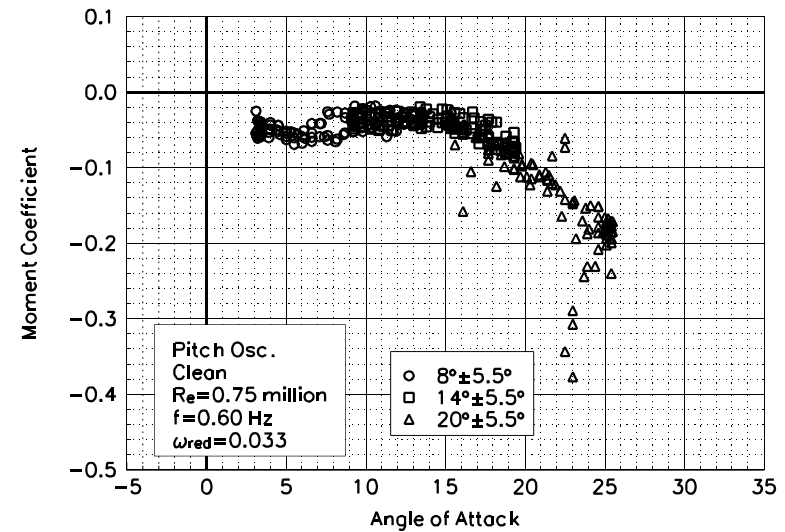


Figure C3. Moment coefficient vs α .

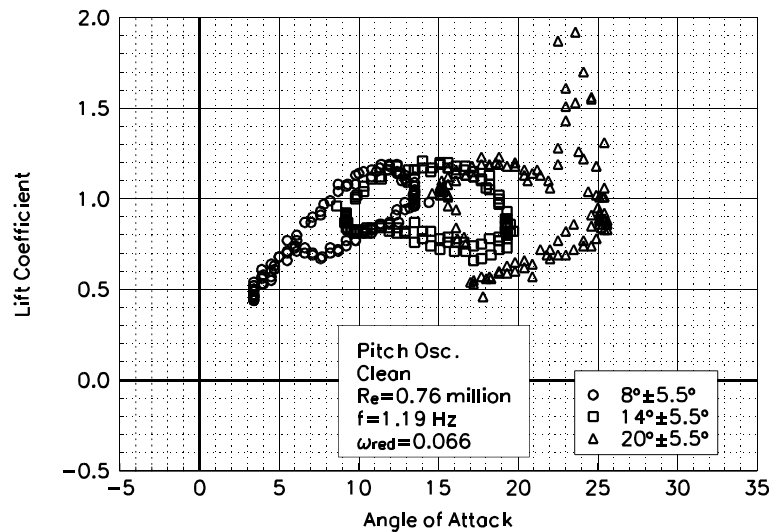


Figure C4. Lift coefficient vs α .

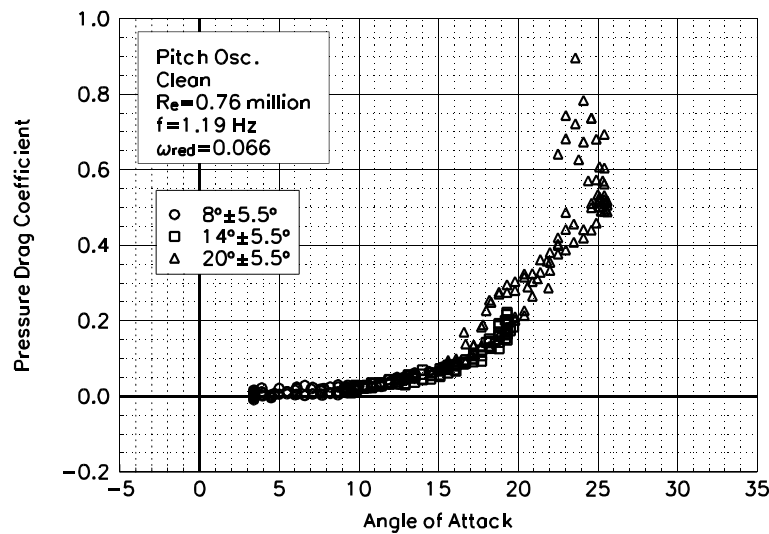


Figure C5. Pressure drag coefficient vs α .

S809
Clean
 $Re=0.76$ million
 $\omega_{red}=0.066$

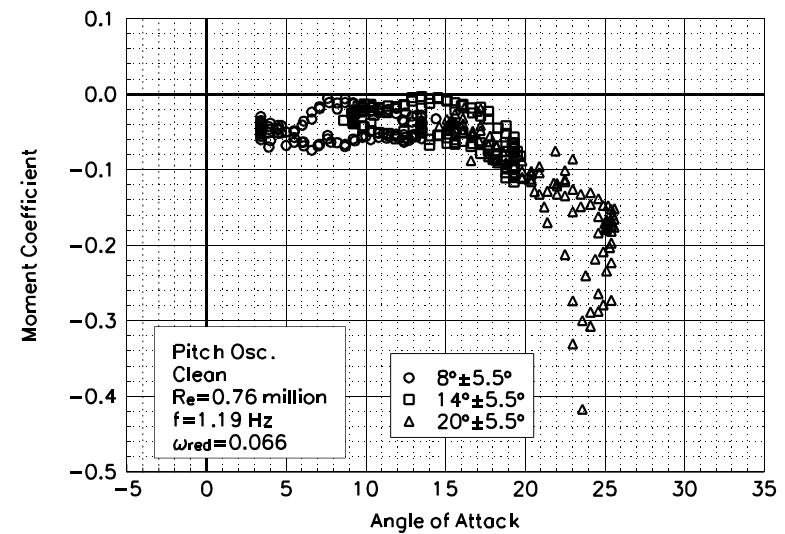


Figure C6. Moment coefficient vs α .

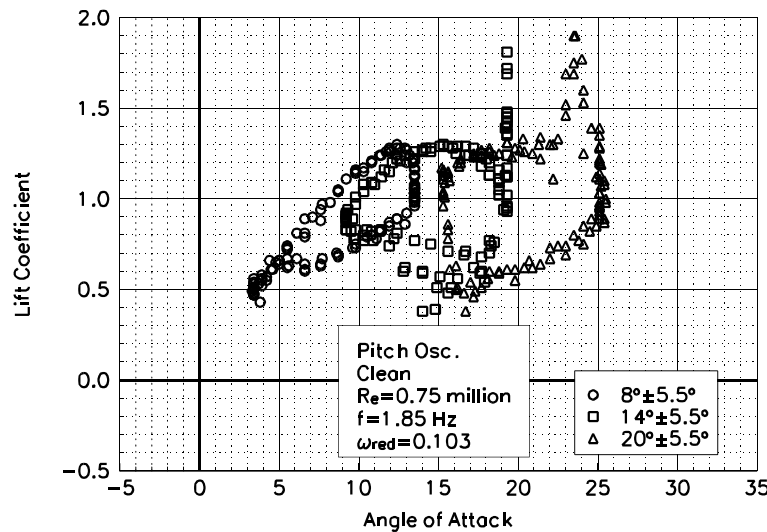


Figure C7. Lift coefficient vs α .

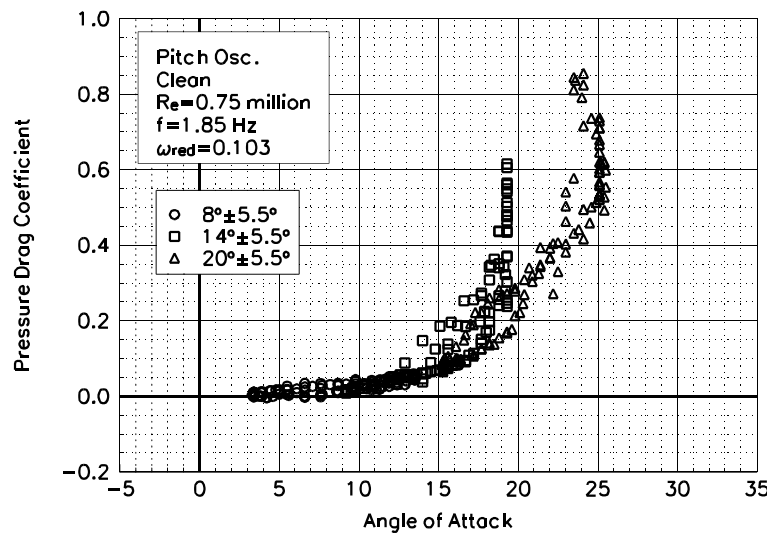


Figure C8. Pressure drag coefficient vs α .

S809
Clean
 $Re=0.75$ million
 $\omega_{red}=0.103$

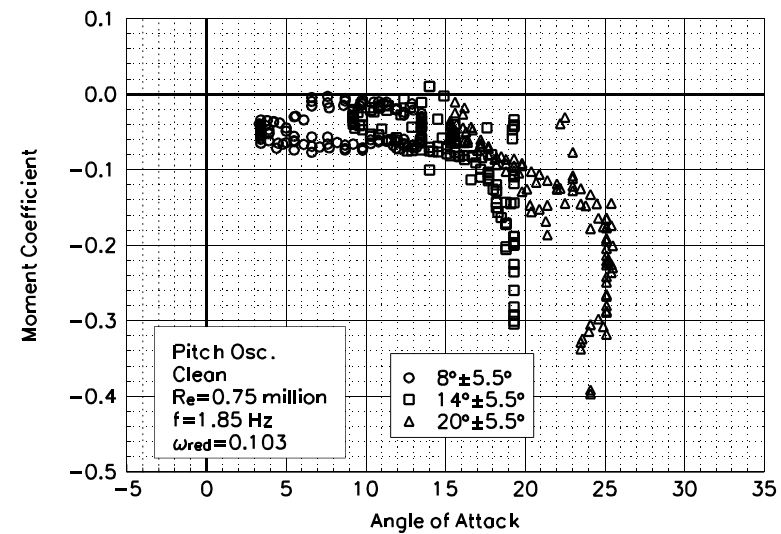


Figure C9. Moment coefficient vs α .

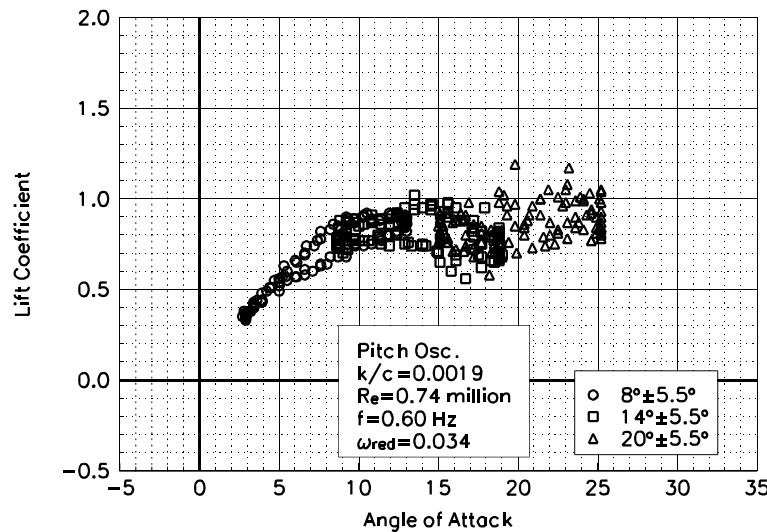


Figure C10. Lift coefficient vs α .

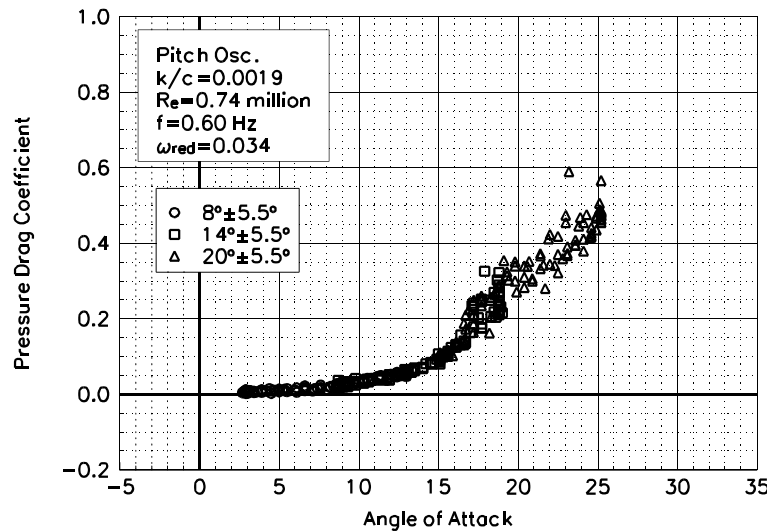


Figure C11. Pressure drag coefficient vs α .

S809
LEGR
 $Re = 0.74$ million
 $\omega_{red} = 0.034$

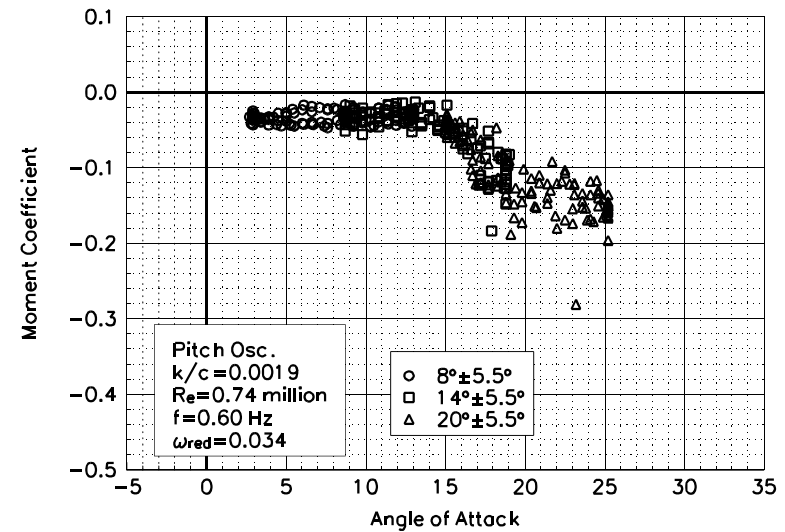


Figure C12. Moment coefficient vs α .

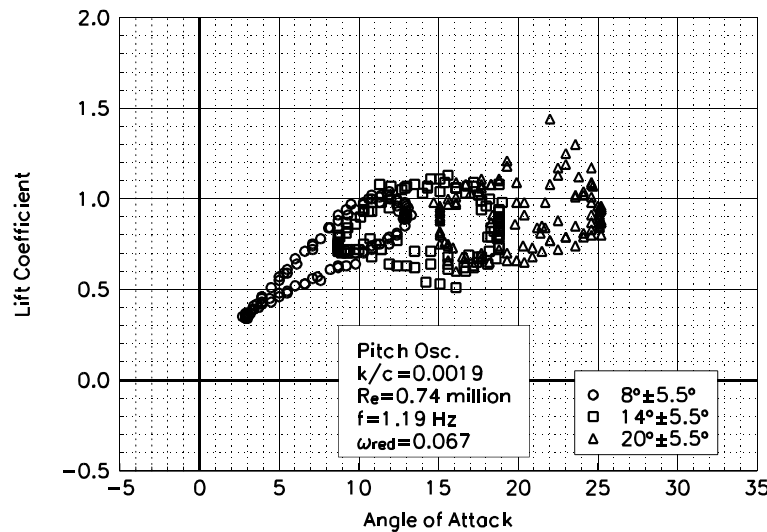


Figure C13. Lift coefficient vs α .

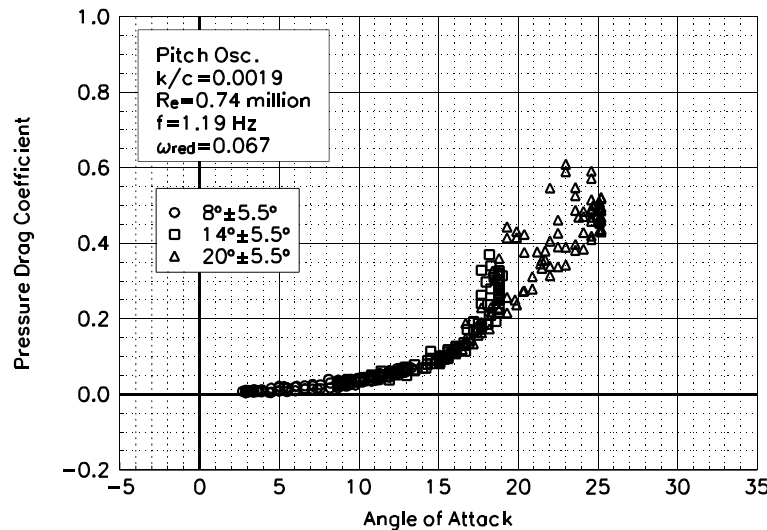


Figure C14. Pressure drag coefficient vs α .

S809
LEGR
 $Re = 0.74$ million
 $\omega_{red} = 0.067$

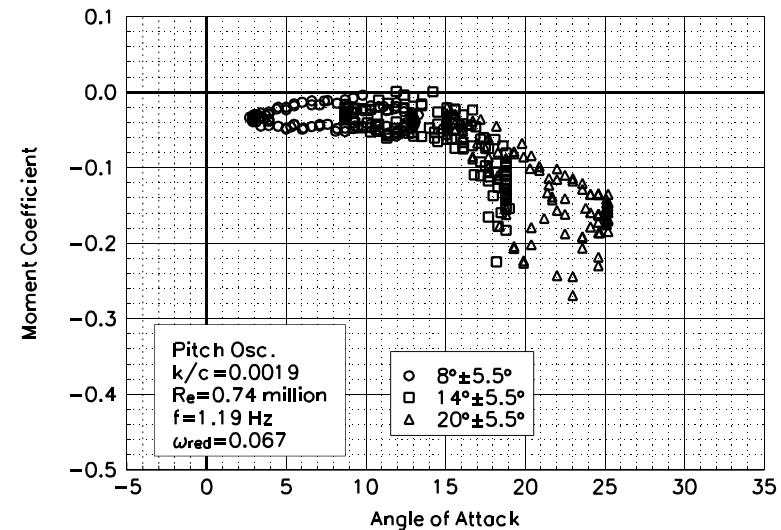


Figure C15. Moment coefficient vs α .

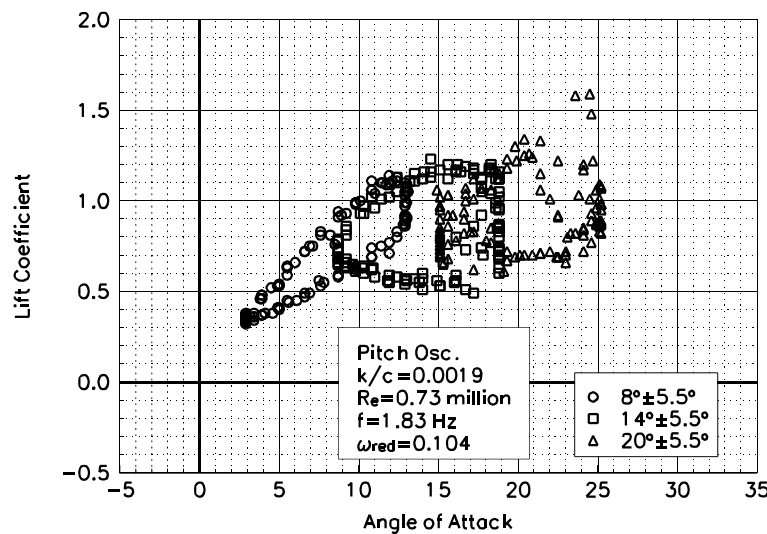


Figure C16. Lift coefficient vs α .

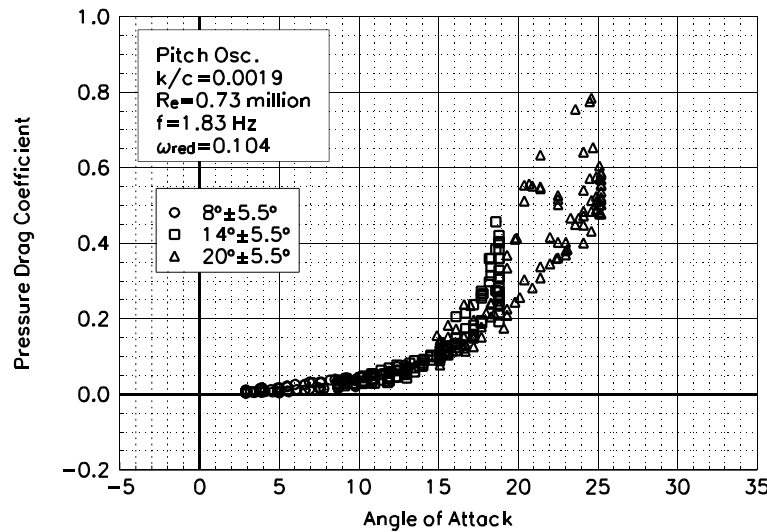


Figure C17. Pressure drag coefficient vs α .

S809
LEGR
Re=0.73 million
 $\omega_{\text{reduced}} = 0.104$

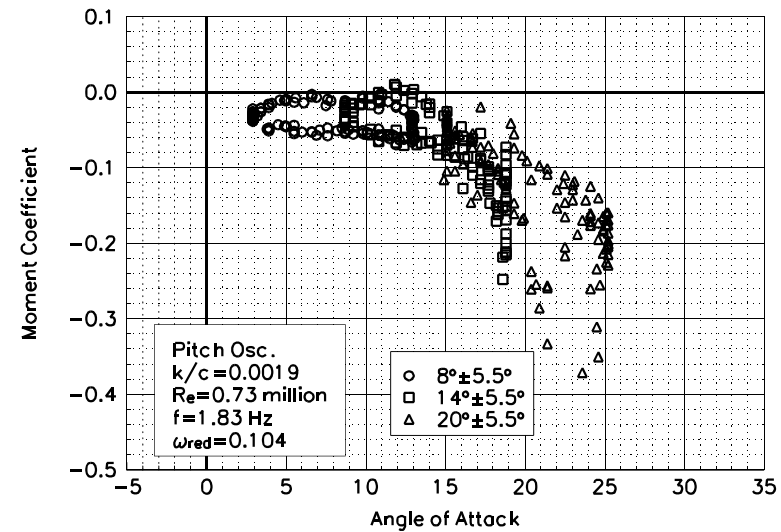


Figure C18. Moment coefficient vs α .

Unsteady Airfoil Characteristics

$\pm 5.5^\circ$ Sine, $Re = 1$ million

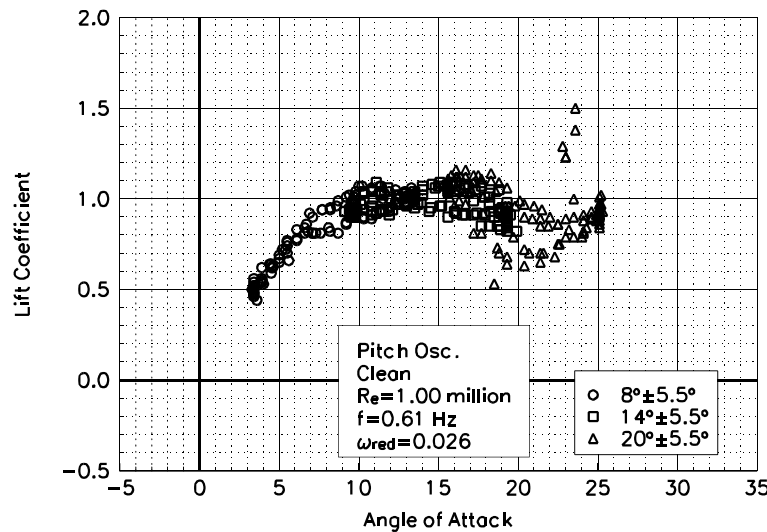


Figure C19. Lift coefficient vs α .

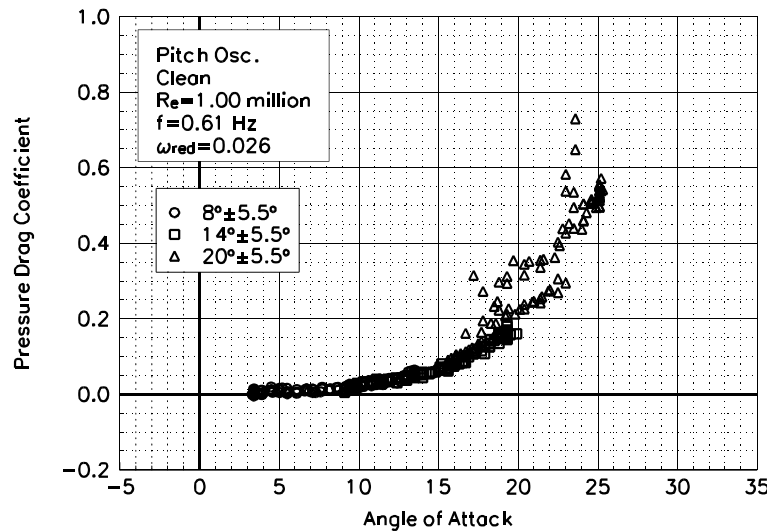


Figure C20. Pressure drag coefficient vs α .

S809
Clean
 $Re=1.00 \text{ million}$
 $\omega_{\text{reduced}}=0.026$

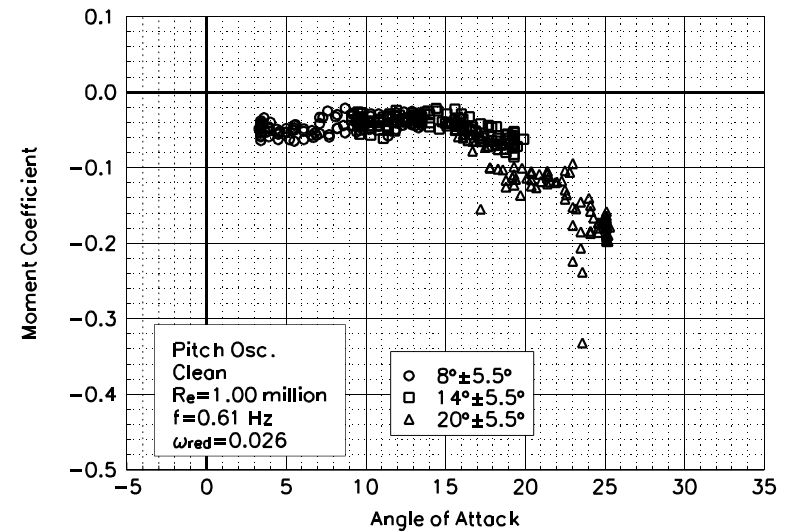
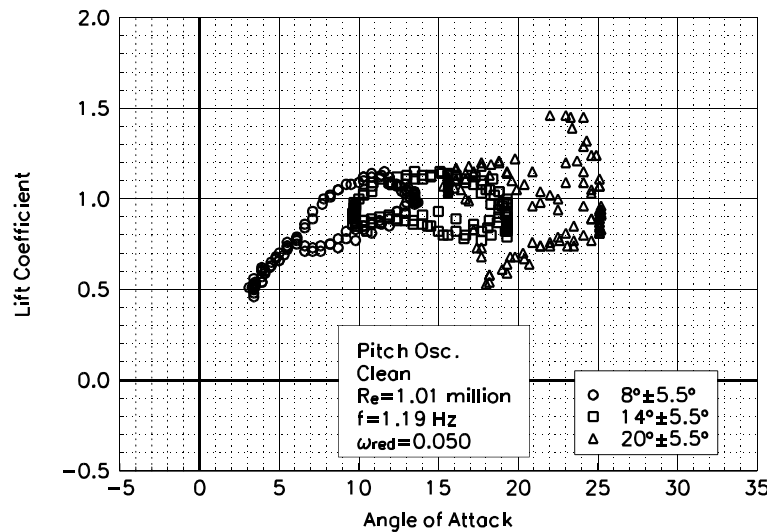


Figure C21. Moment coefficient vs α .



S809
Clean
 $Re=1.01$ million
 $\omega_{reduced}=0.050$

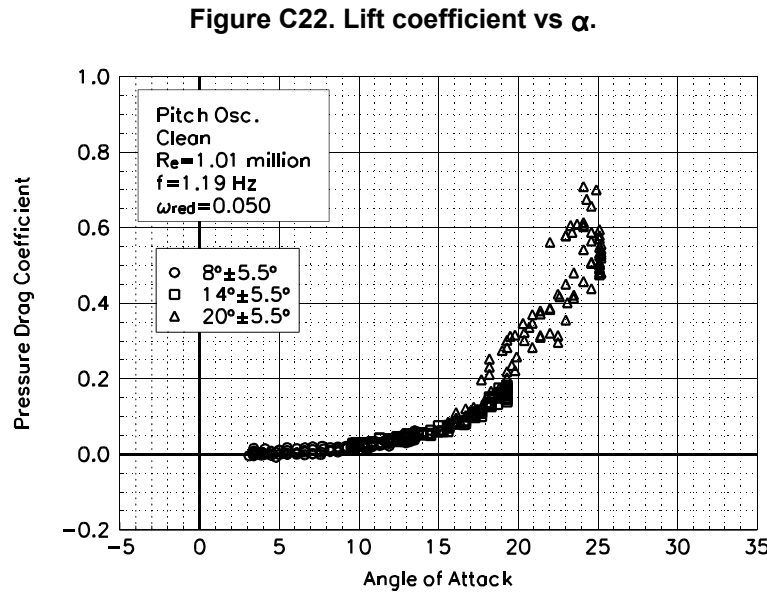


Figure C23. Pressure drag coefficient vs α .

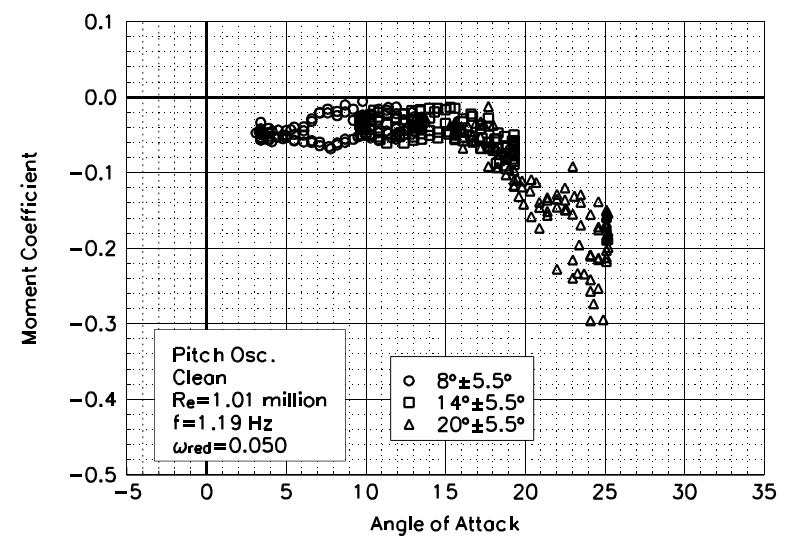


Figure C24. Moment coefficient vs α .

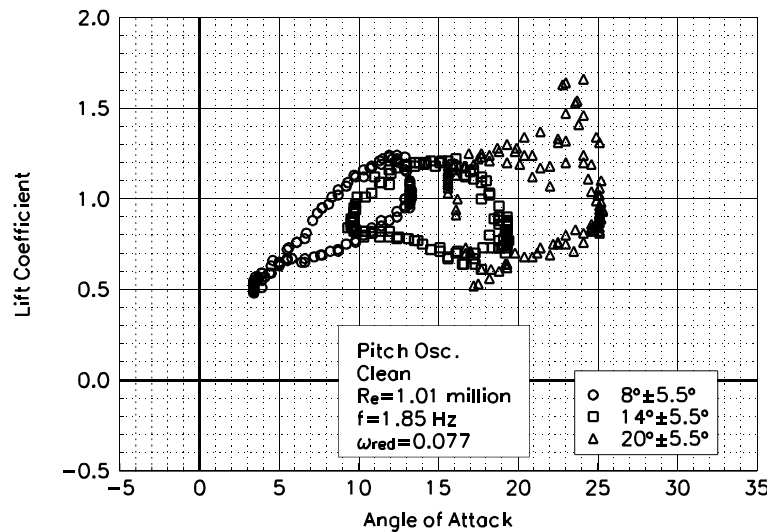


Figure C25. Lift coefficient vs α .

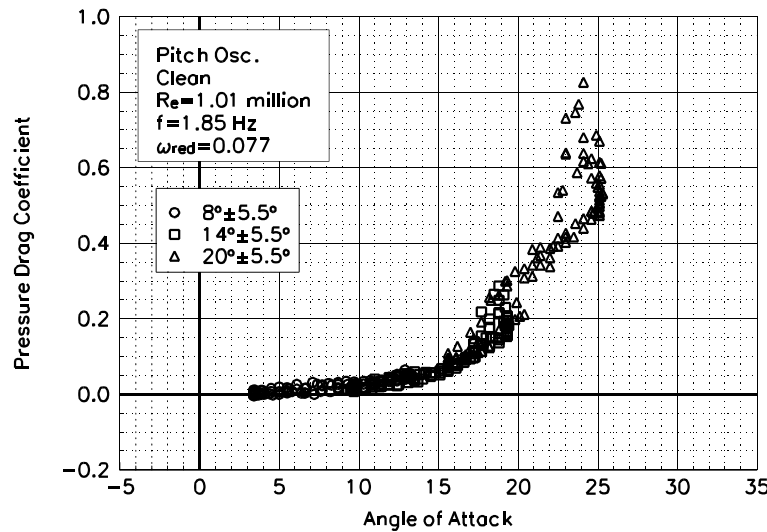


Figure C26. Pressure drag coefficient vs α .

S809
Clean
 $Re=1.01$ million
 $\omega_{reduced}=0.077$

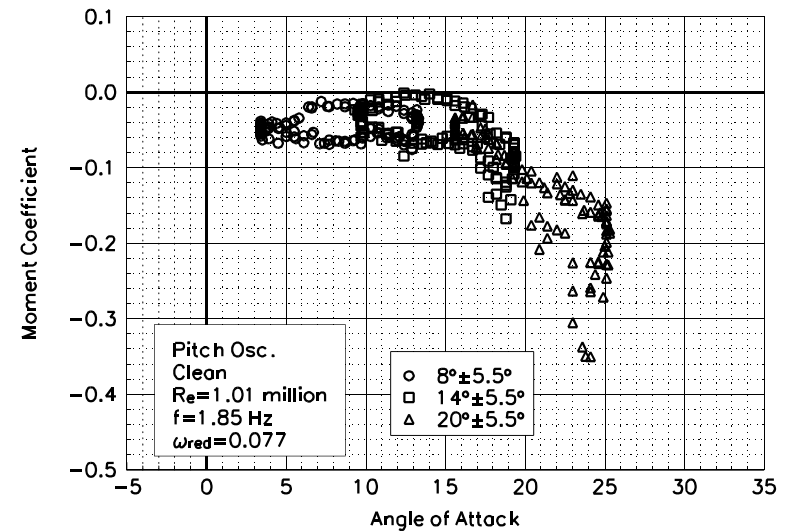


Figure C27. Moment coefficient vs α .

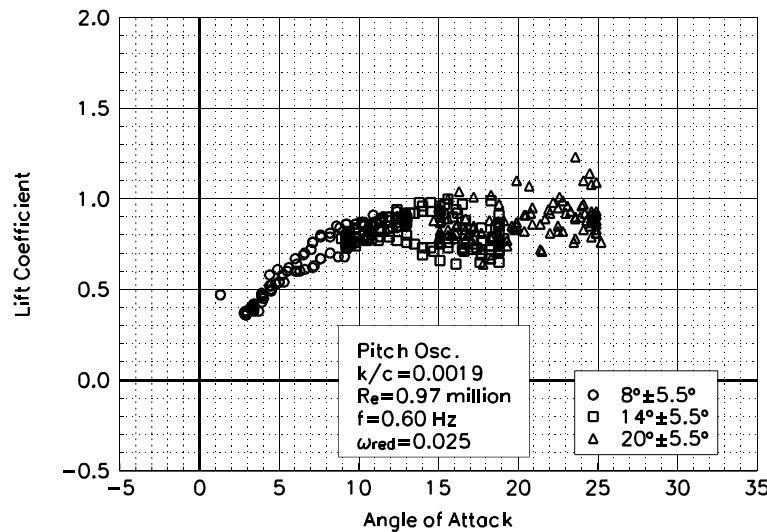


Figure C28. Lift coefficient vs α .

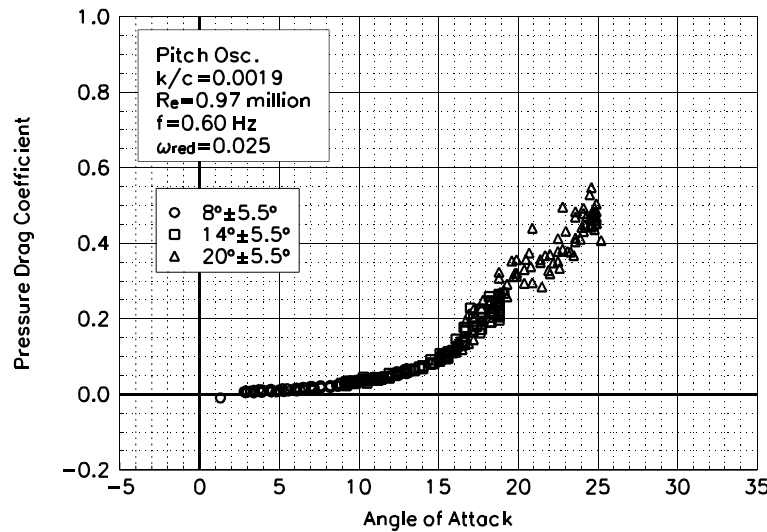


Figure C29. Pressure drag coefficient vs α .

S809
LEGR
 $Re = 0.97 \text{ million}$
 $\omega_{\text{reduced}} = 0.025$

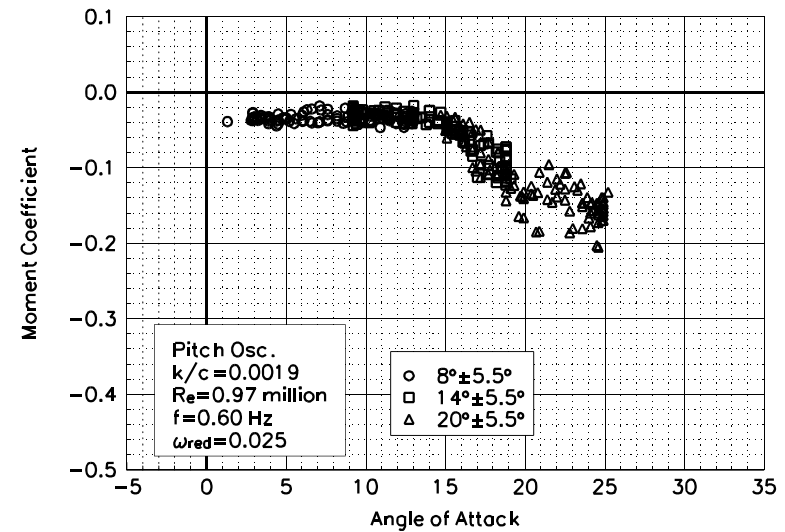


Figure C30. Moment coefficient vs α .

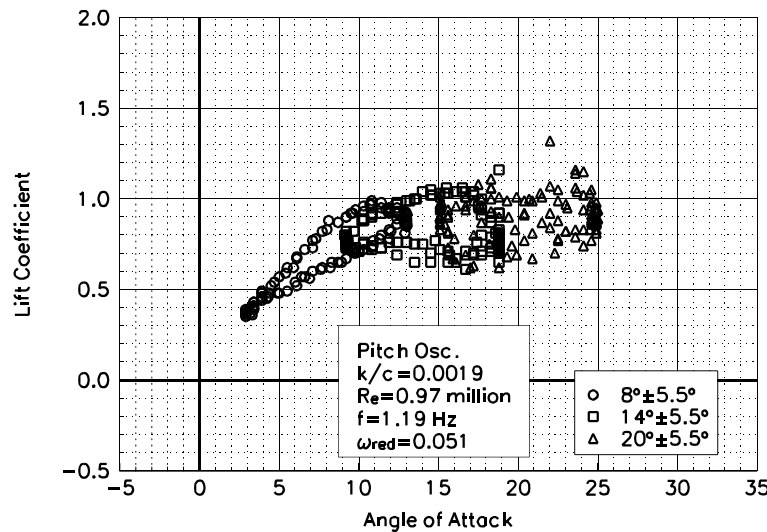


Figure C31. Lift coefficient vs α .

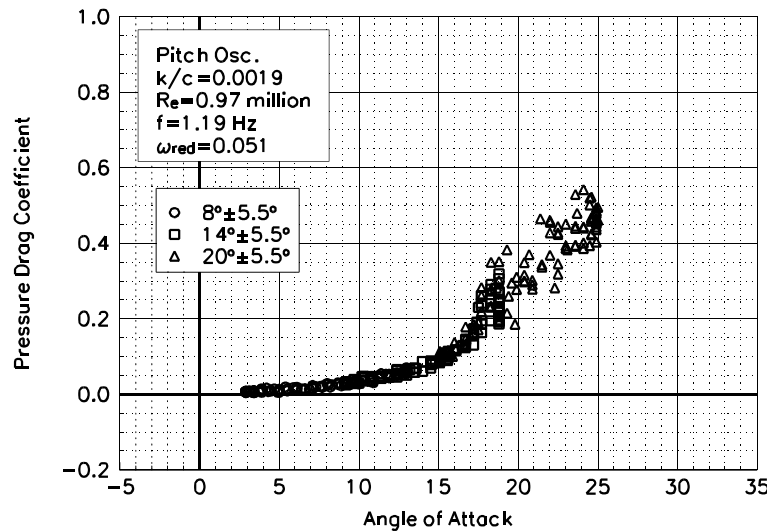


Figure C32. Pressure drag coefficient vs α .

S809
LEGR
 $Re = 0.97$ million
 $\omega_{red} = 0.051$

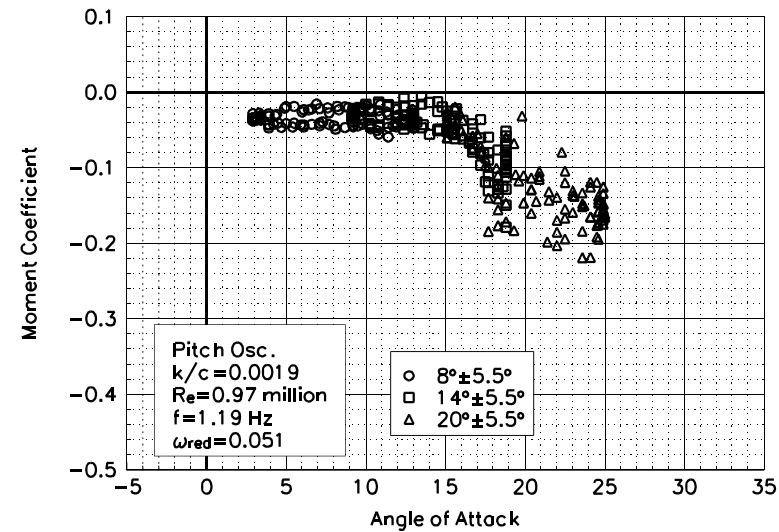


Figure C33. Moment coefficient vs α .

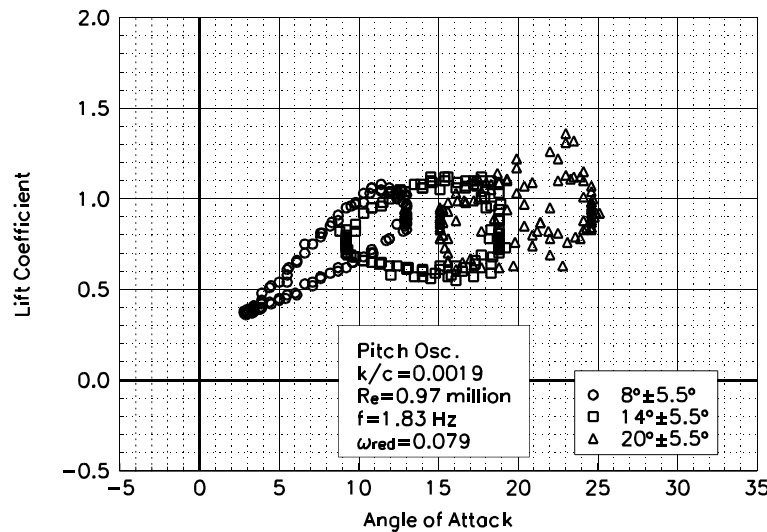


Figure C34. Lift coefficient vs α .

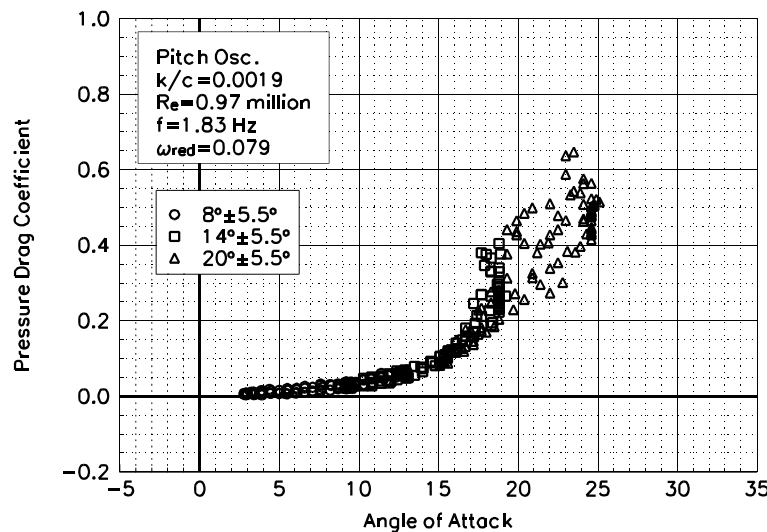


Figure C35. Pressure drag coefficient vs α .

S809
LEGR
Re=0.97 million
 $\omega_{\text{reduced}} = 0.079$

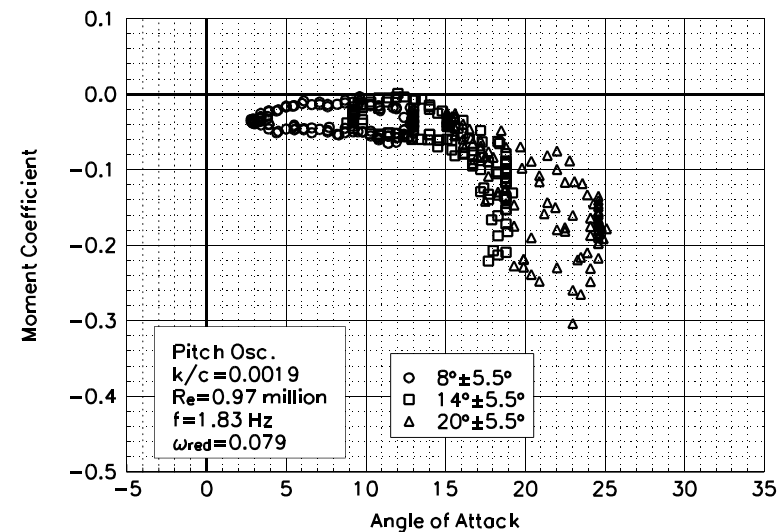


Figure C36. Moment coefficient vs α .

Unsteady Airfoil Characteristics

$\pm 5.5^\circ$ Sine, Re= 1.25 million

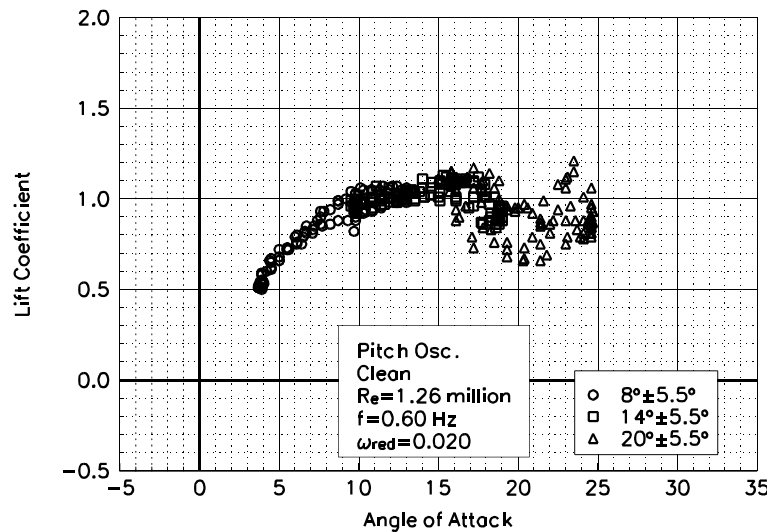


Figure C37. Lift coefficient vs α .

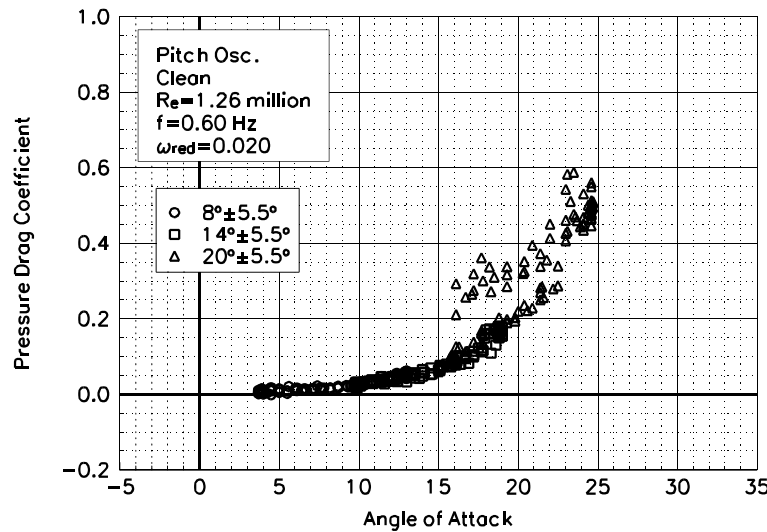


Figure C38. Pressure drag coefficient vs α .

S809
Clean
 $Re=1.26$ million
 $\omega_{reduced}=0.020$

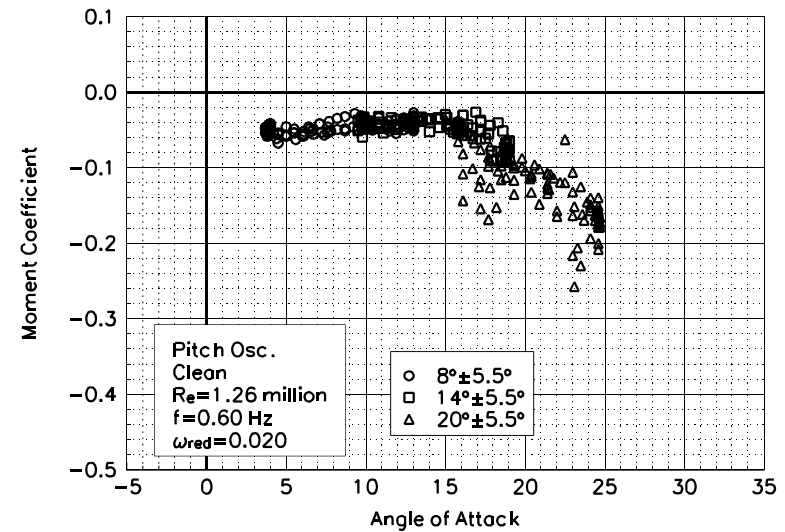


Figure C39. Moment coefficient vs α .

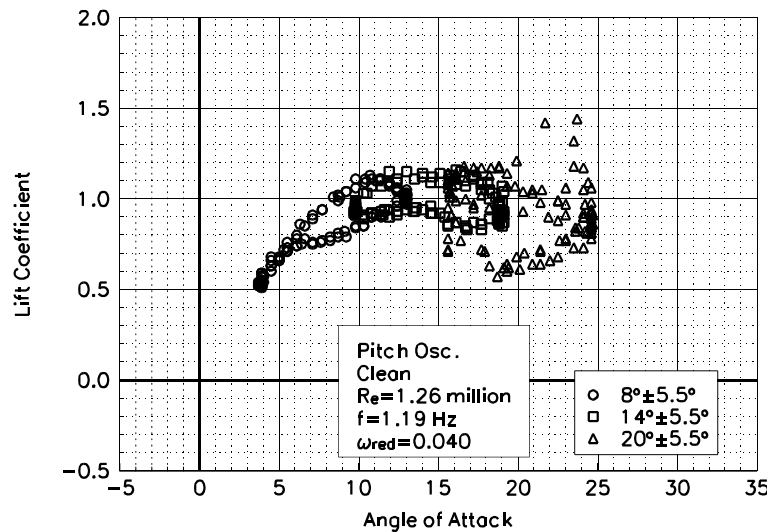


Figure C40. Lift coefficient vs α .

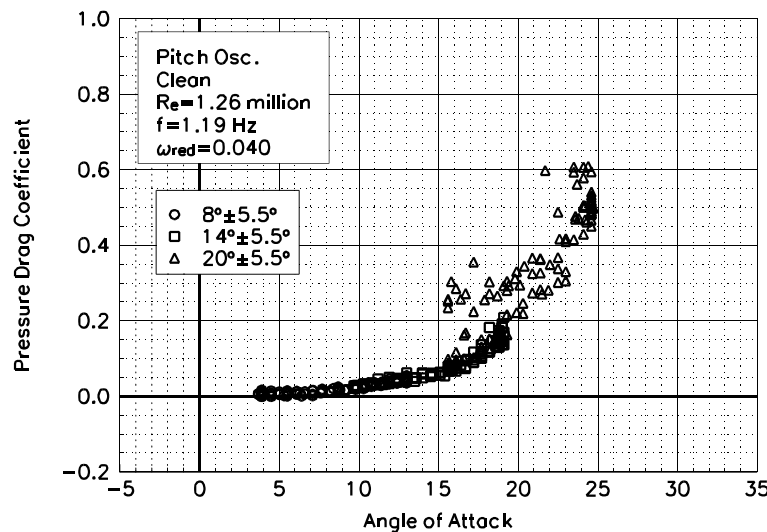


Figure C41. Pressure drag coefficient vs α .

S809
Clean
 $Re=1.26$ million
 $\omega_{\text{reduced}}=0.040$

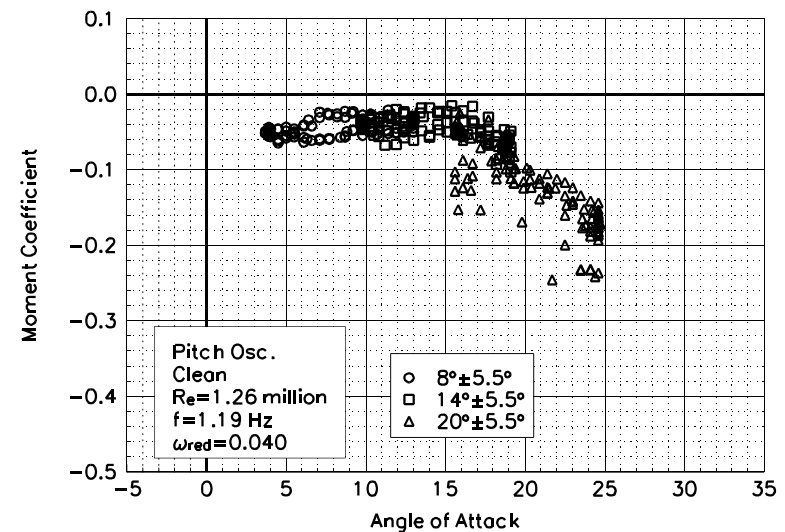


Figure C42. Moment coefficient vs α .

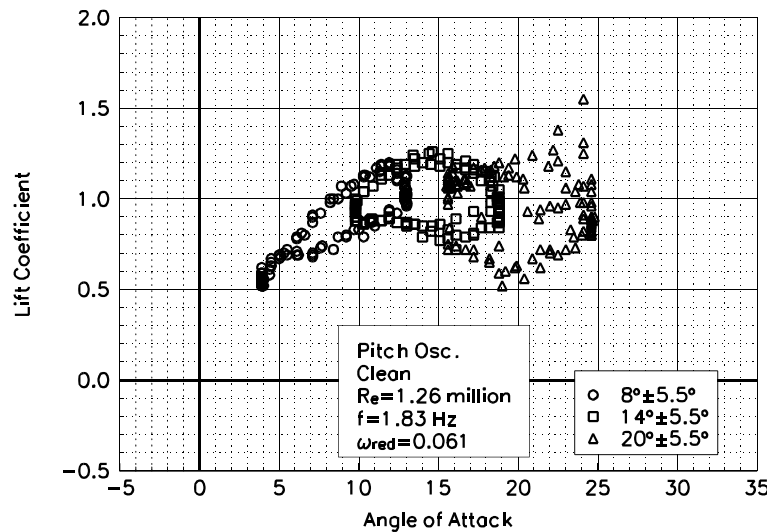


Figure C43. Lift coefficient vs α .

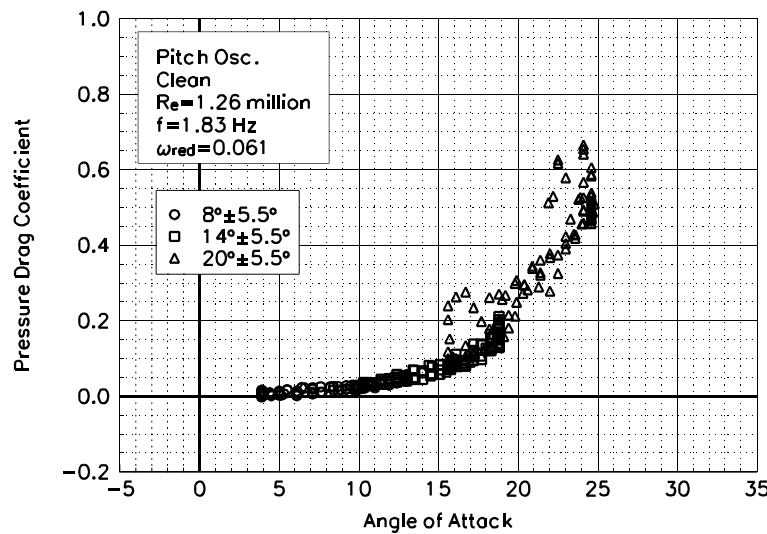


Figure C44. Pressure drag coefficient vs α .

S809
Clean
 $Re=1.26$ million
 $\omega_{\text{reduced}}=0.061$

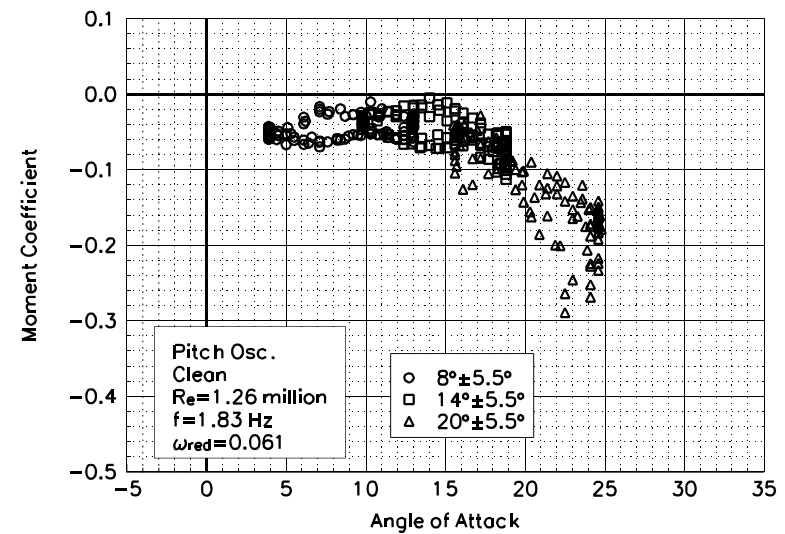


Figure C45. Moment coefficient vs α .

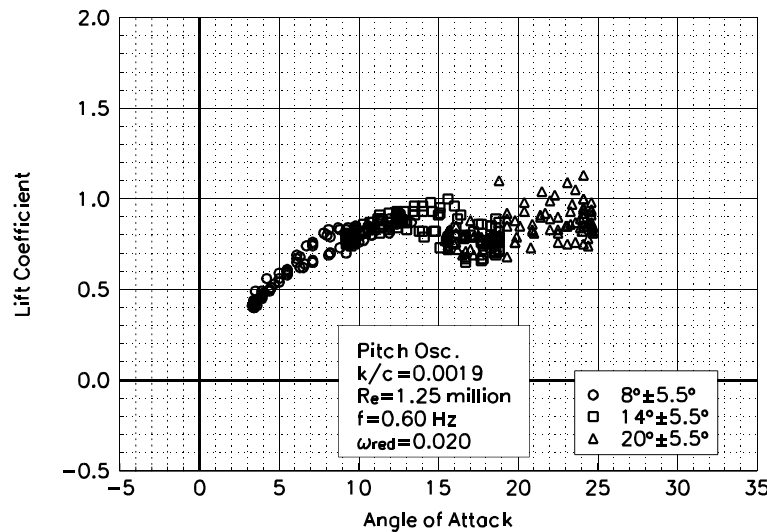


Figure C46. Lift coefficient vs α .

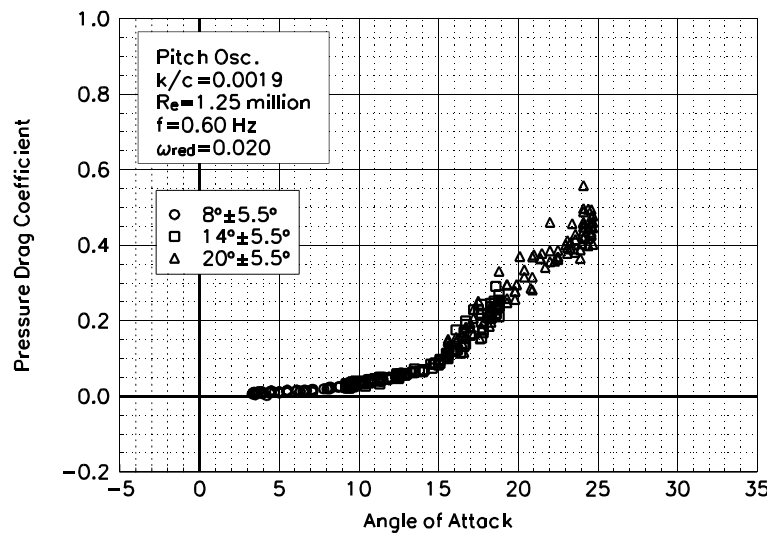


Figure C47. Pressure drag coefficient vs α .

S809
LEGR
 $Re = 1.25 \text{ million}$
 $\omega_{\text{reduced}} = 0.020$

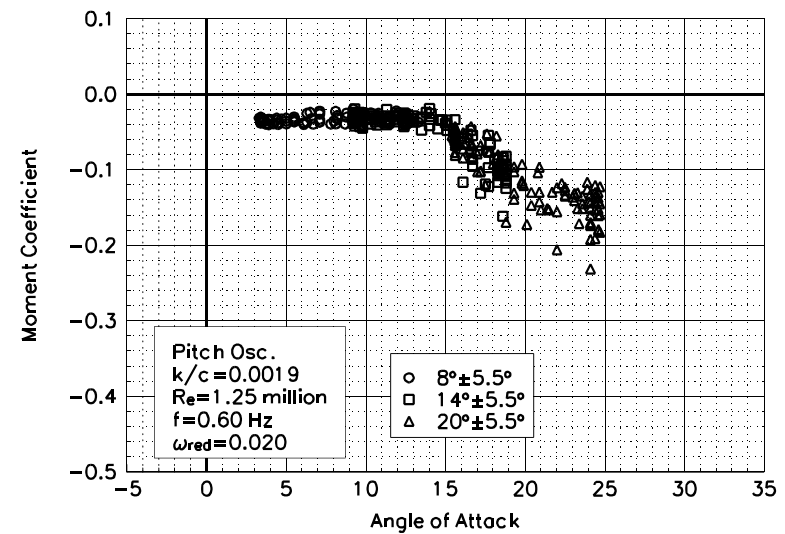
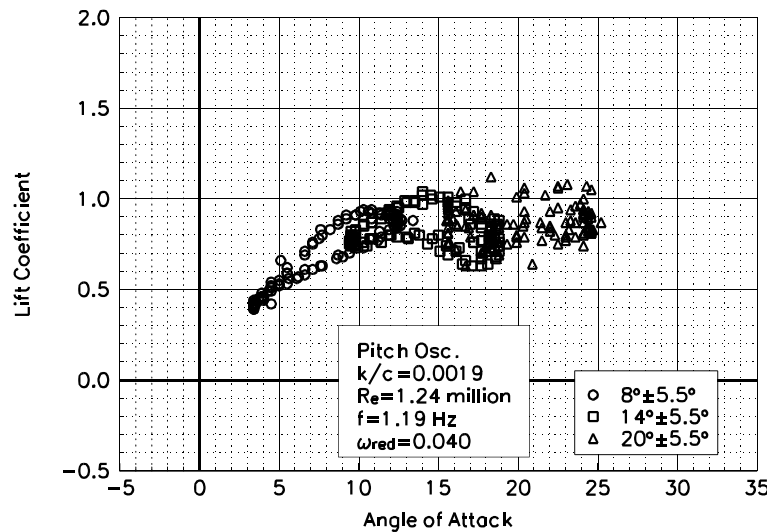


Figure C48. Moment coefficient vs α .



**S809
LEGR
 $Re = 1.24 \text{ million}$
 $\omega_{\text{reduced}} = 0.040$**

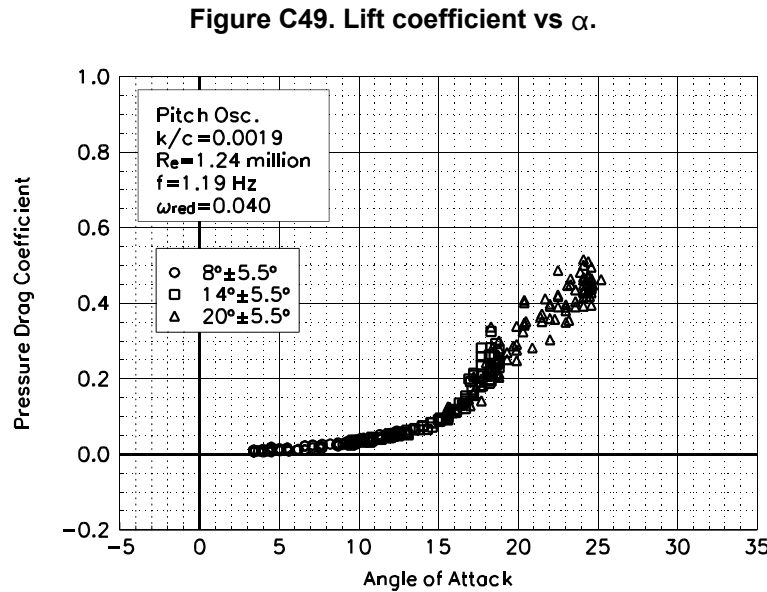


Figure C49. Lift coefficient vs α .

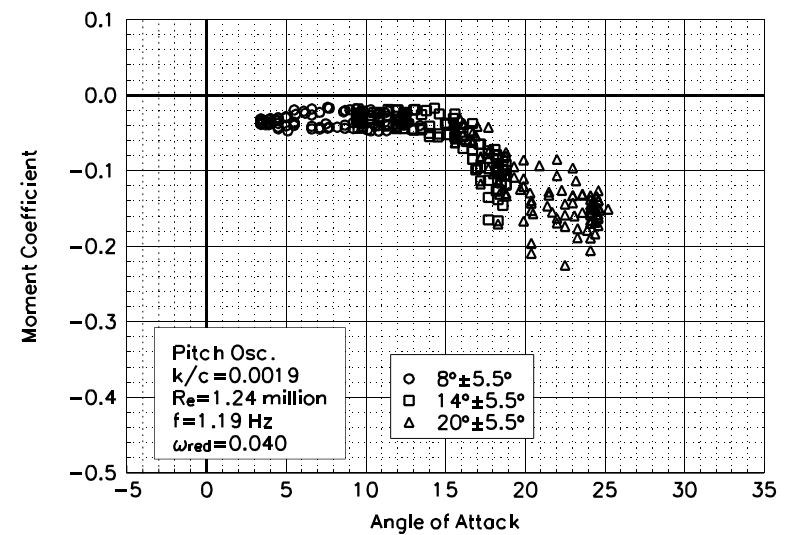


Figure C51. Moment coefficient vs α .

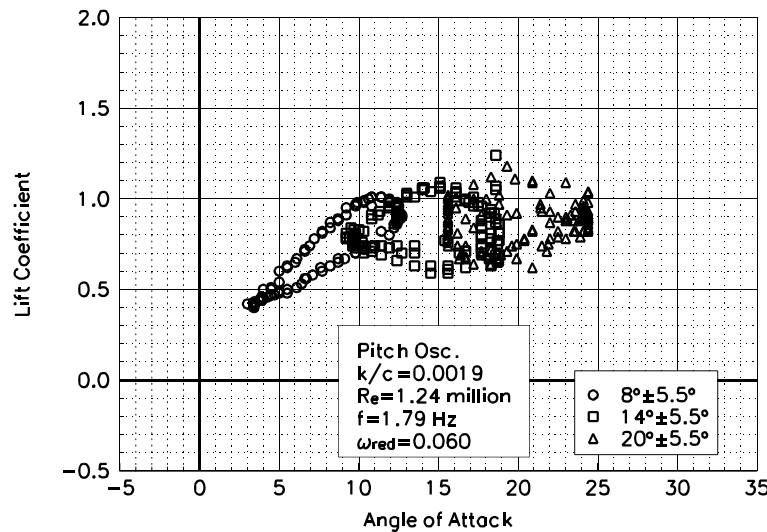


Figure C52. Lift coefficient vs α .

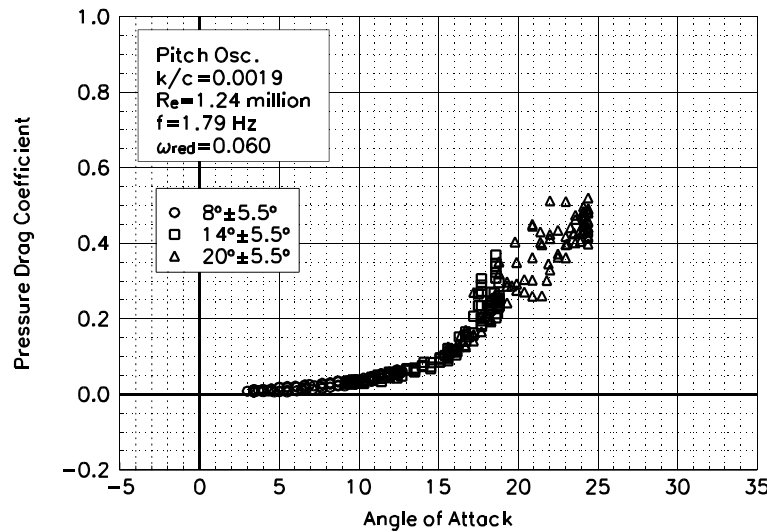


Figure C53. Pressure drag coefficient vs α .

S809
LEGR
 $Re = 1.24$ million
 $\omega_{red} = 0.060$

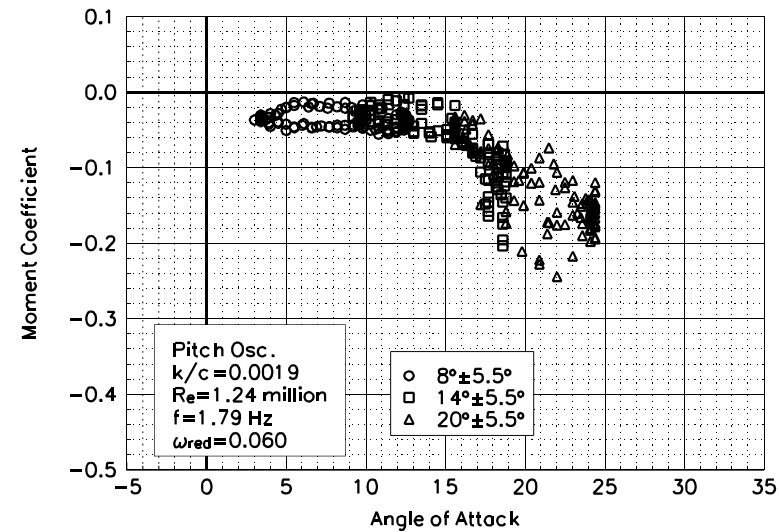


Figure C54. Moment coefficient vs α .

Unsteady Airfoil Characteristics

$\pm 5.5^\circ$ Sine, $Re = 1.4$ million

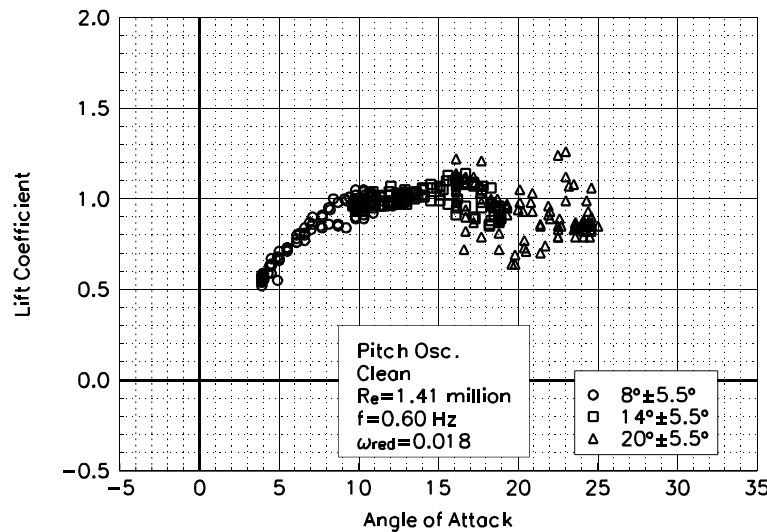


Figure C55. Lift coefficient vs α .

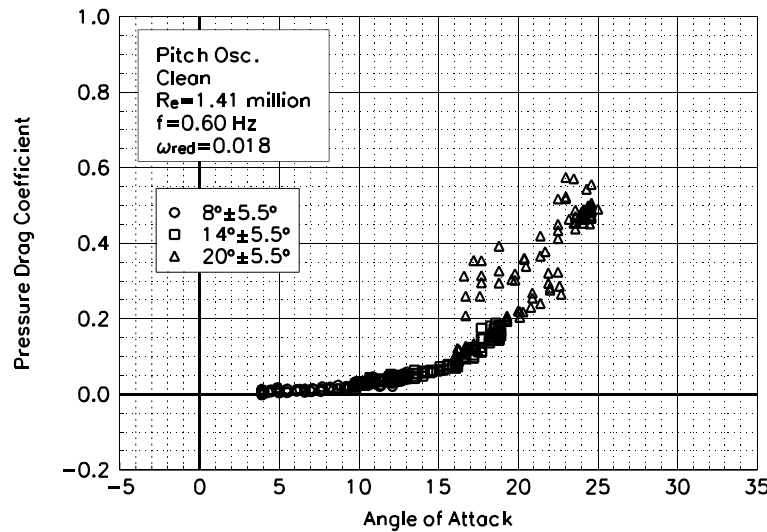


Figure C56. Pressure drag coefficient vs α .

S809
Clean
 $Re=1.41$ million
 $\omega_{reduced}=0.018$

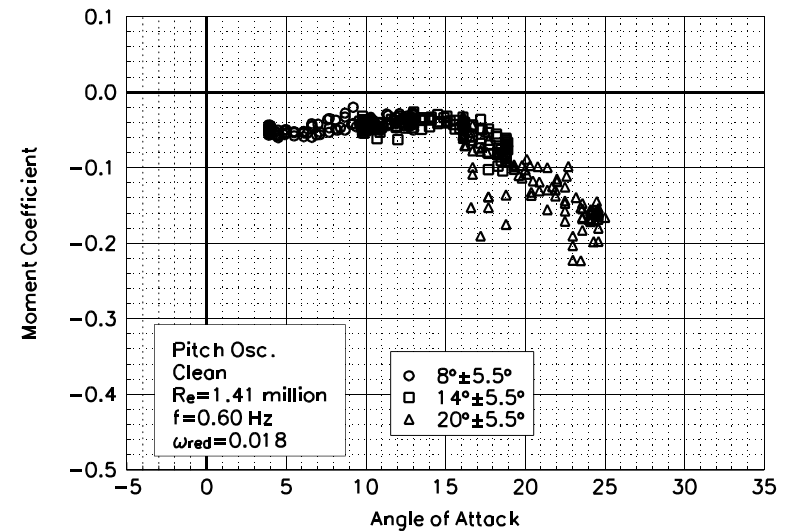


Figure C57. Moment coefficient vs α .

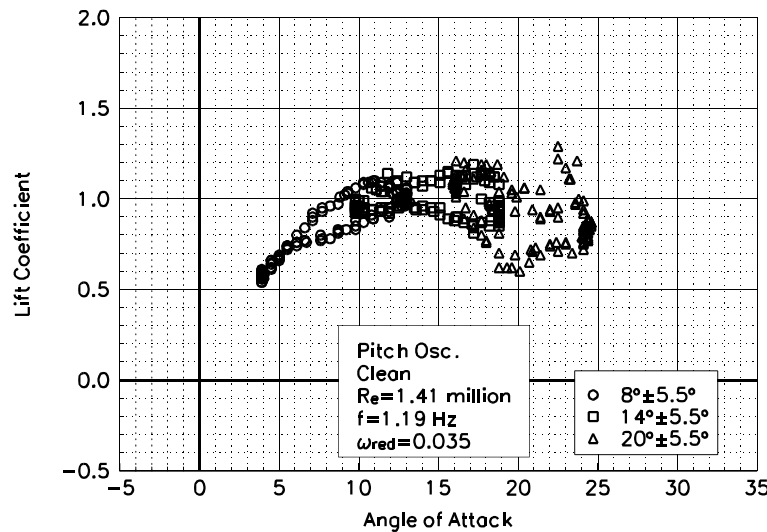


Figure C58. Lift coefficient vs α .

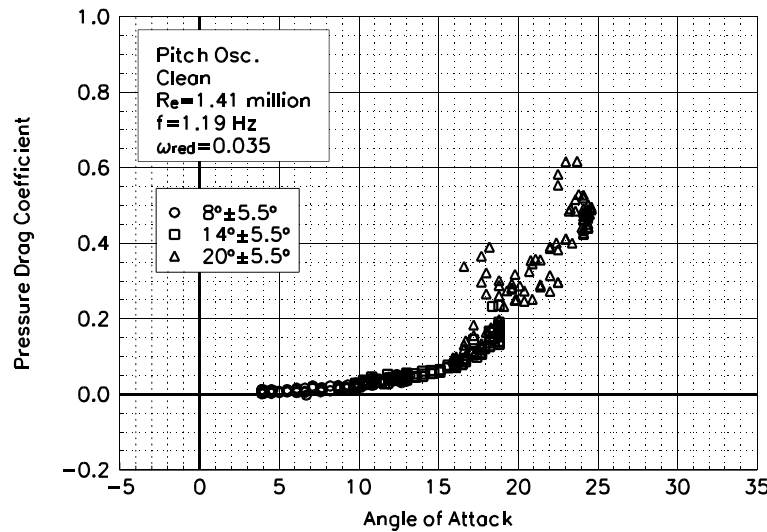


Figure C59. Pressure drag coefficient vs α .

S809
Clean
 $Re=1.41$ million
 $\omega_{reduced}=0.035$

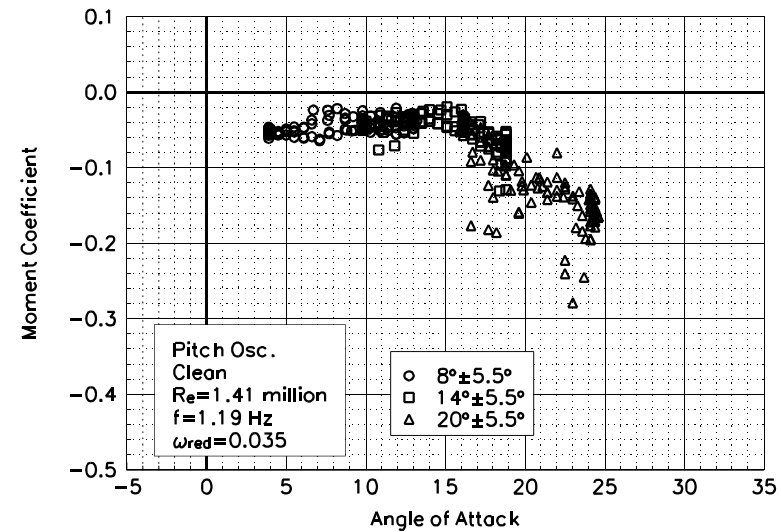


Figure C60. Moment coefficient vs α .

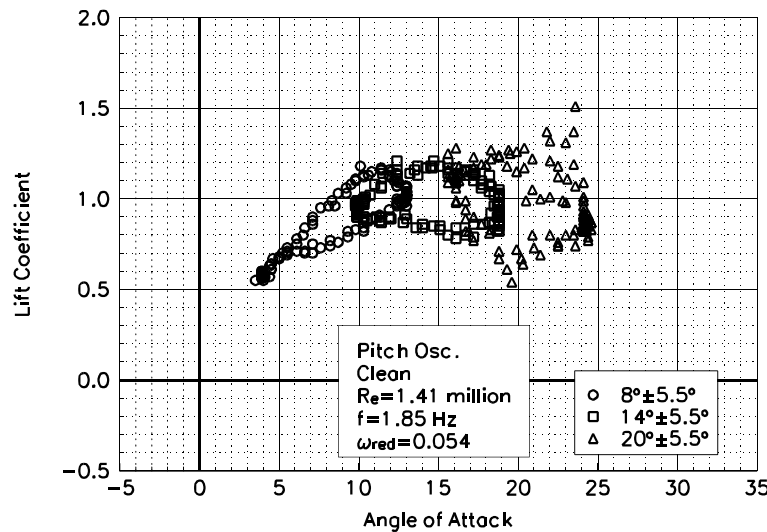


Figure C61. Lift coefficient vs α .

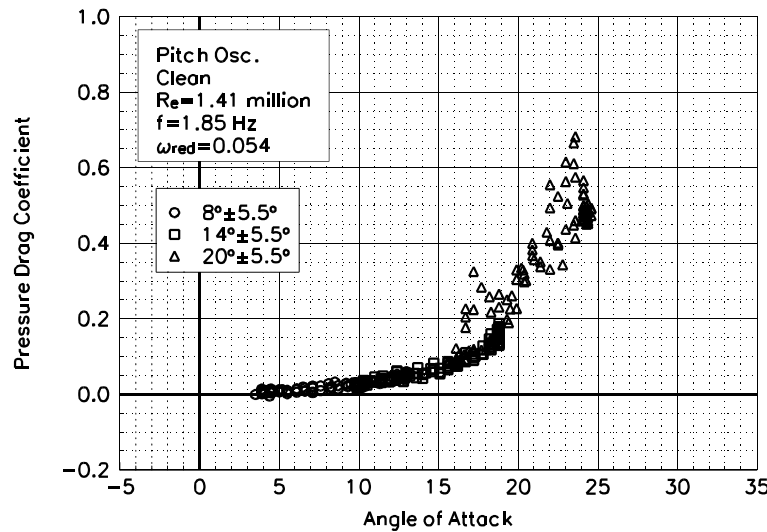


Figure C62. Pressure drag coefficient vs α .

S809
Clean
 $Re=1.41$ million
 $\omega_{reduced}=0.054$

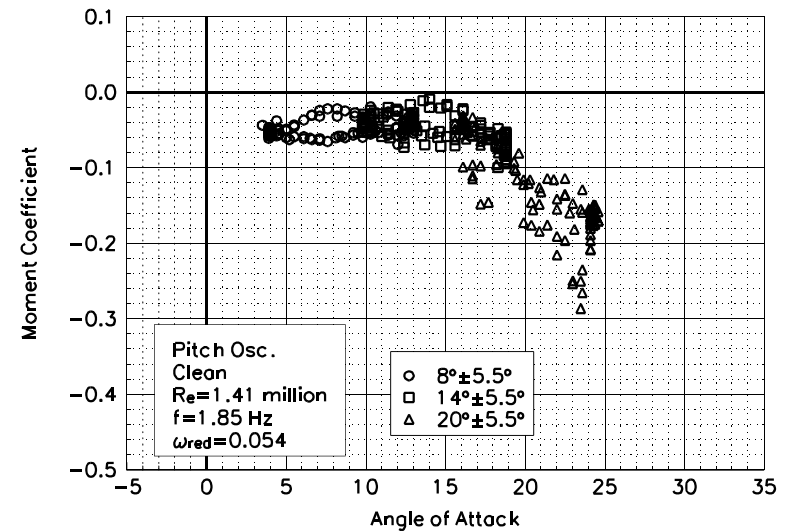


Figure C63. Moment coefficient vs α .

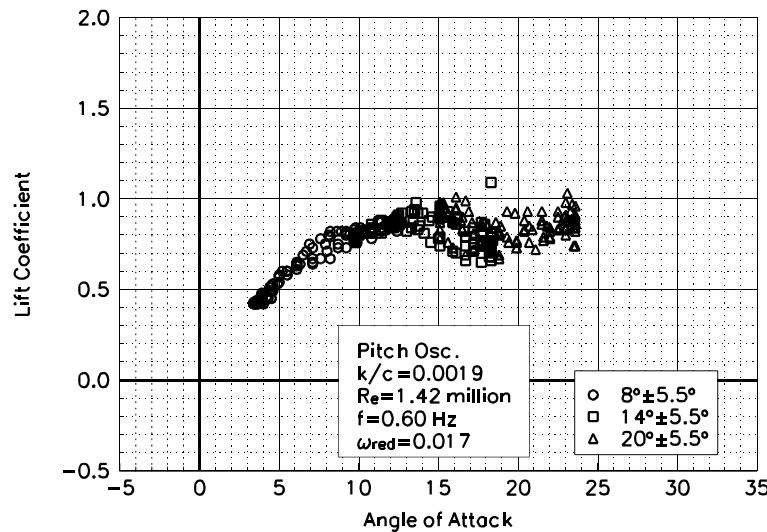


Figure C64. Lift coefficient vs α .

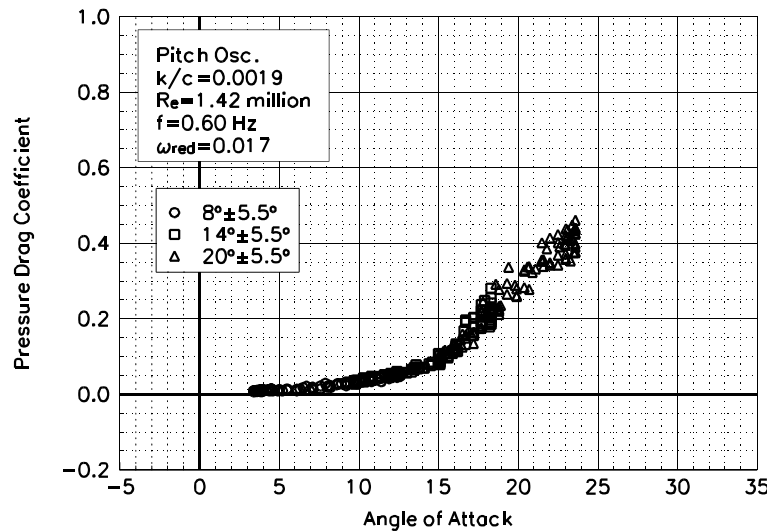


Figure C65. Pressure drag coefficient vs α .

S809
LEGR
 $Re = 1.42$ million
 $\omega_{reduced} = 0.017$

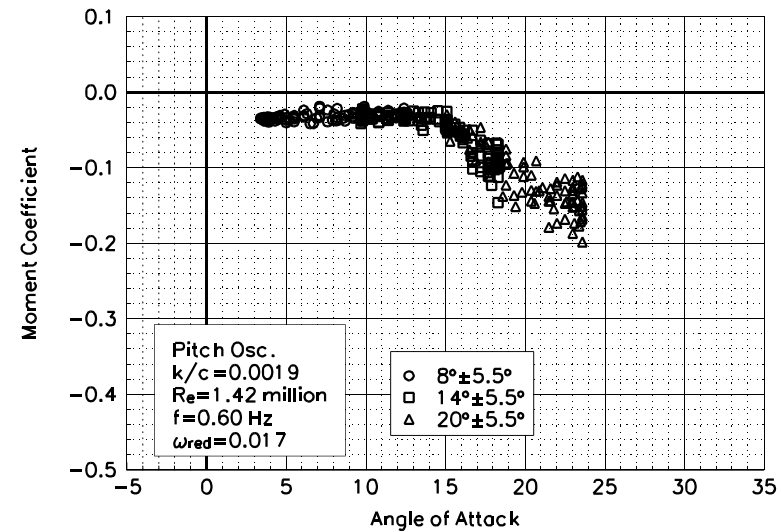


Figure C66. Moment coefficient vs α .

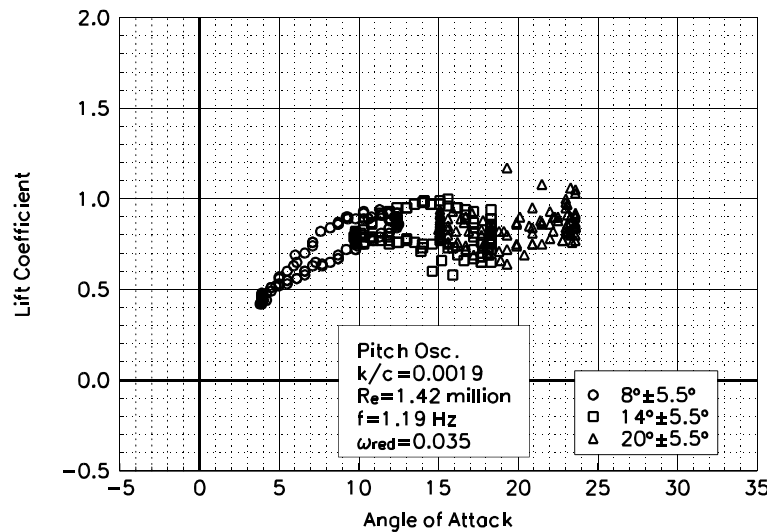


Figure C67. Lift coefficient vs α .

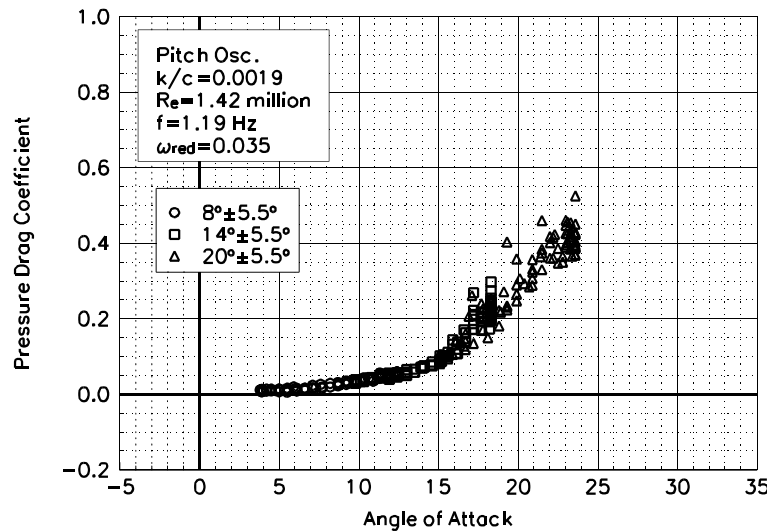


Figure C68. Pressure drag coefficient vs α .

S809
LEGR
 $Re = 1.42$ million
 $\omega_{reduced} = 0.035$

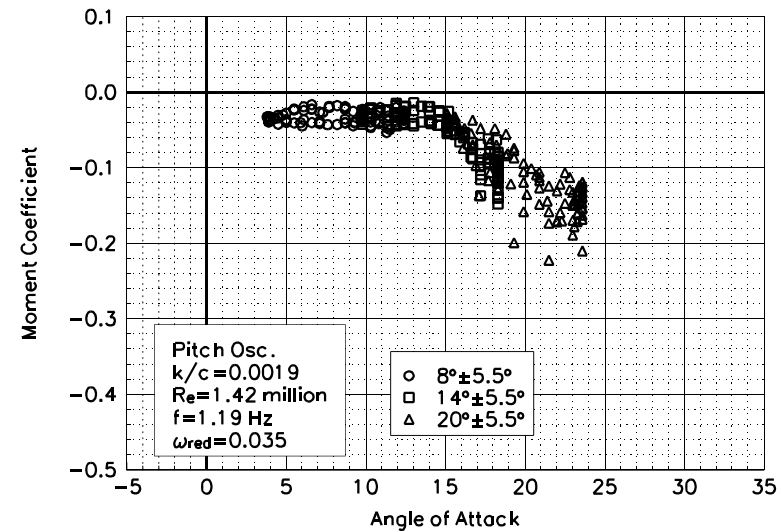


Figure C69. Moment coefficient vs α .

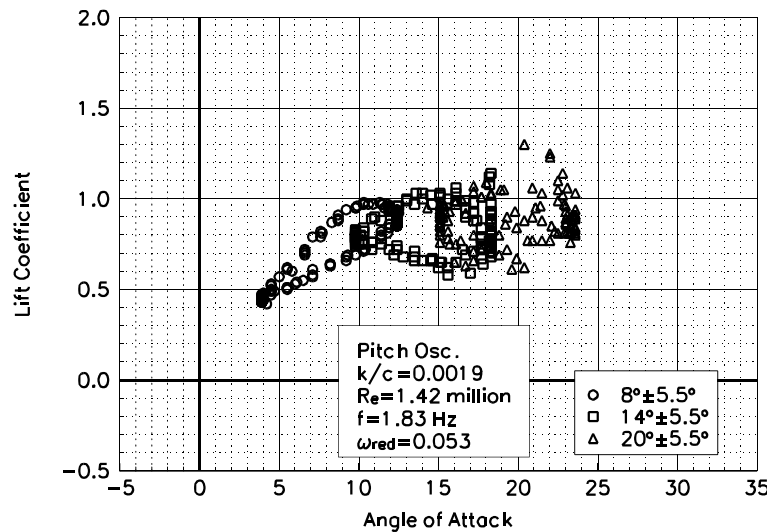


Figure C70. Lift coefficient vs α .

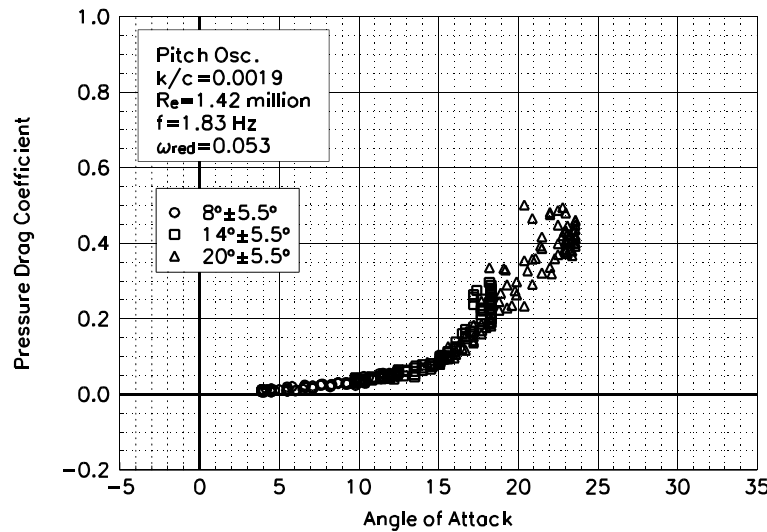


Figure C71. Pressure drag coefficient vs α .

**S809
LEGR
Re=1.42 million
 $\omega_{\text{reduced}} = 0.053$**

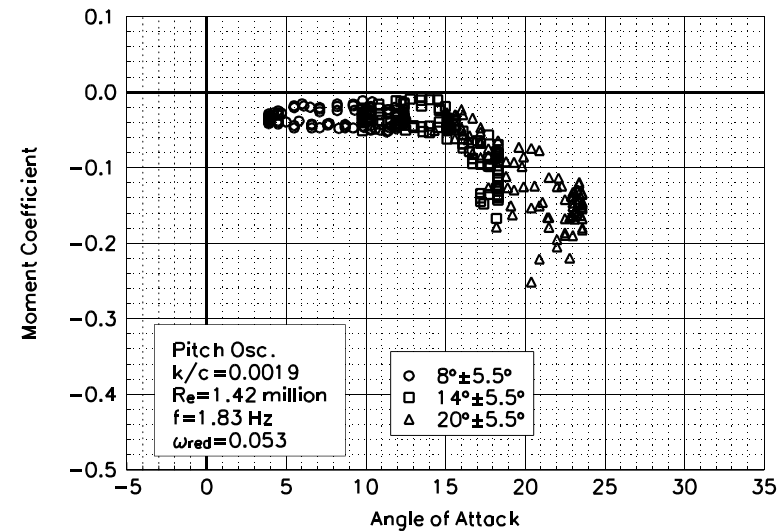


Figure C72. Moment coefficient vs α .

Unsteady Airfoil Characteristics

$\pm 10^\circ$ Sine, $Re = 0.75$ million

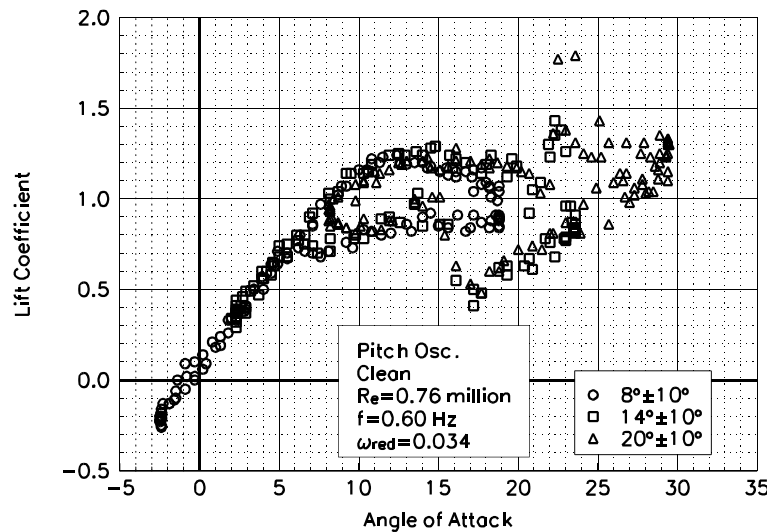


Figure C73. Lift coefficient vs α .

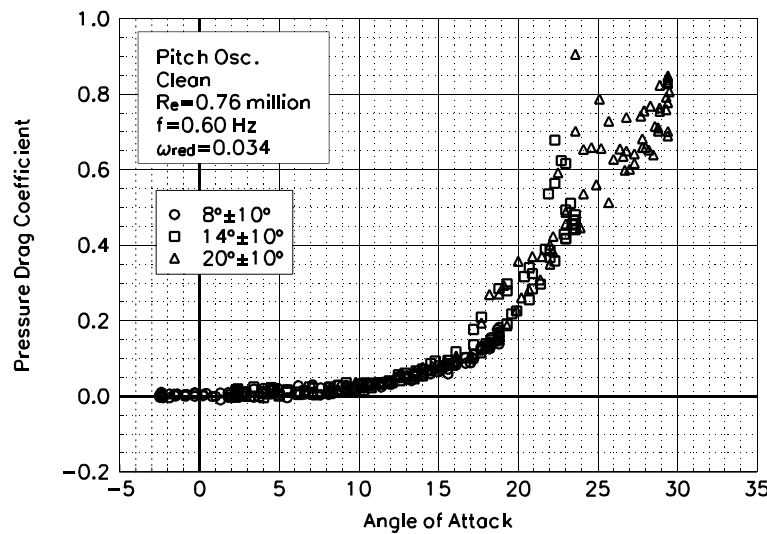


Figure C74. Pressure drag coefficient vs α .

S809
Clean
 $Re=0.76$ million
 $\omega_{red}=0.034$

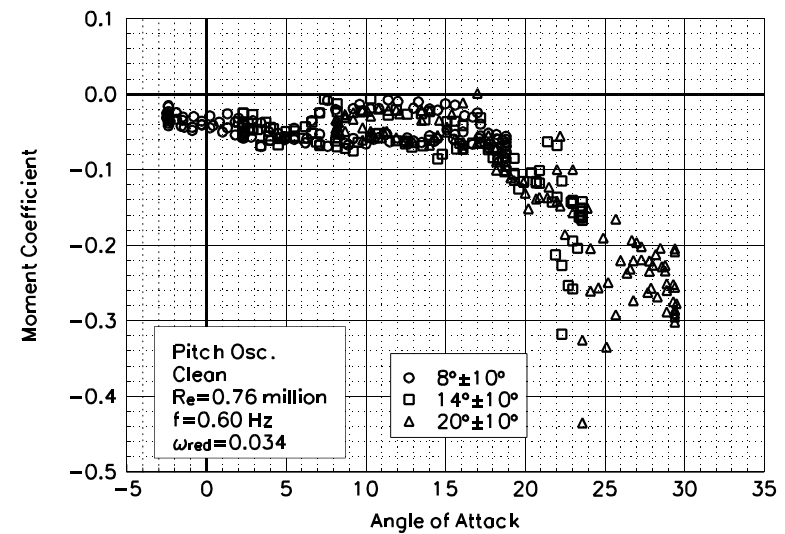


Figure C75. Moment coefficient vs α .

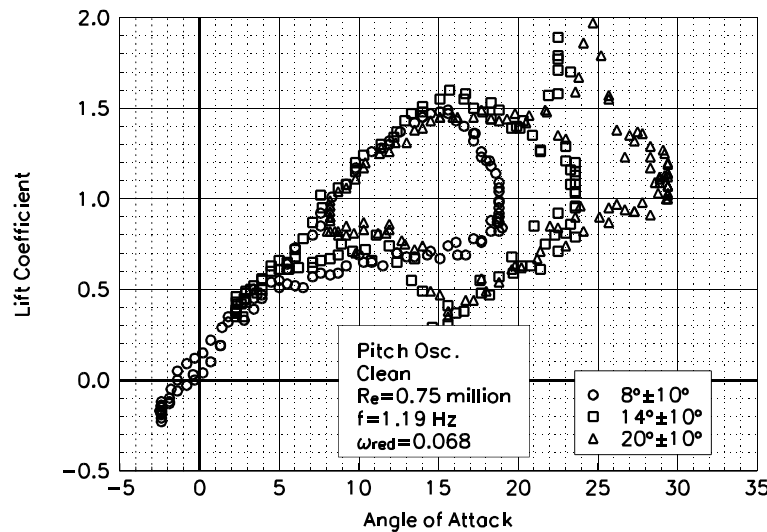


Figure C76. Lift coefficient vs α .

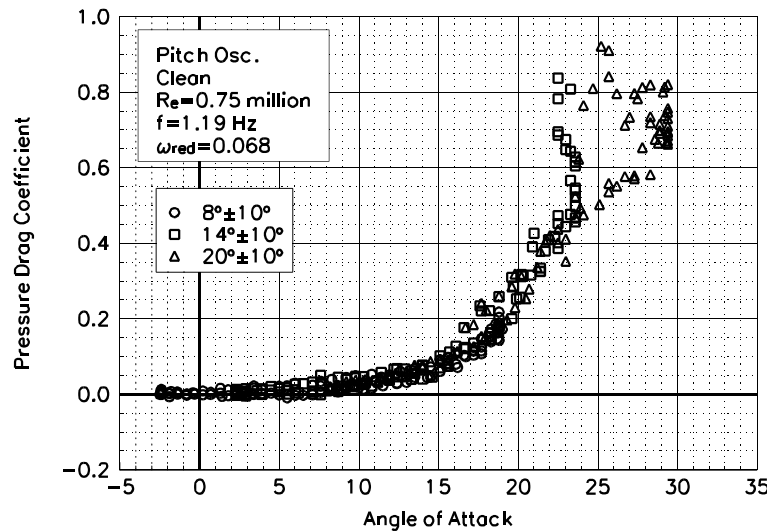


Figure C77. Pressure drag coefficient vs α .

S809
Clean
 $Re=0.75$ million
 $\omega_{red}=0.068$

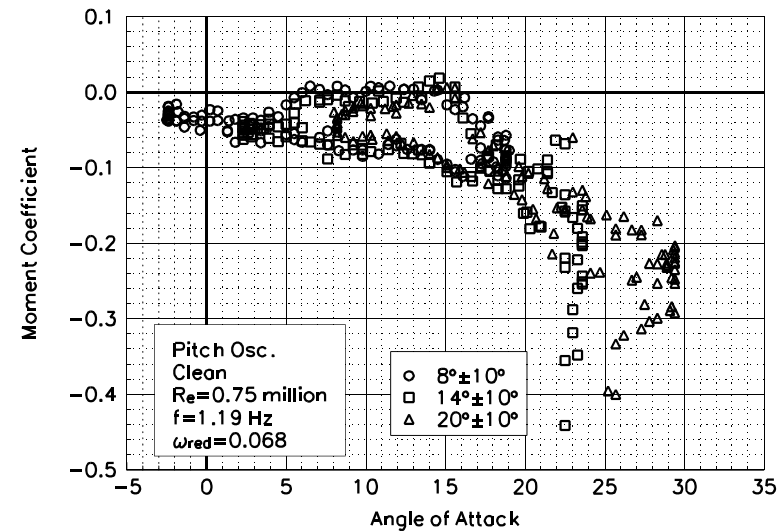


Figure C78. Moment coefficient vs α .

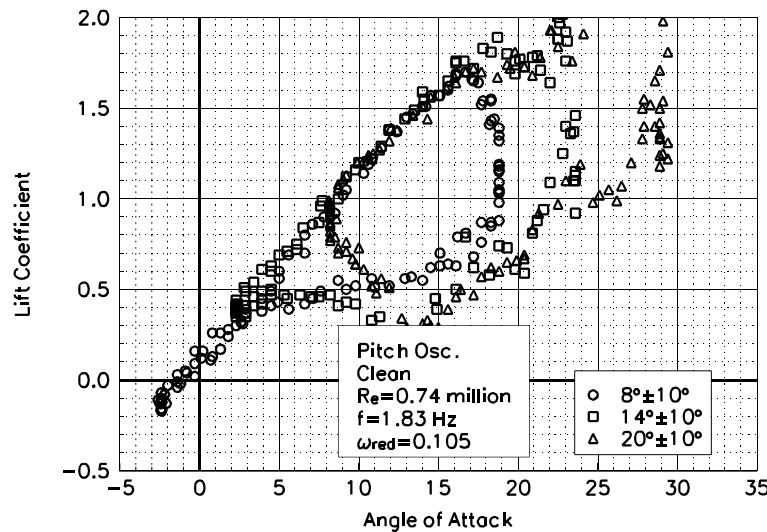


Figure C79. Lift coefficient vs α .

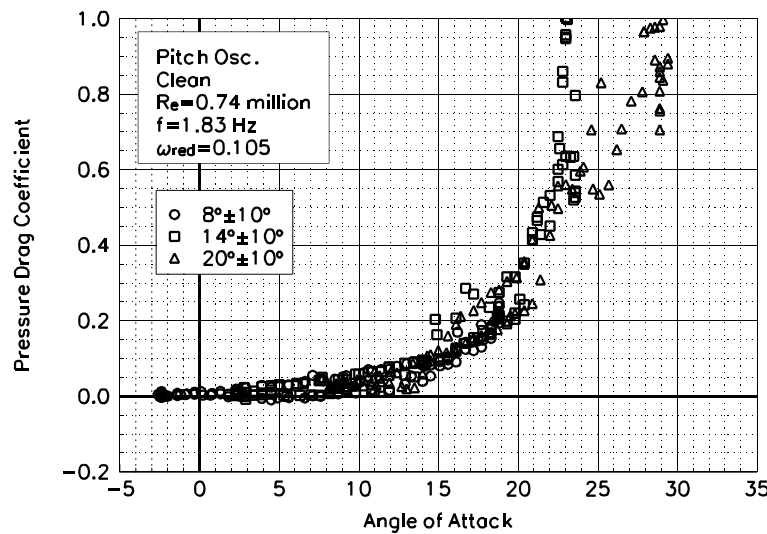


Figure C80. Pressure drag coefficient vs α .

S809
Clean
 $Re=0.74$ million
 $\omega_{red}=0.105$

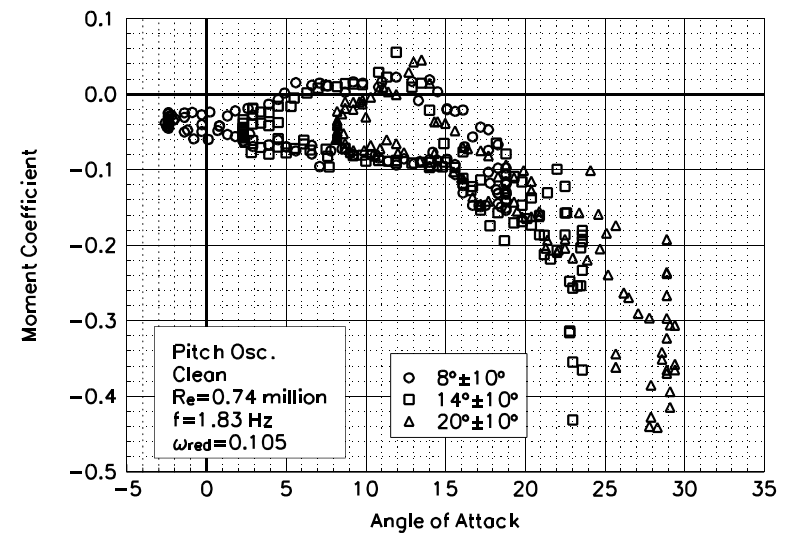


Figure C81. Moment coefficient vs α .

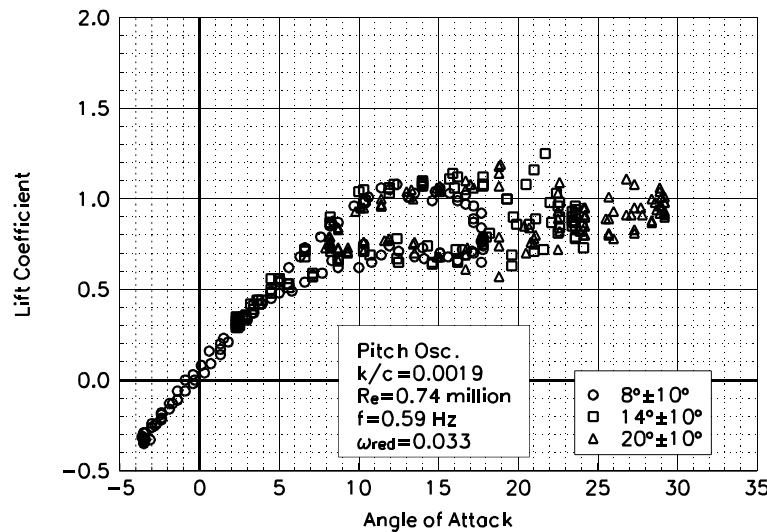


Figure C82. Lift coefficient vs α .

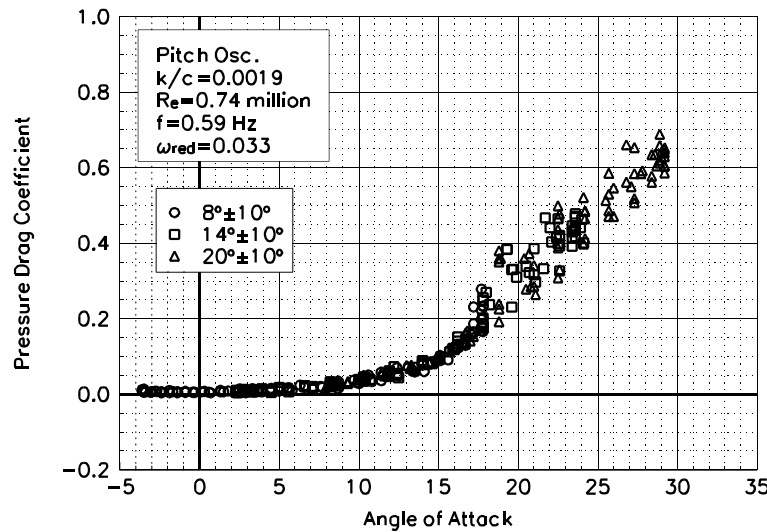


Figure C83. Pressure drag coefficient vs α .

S809
LEGR
Re=0.74 million
 $\omega_{\text{reduced}} = 0.033$

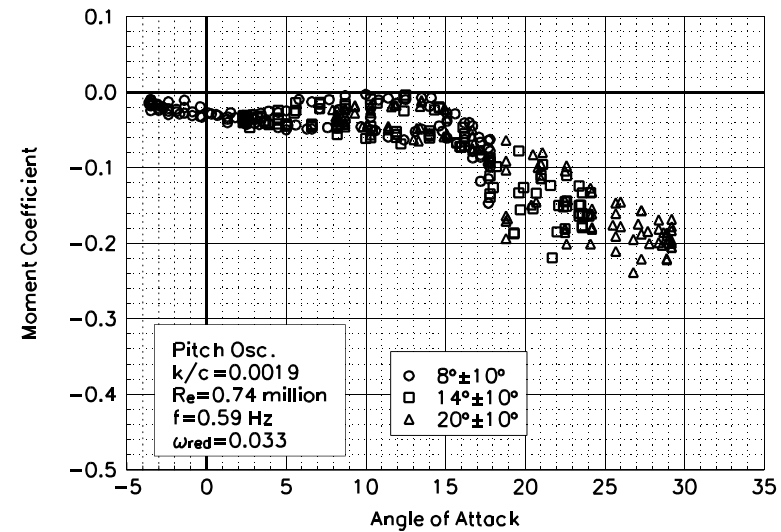


Figure C84. Moment coefficient vs α .

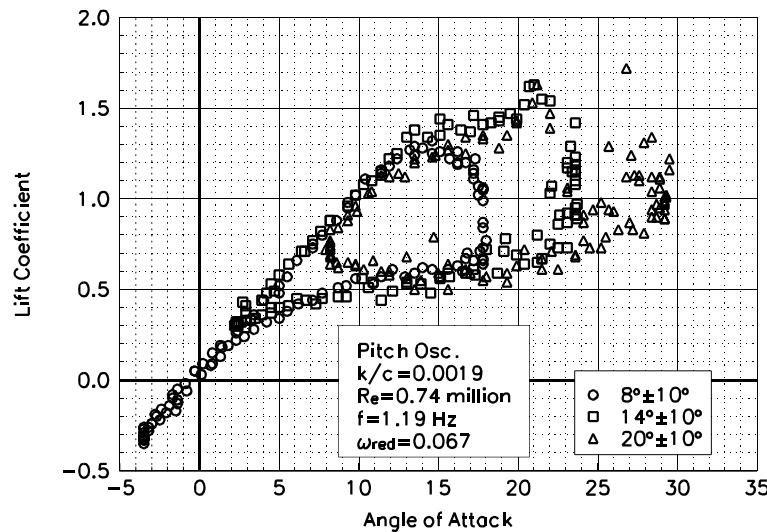


Figure C85. Lift coefficient vs α .

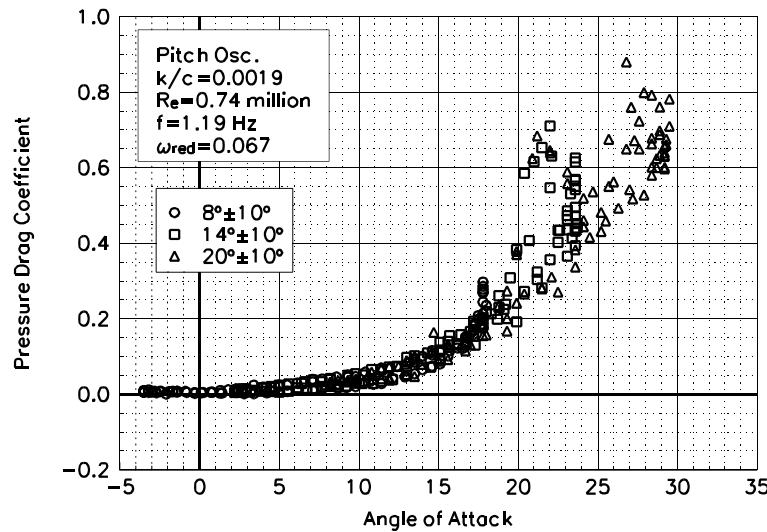


Figure C86. Pressure drag coefficient vs α .

S809
LEGR
 $Re = 0.74$ million
 $\omega_{red} = 0.067$

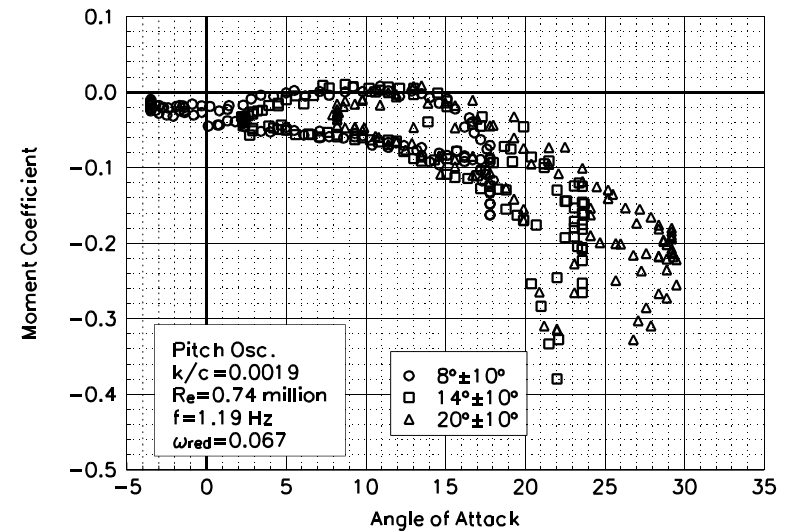


Figure C87. Moment coefficient vs α .

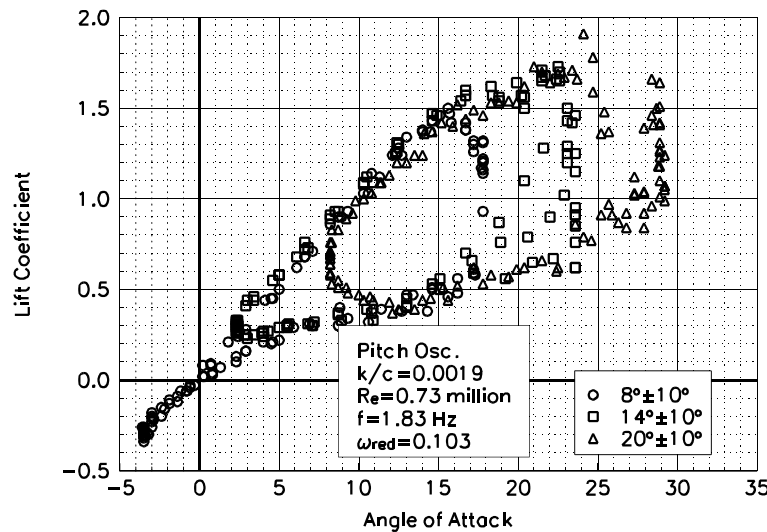


Figure C88. Lift coefficient vs α .

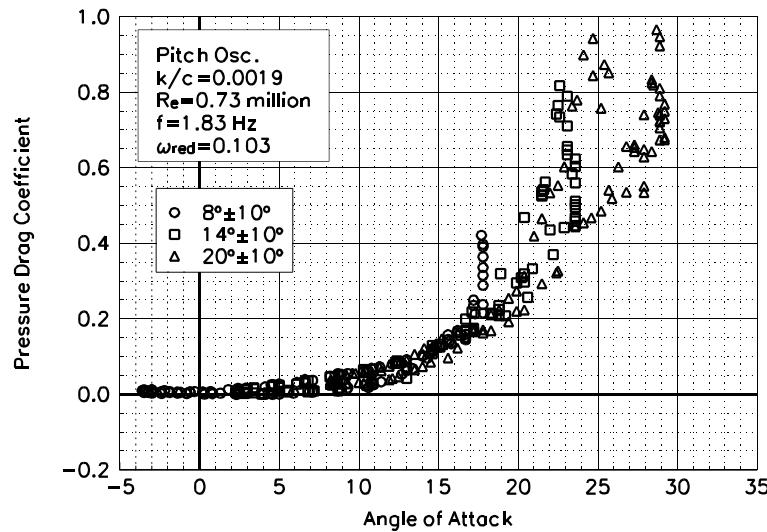


Figure C89. Pressure drag coefficient vs α .

S809
LEGR
 $Re = 0.73$ million
 $\omega_{red} = 0.103$

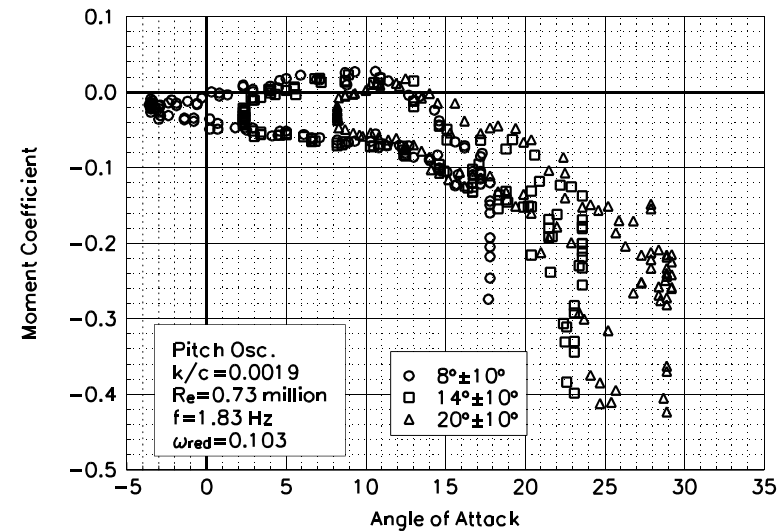


Figure C90. Moment coefficient vs α .

Unsteady Airfoil Characteristics

$\pm 10^\circ$ Sine, $Re = 1$ million

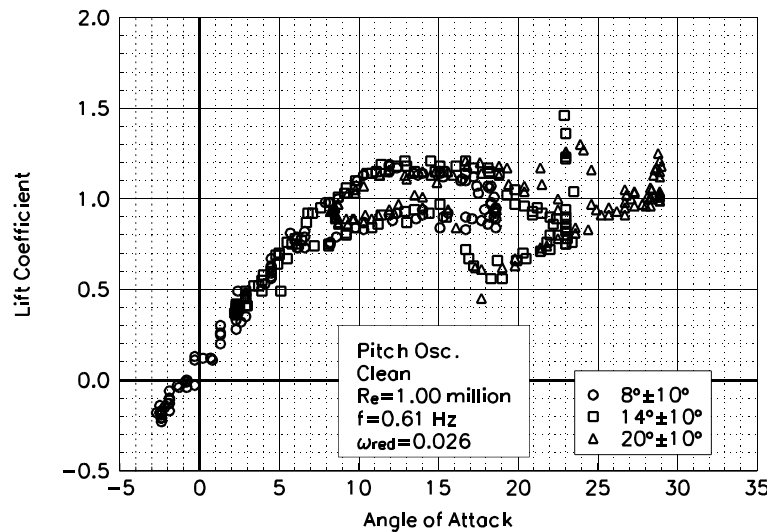


Figure C91. Lift coefficient vs α .

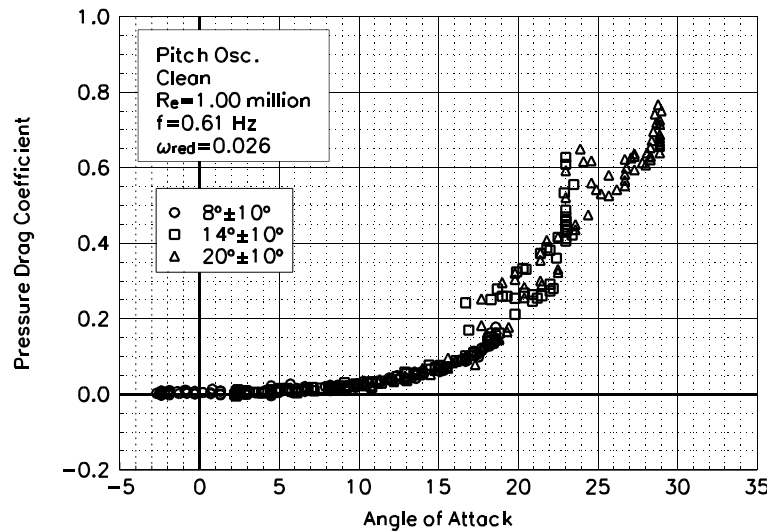


Figure C92. Pressure drag coefficient vs α .

S809
Clean
 $Re=1.00 \text{ million}$
 $\omega_{\text{reduced}}=0.026$

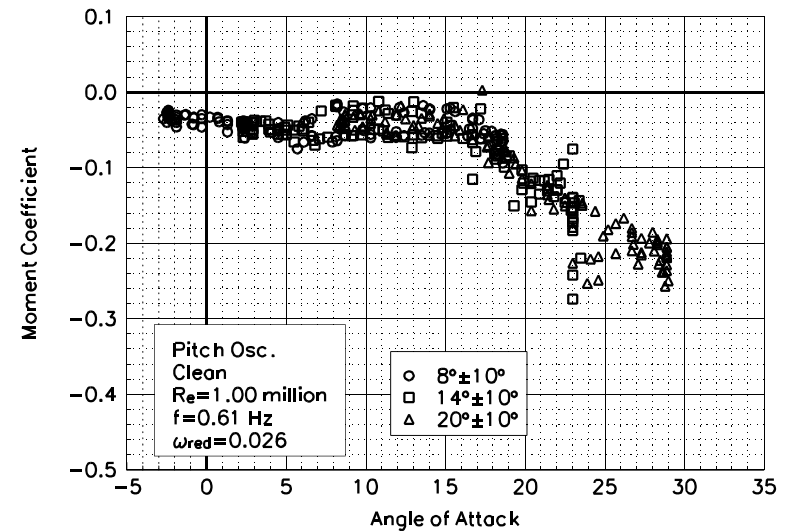


Figure C93. Moment coefficient vs α .

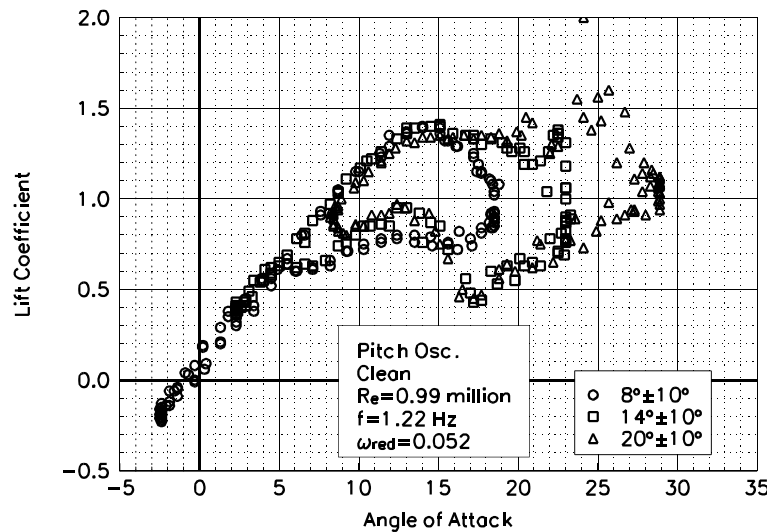


Figure C94. Lift coefficient vs α .

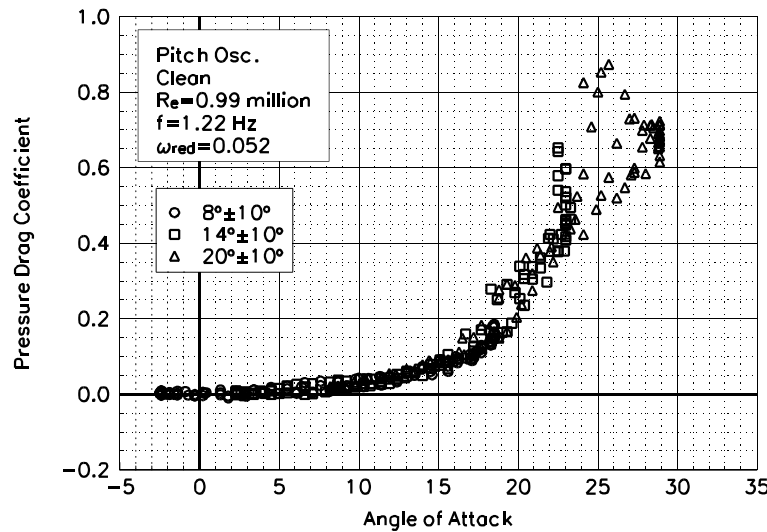


Figure C95. Pressure drag coefficient vs α .

S809
Clean
 $Re=0.99$ million
 $\omega_{red}=0.052$

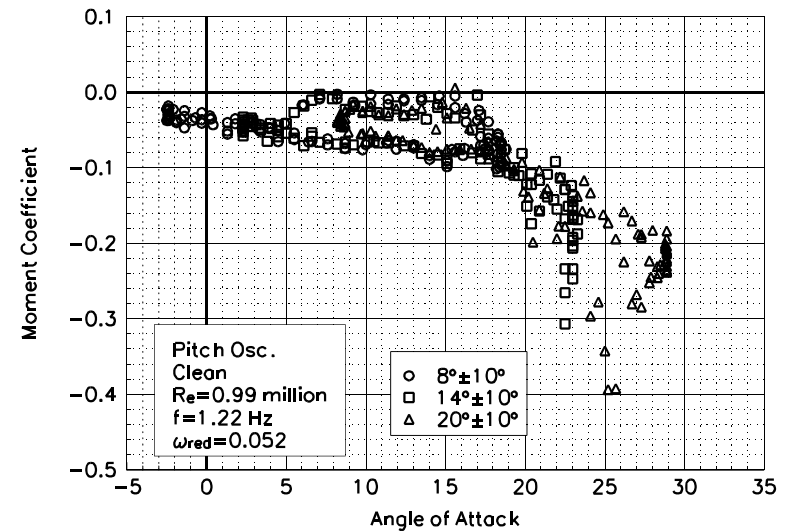


Figure C96. Moment coefficient vs α .

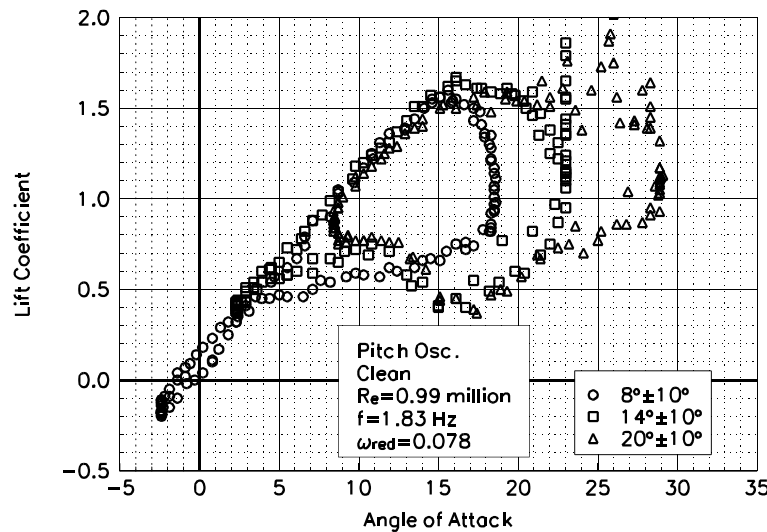


Figure C97. Lift coefficient vs α .

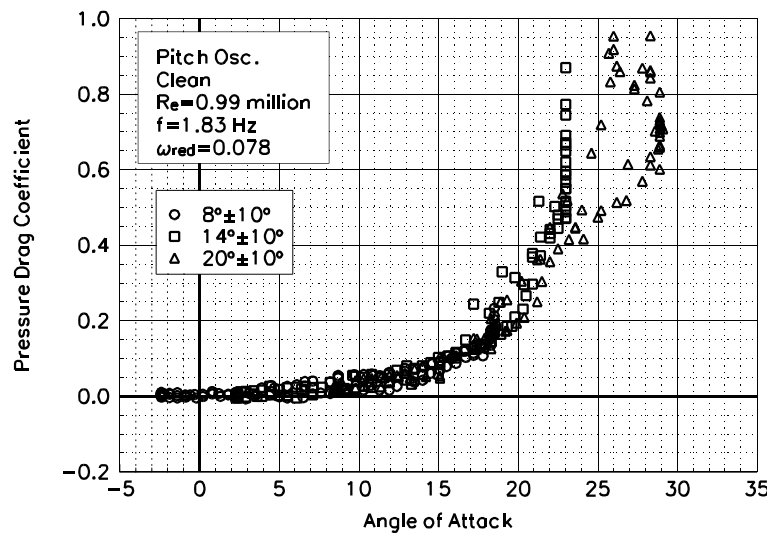


Figure C98. Pressure drag coefficient vs α .

S809
Clean
 $Re=0.99$ million
 $\omega_{red}=0.078$

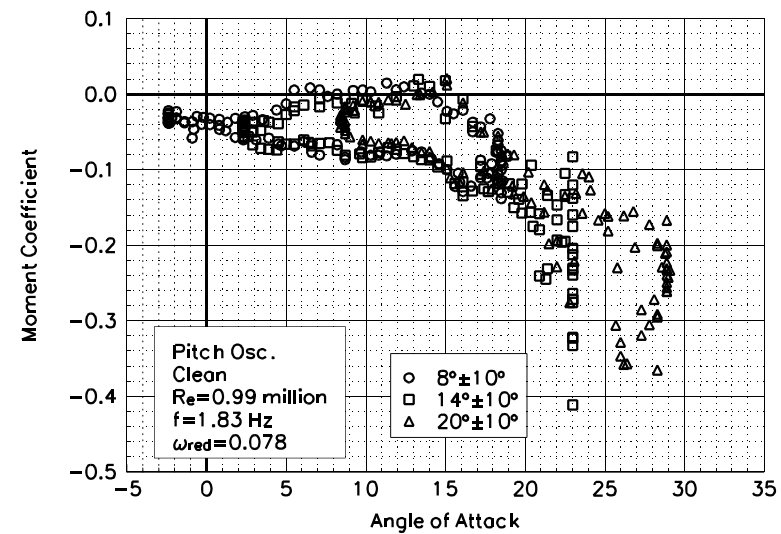


Figure C99. Moment coefficient vs α .

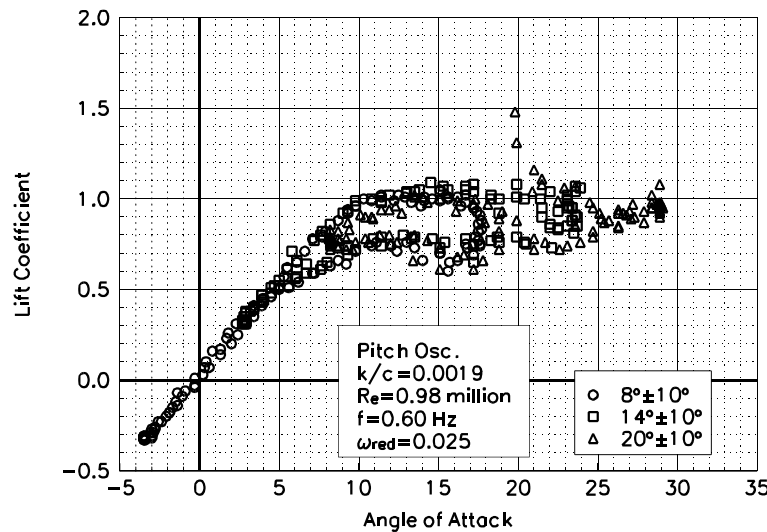


Figure C100. Lift coefficient vs α .

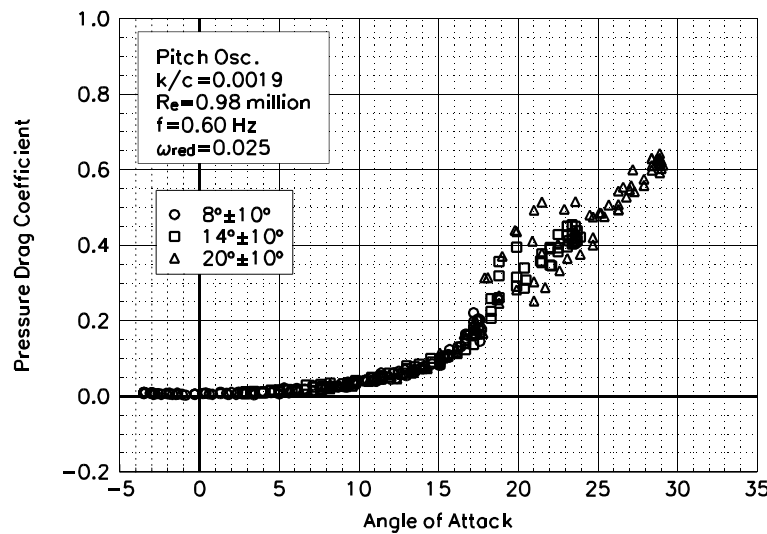


Figure C101. Pressure drag coefficient vs α .

S809
LEGR
 $Re = 0.98 \text{ million}$
 $\omega_{\text{reduced}} = 0.025$

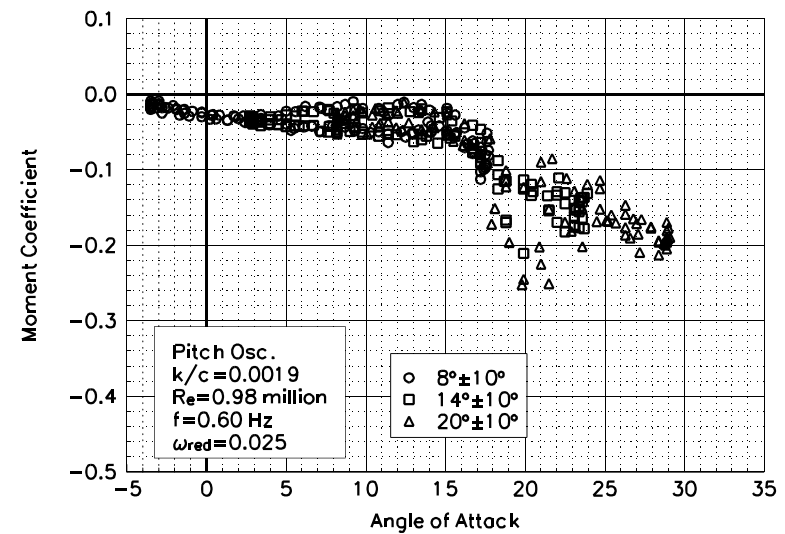


Figure C102. Moment coefficient vs α .

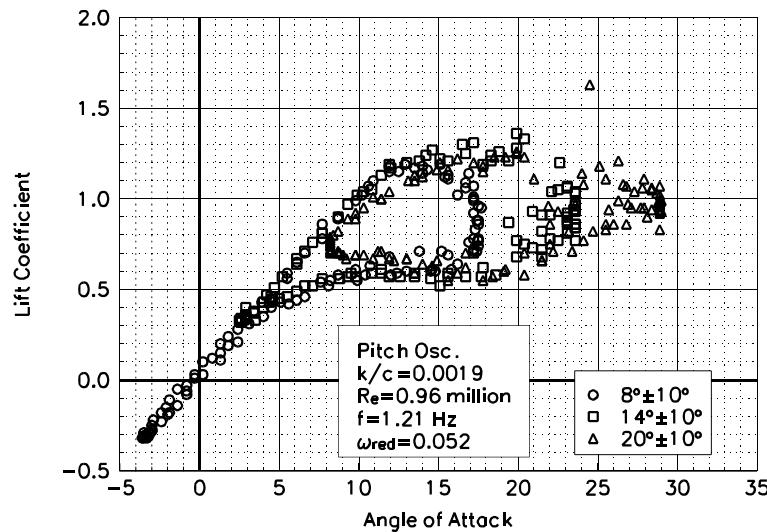


Figure C103. Lift coefficient vs α .

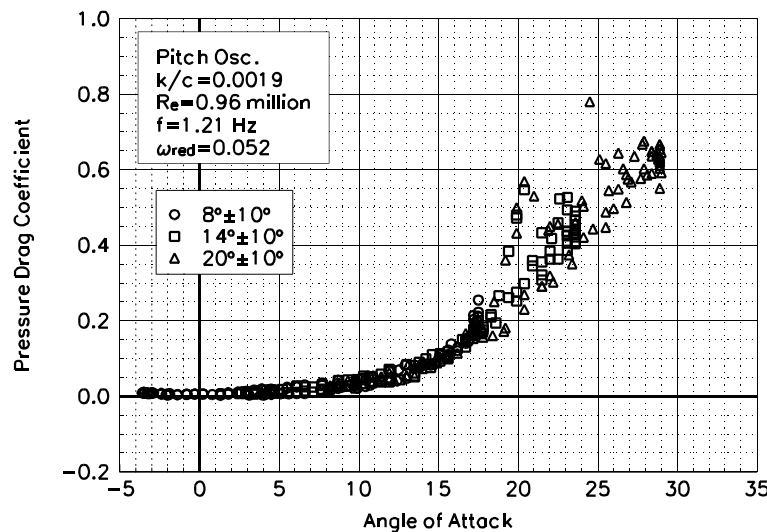


Figure C104. Pressure drag coefficient vs α .

S809
LEGR
Re=0.96 million
 $\omega_{reduced} = 0.052$

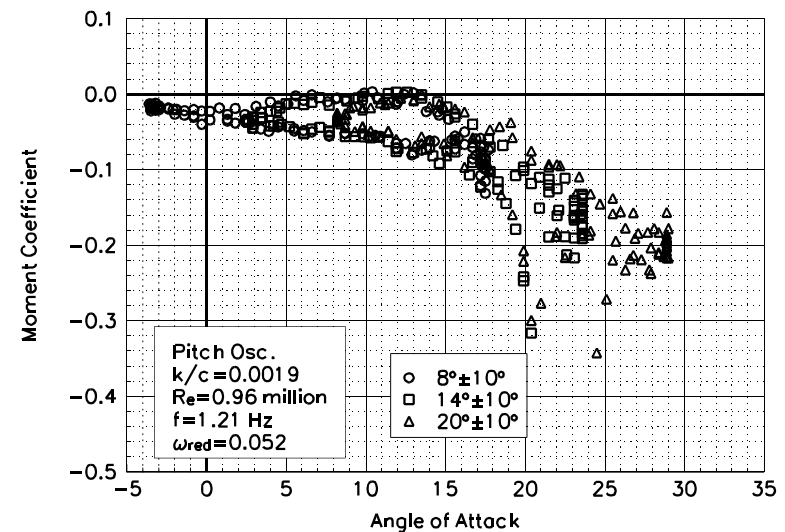


Figure C105. Moment coefficient vs α .

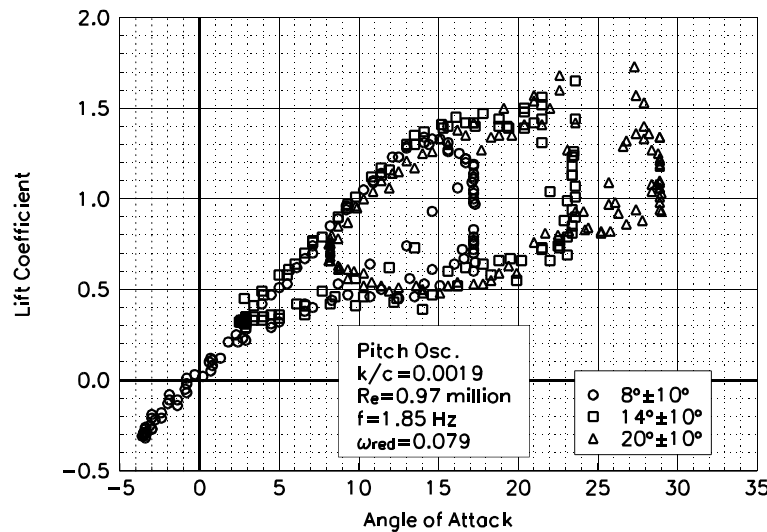


Figure C106. Lift coefficient vs α .

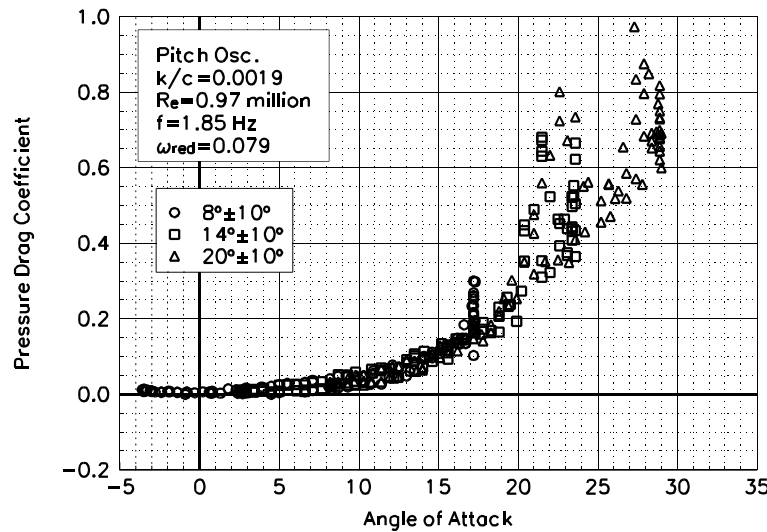


Figure C107. Pressure drag coefficient vs α .

S809
LEGR
Re=0.97 million
 $\omega_{\text{reduced}}=0.079$

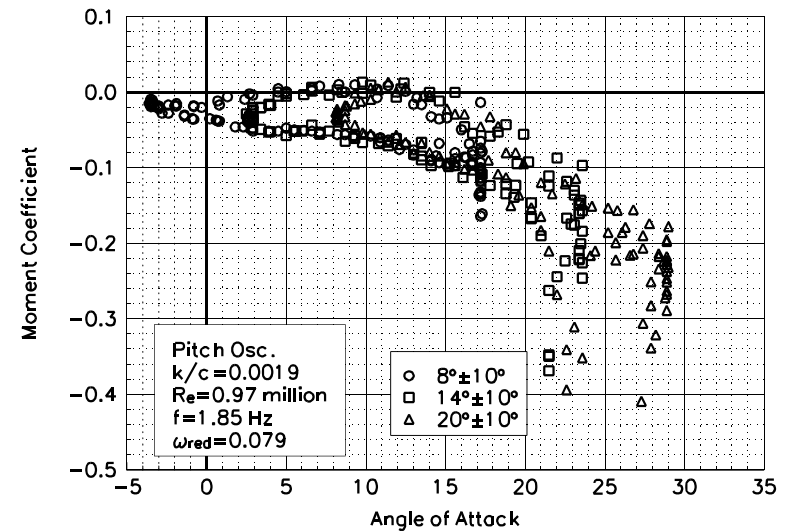


Figure C108. Moment coefficient vs α .

Unsteady Airfoil Characteristics

$\pm 10^\circ$ Sine, Re = 1.25 million

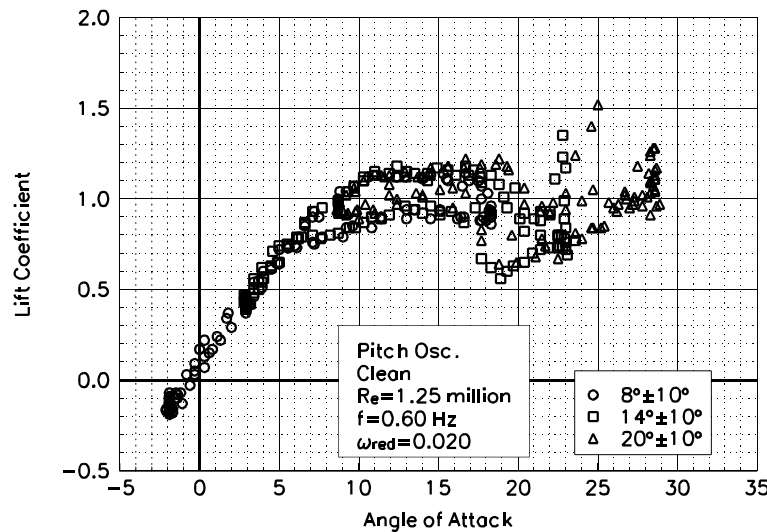


Figure C109. Lift coefficient vs α .

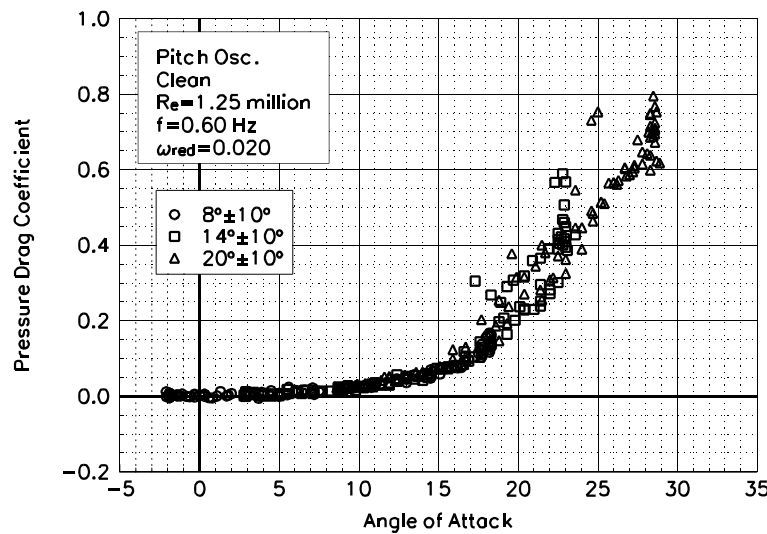


Figure C110. Pressure drag coefficient vs α .

S809
Clean
 $Re=1.25$ million
 $\omega_{reduced}=0.020$

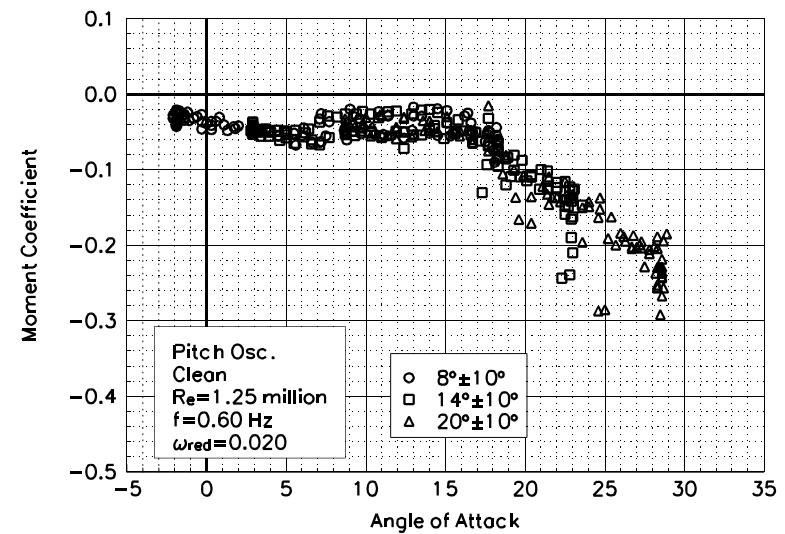


Figure C111. Moment coefficient vs α .

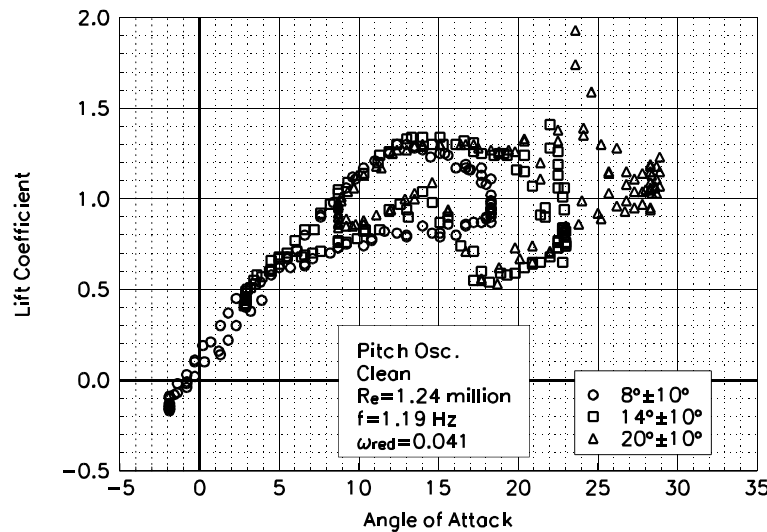


Figure C112. Lift coefficient vs α .

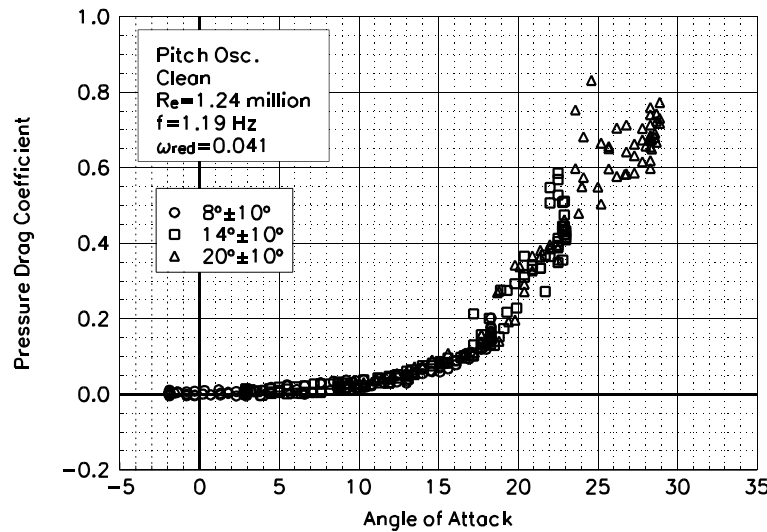


Figure C113. Pressure drag coefficient vs α .

S809
Clean
 $Re=1.24$ million
 $\omega_{red}=0.041$

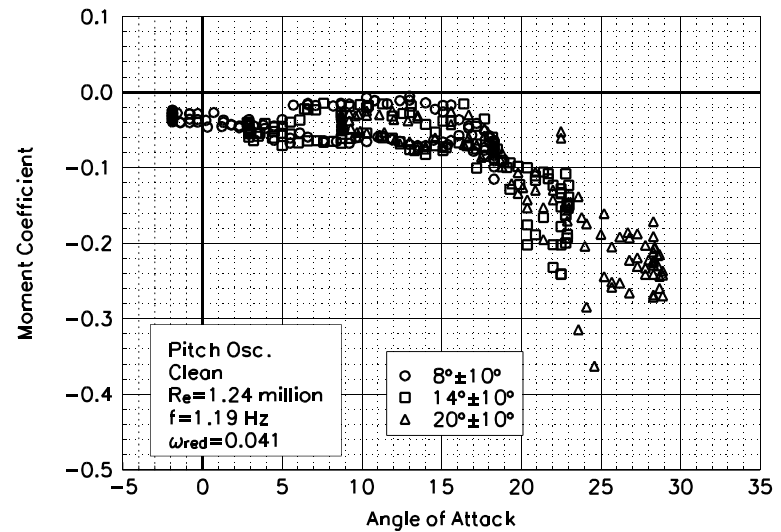


Figure C114. Moment coefficient vs α .

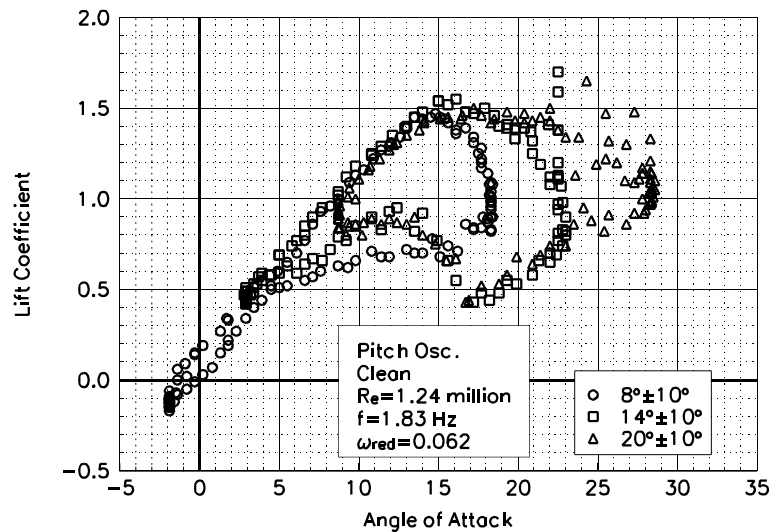


Figure C115. Lift coefficient vs α .

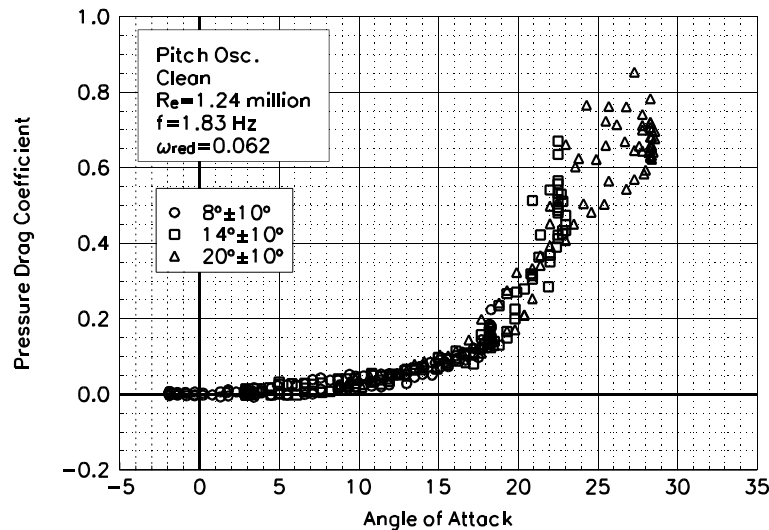


Figure C116. Pressure drag coefficient vs α .

S809
Clean
 $Re=1.24$ million
 $\omega_{red}=0.062$

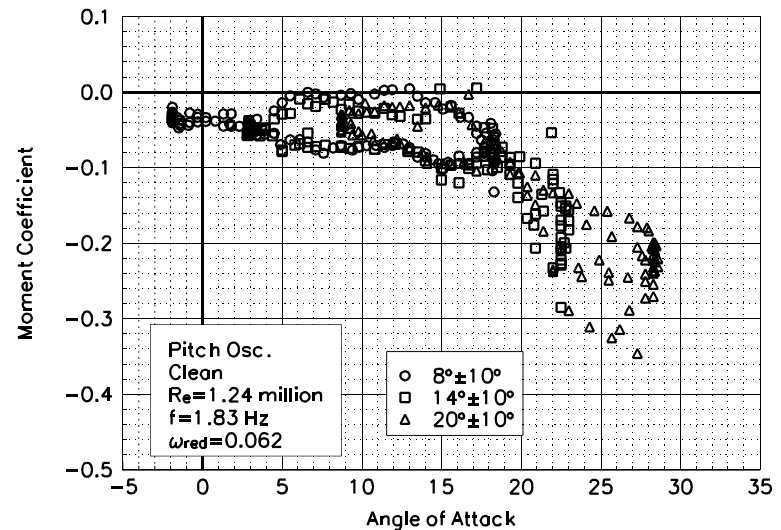


Figure C117. Moment coefficient vs α .

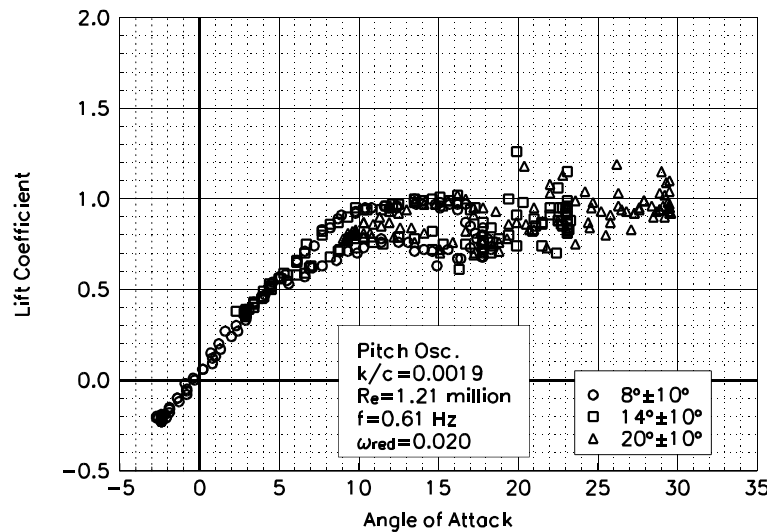


Figure C118. Lift coefficient vs α .

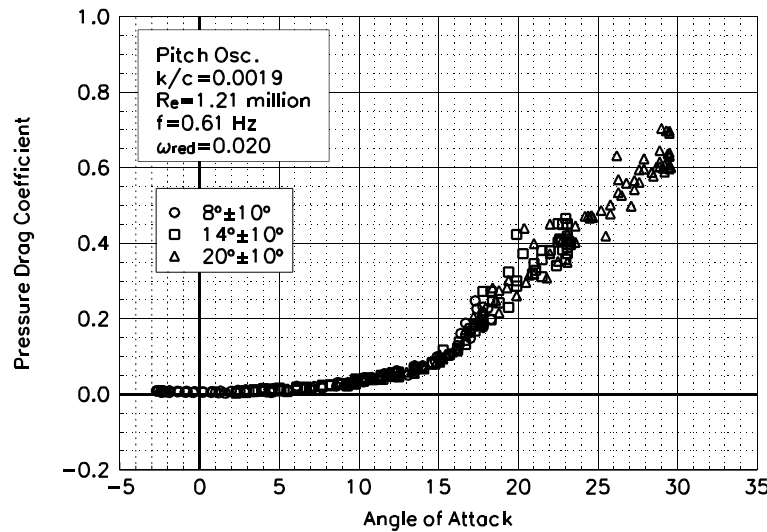


Figure C119. Pressure drag coefficient vs α .

S809
LEGR
 $Re = 1.21 \text{ million}$
 $\omega_{\text{reduced}} = 0.020$

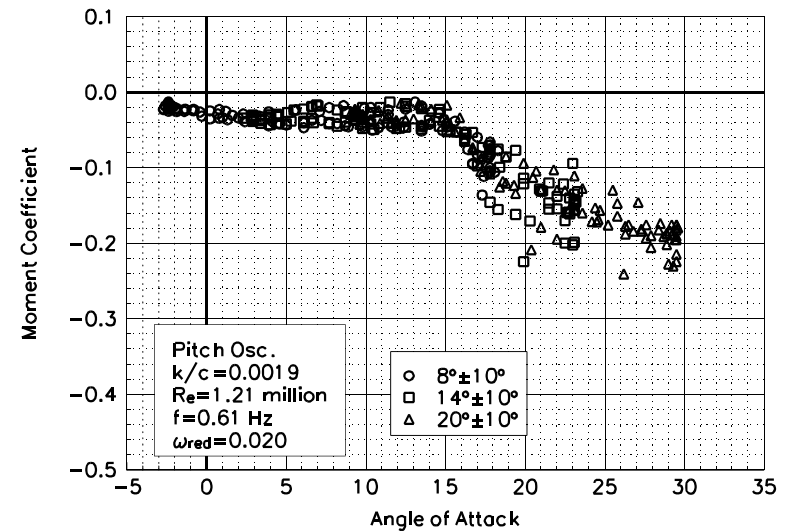


Figure C120. Moment coefficient vs α .

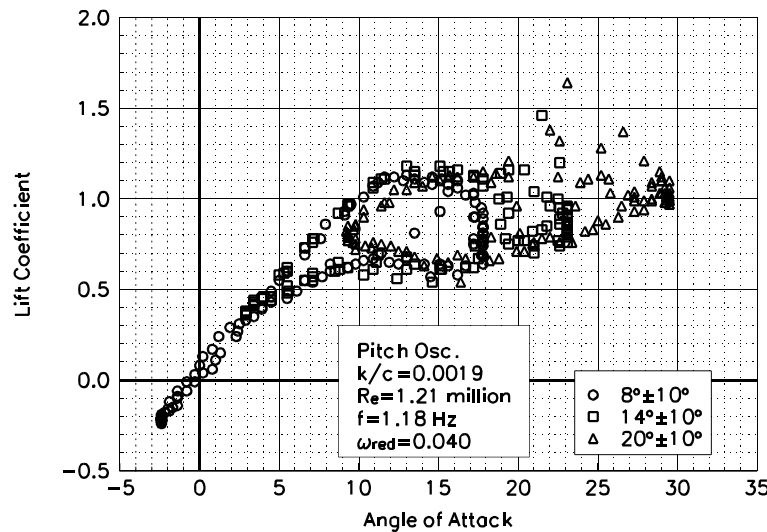


Figure C121. Lift coefficient vs α .

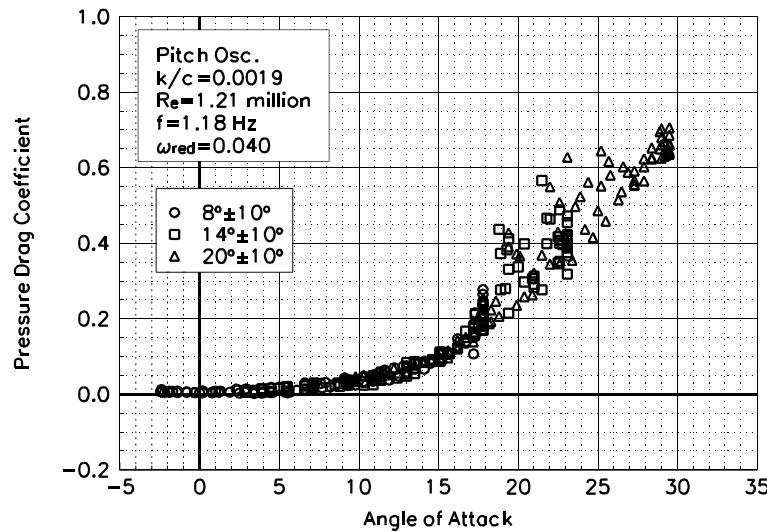


Figure C122. Pressure drag coefficient vs α .

S809
LEGR
Re=1.21 million
 $\omega_{red}=0.040$

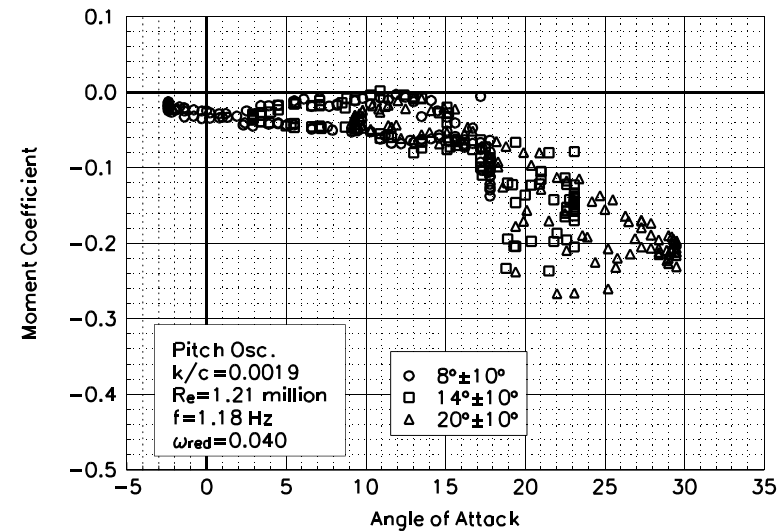


Figure C123. Moment coefficient vs α .

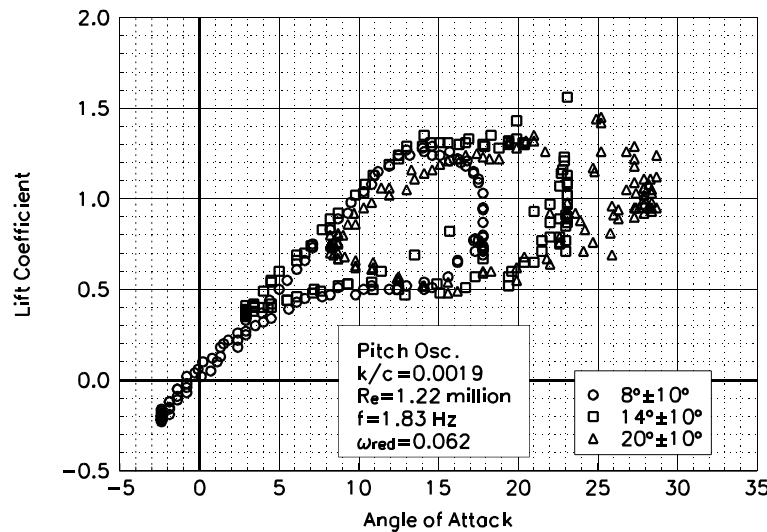


Figure C124. Lift coefficient vs α .

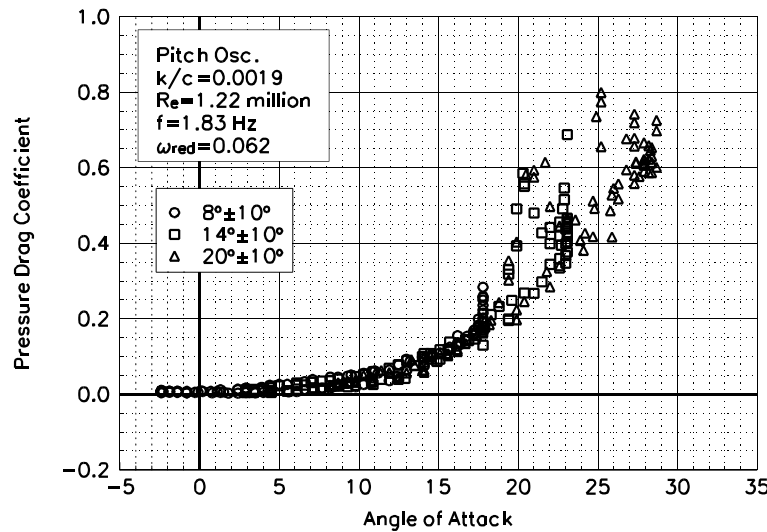


Figure C125. Pressure drag coefficient vs α .

S809
LEGR
 $Re = 1.22 \text{ million}$
 $\omega_{\text{reduced}} = 0.062$

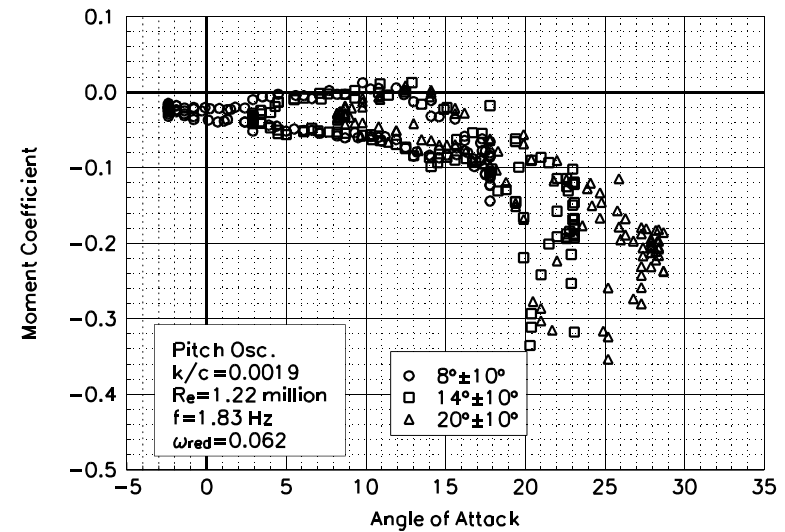


Figure C126. Moment coefficient vs α .

Unsteady Airfoil Characteristics

$\pm 10^\circ$ Sine, $Re = 1.4$ million

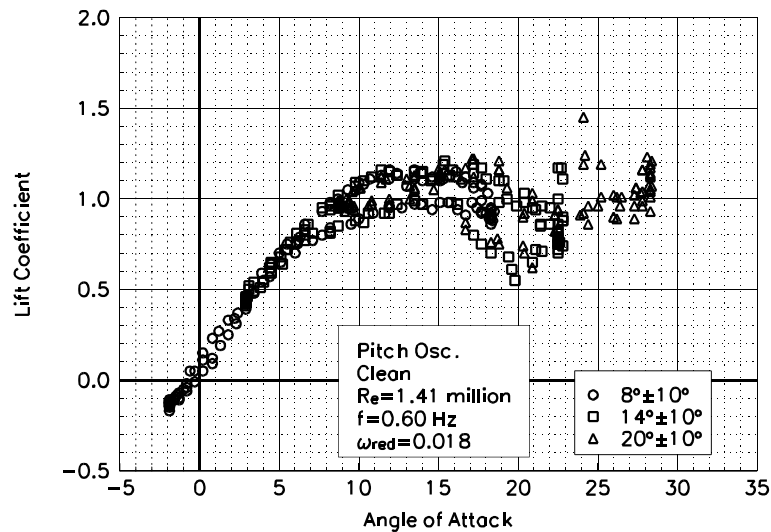


Figure C127. Lift coefficient vs α .

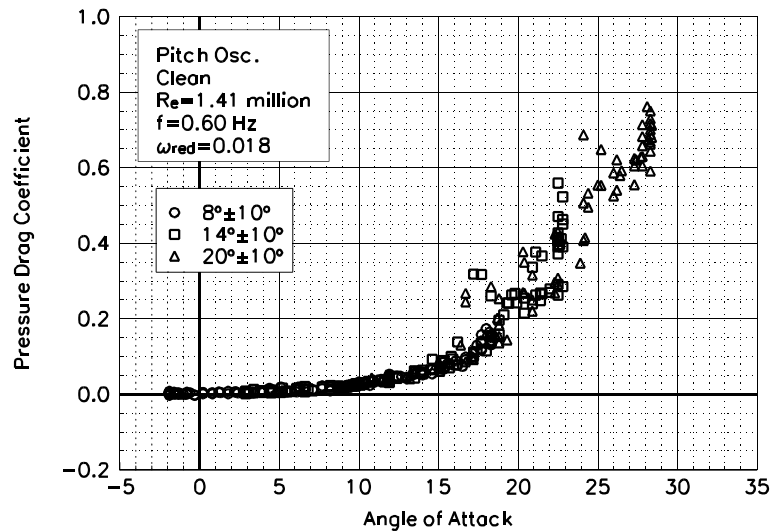


Figure C128. Pressure drag coefficient vs α .

S809
Clean
 $Re=1.41$ million
 $\omega_{reduced}=0.018$

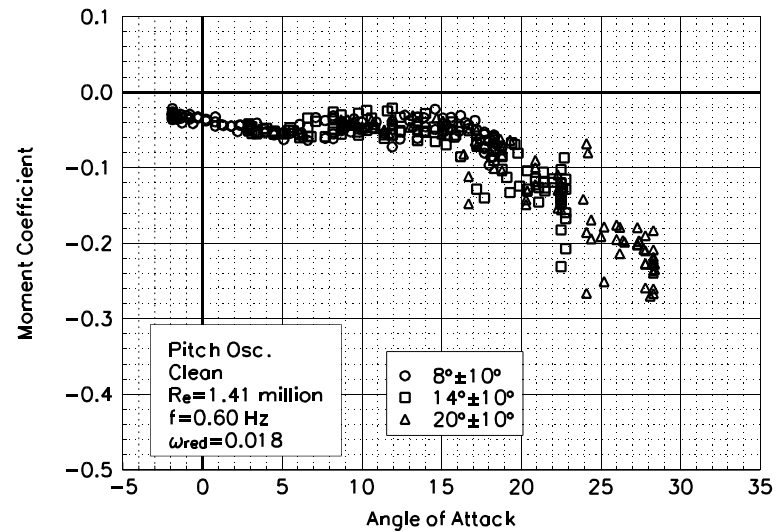


Figure C129. Moment coefficient vs α .

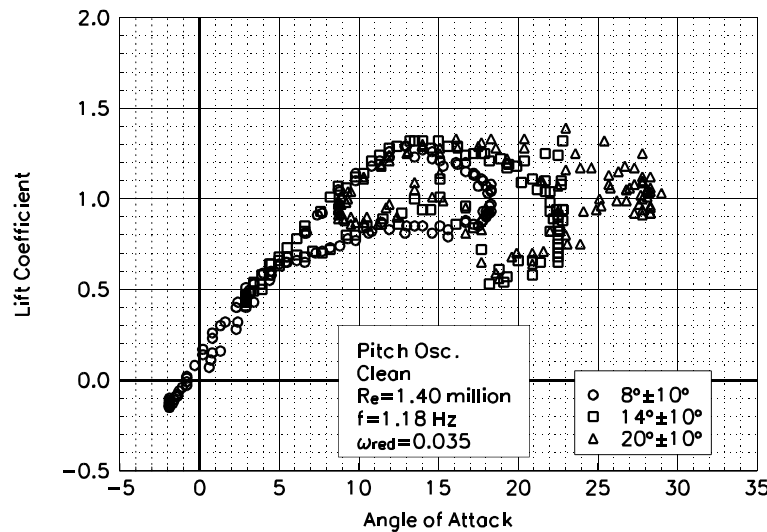


Figure C130. Lift coefficient vs α .

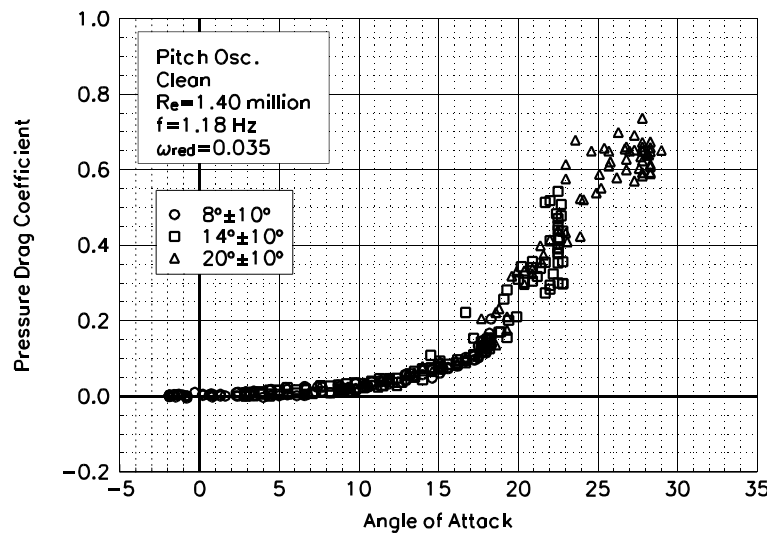


Figure C131. Pressure drag coefficient vs α .

S809
Clean
 $Re=1.40$ million
 $\omega_{red}=0.035$

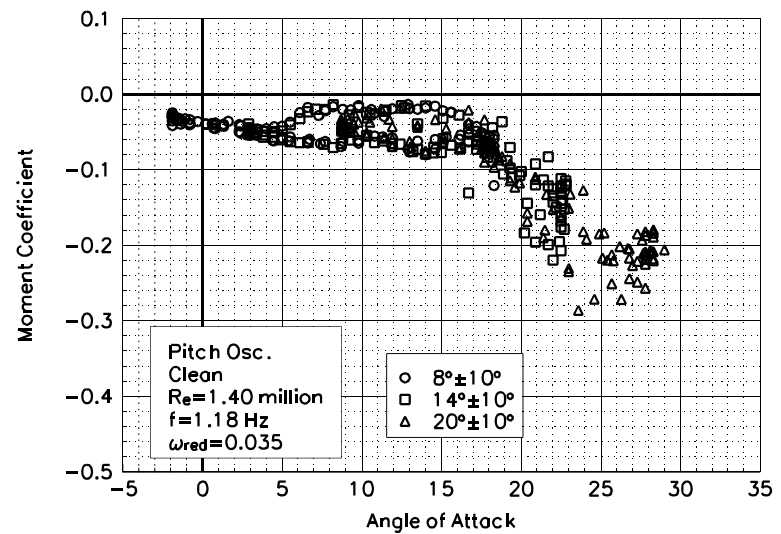


Figure C132. Moment coefficient vs α .

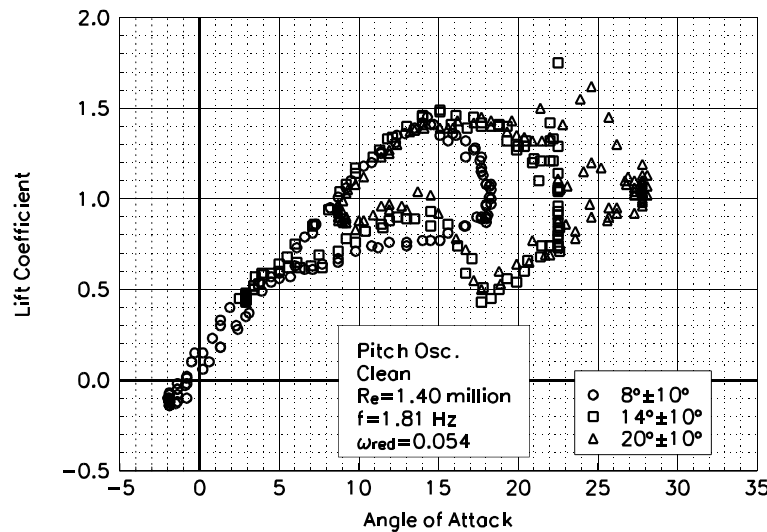


Figure C133. Lift coefficient vs α .

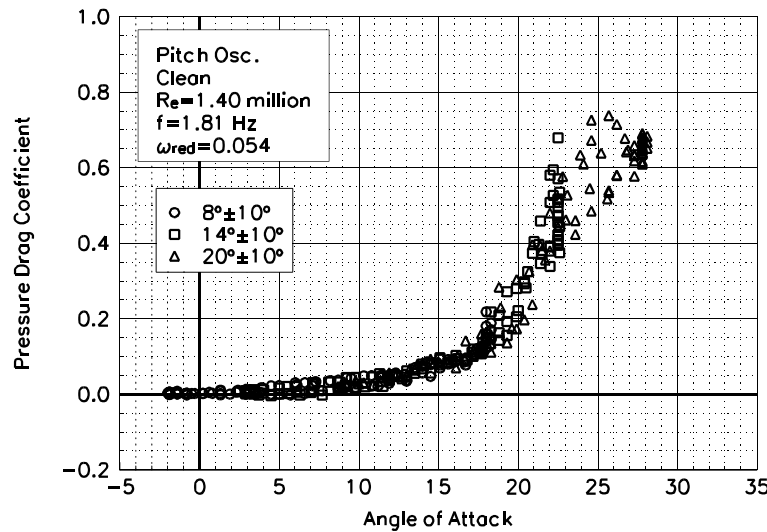


Figure C134. Pressure drag coefficient vs α .

S809
Clean
 $Re=1.40$ million
 $\omega_{red}=0.054$

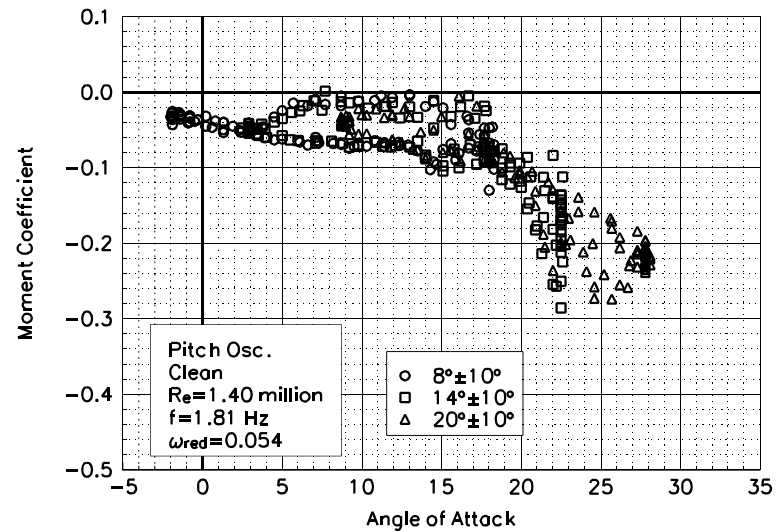


Figure C135. Moment coefficient vs α .

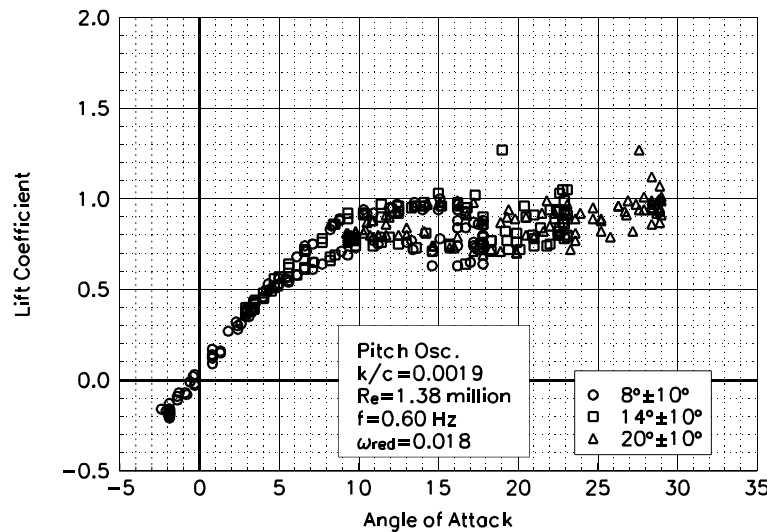


Figure C136. Lift coefficient vs α .

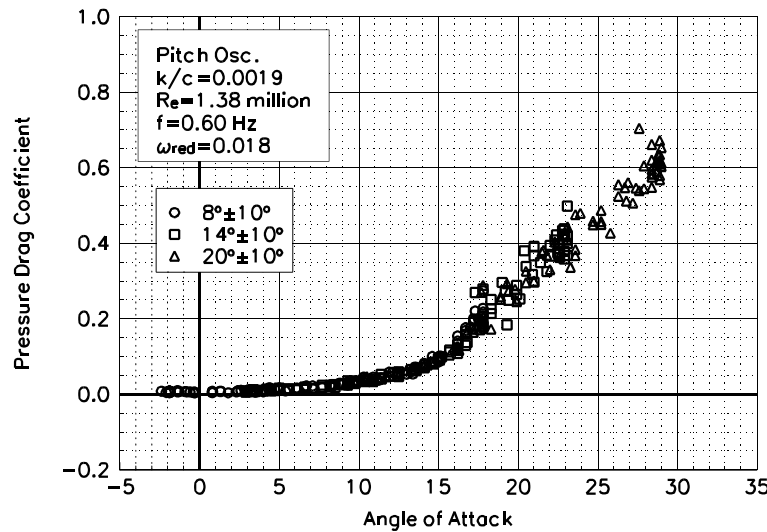


Figure C137. Pressure drag coefficient vs α .

**S809
LEGR
 $Re = 1.38 \text{ million}$
 $\omega_{\text{reduced}} = 0.018$**

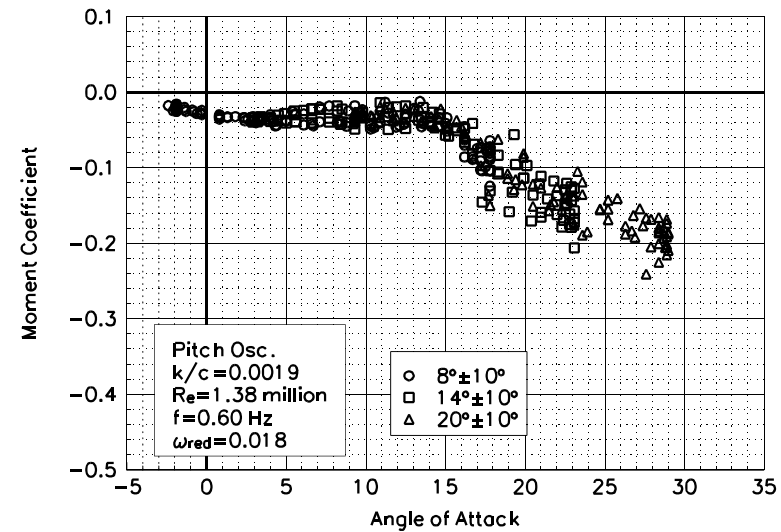


Figure C138. Moment coefficient vs α .

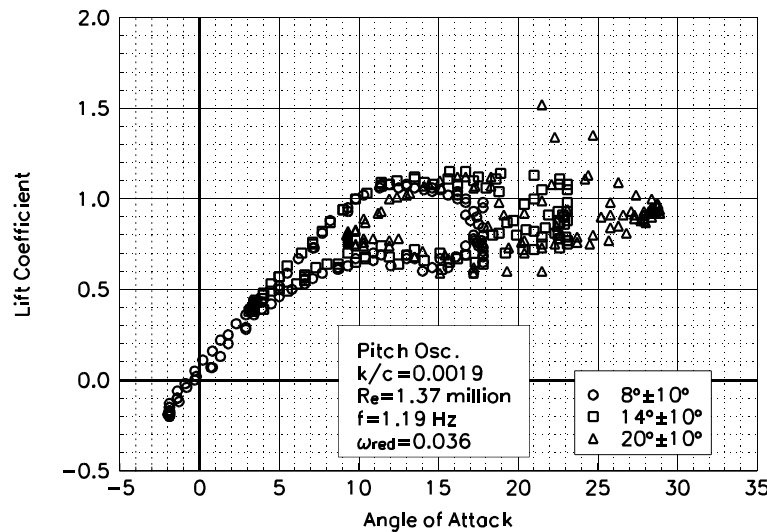


Figure C139. Lift coefficient vs α .

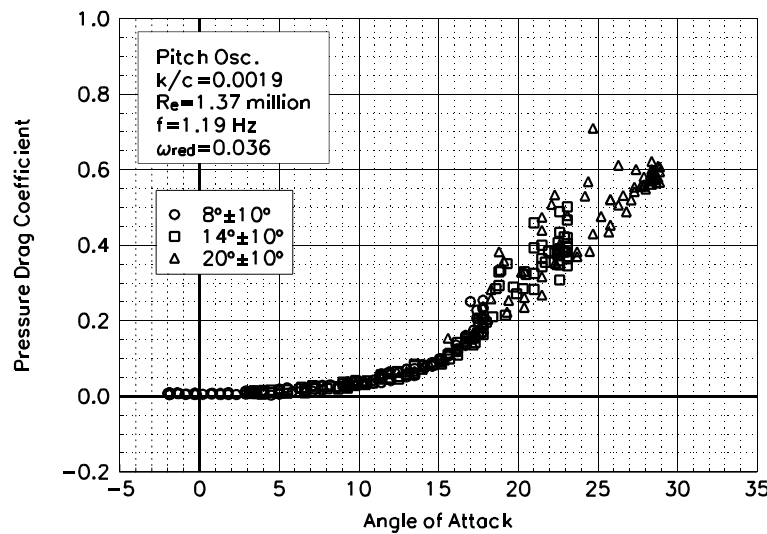


Figure C140. Pressure drag coefficient vs α .

**S809
LEGR
 $Re = 1.37 \text{ million}$
 $\omega_{\text{reduced}} = 0.036$**

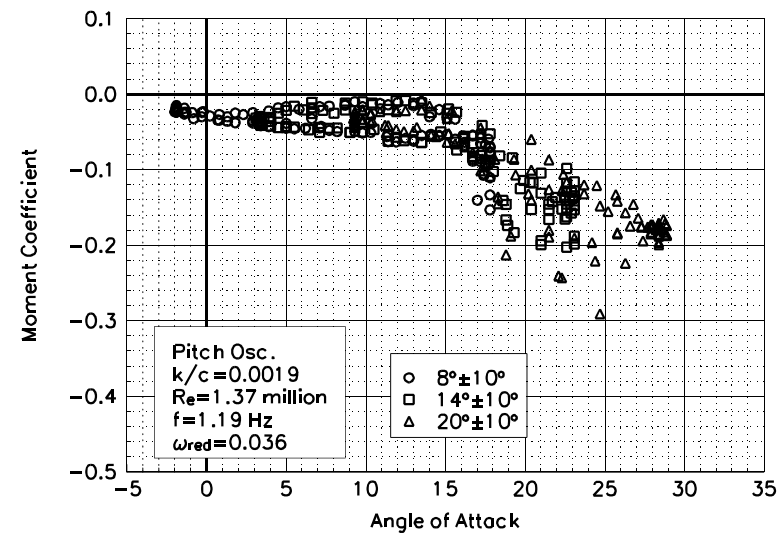


Figure C141. Moment coefficient vs α .

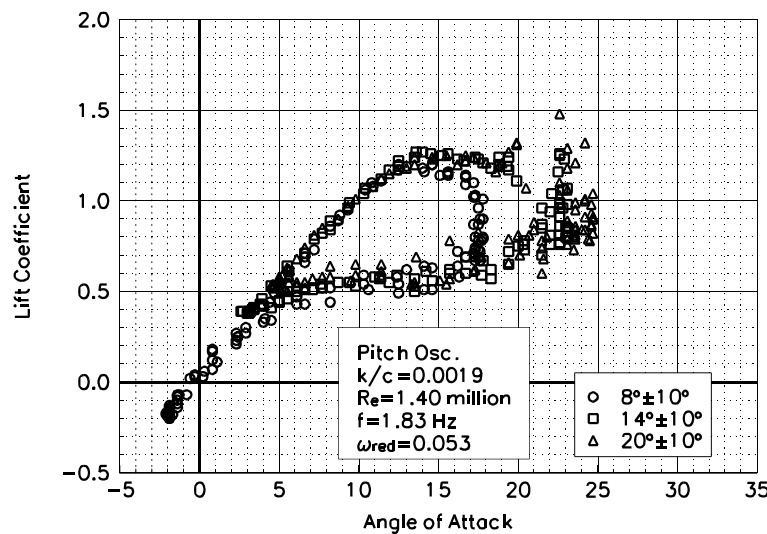


Figure C142. Lift coefficient vs α .

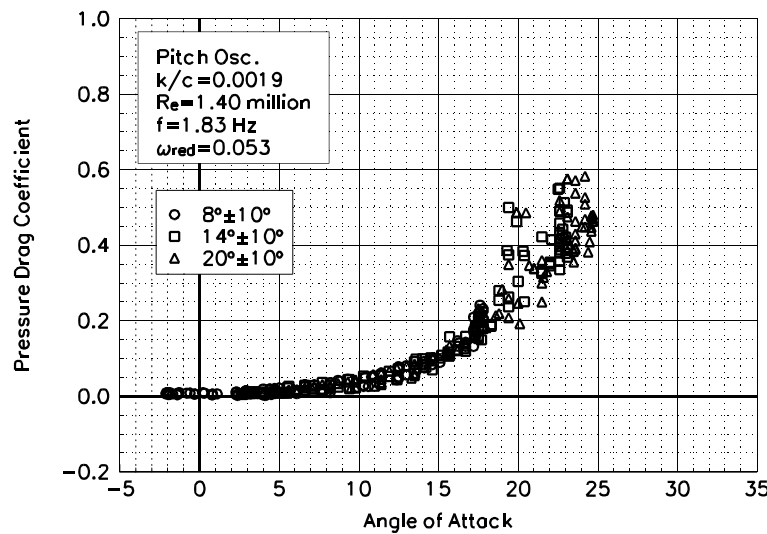


Figure C143. Pressure drag coefficient vs α .

S809
LEGR
 $Re = 1.40 \text{ million}$
 $\omega_{\text{reduced}} = 0.053$

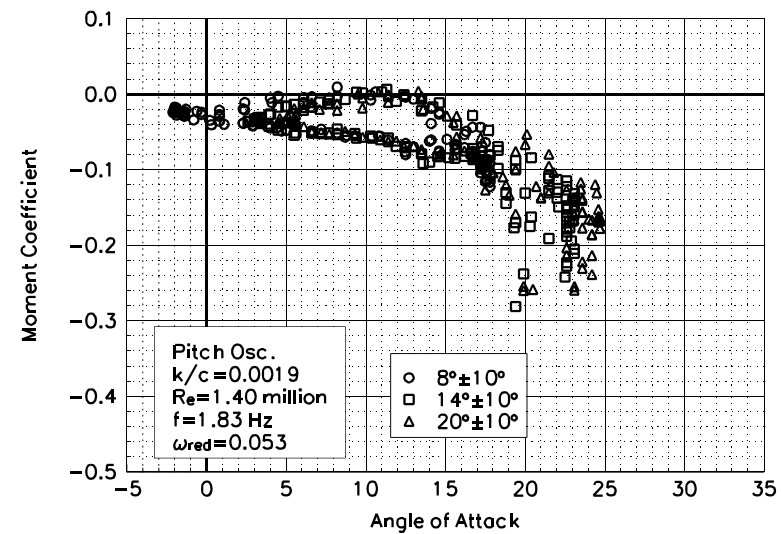


Figure C144. Moment coefficient vs α .